Controlling and upscaling laser induced surface morphology : from tens of microns to tens of nanometres

Fotios Frangelakis

université de BORDEAUX

Thèse présentée

Pour obtenir le grade de

Docteur de l'Université de Bordeaux

École doctorale: Sciences Physiques et de **l'Ingénieur**

Spécialité: Lasers, matières et nanosciences

par Fotios FRANGELAKIS

Controlling and upscaling laser induced surface morphology: from tens of microns to tens of nanometres

Sous la direction de : Inka MANEK-HÖNNINGER, Maître de conférences, HDR

Co-encadré par : John LOPEZ, Ingénieur de recherche

Date de soutenance : 14 Février 2019

Membres du jury :

Pr. Antonio ANCONA	University of Bari	Examinateur
Dr. Jörn BONSE	Bundesanstalt f. Materialforschung und -prüfung Berlin	Rapporteur
Pr. Evelyne FARGIN	Université de Bordeaux	Présidente
Dr. Inka MANEK-HÖNNIGER	Université de Bordeaux	Directrice de thèse
Pr. Gert-Willem RÖMER	University of Twente	Rapporteur
Dr. John LOPEZ	Université de Bordeaux	Invité
Dr. Rainer KLING	ALPhANOV	Invité

Acknowledgements

First of all, I would like to warmly thank Inka Manek-Hönninger, John Lopez and Rainer Kling who supervised me throughout this demanding work. I am particularly grateful to my supervisor and friend Girolamo Mincuzzi, who has been constantly present, dedicating time and effort to guide me through the everyday difficulties. In a combined effort, they provided valuable guidance in the most critical points of this thesis.

Second, because this work was a part of the international training network Laser4Fun, I would like to acknowledge all the people that worked to realise and manage the project. They provided a unique research experience. Within the project, I would like to thank particularly the professors Andres Lasagni and Antonio Ancona along with their groups for the warm hospitality during my secondments. I am grateful for all the nice moments we spent together with the Laser4Fun PhD candidates and friends.

Third, apart the participants of the project, I would like to acknowledge George Tsibidis and Evgeny L. Gurevich for the fruitful discussions we had.

Moreover, I owe special thanks to Benoit Appert-Collin director of ALPhANOV and to Eric Mevel head of CELIA for offering me the chance to work in an interesting and diverse environment. To Marie & Sophie, for their aid in dealing with the scary French administrative system. I also thank my colleagues for welcoming me and making a rather pointless effort to teach me French. To Konstantin Mishchik with whom we shared an office for almost three years, having interesting discussions, evenly shared with long quiet hours.

Lastly, I am truly grateful to my companion Mariellen for her support, and to my friend Marko for the good and bad moments we spent together. Without them these three years would not be as nice and successful as they were.

Funding

This work has been founded by the Horizon 2020 Framework Program (H2020) under the Marie Skłodowska-Curie grant agreement (No 675063) and the project Laser4Fun.

Summary for the public in English

Current industrial markets demand highly value-added products offering new features at a low-cost. Among the most desired functionalities are, surface colouring and blackenning, anti-icing, anti-biofouling, wear reduction and anti-reflectivity. Functional textures found in nature indicate that those properties can be enable by textures in the micro and nanoscale. Laser surface processing holds a virtually endless potential in mimicking bio inspired textures by modifying surface morphology and chemistry. Several techniques such as polarization control and double-pulse irradiation were investigated in order to achieve controlled laser structuring in the submicron regime. Valuable data were provided both in the surface functionalization, in understanding and controlling of laser induced structuring and in upscaling a lab developed process. The presented results contribute to the exploitation of laser texturing in everyday applications applying up to date laser sources and positioning systems.

Summary for the public in French

L'Industrie actuelle demande des produits à haute valeur ajoutée offrant des nouvelles fonctions à moindre coût telles que la coloration ou le noircissement de surface, la réduction des frottements, la génération de surface antiréflexion, antibactérienne, superhydrophobe ou anti-icing. Les surfaces fonctionnelles présentes dans la nature nous indiquent que ces propriétés uniques ne sont possibles par des texturations de surface à l'échelle micro et nanométrique adéquates. La technologie laser révolutionne le champ des possibles et permet de reproduire ces fonctions inspirées du monde du vivant en modifiant la morphologie et la chimie de surface. Nous avons étudié plusieurs techniques de texturation de surface par laser femtoseconde en jouant sur la polarisation et l'irradiation en double impulsion. Ces travaux de recherche apportent une contribution significative dans la compréhension des mécanismes et dans la capacité à produire de telles texturations sur des grandes surfaces.

CONTENTS:

Abstract en français

L'Industrie actuelle demande des produits à haute valeur ajoutée offrant des nouvelles fonctions à moindre coût. Parmi les fonctions on peut citer la coloration de surface, le noircissement de surface, la réduction des frottements, la génération de surface anti-réflexion, anti-bactérienne, superhydrophobe ou anti-formation de glace. Les surfaces fonctionnelles présentes dans la nature nous indiquent que ces propriétés uniques sont possibles par des texturations de surface à l'échelle micro et nanométrique adéquates. Parallèlement à cela, la technologie laser révolutionne le champ des possibles en termes de texturation de surface et permet de reproduire ces fonctions inspirées du monde du vivant en modifiant la morphologie et la chimie de surface. Néanmoins, le développement et le déploiement de telles techniques de texturation laser au niveau industriel nécessite la levée de trois verrous. Le premier est de connecter les propriétés macroscopiques (couleur, résistance mécanique, stabilité chimique, vieillissement) et la morphologie de surface aux échelles nano et microscopiques. Le second d'acquérir une parfaite maîtrise de la morphologie de surface à ces échelles. Le troisième est la transposition du procédé développé en laboratoire en procédé industriel adapté aux traitements de grandes surfaces avec des temps de cycles les plus courts possibles. Nous avons étudié plusieurs techniques de texturation de surface à l'échelle submicronique par laser femtoseconde. Ainsi des « ripples » de quelques dizaines de nanomètres ont être réalisées par laser UV. L'irradiation avec double impulsion apporte une capacité supplémentaire dans le contrôle de la morphologie de surface finale. Différents types de structures, avec différentes symétries, ont ainsi été produites en jouant sur le délai entre les deux impulsions. Des structures LIPSS homogènes triangulaires ou carrées ont été obtenues pour des délais inférieurs à 5 ps et 500 ps respectivement. Des paramètres opératoires, en particulier la fluence et la polarisation, ont été identifiés comme jouant un rôle majeur dans les caractéristiques de la morphologie de surface finale. Des expériences complémentaires ont montré que des résultats similaires peuvent être obtenus en utilisant des cristaux biréfringents pour générer des délais courts. Nous avons également exploré la possibilité d'utiliser des trains d'impulsions uniques pour produire des texturations de surface de dimensions caractéristiques supérieures allant de quelques microns à plusieurs dizaines de microns en faisant varier de manière systématique la fluence, la dose énergétique et le taux de répétition du laser. La comparaison de résultats expérimentaux avec ceux issus de simulation nous avons mis en évidence le rôle majeur de l'accumulation thermique sur les dimensions caractéristiques des structures générées par laser. Par ailleurs, nous avons démontré la capacité du procédé à produire de texturations sub-longueurs d'onde, homogènes, sur des surfaces supérieures à 1 cm², avec des lasers ayant des taux de répétitions allant jusqu'à 10 MHz et des systèmes de positionnement innovants. Des nano-rugosités de surface ainsi produites affichent des propriétés de super hydrophobicité. A titre d'exemple, nous avons atteint un temps de texturation de l'ordre de 1 min/cm², soit 60 fois inférieurs à ce que nous obtenions en début des travaux. Enfin, nous avons démontré un temps de 9 s/cm² pour le noircissement de surface.

Ces travaux de recherche, mettant à profit des sources laser et des équipements de déflection optique de dernière génération, apportent une contribution significative dans la compréhension des mécanismes d'une part, et dans la capacité à contrôler et à produire de telles texturations sur des grandes surfaces d'autre part. Ils devraient favoriser une dissémination rapide de ces technologies de texturation laser dans l'industrie.

Summary

Current industrial markets demand highly value-added products offering new features at a low-cost. Among the most desired functionalities are surface colouring and blackening, anti-icing, anti-biofouling, wear reduction and anti-reflectivity. Laser surface processing holds a virtually endless potential in surface functionalization since it can generate versatile surface properties by modifying surface morphology and chemistry.

Nevertheless, developing functional surfaces for implementation in the industry requires action on three levels. The first is to connect the macro-scale surface properties (colour, mechanical resistance, chemical stability, ageing) and the micro & nano-scale morphology. The second is to increase the level of control over the laser induced morphology in the near micron and submicron scale. The third is to upscale the lab-developed process both in terms of processed area and cycle time.

Functional textures found in nature can be used as a guideline for connecting the surface texture with the surface property. It is well established that different textures can enable different functionalities. Nevertheless, the level of control of the laser induced morphology has to be improved significantly in order to allow one to mimic nature's examples. Increase of control requires an in-deep understanding of the physical mechanisms that lead to nanostructure formation. To this end, we carry out a comprehensive parametric study of fs processing on stainless steel. The impact of wavelength, spot overlap, fluence, dose, repetition rate, polarization and interpulse delay in the induced morphology was investigated.

We investigate several techniques to achieve controlled laser structuring in the submicron regime. Ripples of a few tens of nanometres were obtained with a UV laser. Double pulses were employed to further control the submicron structures. Structures of different size and symmetry were obtained in different delays underlining the key role of the interpulse delay ($\Delta\tau$). Homogeneous triangular and square 2D-LIPSS were obtained for $\Delta\tau$ smaller than 5 ps and 500 ps, respectively. Process parameters and particularly fluence and polarization were found to play also a role in the laser induced feature characteristics. In a complementary set of experiments, we show that similar results can be obtained for small delays with a robust setup of birefringent crystals.

In the above micron regime, trains of single pulses were employed for controlling the surface morphology. Fluence, dose and repetition rate, were varied to show a systematic variation of spikes in the range of tens of micrometers. Combining our experimental results with simulation data we underline the key role of heat accumulation on the structures size. Finally, we proposed an upscaling strategy showing the possibility to exploit repetition rates up to 10 MHz for laser texturing.

In the upscaling part, areas much larger than the spot size were textured homogenously using high repetition rate laser and innovative laser positioning systems. Nanometric ripples induced by UV laser act as a subwavelength grating. Laser induced nano roughness exhibits superhydrophobic properties. Uniform distribution of well-defined, sub-wavelength, 2D-LIPSS was successfully generated over ~1 cm^2. The final surface exhibits multiple axis iridescence giving a holographic effect. Employing a 10 MHz fs laser, surface was textured homogeneously with spikes at a rate of ~ 1 min/cm^2. Lastly, surface blackening was achieved at a rate of ~ 9 sec/cm^2.

In conclusion, valuable data were provided both in surface functionalization, in understanding and controlling of laser induced structuring and in upscaling a lab developed process. We believe that our results open the way for exploiting fs laser texturing in everyday applications employing up to date laser sources and positioning systems.

Synopsis en français

L'Industrie actuelle demande des produits à haute valeur ajoutée offrant des nouvelles fonctions à moindre coût. Des structures à l'échelle micro ou nanométrique ayant des symétrie 2D doivent en principe permettre de conférer des propriétés spécifiques à des surfaces solides. Parmi les fonctions on peut citer la coloration de surface[1], le noircissement de surface[2], la réduction des frottements, la génération de surface anti-réflexion[3], anti-bactérienne[4], superhydrophobe[5] ou anti-formation de glace. Les surfaces fonctionnelles présentes dans la nature nous indiquent que ces propriétés uniques sont possibles par des texturations de surface à l'échelle micro et nanométrique adéquates.

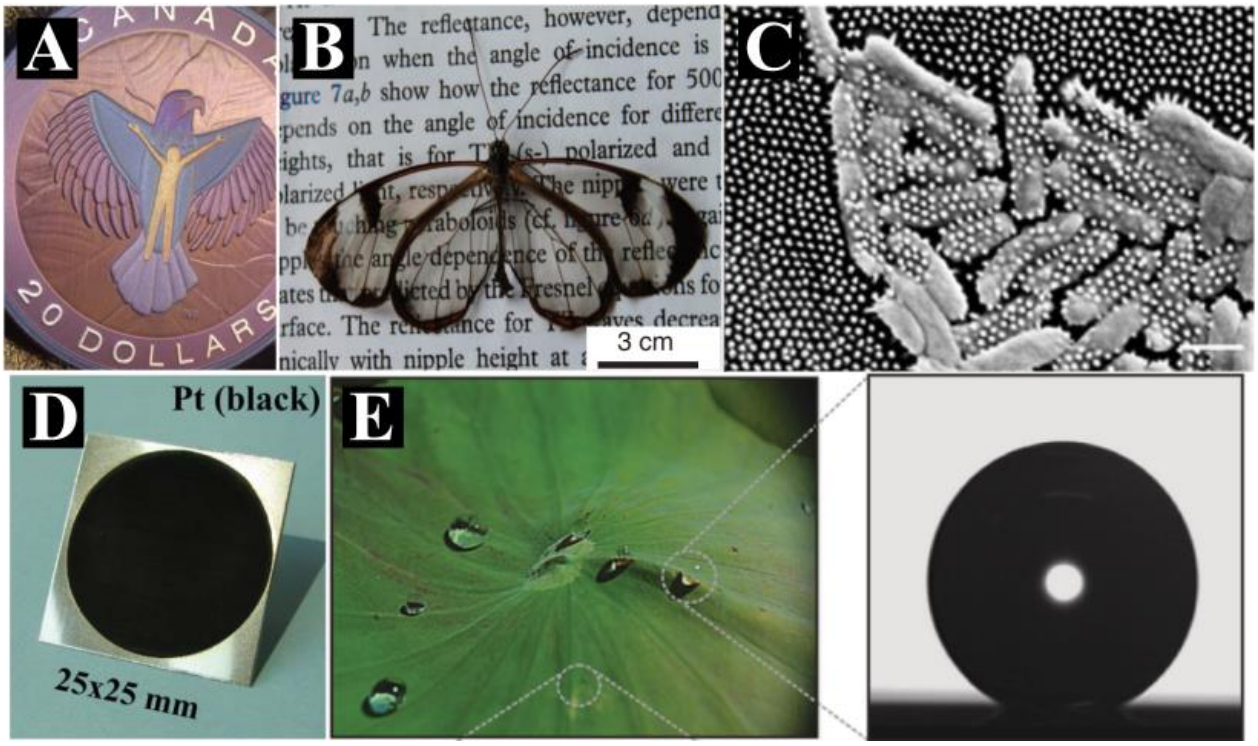

Figure 1 Structures fonctionnalisées; A : pièce de monnaie en argent texturées par laser [1] ; B : ailes d'insecte « Glaswing Butterfly » avec propriétés anti-réflectives [3]; C : bactéries mortes sur aile de cigale [4] ; D : surface de Platine noircie au laser [2] ; E : goutte d'eau sur feuille de Lotus.

Parallèlement à cela, la technologie laser révolutionne le champ des possibles en termes de texturation de surface et permet de reproduire ces fonctions inspirées du monde du vivant en modifiant la morphologie et la chimie de surface. Néanmoins, le développement et le déploiement de telles techniques de texturation laser au niveau industriel nécessite la levée de trois verrous. Le premier est de connecter les propriétés macroscopiques (couleur, résistance mécanique, stabilité chimique, vieillissement) et la morphologie de surface aux échelles nano et microscopiques. Le second d'acquérir une parfaite maîtrise de la morphologie de surface à ces échelles. Le troisième est la transposition du procédé développé en laboratoire en procédé industriel adapté aux traitements de grandes surfaces avec des temps de cycles les plus courts possibles. Les structurations de surface fonctionnelles présentes dans la nature peuvent servir de guide pour relier la topographie aux propriétés de surface (Figure 1, D, C, E). Ces propriétés dépendent de la topographie et de la physico-chimie de surface.

Cependant, notre capacité à contrôler de telles morphologies de surface induites par irradiation laser doit être améliorée afin d'imiter les exemples présents dans la nature, laquelle nécessite la parfaite compréhension des mécanismes physiques conduisant à de telles structures. Dans cette optique, nous avons

mené une étude paramétrique sur la structuration de surface induite par laser femtoseconde sur acier inoxydable pour accroître notre capacité à contrôler ces structures aux échelles micro et nanométriques. L'influence de la longueur d'onde[6], du recouvrement spatial, de la fluence[7], de la dose, du taux de répétition[8], de la polarisation, du délai entre les impulsions a été étudié[9–11]. Nous avons également mis en œuvre et étudié plusieurs techniques de telles structures submicrométriques.

Des structures submicroniques, telles des « ripples » par exemple, ont été réalisées et maîtrisées avec succès avec un laser femtoseconde émettant dans l'ultraviolet[12]. La Figure 2 présente trois structures de surface obtenues avec un nombre croissant d'impulsion (pps_{tot}). Néanmoins, la variation de paramètres clefs comme la fluence ou le nombre d'impulsions incidentes ne permet pas de contrôler la symétrie de surface.

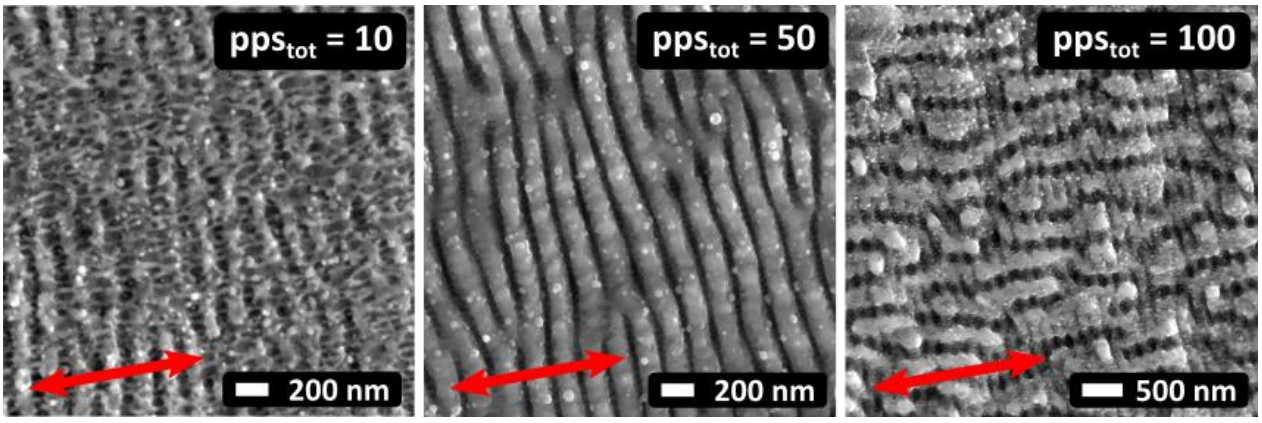

Figure 2 Micrographies MEB de morphologies de surface produites sur acier inoxydables par irradiation avec une longueur d'onde de λ = 257 nm, une fluence de Φ = 0.11 J/cm^2 et un nombre variable de nombre total d'impulsios par point pps_{tot}. La flèche en rouge indique l'orientation de la polarisation. Le nombre total d'impulsion est mentionné sur chaque micrographie. Les structures HFSL sont formées pour pps_{tot} = 10, les "ripples" (LFSL) pour pps_{tot} = 50 et les sillons pour pps_{tot} = 100.

L'irradiation avec double impulsion apporte une capacité supplémentaire dans le contrôle de la morphologie de surface finale[9–11]. La première impulsion induit un état transitoire qui change les propriétés de la matière vue par la seconde impulsion, lesquelles dépendent directement du délai entre les deux impulsions $\Delta\tau$. Ce delai est donc le paramètre d'influence principal. Différents types de structures, avec différentes symétries, ont ainsi été produites en jouant sur le délai entre les deux impulsions et le type de polarisation. La Figure 3 présente des nanostructures par irradiation à double impulsions laser sur une surface d'acier inoxydable,

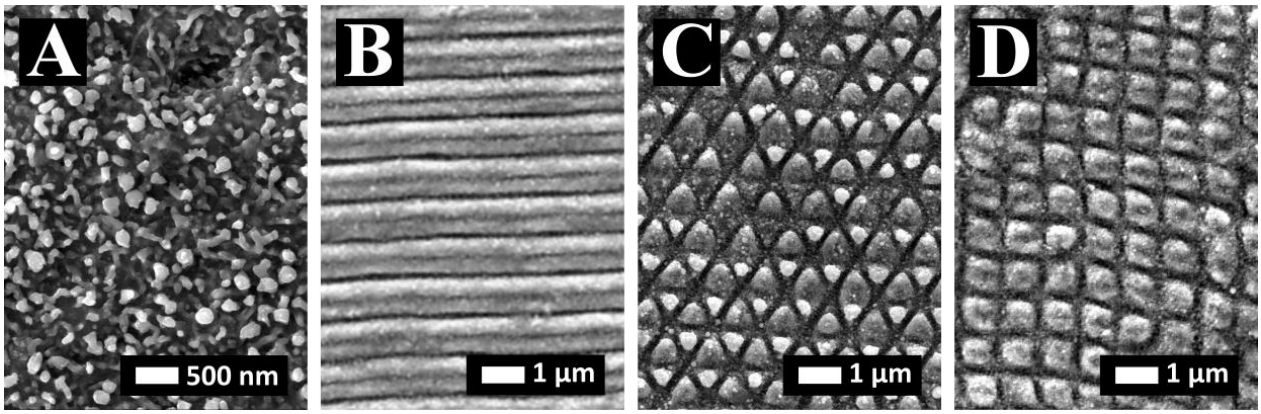

Figure 3 Structures produites par irradiation à double impulsion sur acier inoxydable; A : Φ = 0.1 J/cm^2, $\Delta\tau$ = 20 ps, H = 1 µm et CP (publié dans [11]); B : Φ = 0.1 J/cm^2, $\Delta\tau$ = 0.5 ns, pps = 10 and H = 1 µm et XP; C: Φ = 0.1 J/cm^2, $\Delta\tau$ = -1 ps, pps = 10, H = 1 µm and CP D: Φ = 0.15 J/cm^2, $\Delta\tau$ = 0.5 ns, pps = 10 and H = 1 µm et CP (B,C &D publiés dans [12]).

tels des plots 2D (Figure 3, A, et Figure 4 C et 4C'), des « ripples » longues et homogènes (Figure 3, B), des structures LIPSS 2D [7], des triangles (Figure 3, C), ou des carrés (Figure 3, D).

Des structures LIPSS homogènes triangulaires ou carrées ont été obtenues pour des délais inférieurs à 5 ps et 500 ps respectivement[9]. Des paramètres opératoires, en particulier la fluence et la polarisation, ont été identifiés comme jouant un rôle majeur dans les caractéristiques de la morphologie de surface finale. Le procédé a été optimisé pour produire de telles morphologies sur des surfaces étendues afin de mettre en avant leur aspect visuel macroscopique.

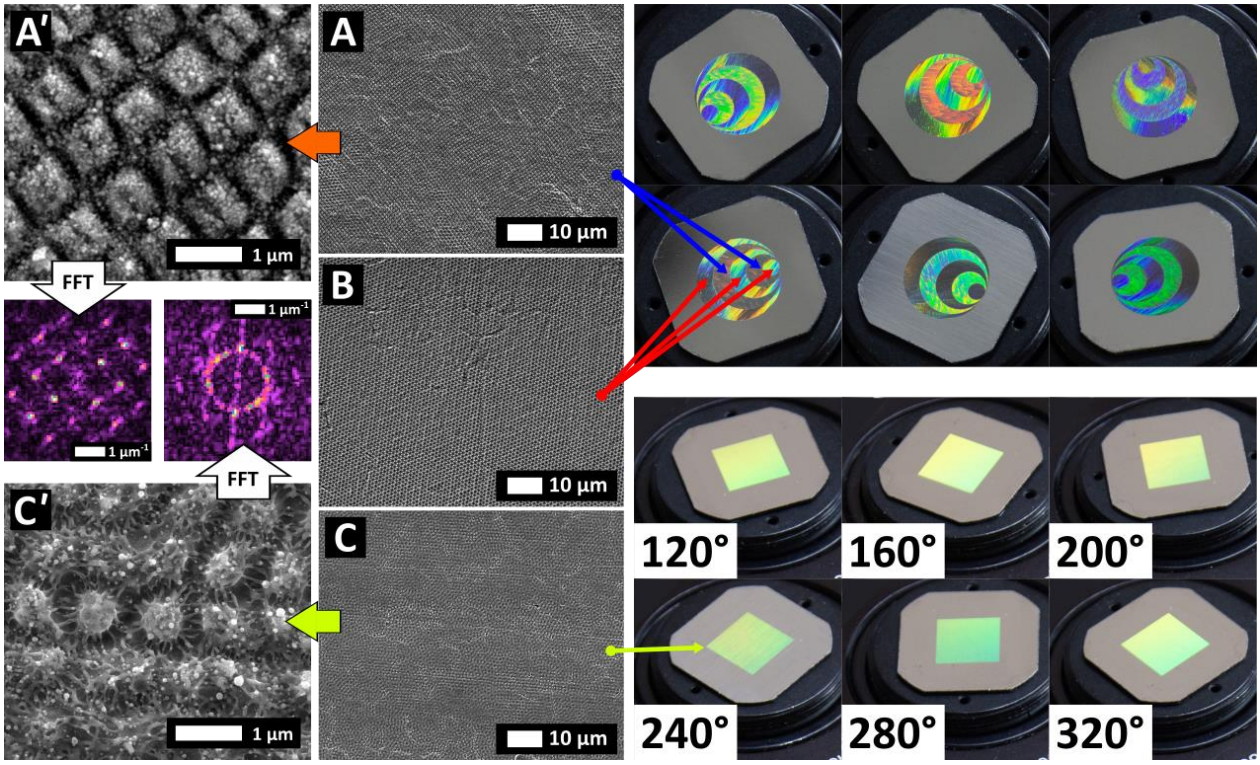

Figure 4 A gauche : micrographies MEB de structures 2D obtenues sur acier inoxydable ; carrés (A et A'), mélange de ripples et plots (C et C'). Clichés correspondant obtenus après Transformée de Fourrier. A droite : photographies de surfaces étendues texturées par laser correspondant aux micrographies MEB indiquées par les flèches rouges et bleues. En haut : motif holographique à deux couleurs obtenue à partir de structurations en carrés ou en triangles comme indiqué. En bas : surface de 8x8 mm texturées avec des « ripples » aléatoires. L'angle indiqué est l'angle azimuthal des platines de rotation.

Des expériences complémentaires ont montré que des résultats similaires peuvent être obtenus en utilisant des cristaux biréfringents pour générer des délais courts. Nous ainsi avons démontré que l'irradiation à double impulsions peut être réalisée avec un montage robuste.

Nous avons également exploré la possibilité d'utiliser des trains d'impulsions uniques pour produire des texturations de surface de dimensions caractéristiques supérieures allant de quelques microns à plusieurs dizaines de microns en faisant varier de manière systématique la fluence, la dose énergétique et le taux de répétition du laser[8]. La comparaison de résultats expérimentaux avec ceux issus de simulation nous avons mis en évidence le rôle majeur de l'accumulation thermique sur les dimensions caractéristiques des structures générées par laser. Par ailleurs, nous avons démontré la capacité du procédé à produire de texturations sub-longueurs d'onde, homogènes, sur des surfaces supérieures à 1 cm², avec des lasers ayant des taux de répétitions allant jusqu'à 10 MHz et des systèmes de positionnement innovants. Des nano-rugosités de surface ainsi produites affichent des propriétés de super hydrophobicité. A titre d'exemple,

nous avons atteint un temps de texturation de l'ordre de 1 min/cm². Enfin, nous avons démontré un temps de 9 s/cm² pour le noircissement de surface.

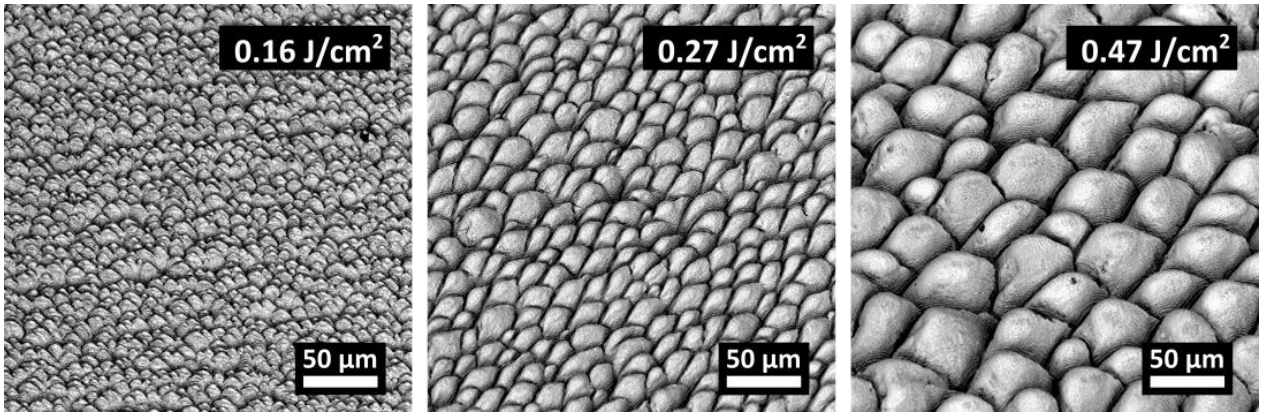

Figure 5 Micrographies MEB illustrant la variation progressive du diamètre équivalent δ avec la fluence croissante. Ces micrographies ont été obtenus avec un angle d'observation de 45°. Les valeurs de fluence sont mentionnées sur les clichés.

Ces travaux de recherche, mettant à profit des sources laser et des équipements de déflection optique de dernière génération, apportent une contribution significative dans la compréhension des mécanismes d'une part, et dans la capacité à contrôler et à produire de telles texturations sur des grandes surfaces d'autre part. Ils devraient favoriser une dissémination rapide de ces technologies de texturation laser dans l'industrie.

1. Introduction

Current industrial markets demand highly value-added products offering new features at a low-cost. Among the most desired ones are decorative applications, anti-icing surfaces for aeronautic industry, enhanced absorption materials for photovoltaic devices, anti-biofouling components in home appliances and medical applications, wear reduction in automotive industry and anti-reflective properties for photonics applications. Laser surface processing holds a virtually endless potential in surface functionalization since it can generate versatile surface properties by modifying surface morphology and chemistry. Moreover, it is advantageous compared to other techniques used for surface functionalization. For example, creation of composites or applying coatings on a material surface include the use of chemical treatment significantly changing the surface chemistry. Laser processing is more environmentally friendly in this sense, it is long term stable and, in some cases, maintains the surface's bio compatibility.

Nevertheless, several issues must be tackled prior to laser surface processing implementation in industry. At first, the correlation between the macro-scale properties (colour, mechanical resistance, chemical stability, ageing) and the micro & nano-scale morphology has to be clarified. Secondly, understanding the microstructure formation mechanism will in principle increase the level of control over the laser induced morphology, which we consider limited especially in the submicron regime. The third issue is the limits of the process in terms of surface area process and production cycle time. In parallel to the advances of the laser industry, which can combine high average power laser systems with high speed positioning modules surface processing can deal with large area texturing in the order of 1 s/cm^2 [13,14]. Nevertheless, the study on controlling laser surface structures is often limited to areas in the order of mm^2 and processing rates in cm^2/hour.

In this thesis, both issues will be considered. Industrial high throughput femtosecond (fs) laser sources and innovative laser positioning systems will be employed to demonstrate the feasibility of significantly reducing cycle time while developing novel surface morphologies. Physical phenomena that are subsequent from the increase of average power will be also considered and overcome. Furthermore, considering and implementing innovative spatiotemporal beam shaping and polarization modification can increase control over the structure morphologies from a few tens of microns down to a few tens of nanometres.

The outstanding performance of bio textures on specific functionalities offers valuable information on the characteristics of the optimum nanostructure for inducing specific functionalities. The effort to reproduce bio morphologies using technical means aiming to change surface properties is known as biomimetics. Nature produces a variety of functional surfaces in daily life. Resulting from adaptation to environmental condition biological systems have developed highly efficient functional textures. Specialized macroscopic surface functionalities derive from a particular micro or nanoscale morphology and chemical surface

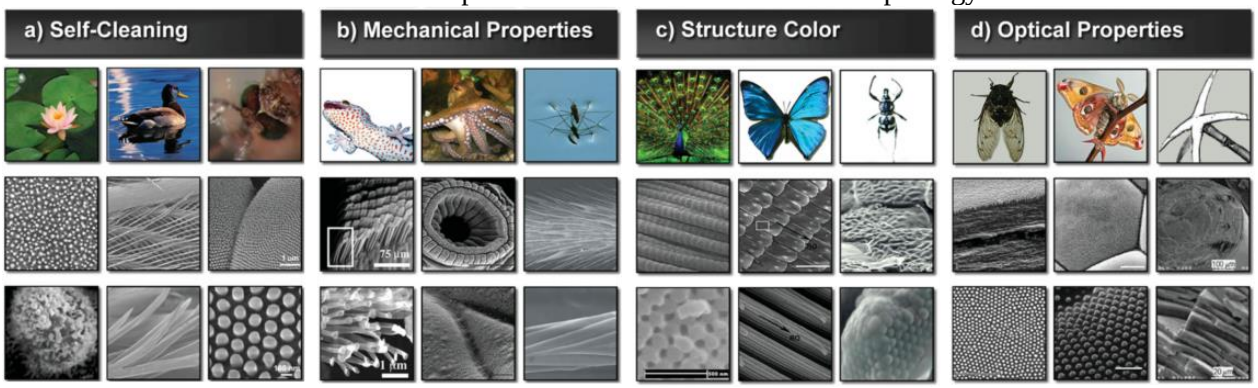

Figure 6: Functional morphologies and surfaces found in nature reproduced from Fan Xia and Lei Jiang (2008)[15]. Top: pictures of the living organism. Middle & Bottom: SEM images of the surface textures.

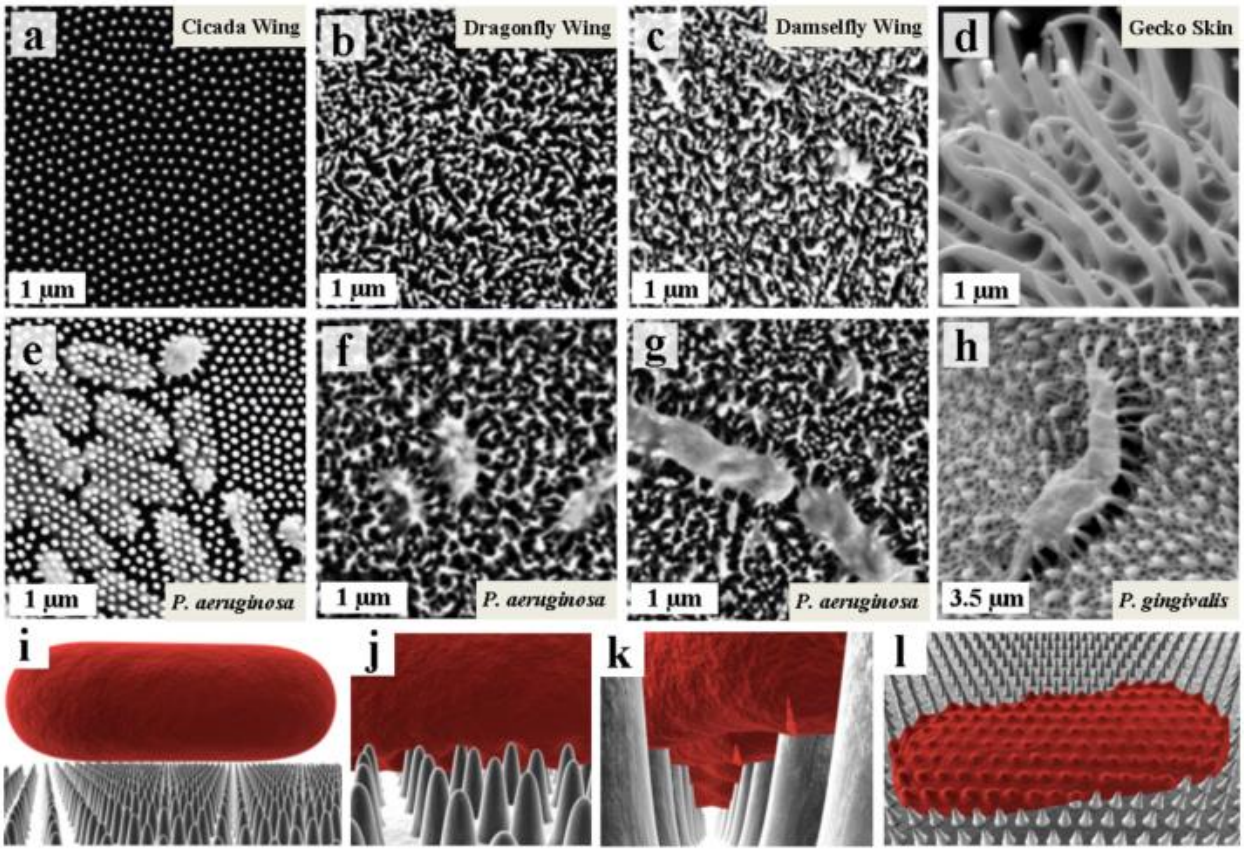

Figure 7 Bactericidal surface textures found in bug wings reproduced from A. Elbourne et al. (2017)[16]. Top: SEM images of (a) Cicada Wings (Psaltoda claripennis), (b) Dragonfly Wings (Diplacodes bipunctata), (c) Damselfly Wings (Calopteryx haemorrhoidalis), and (d) Gecko Skin (Lucasium steindachneri). Middle: SEM images of the wing surfaces when inoculated with (e, f, & g) Pseudomonas aeruginosa ATCC 9027 (P.aeruginosa) and (h) Porphyromonas gingivalis (P. gingivalis). Bottom Row: Schematic representation of bacterial attachment onto the cicada wing nano-pillars showing (i) cellular approach, (j) initial adhesion buckling the cell membrane, (k) the apparent rupture of the cell wall in the region suspended between the nano-pillars, and (l) cell collapse (death) onto the nano-pillars.

composition. Figure 6 illustrates a few examples of microscale functional textures that can be found in nature.

A self-cleaning effect can be found on lotus leaves and duck feathers (Figure 6 , a)[15]. This self-cleaning effect is generated on a superhydrophobic surface, when the water droplets exhibit a very high contact angle and small sliding angle, that facilitates the sliding of the droplet washing away any contaminants[16]. Adhesive behaviour is observed in gecko feet and octopus tentacles. Special optical properties such as colouring are observed in peacock feathers, butterfly wings and beetle shells. Lastly, anti-reflective behaviour is observed in cicada wings and moth compound eyes[15]. Anti-friction textures can be found in the katydid leg joints[17].

Figure 7 shows SEM surface images of dragonfly and damselfly wings as well as on gecko skin exhibiting anti-bacterial properties[16]. The surface is shown before (Figure 7, a-d) an after (Figure 7, e-h) inoculation with bacteria. In all cases the bacteria where killed, whether they can adhere or not on the surface. Elbourne et al.[16] coated the cicada wing surface with a 10 nm gold layer to show the effect of the surface morphology rather than surface chemistry. Interestingly, the gold coated wing maintained the bactericidal behaviour proving that the surface functionality derives from the nano-morphology. In detail, the bacteria's membrane was distorted and split leading to the death of the cell[16]. The bactericidal property of the nanostructures is observed for specific proteinic compositions of the cell membranes and it does not depend on the cells'

shape[4]. Similar findings for the importance of the morphological characteristics of the texture were found also in the case of transparent surfaces. In that case the structure size, shape and spacing play a key role in the anti-reflective behaviour[3].

Developing competence in reproducing the astonishing diversity of bio nanostructures will enable us to induce specialized surface functionalities on a wide variety of materials. Figure 8 (taken from ref. [18]) summarizes the capabilities of different techniques in terms of fabrication speed and feature size. The goal is to achieve control over the feature size in the near micron scale while increasing the processing speed up to m^2/min in order to cope with the standards of industrial production. Among other techniques like lithography, ion beam etching etc, pulsed laser surface processing is a well-established way, utilized to tune the surface of solid materials and its properties. Several approaches of laser processing are commonly employed, namely; direct laser writing (DLW), direct laser interference patterning (DLIP) and surface self-organization.

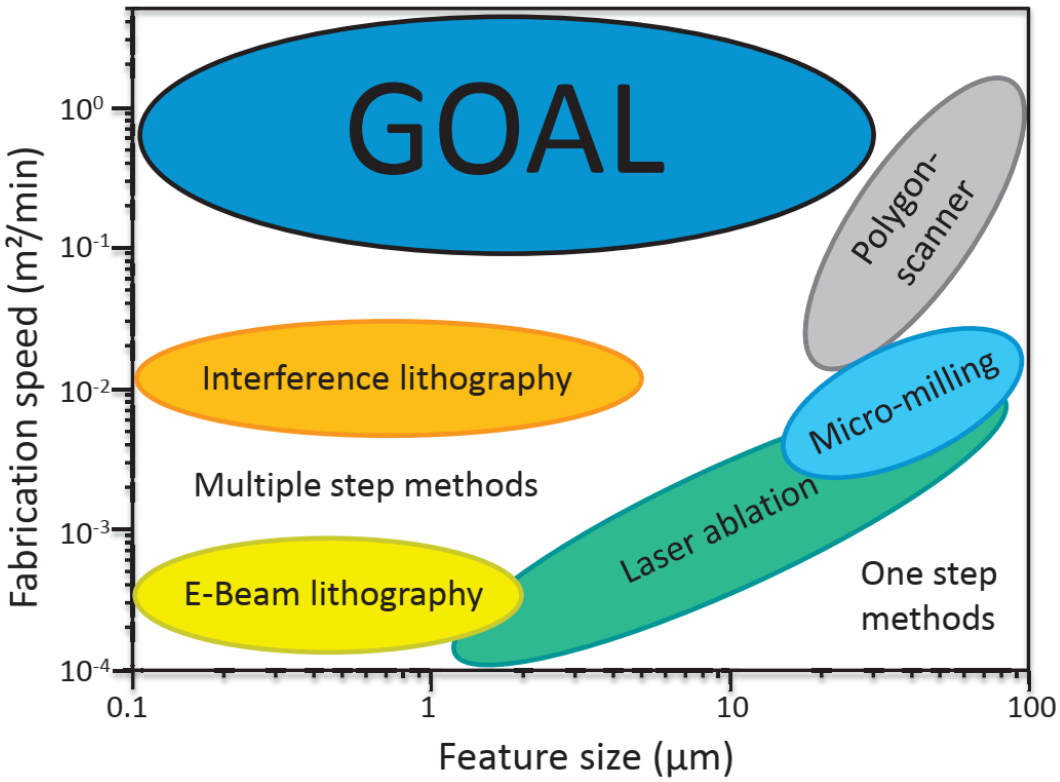

Figure 8 Summary of the different techniques and the feature size that can be produce. Reproduced from A. Lasagni et al. (2014), ref. [18].

Direct laser writing (DLW) employs the laser beam to ablate the solid surface and form the structures. The depth of the structures can be defined by the number of laser shots in each point. Short pulse lasers improved the accuracy and reduced the detrimental thermal effect. The main limitation of the technique considering non transparent solid materials is that minimizing the structure size in the submicron scale comes with significant constraints concerning the process throughput[19]. However, DLW is a very powerful process for in-volume modifications in transparent materials[20].

Direct laser interference patterning (DLIP) is another technique utilized for surface texturing. Structuring with DLIP is based on the generation of an interference pattern of light on the material surface. The inhomogeneous irradiation entails the generation of a temperature gradient followed, depending on the fluence, by surface localized ablation or by microfluidic flow driven from temperature gradients leading to

structure formation. Similarly, to the DLW process, the depth of the structures depends in principle on the fluence and the number of the incident pulses (N_p). Nevertheless, the pulse duration plays a key role and realization of structures with periods in the order of $\Lambda_{DLIP} < \sim 10$ μm) can form solely with ultrashort pulses[21,22]. The main advantage of the technique lies in the fact that the size of the structures can be varied continuously, and the symmetry can be defined by the number of the interfering beams. Moreover, DLIP can be applied in a variety of solid materials like transparent materials, metals and polymers[23] generating biomimetic surface structures[21].

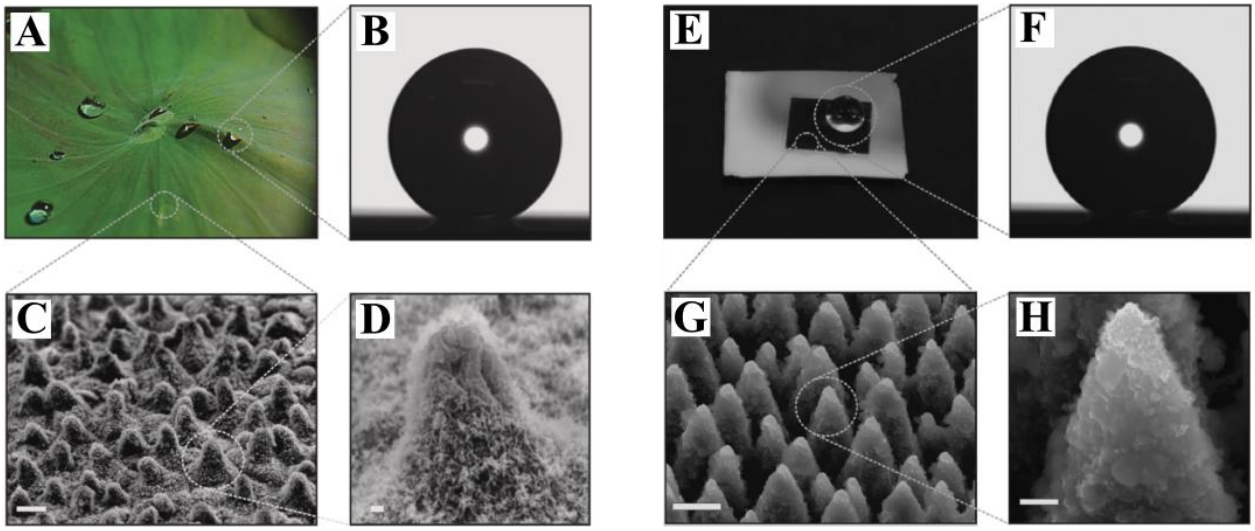

Figure 9 Reproduced from V. Zorba et al. (2008), ref. [5]. Lotus leaf (A). Profile of water droplet on lotus leaf (B). SEM images of lotus leaf micro (C) and nano (D) surface texture. Biomimetic, superhydrophobic surface of laser processed silicon (E). Profile of water droplet on laser textured surface. SEM images of laser induced texture on silicon (G & H). Scale bars for C, D, G & H are 10 μm, 1 μm, 5 μm & 1 μm, respectively.

Femtosecond laser surface texturing can be employed to fabricate surface features ranging from a few tens of microns to a few tens of nanometres radically modifying the macroscopic surface properties. The structures appear on the surface after self-organization of the irradiated material, and their formation mechanism is not fully understood up to date. Key process parameters like pulse duration, fluence, number of incident pulses and pulse polarization appear to have huge bearing on the structure morphologies.

Laser texturing has been utilized for surface functionalization, and there are several reports of successful fabrication of biomimetic surfaces. Figure 9 illustrates the reproduction of the spiky structures found in lotus leaf (A, C, D), and created by femtosecond laser irradiation on silicon surface (E, G, H). The lotus leaf exhibits superhydrophobic properties due to its hierarchical morphology on micro and nanoscale. The water contact angle on its surface forms a very high contact angle (>150°) as shown in Figure 9, B and a small value of contact angle hysteresis (<5°) is measured. Employing a fs laser source to process silicon surfaces under the presence of a reactive gas[5], it is possible to generate hierarchical surface morphologies similar to the lotus leaf. After surface silanization, the wetting properties are modified radically. The textured surfaces exhibit contact angle values of 154°±1° (Figure 9, F) and hysteresis angles of 5°±2° similar to the lotus leaf[5]. Hydrophobic metal surfaces can be obtained by inducing similar hierarchical structures. Interestingly, the wettability of a variety of metallic surfaces has been found to increase progressively after laser irradiation with time due to the uptake of carbon from the atmosphere[24]. The self-cleaning effect was demonstrated as well in metallic surfaces processed with fs laser pulses[25]. Recently, the fabrication of surfaces with variable wetting properties has been demonstrated highlighting the possibility to achieve unidirectional fluid transport.[26]

Femtosecond lasers can be as well employed for the fabrication of structures in the submicron regime. As discussed above (§1), submicron structures are ideal for enabling unique surface properties such as bactericidal and antireflective. So called laser induced periodic surface structures (LIPSS) have been fabricated in a variety of materials such as semiconductors[27,28], metals[29,30] and transparent materials[31,32]. LIPSS are found to be quite effective on enabling antibacterial and anti-friction properties[33]. Femtosecond irradiation has been employed to mimic bio-, micro- and nano-texturing in order to reproduce nature functionalities on solid surfaces [5,26]. Several previous works refer to modifications of optical properties like surface blackening[34], tribological performances[35], surface wettability[5] and bacterial adhesion selectivity.[33,36]

Comparative studies between different nanostructures fabricated on stainless steel surface, showed that hydrophobic spikes are not bactericidal[37] providing further support to the hypothesis that specific surface functionalities derive from specific surface morphologies. Therefore, controlling the surface morphology and especially in the submicron regime is essential for developing functional surfaces.

In this thesis, §2 will be dedicated to the fundamental aspects of laser mater interaction and the proposed mechanisms that lead to laser induced structure formation. In §3 the experimental methods will be discussed. In §4 the results on controlling and upscaling laser induced morphology are presented. Finally, conclusions will be summarized in §5 and an outlook on potential nanostructure applications will be presented.

2. Femtosecond self-organised laser structures

Controlling laser induced self-organized morphologies requires an in-depth understanding of the fundamental processes that lead to their generation. It is reported that multi-pulse, or under specific conditions single pulse[38] irradiation of solid surfaces leads to formation of laser induced periodic surface structures the so called LIPSS[39]. Femtosecond lasers facilitate the generation of LIPSS in a variety of materials ranging from semiconductors[27,28] to metals[29,30] and transparent materials[31,32]. LIPSS morphological characteristics such as period, depth and structure homogeneity[40] are predominantly determined by the laser wavelength, polarization[41–44], fluence[34], the number of incident pulses[34,45–47] and the temporal intensity profile of the irradiation[48,49]. Moreover, it is reported that structure formation can be also influenced by the spot size[40], the ambient gas presence and pressure[45].

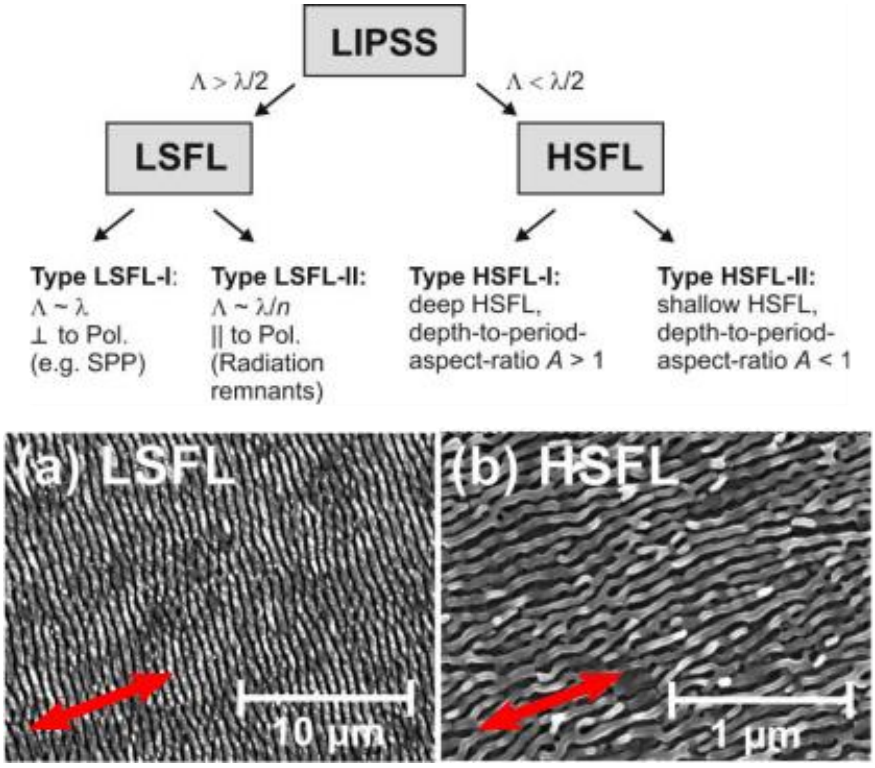

Figure 10 (Reproduced from ref. [42]) Top: classification of LIPSS types. Bottom: SEM images of Titanium alloy textured with a: LSFL, b: HSFL

A classification of the laser induced periodic structures is presented in Figure 10, top. High spatial frequency LIPSS (HSFL) appear for low fluence value (Φ = 0.08 J/cm^2)[i] on the surface[42,50–53] perpendicular to the lasers polarization in highly absorptive materials[42] (Figure 10 bottom, b). Low spatial frequency LIPSS (LSFL) are formed when a dose threshold (either in terms of fluence or number of pulses) is exceeded[51]. In Figure 10 bottom A, LSFL are shown obtained with Φ = 0.11 J/cm^2. Afterwards and above a specific fluence threshold[53,54], for large number of pulses (N_p > ~10) grooves and then spikes are formed on the surface of semiconductors[46,54–56] and metals.

In the case of femtosecond irradiation of solid surfaces, the structure formation mechanisms remain quite unclear and several theories attempt to interpret LIPSS formation. We mention for instance: surface plasmon polariton excitation[39], surface self-organization [57] , or the interaction between surface roughness and the incident electromagnetic field[58]. Generally, the structures result from inhomogeneous energy

[i] A specific threshold is observed depending on the material for the LSFL formation. Below that point and above the melting threshold of the material, HSFL are formed in semiconductors[55] and metals.

absorption during the irradiation[39] that leads to a periodic temperature profile on the material surface followed by microfluidic movement of the molten material[27,46,48]. An insight on the surface evolution during the ripple formation has been acquired by pump-probe experiments in silicon[59–61] and in metals[62]. The complex dynamical processes of interaction will be discussed in §2.1 and the proposed mechanisms of structure formation in §2.2 - 2.4.

2.1. Femtosecond interactions with metals: Ultrafast processes

In the case of femtosecond laser irradiation of semiconductors[63] and metals, the electrons absorb a part of the incident laser pulse energy in the order of 30% - 40%[50,64] with the rest being reflected or scattered by the surface. The absorbed energy initiates several interdependent relaxation mechanisms that determine the overall process, each one with a characteristic time scale:

2.1.1. Electron relaxation

When the electron-phonon coupling time is longer than the pulse length, as for sub-picosecond pulses, the electrons and the lattice have different temperatures immediately after the laser irradiation[65]. Excited electrons relax, transferring the energy to the lattice thanks to electron-phonon coupling within a few picoseconds[27,64,66–68]. As shown schematically in Figure 11 A, a group of electrons that absorbed the pulse energy are excited above the Fermi level. Afterwards the electrons reach thermal equilibrium (Figure 11 B).

Electron excitation modifies the optical properties of the surface of the material within the first picoseconds after irradiation[50,69]. Changes in the surface reflectivity R can be visualized and measured via pump-probe experiments. In detail, the relation between the relative change of reflectivity $\Delta R/R$[ii] and the electron

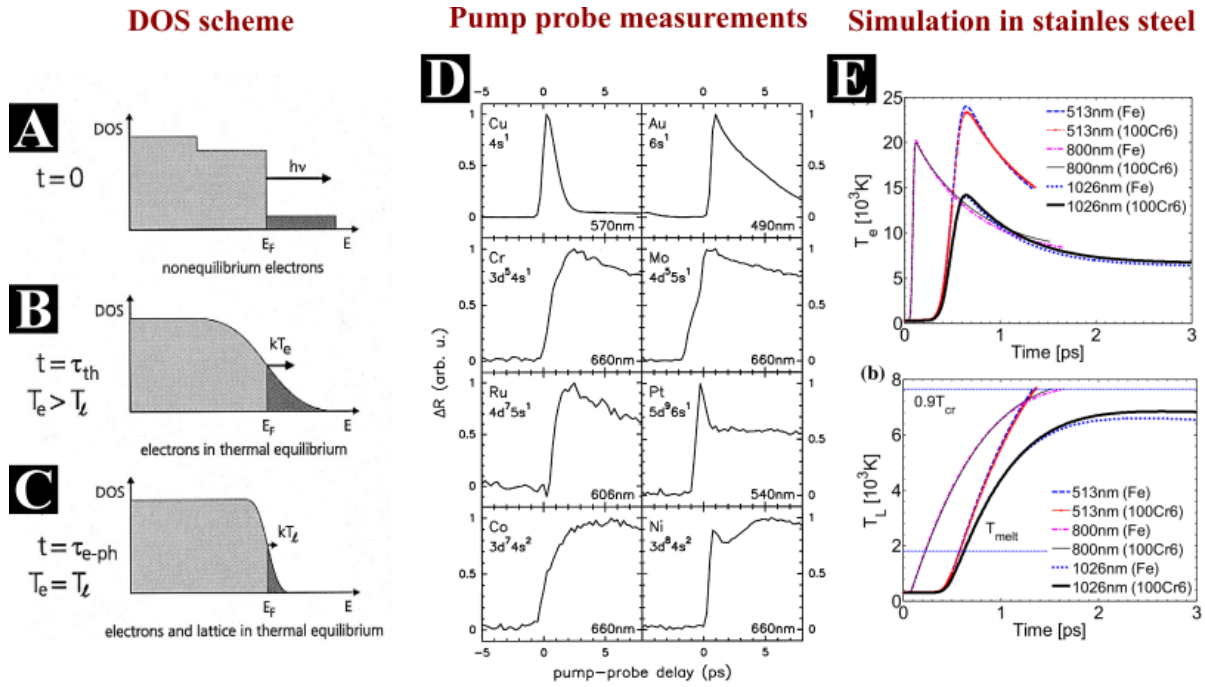

Figure 11 Electron phonon interactions, theory measurement and simulations A, B, C Density of state (DOS) scheme. Reproduced from ref [65]. D pump-probe measurements of the reflectivity changes after irradiation with fs pulses reproduced from[65]. E: Simulations of electron relaxation and lattice thermalization in 100cs steel for different wavelengths and pulse durations reproduced from [64].

ii $\frac{\Delta R}{R} = \frac{R(T_e) - R(293K)}{R(293K)}$ as described in ref. [65]

temperature T_e, which depends on the electronic band structure and the probe wavelength, permits the direct measurement of the electron lattice equilibration process[65]. Two mechanisms are responsible for electron relaxation, hot electron diffusion and electron phonon interactions[65]. The electron diffusivity and thermal conductivity vary with the electron temperature[70]. Lastly, the strength of the electron phonon coupling determines the time that the electrons need to equilibrate with the lattice (Figure 11 B)[65]. Pump-probe measurements of the electron relaxation behaviour show a varying characteristic time behaviour for different metals (Figure 11 D)[65].

Our study will be focused on nanostructuring of stainless steel, and therefore defining the time of electron relaxation is essential for the data interpretation. Recent simulation studies on LIPSS formation on 100CR steel gives the characteristic timescales for this material[64]. Figure 11 E, shows the electron (top) and the lattice (bottom) temperature on 100CR steel surface after excitation of femtosecond pulses with different pulse durations and wavelengths. A characteristic time in the order of 1-2 ps is necessary for the lattice thermalization[64].

2.1.2. Thermal effects and resolidification

After the lattice thermalization, if a specific energy threshold is exceeded, the material surface undergoes a phase transformation. Depending on the fluence of the laser pulse the material surface can undergo melting, photomechanical spallation driven by a laser induced shockwave or an explosive disintegration of an overheated surface layer[71] with a remaining molten layer. For ultrashort pulse (USP) irradiation, the heating of the material is realized in timescales that do not permit the smooth transition between the phases of the material. If the deposited energy is sufficient for the material to exceed the boiling point, the material will be in an unstable phase. That will prevent the boiling of the material (heterogeneous nucleation) and the sudden increase of surface temperature will lead to homogeneous nucleation and ablation[72]. The resolidification time is estimated to be in the nanosecond regime[63,71]. Furthermore, it is shown that the

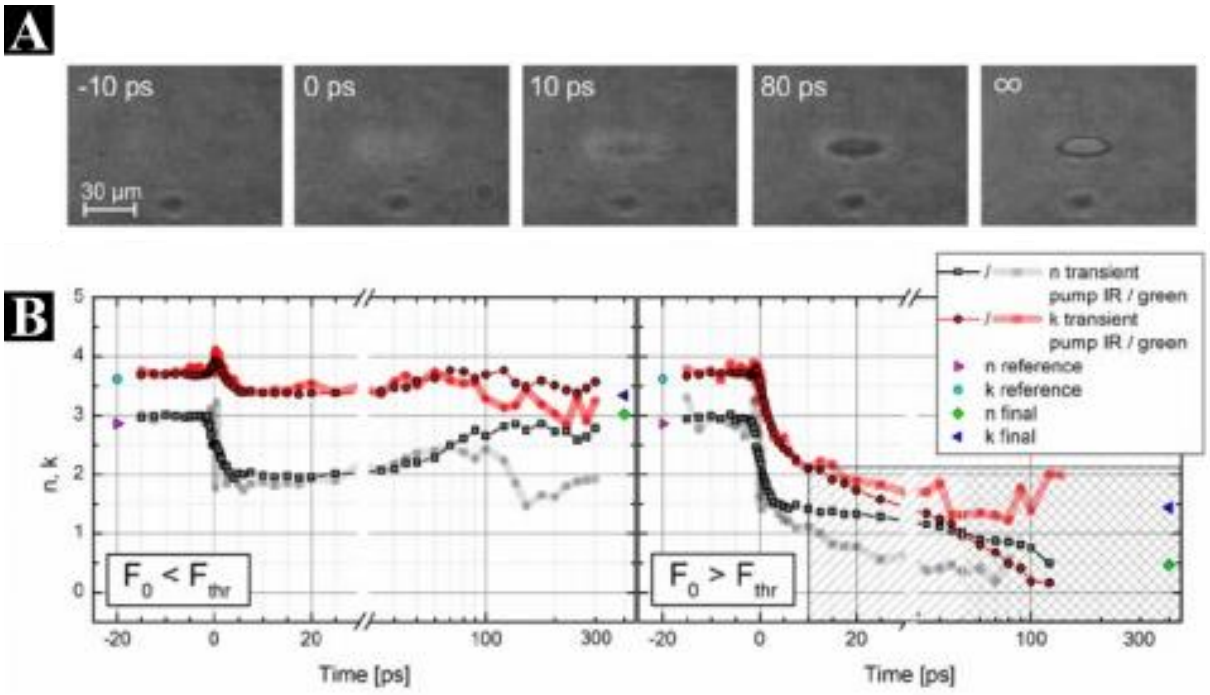

Figure 12 (reproduced from ref [75]) Ellipsometric pump-probe measurements. A: microscope images of Mo sample after irradiation with Φ = 0.8 J/cm^2. The probe time delay is indicated. B: Evolution of n and k after irradiation with different wavelengths as indicated. Left: Φ = 0.3 J/cm^2 (below ablation threshold), right Φ = 0.8 J/cm^2 (above ablation threshold).

portion of material in the molten phase depends on the laser wavelength[64] and the fluence[73] as well as on the occurrence of ablation[71].

Pump-probe measurements during the transient surface state provide detailed information on the characteristic timescales of the processes. Pump-probe ellipsometry measurements can be utilized for deriving the values of the real part (n) and the imaginary part (k) of the material's refractive index [74,75]. Ellipsometry measurements require a non-zero incident angle and a known polarization state for the probing beam[76]. After the reflection of the pulse, its polarization state is changed, and the analysis of the polarization components provide information about the properties of the material[75]. Figure 12 illustrates results obtained with a pump-probe ellipsometric measurement after irradiation of a molybdenum surface. A series of images of molybdenum surfaces is shown (Figure 12 A) after irradiation by a $F_0 = 0.8$ J/cm^2, $\tau = 680$ fs, $\lambda_{IR} = 1056$ nm (pump pulse) and probed by a $\tau = 540$ fs, $\lambda = 528$ nm pulse. The delay of the probe pulse is indicated.

The values of k and n shown in Figure 12 B are derived from the acquisition data for two different fluence values Φ[iii]; below the ablation threshold when $\Phi = 0.3$ J/cm^2 (Figure 12 B left) and above the ablation threshold when $\Phi = 0.8$ J/cm^2 (Figure 12 B right)[75]. The solid and opaque lines represent excitation by IR and green pump pulses, respectively[75]. Transitions are observed at zero when the irradiation of the pump pulse occurs. Below the ablation threshold (Figure 12 B left), the n value decreases within the first 5 ps and remains stable until 40 ps. This transition is correlated to the heating and phase changes expected to occur in that timescale. Later, n increases again until stabilizing between 100 ps and 300 ps while almost reaching the initial value[75]. The stabilization of n is linked to the solidification process expected at that regime[77]. Yet the final value of k is slightly lower than the initial indicating the permanent change in the optical properties of the material. Similar behaviour is observed for both wavelengths[75]. By increasing the fluence above the threshold the overall behaviour changes: The first transition occurring below 5 ps is steeper and is followed by a continuous decline[75]. These transitions can be identified with the surface heating and ablation onset expecting to occur between 10 ps and 50 ps[75].

Similar times for the initiation of the thermal effects were obtained for metals and semiconductors. For example, in Cr irradiated with 200 fs and with an absorbed fluence of $\Phi = 0.2$ J/cm^2 - 0.3 J/cm^2 material expansion starts at 5 ps[78] and the ablation depth is estimated to be in the order 40 nm[78]. In thin film Ag irradiated with $\Phi = 0.46$ J/cm^2 a signal decrease in the first 30-50 ps indicates the melting of the surface. The resolidification starts for $t > 50$ ps and is completed within 200 ps – 300 ps[79]. Pump-probe measurements in silicon[59] show the sequence of surface states for single pulse irradiation and fluence $\Phi = 0.14$ J/cm^2. The first effects are observed at $\Delta\tau_{probe} = 150$ fs when a slight increase of the reflectivity is observed. The change is intensified within a few hundreds of fs and is stabilized after a couple of ps, when thermal melting of the material is expected[59]. In germanium irradiated by fs pulses and $\Phi = 1.32$ J/cm^2 (above ablation threshold), the irradiation induces an increase of the surface reflectivity directly after the pump pulse due to electron excitation which can destabilize the lattice structure[59,80]. The onset of ablation is expected approximately 100 ps after the irradiation[80].

Simulations of the post irradiation behaviour of the excited surface affirm the timescales derived from pump-probe experiments. Characteristically, a comparative study including simulation and experiments in copper indicates that electron-phonon relaxation is completed within ~3 ps, the maximum ion temperature is reached after 10 ps (1.9 J/cm^2 $\tau = 680$ fs and $\lambda = 1056$ nm), and the ablation process with mechanical motion starts after ~20 ps[81]. In Figure 13 A the evolution of the molten surface layer and the temperature are shown[73]. Simulations in Ni,[71] showed that irradiation with 1 ps laser pulses for fluences within the range of $\Phi_{eff} = 0.03$ J/cm^2 to $\Phi_{eff} = 0.17$ J/cm^2 entails fast and slow melting of the surface[71]. The two melting speeds

[iii] Φ is the fluence value. See §3.1 for details.

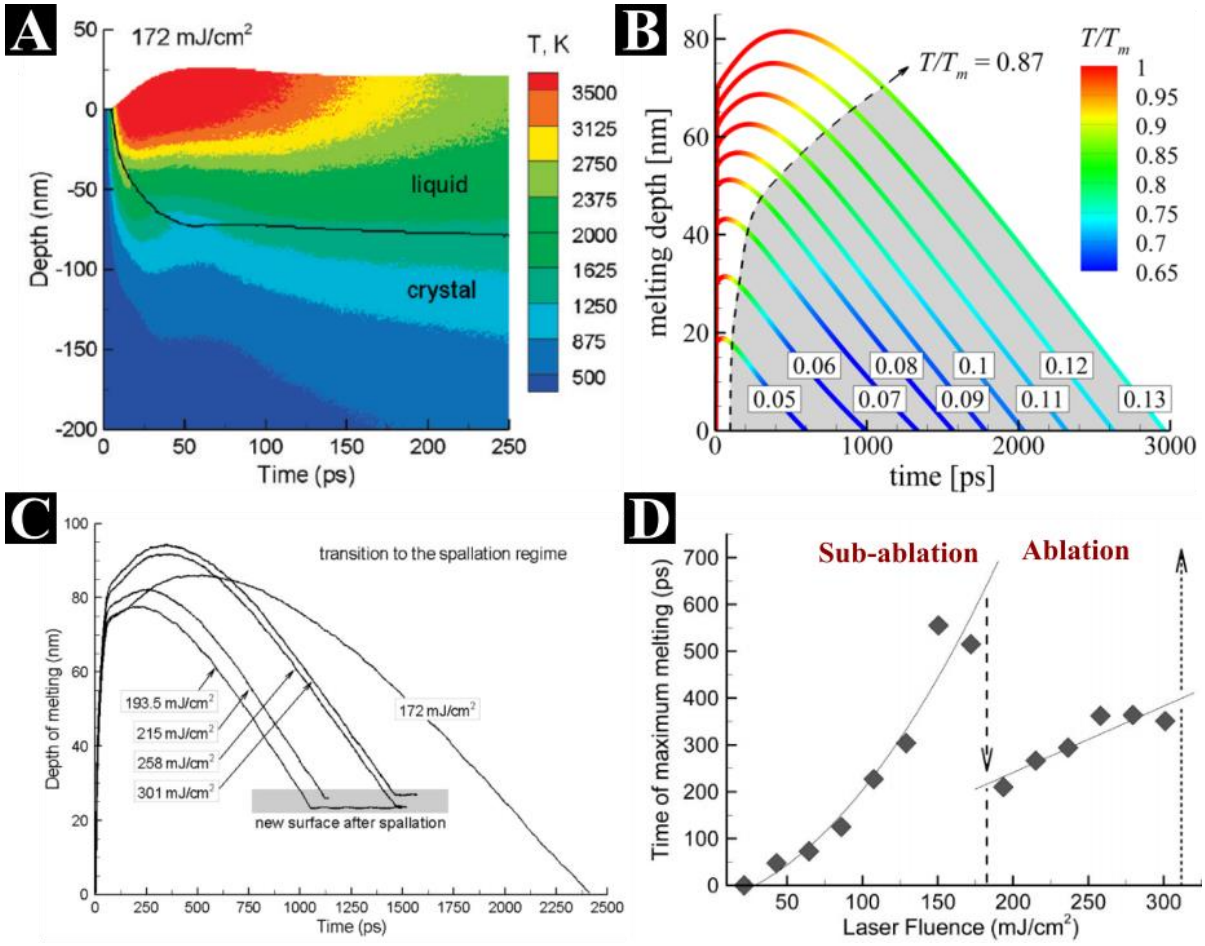

Figure 13 A: Simulation of the evolution of the depth of molten part in the surface of Ni and the surface temperature (reproduced from ref[71]). B: Melting depth and resolidification times in subablation conditions after irradiation of Ni surface with a 50 fs laser pulse at different values of absorbed laser fluence (marked in the plot in units of J/cm^2), reproduced from ref [73]. C: Melting depth and resolidification times after irradiation of Ni surface with different fluence values around the ablation threshold (reproduced from ref [71]). D: Time of maximum melting of Ni surface after irradaition with different fluence values (reproduced from [71]).

derived from the graphs; as shown in Figure 13 C show that fast melting results in liquification of 50 nm within 30 ps and an increase of the melted layer of additional 15 nm due to slow melting within 500 ps[71]. The heating and the hydrodynamic motion of the material that leads to surface expansion could last several tens[71] or in some cases hundreds[62] of ps. The surface deformation is related to the physical mechanism of pressure relaxation governing a highly pressurized melted surface layer[62]. A characteristic timescale in the case of ablation related to the speed of sound $t_s \approx 90$ ps was derived for Zn[62].

As intuitively expected, in sub-ablation conditions the depth of molten layer as well as the resolidification time depend on the amount of effective energy delivered on the surface[73]. Simulations on Ni unveil the role of fluence in determining the depth of molten layer and the resolidification time [71,73]. The dependence of the molten layer depth on the fluence is explicitly illustrated in Figure 13 B, where simulation results are depicted from irradiation of Ni targets by a 50 fs laser pulse at different values of absorbed laser fluence (marked in the plot in units of J/cm^2)[73]. Simulations of fs-induced melting of bulk Ag are in line with this approach describing surface expansion and homogeneous void generation 25 to 55 ps after irradiation[82]. Interestingly, as the fluence increases and the ablation threshold is surpassed (Φ_{eff} > 0.17 J/cm^2), the resolidification time becomes smaller due to the reduction of the molten layer thickness[71]. The time for

reaching the maximum depth of molten layer (Figure 13 D) follows the same trend[71]. In sub ablation conditions a maximum is observed around 500 ps[71]. The maximum depth of the melted layer is as well fluence dependent and decreases when the ablation regime is entered as shown in Figure 13 C.

At longer times the cooling of the material due to heat dissipation from the surface to the bulk leads to resolidification of the surface molten layer. The fluence has a big impact in determining the resolidification time (τ_{solid}). In Figure 13 B a proportional relation of absorbed fluence value (marked in the plot in units of J/cm^2) to the resolidification time can be observed[73]. In this case it varies from $\tau_{solid} \approx 600$ ps for $\Phi_{eff} = 0.03$ J/cm^2 to $\tau_{solid} \approx 3$ ns for $\Phi_{eff} = 0.17$ J/cm^2. In another work, irradiation with $\Phi_{eff} = 0.17$ J/cm^2 which is defined as the ablation threshold on Ni surface, a resolidification time of 2.4 ns was derived[71]. Simulations in Cr of irradiation with $\Phi = 0.2$ J/cm^2 - 0.3 J/cm^2 show that the surface remains liquid for at least 2 ns[78]. An estimated time for the resolidification of $\tau_{solid} \approx 2.5$ ns was derived for Al[83].

Depending on the material, pump-probe measurements give slightly longer times for resolidification. For pump-probe in silicon, the melted phase of the material is reported to end in between 3 ns and 4 ns[59]. Pump-probe measurements in germanium report that depending on the fluence, the material solidifies after a few to a few tens of ns[80]. Similar observations carried out with pump-probe techniques, elaborating on the fluence impact on the resolidification time of Zn give τ_{solid} in the order of tens of ns[62].

After resolidification the surface of the material maintains several hundreds of degrees and the time of cooling of the material to room temperature is estimated to about 10 μs[77]. During high repetition rate surface processing, when the repetition rate of the laser is set above a few hundreds of kHz, the time interval between the pulses is not sufficiently large for the heat to be dissipated[84].

2.2. LIPSS formation

In this paragraph, LIPSS formation is discussed. At first, an introductive part will be dedicated to the observation of LIPSS formation via pump-probe experiments. That way the characteristic timescales of the process will be mentioned. Afterwards, a detailed discussion of the proposed physical mechanisms that lead to LIPSS formation will be presented.

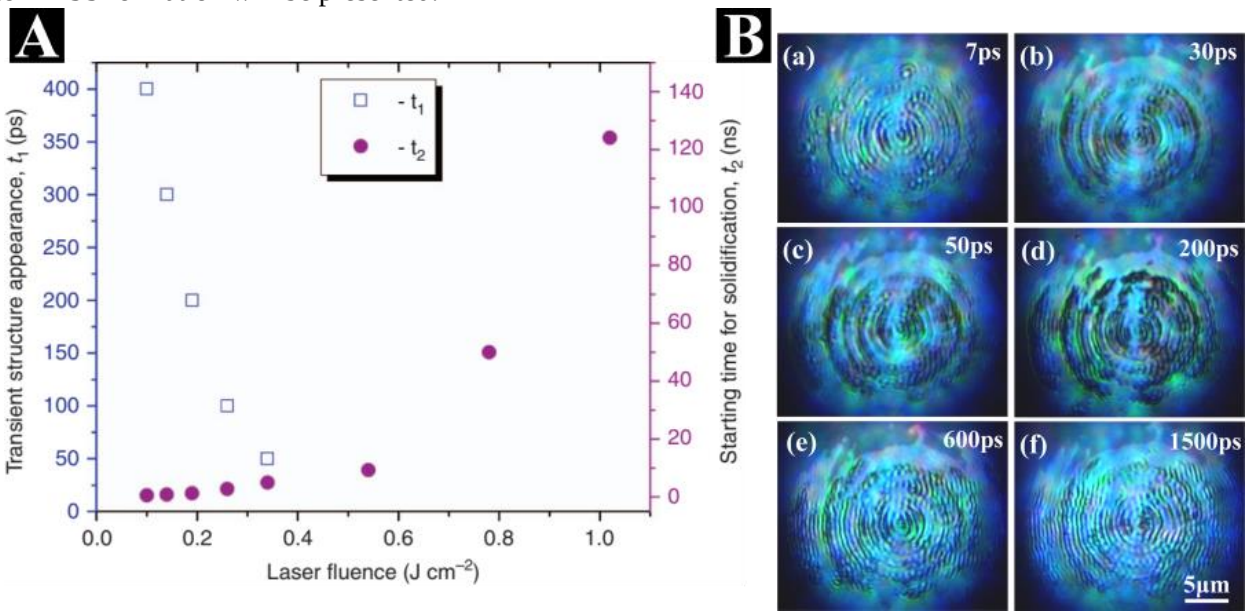

Figure 14 Characteristic times for structure appearance (t_1) and starting time for resolidification (t_2) of Zn after irradiation with different fluence values as indicated. Reproduced from[62]. B: Optical micrographs showing ripples emerge on silicon surface after irradiation with the third femtosecond pulse (N=3). The images indicate the probe pulse delay. Reproduced from ref [60].

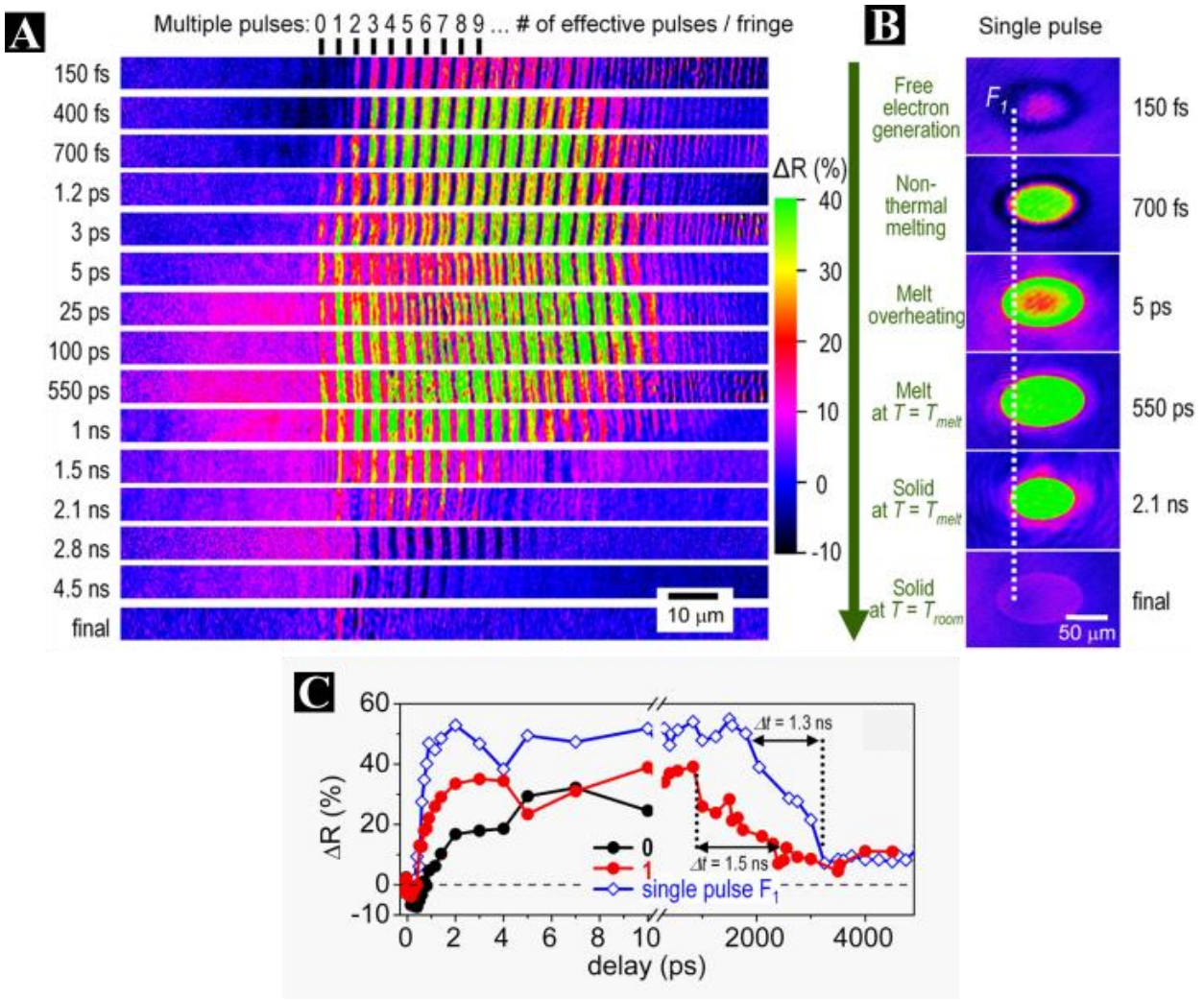

Figure 15 (reproduced from ref[59]) A: reflectivity measurements of silicon surface at different probe pulse delays B: Single shot reflectivity measurements on silicon surface indicating the timescales of ultrafast processes. C: Relative change in the reflectivity

At suitable conditions, usually close to the ablation threshold, ultrashort pulse laser irradiation of solids entails the formation of structures on the surface. The surface morphology changes during the transient surface state, and when it is solidified the novel features are permanently integrated on the material surface. Their formation mechanism will be discussed in this chapter.

As extensively discussed in § 2.1, the laser induced morphological changes on the surface starts in the time regime of tens to hundreds of picoseconds[60] and the surface resolidifies in the nanosecond timescale[59,62,71,73,85]. LIPSS appearance occurs in the time in between the two processes. The graph in Figure 14 A, gives a general overview of the structural appearance time with respect to the irradiated fluence of the incident pulse in the case of Zn irradiated with a 65 fs-pulse at a wavelength of $\lambda = 800$ nm. Comparing the images of the transient surface state and the images of the surface at a final state, significant statements can be made for the structure formation timescales[62]. For example, in the case of $\Phi = 0.1$ J/cm^2 the surface structures begin to appear at a time delay ($\Delta\tau_{probe}$) of 400 ps, the observed structures are considered transient since they are not alike to the final morphology[62]. Similarities between the morphology observed at $\Delta\tau_{probe}$ = 527 ps and the final structures indicate the starting of the resolidification[62]. Around 90% of the structures are frozen at $\Delta\tau_{probe}$ = 50 ns[62]. In the regime of 0.1 J/cm^2 - 0.14 J/cm^2 the onset of a transient structure

formation occurs between $\Delta\tau_{probe}$ = 400 ps and $\Delta\tau_{probe}$ = 300 ps, respectively, due to the time delay necessary between the melting process and the hydrodynamic motion of the material[62].

Pump-probe visualization of the ripple formation process was also carried out in silicon[60]. In Figure 14 B the evolution of a silicon surface after irradiation with a 120-fs laser pulse with λ = 800 nm is shown for different probe delays ($\Delta\tau_{probe}$). The temporal resolution of the experiments was 1 ps. The fluence was Φ = 0.61 J/cm^2 and the probe images were obtained after the third pump pulse incident on the same spot (N = 3)[60]. The morphology does not change before $\Delta\tau_{probe}$ = 7 ps[60]. Between $\Delta\tau_{probe}$ = 7 ps and $\Delta\tau_{probe}$ = 200 ps the destroyed regions become darker, due to absorption of the incident pulse by charged particles and silicon atoms ejected from the surface[60]. This observation is in agreement with the expected time of ablation as discussed in §2.1.2. The rudiment of ripples is found at $\Delta\tau_{probe}$ = 50 ps and their formation lasts until $\Delta\tau_{probe}$ = 600 ps whilst after $\Delta\tau_{probe}$ = 1500 ps the surface morphology does not change[60]. Similar results were obtained for a pump-probe experiment that is capable to visualize simultaneously the response for different pulse numbers on the silicon surface[59]. Thanks to the ultrafast moving spot microscopy, visualization of ripples irradiated with a different number of pulses was possible[59]. In Figure 15 B the temporal evolution of the reflectivity of silicon surface is presented after irradiation for a single laser shot having Φ = 0.17 J/cm^2. The differences in the reflectivity are linked to different stages of the surface transient state; electron population temperature and band structure as well as lattice temperature and surface's phase. The peak of reflectivity is observed for $\Delta\tau_{probe}$ = 7 ps and points towards thermal melting related to electron lattice equilibration[59]. A detailed view in time and in number of incident pulses is presented in Figure 15 A. Figure 15 C shows the evolution of the reflectivity over time for different numbers of pulses demonstrating the change of the optical properties of the material change upon an increasing number of pulses and nanostructure generation[59]. The resolidification process starts around $\Delta\tau_{probe}$ = 1 ns and lasts 1.3 to 1.5 ns. Finally, the material surface resolidifies before $\Delta\tau_{probe}$ = 4 ns[59].

Even though the visualization of LIPSS formation is accomplished and ripple appearance was found to coincide with the ablation process[60,62] and the surface's melted phase[59,60,62] their formation mechanism is highly debated and still remains unclear. The main debating point is whether the ripple formation results from the way the laser pulse is absorbed or from the way the surface relaxes after excitation[42]. The first approach attributes the ripple periodicity to the excitation of a surface plasmon wave[39,69] while the second in the self-organization of the surface[57]. The proposed mechanisms of ripple formation will be discussed in the following chapters.

2.2.1. Inhomogeneous energy absorption

It is generally proposed that during surface irradiation, periodic fluence allocation on the materials' surface occurs during irradiation driving LIPSS formation. Strong experimental indications point out in this direction[50,59,86]. A systematic study of the cavitation formation on Ni surface provide proof for the inhomogeneous absorption of the laser light during the irradiation[50]. At first by observing a cross section of Ni surface before ripple formation, it is demonstrated that the cavitation formation is fluence dependent (Figure 16)[50]. In the areas that are in the outer rim of the crater (distance from the center > 5μm), which have received smaller fluence during irradiation due to the pulse's gaussian profile, cavities are formed just below the surface (Figure 16, B, top)[50]. As the radial distance decreases below 3 μm, the cavities disappear and surface nanostructures with periods smaller than 200 nm are formed (Figure 16, B, bottom). After increasing the number of pulses, a structured area including HSFL and LSFL is produced (Figure 16, C). As shown in Figure 16, below the surface of the crest areas, nanovoids are formed and frozen indicating low absorption intensity while the absence of voids in the valleys point out high intensity. Therefore, a

periodic alteration of cavities and crests results from the periodic intensity distribution during the irradiation indicating constructive and destructive interference of the incident electromagnetic wave[50].

Similar findings were acquired in the sub-ablation regime where an amorphous grating mark was formed on a GeTe surface after irradiation with fs laser pulses[86]. The origin of the periodic crystal and amorphous pattern is attributed to the interference of the incident pulse with a surface electromagnetic wave or Rayleigh scattering[86]. The understanding of the laser-surface coupling was enriched during the past decades. An overview of the works that founded this understanding will be presentenced here.

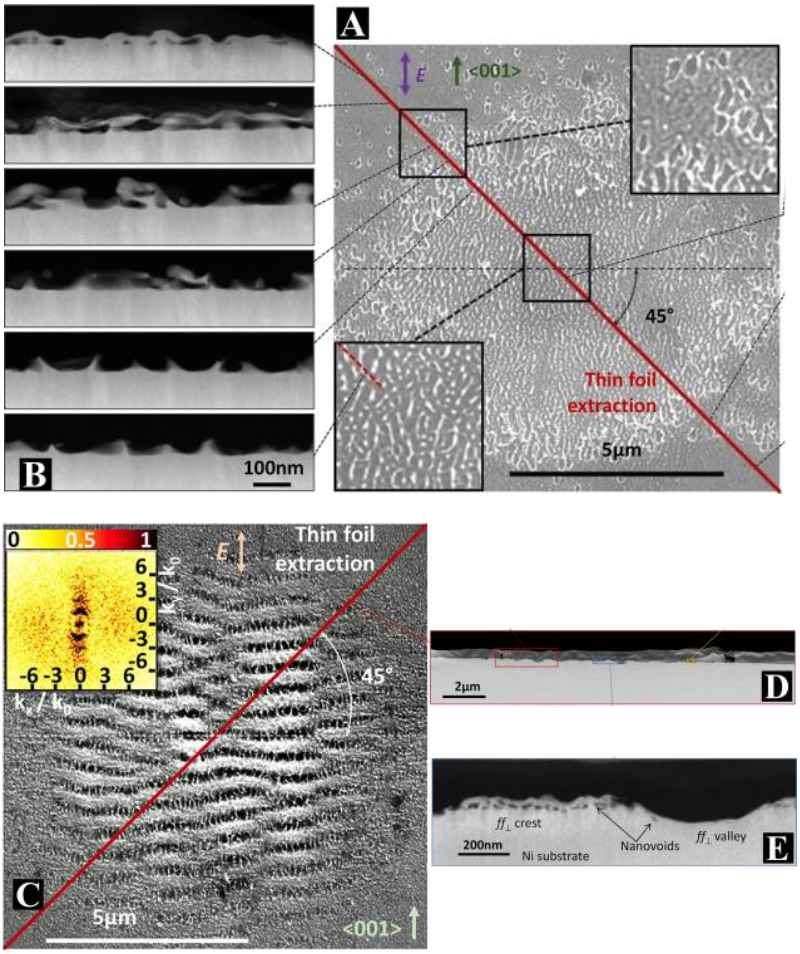

Figure 16 (reproduced from ref. [50]) SEM and cross sections of Ni surface after irradiation with fs pulses. A: Φ = 0.38 J cm^{-2}, N = 2. B: Cross section of areas corresponding to different radial distances from the center as indicated.

2.2.1.1. Light interference and the efficacy factor

The mechanism that is ultimately leading to periodic absorption of laser light and the ripple formation has been investigated under different perspectives. Emmony et al.[87] proposed that the origin of ripple formation was the interference of the incident electromagnetic wave with a secondary wave produced by light scattered from a surface feature and he introduced Equation 1 for the ripple period[87].

Equation 1: relation between the ripple spacing (d), the incident angle (θ) and the irradiation wavelength (λ).

$$d = \lambda/(1 \pm sin\theta)$$

Z. Guosheng, et al. proposed a model according to which an interference of the incident beam with an optical wave travelling along the surface was responsible for the ripple formation[88]. The model was based on the observation that the laser period varies with respect to the incident angle[89]. In his model the surface roughness consists of random surface features[88]. These features can be viewed as a superposition of many different surface gratings with different spatial periods each one diffracting the incident light into a number of diffracting orders[88]. The diffracted light will interfere with the primary incident wave to produce an intensity pattern[88]. The components with periods given by Equation 1 will diffract light along the surface of the material.

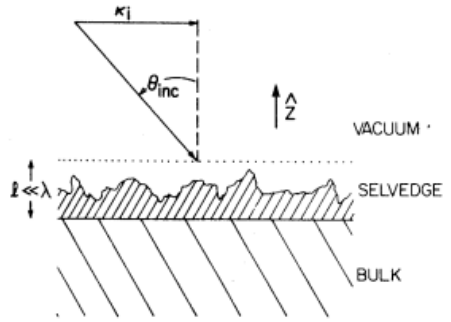

Figure 17 (Reproduced from ref. [39]) The geometry of incident light on a rough surface.

Sipe et al.[39] further developed this model, describing analytically the mechanism behind inhomogeneous energy absorption by the surface. A thin rough layer ($d<<\lambda$) shown schematically in Figure 17, scatters the incident electric field, generating a component which interferes with the refracted beam and leads to inhomogeneous absorption just below the rough surface (selvedge)[39]. The absorption of the incoming laser energy depends on the cross product of the absorption efficacy factor (**η)** and the roughness amplitude (**b**), **η**×**b**. The so called "efficacy factor", **η**, is a function describing the efficacy that a surface roughness leads to inhomogeneous absorption. In this concept, surface roughness can be analysed by a superposition of gratings with different spatial frequencies. **b** is a measure of amplitude of surface roughness at **k,** which is the incident wavevector parallel to the surface of magnitude $|k| = (2\pi/\lambda)\ sin\theta_{inc}$[39]. The efficacy factor η exhibits sharp peaks at frequencies close to the incident wavevector which can be correlated to the ripple period[39,69]. After ripple formation, **b** exhibits also sharp peaks which coincide with the peaks of **η,** entailing the significant increase of the efficiency of inhomogeneous absorption[69] and described as feedback of the structures[90].

A flat surface is progressively roughened by the incident pulses. During the first shots the surface is progressively roughened randomly[50,90]. The coupling of the electromagnetic radiation with the surface is determined by the pre-existing surface morphology[50] as well as by other factors like polarization and fluence that affect the optical properties of the material[50]. The roughness which is laser induced enables the scattering of the following incident laser pulses entailing the ripple formation[90]. The relation of the ripple orientation with respect to the laser polarization can be attributed to the interference between the scattered surface wave and the incident light that defines the axis of the periodic modulation of the absorbed light intensity[90].

The efficacy factor model was employed in a comparative study between simulation results and experimental data of irradiation of indium phosphide with fs pulses. A theoretical prediction of the ripple period was in good agreement with the experimental data[90]. The experimental part includes the irradiation of indium phosphide with λ = 800 nm, τ_p=130 fs and Φ = 0.58 J/cm^2. On the surface, after irradiation with the first laser shot a crater is formed. For N[iv] ≥ 2 ripples appear on the surface. The 2D-FT maps of the scanning force microscopy (SFM) images of the surface are shown in Figure 18 for different numbers of pulses (a: N_p = 1, b: N_p = 2, c: N_p = 3, and d: N_p = 4). After the second laser shot periodical features on the surface, with a period close to the laser wavelength are observed (Figure 18, b). Upon increasing the number of pulses, the amplitude of the 2D-FT diagram corresponding to the period of the ripples is becoming clearer (Figure 18 c & d). The extracted period value is $\Lambda \sim \pm$ 750 nm and very close to the irradiation wavelength

[iv] N_p is the number of incident pulses. See §3.1 for details.

(λ = 800 nm)[90]. The results of simulations of the pulse incident on rough but not rippled surface, predict two types of structures: Structures oriented perpendicular with respect to the laser polarization with periods ranging between $\Lambda \sim 800$ nm and $\Lambda \sim 600$ nm which correspond to observed LSFL[90]. Structures oriented parallel to the laser polarisation with a period around $\Lambda \sim 250$ nm which are not experimentally observed in this case[90]. Nevertheless, the formation of the predicted HSFL$_{\parallel}$ (parallel to the laser polarization) are reported for other materials[42,50–52,55]. Simulations of the coupling of the electric field on rippled silicon surface demonstrated that HSFL$_{\parallel}$ could also be the result of local field enhancement in between pre-existing ripples[56].

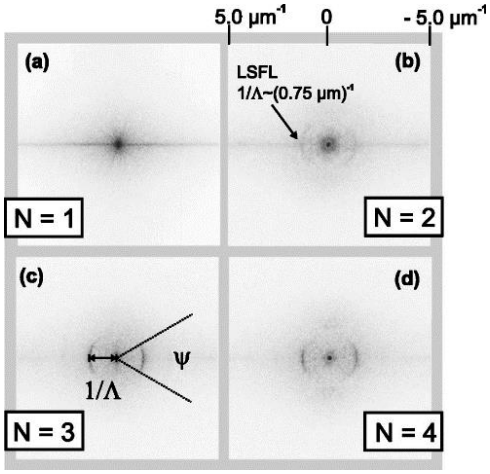

Figure 18 (taken from ref [90]) 2D-FT of phosphide SFM images after irradiation with (a) N=1, (b) N=2, (c) N=3, and (d) N=4 Φ = 0.58 J/cm^2, λ = 800 nm, τ_p=130 fs).

Upon increasing the number of pulses, the opening angle in the 2D-FT reduces from 100° for N = 2 to 30° for N = 100[90]. This signifies that the ripples which were initially curved around the center of the crater, now form a pattern of more straight lines with an increase of the irradiation shots[90]. More importantly, the period of the structures is reduced from 750 nm for N=2 to 590 nm for N = 100. This behaviour reported in other works[64,91] cannot be interpreted solely by Sipe's model. The transient changes on the material properties during the irradiation and as well as the surface evolution upon an increasing number of pulses is not taken into account by the efficacy factor theory.

2.2.1.2. Surface plasmon

Excited electrons on a metal-dielectric interface can oscillate in a collective and coherent way. The oscillation is longitudinal along the surface and is called surface plasmon. The oscillation frequency, ω is called plasma frequency. The electric field is described by[92]:

Equation 2 taken from ref. [92]

$$E = E_0^{\pm} \cdot e^{i[k_x x \pm k_z z - \omega t)]}$$

The wave vector $k_x = 2\pi/\lambda_p$ is parallel to the x direction and λ_p is the wavelength of the plasma oscillation.

Equation 3 taken from ref. [92]

$$k_x = \frac{\omega}{c}\left(\frac{\varepsilon_1 \varepsilon_2}{\varepsilon_1 + \varepsilon_2}\right)^{1/2}$$

Where ε_1 and ε_2 are the dielectric permittivities of the metallic surface and the dielectric medium, respectively. Considering $\varepsilon_2 = 1$ for air, the wavelength of the surface plasmon is given by the expression[64]:

Equation 4 taken from ref. [64]

$$\lambda_{sp} = Re\{\left(\frac{1+\varepsilon_1}{\varepsilon_1}\right)^{1/2}\}$$

Upon irradiation on a metallic surface, plasma oscillations can take place. The interference of the incident light with the surface plasmon is called surface plasmon polariton (SPP).

2.2.1.3. Sipe - Drude model

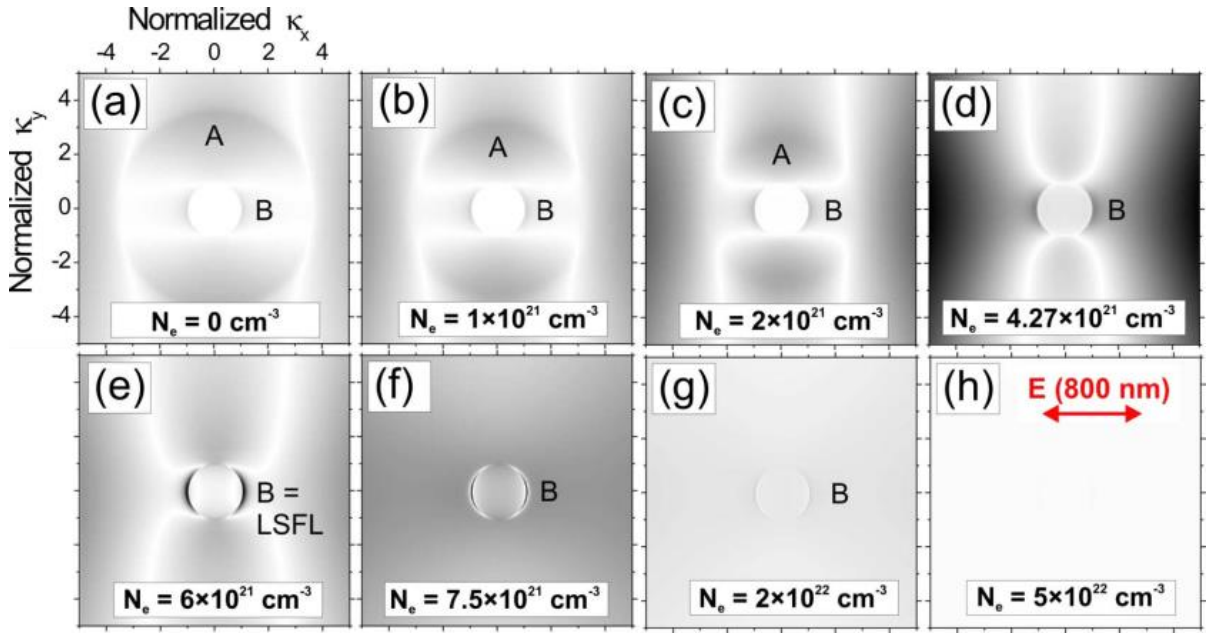

Figure 19 (taken from ref.[69]) 2D grayscale maps of the efficacy factor for single-crystalline silicon as a function of the normalized LIPSS wave vector x, y=-5.0⁻5.0 for different excitation levels of the material. The beam incident is normal (θ = 0°) and λ =800 nm; the polarization E is indicated in h. The values of η are encoded in a common linear grey scale with dark colours representing larger values. The symbols A and B label some characteristic features.

Intense irradiation of a semiconductor entails dramatic changes of the optical properties of the material due to carrier excitation. For USP irradiation, the refractive index and the reflectivity of the material will be transiently modified. The Drude model can be employed in order to describe those changes and a combination of the Sipe's theory with the Drude model leads to a more complete interpretation of the surface behaviour[69]. The excitation of a surface plasmon wave (SP) and its interaction with the incident light during the ultrashort pulse irradiation is proposed to be the physical mechanism of the inhomogeneous energy distribution[27,39,50,69]. An explanation was provided in the frame of surface plasmon polariton excitation theory at first for the range of the ripple period ranging $0.62\,\lambda < LSFL < \lambda$ and secondly for the narrow threshold for ripple formation in semiconductors[69]. According to that, for silicon irradiated with $\lambda = 800$ nm, τ_p=130 fs the dielectric function will be transiently modified due to changes in the carrier density on the surface affecting the efficacy factor[69]. Figure 19 shows 2D grayscale maps of the efficacy factor **η** with respect to the carrier density. The range between Figure 19 b and Figure 19 f corresponds roughly to the ranges between multi (Φ = ~0.2 J/cm^2, 1.4·10^{21} cm^{-3}) and single (Φ = 0.56 J/cm^2, N_e[v]= 6.7·10^{21} cm^{-3}) pulse ablation threshold. In Figure 19 feature B, which corresponds to LSFL, becomes more pronounced when the carrier density increases above a threshold value. Bonse et al. propose that the excitation of SP is possible when the free carrier density is high enough and

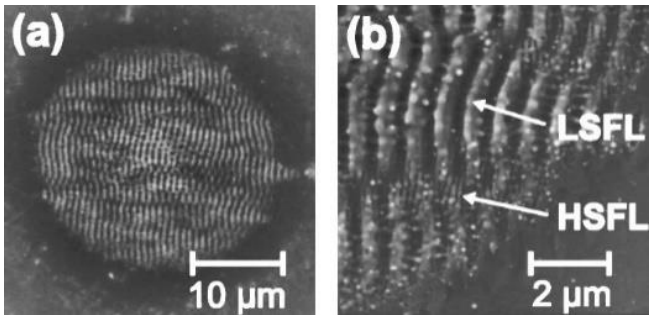

Figure 20 (taken from ref. [90]) SEM images of indium phosphide irradiated with N=10, Φ = 0.24 J/cm^2, λ = 800 nm, τ_p=130 fs (a) overview, (b) detail. The LSFL and HSFL rippled regions are marked by arrows in (b).

[v] N_e represents the free carrier density

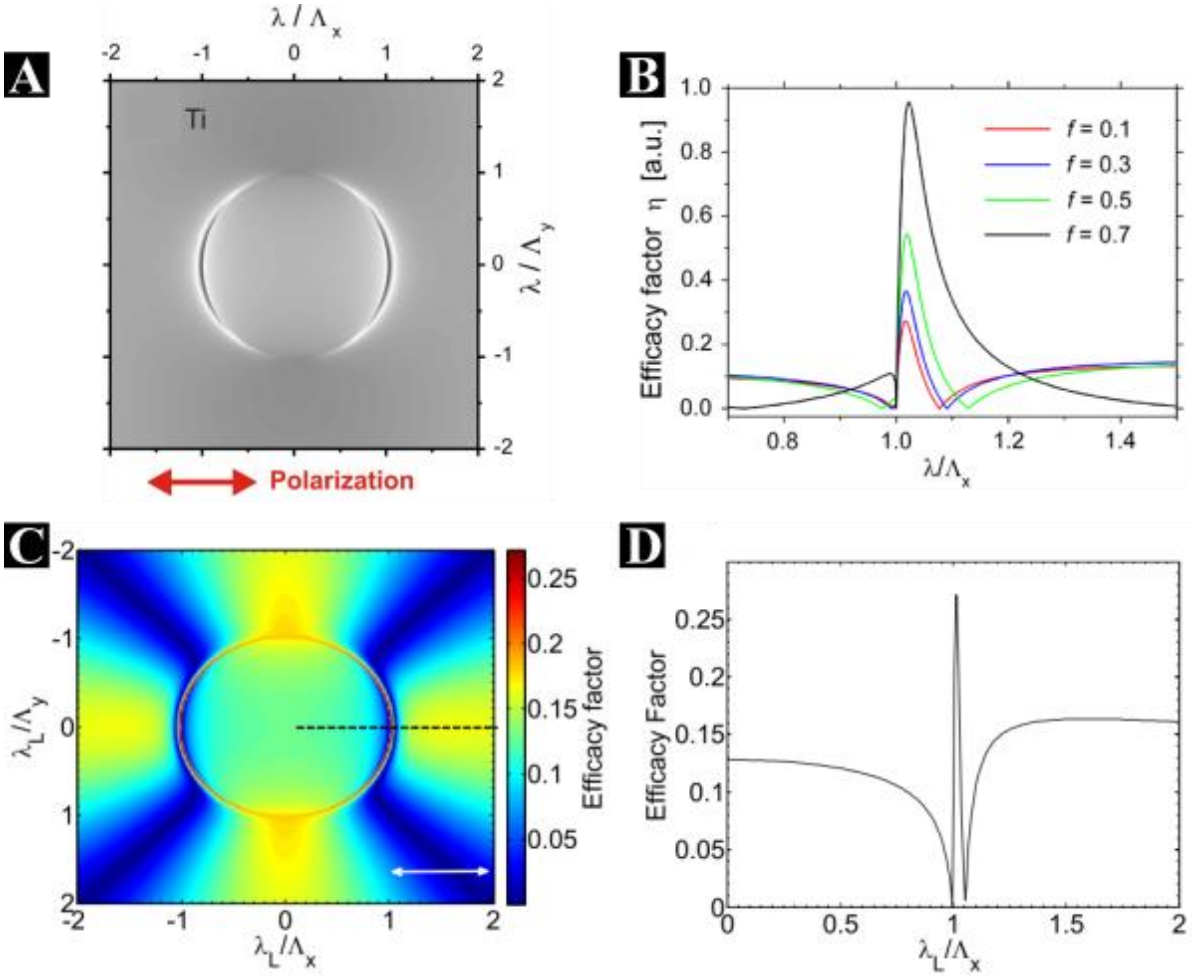

Figure 21 A: (reproduced from ref. [53]) 2D gray scale maps of the efficacy factor η for titanium for f = 0.1. The red arrow indicates the polarization. B (reproduced from ref. [53]): Efficacy factor η for titanium as a function of the normalized LIPSS wave vector $\kappa x = \lambda/\Lambda x$ ($\kappa y = \lambda/\Lambda y = 0$) for different values of the filling factor f between 0.1 and 0.7. (λ = 790 nm, s = 0.4). C: (reproduced from ref. [53]): Efficacy factor (η) map for 100cr steel (s = 0.4, f = 0.1 and λL=1026 nm). The double arrow indicates the direction of the polarisation vector of the optical radiation. D: (reproduced from ref. [53]), Efficacy factor η along $\lambda L/\Lambda x$ (black dashed line in b).

its excitation could dominate LIPSS formation in the early stages (low number of pulses)[69]. Non-metallic surfaces can be transiently transformed into metallic after excitation with a laser pulse. In that case the absorbed energy increases significantly the number of free electrons in the conduction band. When the transient metallic state is reached, SP can be excited on the surface. That is a plausible interpretation for the fact that ripple formation is observed only for specific fluence values[69].

In the same material for low fluence (Φ = 0.24 J/cm^2) and N= 5-30, HSFL$_\perp$ (perpendicular to the laser polarization) are observed on indium phosphide (Figure 20)[90]. Their period is smaller than $\lambda/2$ and varies between 360 nm and 330 nm[90]. Their formation cannot be interpreted by the Sipe-Drude model neither by the SPP theory. It is attributed to the nonlinear response of the surface and the second harmonic generation on the surface since the materials nonlinear response is very high[90].

Similar findings on ripple formation were acquired from studies in metals. The difference concerning metals is that most of them are inherently plasmonically active at wavelengths in the optical and near infrared range. In titanium, where the SP can be excited at 800 nm wavelength, LSFL formation occurs for a much wider range of periods with the lowest to be 200 nm and the highest 700 nm and fluence ranges (Φ = 0.03 -

0.7 J/cm^2) compared to semiconductors[53]. The 2D map of the efficacy factor in this case is shown in Figure 21, A. In Figure 21, B a 1D curve shows the behaviour of η for different values of the filling factor *f* between 0.1 and 0.7 underlining the significance of the surface roughness[53]. In titanium, LSFL were observed experimentally, after irradiation with fluences ranging from Φ = 0.09 to 0.35 J/cm^2, with periods between 405 and 800 nm matching for low numbers of pulses the period derived from the efficacy factor diagram[53]. For lower fluences close to the damage threshold and within a narrow window ranging from Φ = 0.05 J/cm^2 to Φ = 0.09 J/cm^2 (for N_p = 50), $HSFL_{\parallel}$ formation is reported[53].

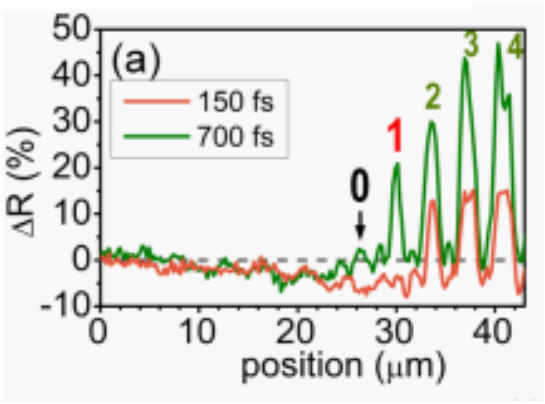

Figure 22 (Reproduced from ref. [59]) Horizontal cross sections of the transient reflectivity map of silicon surface after irradiation at delays t = 150 and 700 fs. The labels refer to the fringe #.

On stainless steel (100Cr6 steel), the condition of the SPP excitation is matched for a rough surface, giving the possibility for a production of a propagating electromagnetic wave which can interact with the incident laser beam[64]. An estimation of the resulting ripple period was carried out employing two different approaches: Sipe's theory[39] and the hypothesis that the ripple period was determined in the early stages by the SPP period[64]. Strikingly, the results obtained from the calculation of the efficacy factor (shown in Figure 21, C & D for λ = 1026 nm) and the SPP are in excellent agreement for the early stages of ripple formation[64].

An indication of surface plasmon excitation on silicon surface during ripple formation was obtained by pump-probe measurments[59]. A few tens to hundreds of fs after laser irradiation the carrier density in an irradiated semiconductor is significantly increased and the material is exhibiting metallic behaviour. That way SPP can be excited on the surface[59]. The transient SPP

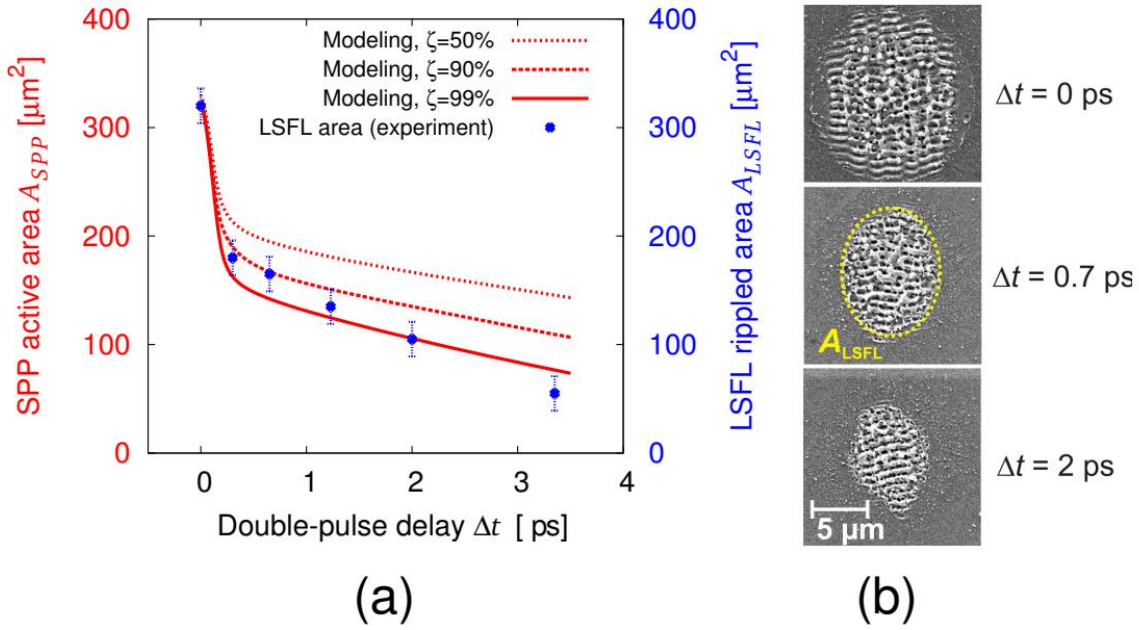

Figure 23 (Taken from ref. [94]) a: Calculated SPP active area A_{SPP} as a function of the double-pulse delay Δ*t* for three different values of ζ = 50%, 90% and 99% (corresponding to the time that the amplitude of the second pulse drops to the ζ value compared to the peak intensity) (a). The blue data points of the LSFL rippled area A_{SPP} are taken from[118] for comparison. Model parameters: F_0 = 0:40 J/cm2, *t* = 150fs, λ= 800 nm, w_0 = 16:5 *m*m. In (b), representative scanning electron micrographs for delays up to 2 ps are shown. The LSFL rippled area is marked at D*t* = 0:7 ps.

excitation creates a periodic modulation of the surface reflectivity[59]. In Figure 22 a horizontal cross section of the reflectivity map of a silicon surface is shown after irradiation at delays t = 150 and 700 fs. Fringe #0 refers to the ripple being formed by the laser pulse used to record the image. A periodic modulation is observed for $\Delta\tau_{probe}$ = 150 fs in the form of dark fringes that attenuate fast due to the absorption of the material that can be attributed to SPP excitation[59].

Further literature reports on the role of surface plasmon polariton interaction on ripple formation and was provided by Derrien et al. where the authors predicted with good reproducibility the ripple periodicities under varying angles of incidence[93]. In another work, the size of the rippled area formed on a silicon surface was studied for variable interpulse delays[94]. A theoretical investigation suggests that, as the interpulse delay between the two incident pulses increases in the range of a few ps, the size of the area where the SPP can be excited is shrinking. This trend was accurately validated with experiments of fs irradiation on silicon surfaces[94]. Figure 23, a, shows a graph of the values of the SPP active area, which were theoretically derived (red lines) and the experimentally measured values of the rippled area. In Figure 23, b SEM images are shown of the surface after irradiation with various delay values as indicated.

2.2.1.4. Modelling of light surface coupling

Another approach to the LIPSS formation is introduced by modelling of the electromagnetic incidence on the material surface. J.Z.P. Skolski et al. used the finite-difference time-domain (FDTD) method to simulate the inhomogeneous absorption of the laser radiation below a rough surface and made a comparison with the Sipe's theory[95]. The aim of this approach is to overcome the limitations of the Sipe's theory related to the transient changes on the surface during irradiation, the influence of the pulse duration, the dependence of η upon the material depth and, more importantly, the fact that it is not possible to study the interpulse feedback mechanisms in multi-pulse experiments [54,95].

The results of the simulation give a detailed map of the absorbed light intensity below the surface of the irradiated material either by depicting the light intensity map[95] or the FT of the intensity of the field (FDTD-η map)[96,97], where regions corresponding to different structures can be identified. A schematic guide to interpret the observed features in the inversed space is shown in Figure 25, peaks of intensity in each region marked with solid lines correspond to different types of structures as indicated[58]. The polarization direction is illustrated in Figure 25 by a double black arrow. The dotted and dashed circles indicate $\|k\| = 1$ and $\|k\| = \mathrm{Re}(\tilde{n}*)$ where $\tilde{n}*$ is the complex refractive index and Λ indicates the structure's period. An ablation model can be integrated in the simulations to study multi-pulse irradiation cases that produce the map of surface topography where the structure formation can be observed[54,58]. A variety of structures was predicted utilizing this method among others $LSFL_{\parallel}$ with periods close to the irradiation wavelength $HSFL_{\perp}$ and $HSFL_{\parallel}$[58], grooves[54,58] and crossed like structures[97].

In semiconductors as discussed in §2.2.1.3 (Sipe - Drude model) the electron density affects the optical properties of the material. This effect can be observed in the FDTD-η maps. In Figure 24 the results of the two approaches, 2D η maps (left) and the FDTD-η maps (right) are compared for three different electron densities[95] ($N_e = 2 \times 10^{27}$ m^{-3} (Figure 24 a & b), $N_e = 3 \times 10^{27}$ m^{-3}. (Figure 24 c & d), and $N_e = 4 \times 10^{27}$ m^{-3} (Figure 24 e & f)). The FDTD-η maps correspond to a depth in z = -15 nm computed with $\theta = 0$, λ = 800 nm, and (F,s) = (0.1,0.4). The FDTD-η maps are obtained with $x = y$ = 16 nm, z = 5 nm, t = 0.01 fs, $Nx = Ny$ =421, Nz = 50, and z = -15 nm.

The FDTD-η maps, product of the FDTD simulations are based on the inhomogeneously absorbed energy while the efficacy factor η is an analytical solution showing the efficacy with which the roughness leads to this inhomogeneous energy absorption[95]. In both maps, the location and the relative intensities of the type-

s (LSFL) and type-d (HSFL$_{\|}$) features follow the same trends[95]. Interestingly, the intensity of the features that correspond to the HSFL (type r) decreases rapidly and fades at z ≈ 60 nm below the roughness layer, for $N_e = 4 \times 10^{27}$ m^{-3} pointing out that they are "roughness dependent" [95]. Moreover, type r features corresponding to HSFL appear in FDTD-η maps for lower values of N_e. Considering the proportionality between the fluence and N_e, in case of linear absorption, this observation is in agreement with the fact that HSFL appear experimentally for lower fluence values than HSFL[95].

Another benefit of the method is that features with periodicities above the irradiation wavelength can be considered. While in the η maps the inner part of $||k|| = 1$ is forbidden, in the FDTD-η maps show the possibility to have an energy deposition with a periodicity larger than the wavelength of the laser light[95]. Those bright areas could be in principle associated with groove formation[95,96].

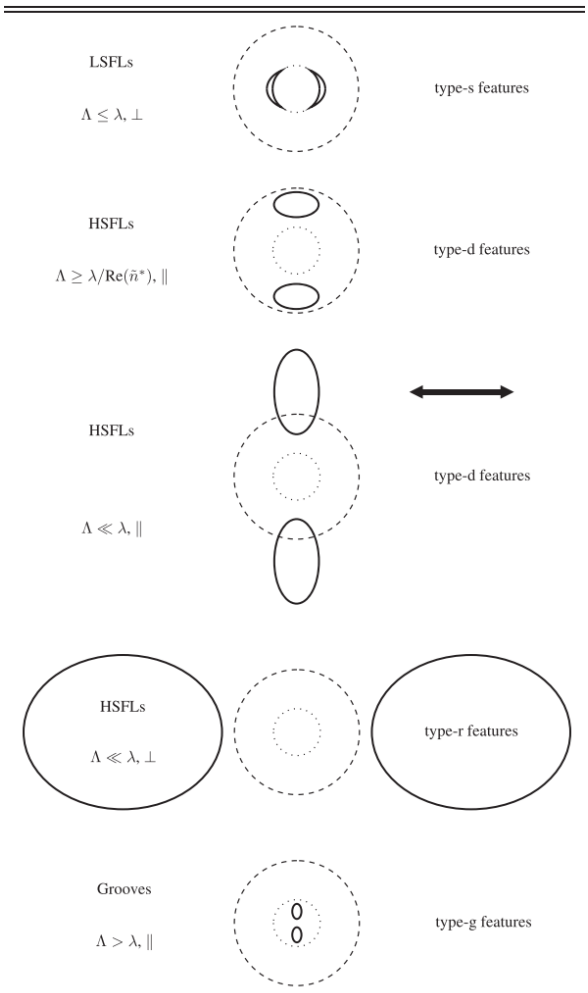

Figure 25 (Taken from ref. [58]) Summary of the different LIPSSs predicted by the FDTD-feedback simulations along with their signature in the frequency domain. The dotted and dashed circles indicate $||k|| = 1$ and $||k|| = \mathrm{Re}(\tilde{n}*)$, respectively. Λ indicates the structure's period.

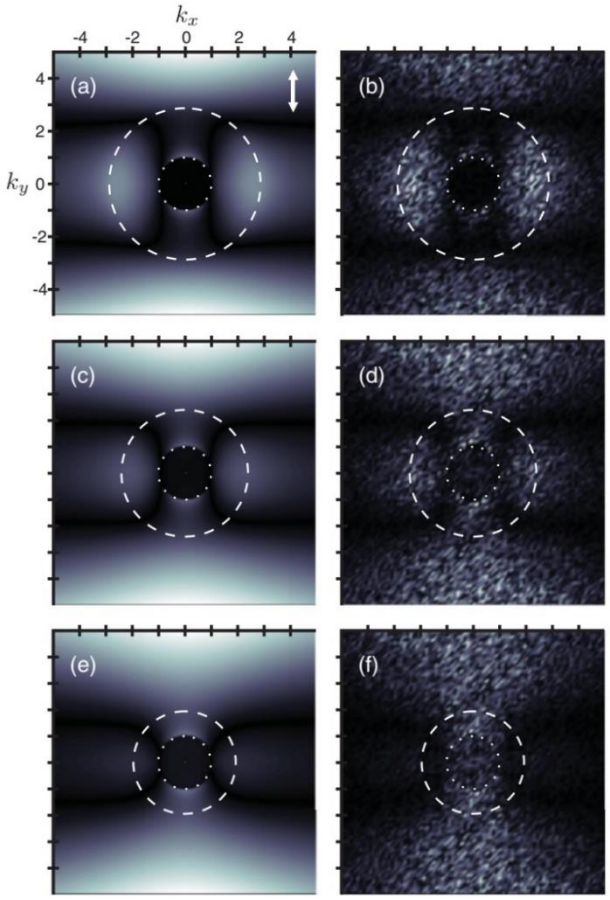

Figure 24 (Taken from ref. [95]) η and FDTD-η maps For panels (a) and (b), $N_e = 2 \times 10^{27}$ m^{-3}, $N_t = 26794$, $\tilde{n}* = 2.868 + 0.382i$. For panels (c) and (d), $N_e = 3 \times 1027$ m^{-3}, $N_t = 13436$, and $\tilde{n}* = 2.401 + 0.679i$. For panels (e) and (f), $N_e = 4 \times 10^{27}$ m^{-3}, $N_t = 13421$, and $\tilde{n}* = 1.943 + 1.116i$. The polarization direction is indicated by the white arrow in (a). The dotted and dashed circles represent $||k|| = 1$ and $||k|| = \mathrm{Re}(\tilde{n}*)$, respectively. A linear grayscale colourmap is used, the brightest areas have the largest values.

2.2.1.5. Feedback of the structures & Multi pulse irradiation

The collective effect of the surface roughness is shown here, and two cases were investigated under FDTD simulation on Ni [50]. The roughness is represented with particles of different sizes and the corresponding densities. Figure 26 illustrates an example of how the size and average distance of surface features impact the inhomogeneous distribution of laser intensity on the surface in a collective way[50]. The first case (Figure 26, a) considers particles with radius r = 30 nm with a concentration C = 2% (average interhole distance d_{hh} = 120 nm). The second case considers larger nanovoids of r = 50 nm with a lower concentration C = 0.2% (d_{hh} = 550 nm). Simulations of the resulting intensity distribution 20 nm below the material's surface are shown in Figure 26 for two roughness cases[50]. The electric field exhibits a periodic modulation in both cases and the period of the intensity variation changes with respect to the surface roughness. The intensity distribution resulting from small and dense features is oriented perpendicular to the polarization direction and ranges between λ/6 and λ/4 (Figure 26, a & d) corresponding to HSFL formation. In the second case (Figure 26, b & g), for larger and less dense features, the periodic modulation of the electric field is oriented perpendicular to the laser polarization with a period larger than λ/2 corresponding to LSFL formation[50].

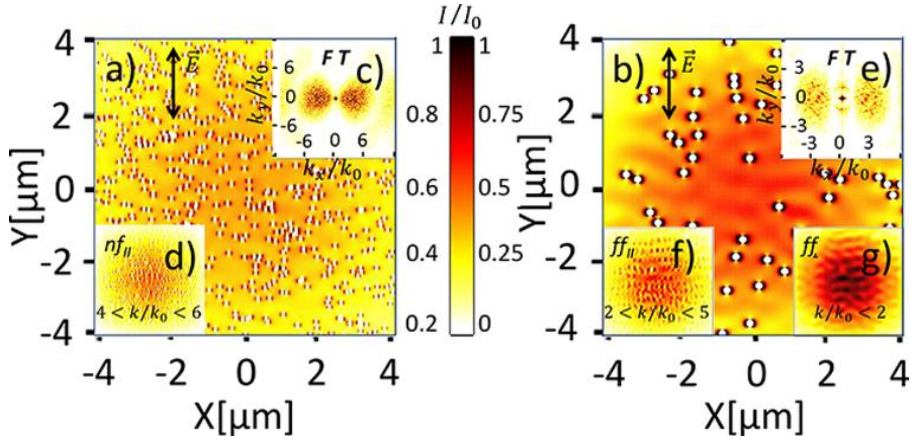

Figure 26 (reproduced by ref [50]) (a, b) Intensity distributions $I = |\vec{E}|^2$ calculated by 3D-FDTD simulations 20 nm below the Ni rough surface in the transverse plane perpendicular to laser propagation and (c, e) their Fourier transforms (FT). The distributions with the frequencies of interest, corresponding to $nf_{\parallel}$, $ff_{\parallel}$, and $ff_{\perp}$ features, are filtered for (d) $4 < k/k_0 < 6$, (f) $2 < k/k_0 < 5$, and (g) $k/k_0 < 2$, where $k_0 = 2\pi/\lambda$ is the wavenumber for the corresponding laser wavelength λ = 800 nm. The rough surface consists of (a) nanovoids of R = 30 nm with a high concentration C = 2% or (b) larger nanovoids of R = 50 nm with a lower concentration C = 0.2%.

2.2.1.5.1. Collective structure feedback

Since the first observation of LIPSS formation, the strong influence of surface features on the ripple formation is evident. It is generally accepted that the ripple formation will affect the way that the electromagnetic wave is distributed on the surface. Either viewed from the perspective of the efficacy factor, surface plasmon polariton or the simulation of the electromagnetic coupling, the ripple appearance on the surface will modify the conditions of electromagnetic radiation coupling to the surface.

FDTD simulations of multi-pulse irradiation taking into account the ablation phenomena showed how the structures evolve upon an increasing number of pulses[54,58]. In each simulation step, representing a single pulsed irradiation, the energy distribution on the material surface is calculated and the parts of the surface that absorb energy above a specific ablation threshold are removed. That way the surface roughness evolves upon an increasing number of pulses[54]. Figure 27 shows the evolution of surface morphology upon an increasing number of irradiations as indicated. The dark regions indicate the deeper parts of the surface.

The simulations were performed with Δ_a = 50 nm and a complex index of refraction of n = 1.339 + 3.22 *j*, corresponding to a density of free electrons in the conduction band of silicon of $N_e = 8 \cdot 10^{27} m^{-3}$.

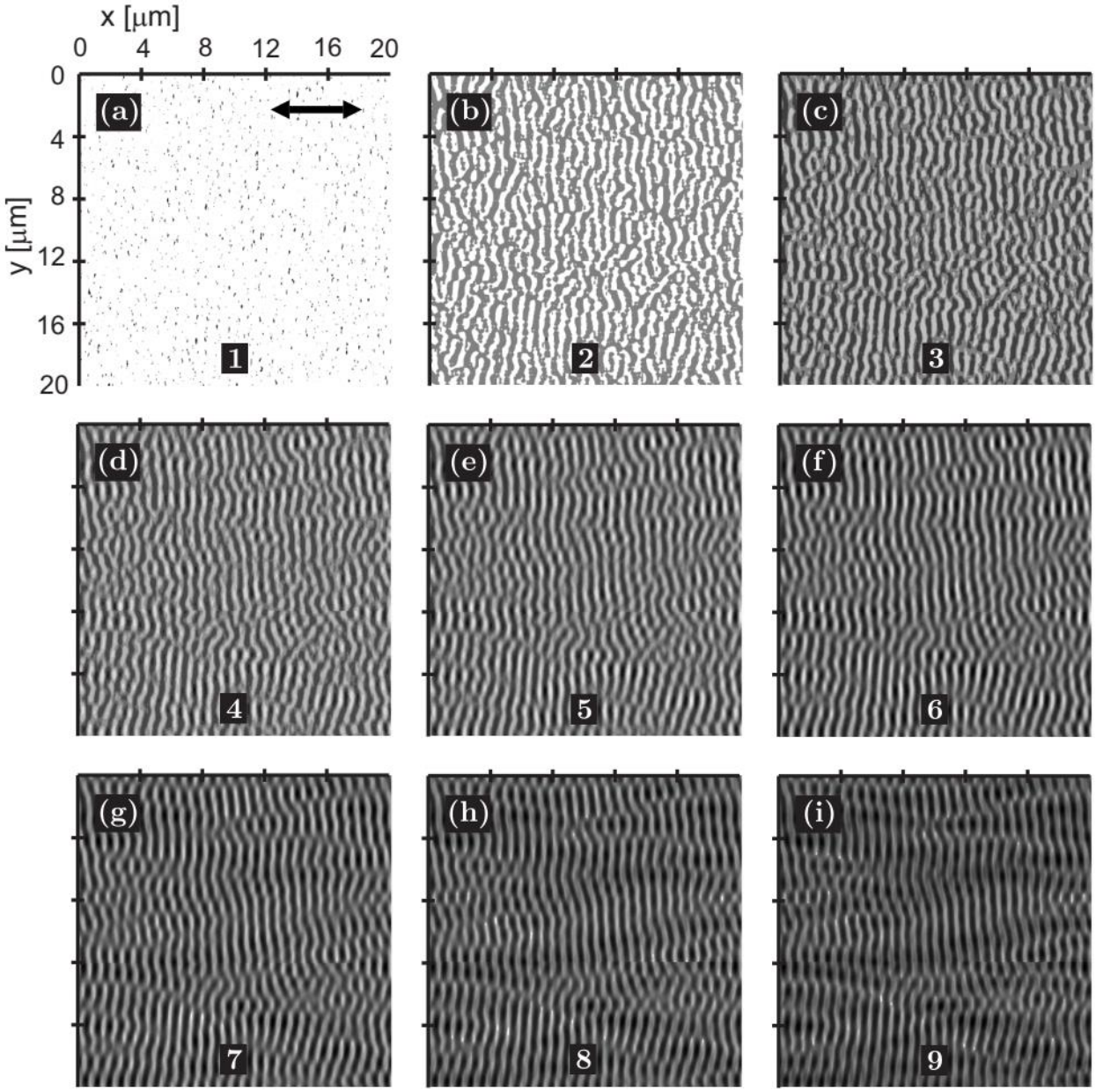

Figure 27 (Taken from ref. [54]). Top view of the surface morphology and the LIPSS appearance upon an increasing number of irradiation cycles as indicated. The black arrow in graph (a) indicates the polarization direction of the laser radiation. In these graphs, peaks of the LSFL are indicated in the bright(er) scales of gray, whereas the darker gray indicates the valleys of the LSFL.

After the first cycle the initial surface roughness is removed. Periodic structures are formed and further developed, becoming more and more regular upon increasing the number of simulation cycles[54]. The period of the structures in the 9th cycle is estimated to $\Lambda \approx 750$ nm for an irradiation wavelength of $\lambda = 800$ nm in agreement with the reports in literature for the LSFL size[54]. Moreover, supra-wavelength structures with periods ranging from 1.5 μm to 3.3 μm were observed in Figure 27, i, corresponding to groove formation[54].

The evident change in the ripple period upon an increasing number of pulses which is reported in numerous works[27,29,64,90,91,98] can be interpreted by employing the SP excitation model[29,64,90,91,98]. An extensive study of the ripple formation in metals, semiconductors and dielectrics, correlate the decreasing trend of the ripple period upon an increase of number of pulses, which is correlated with the deepening of the relief between the structures[91]. The progressive deepening changes the interaction geometry of the grating assisted light coupling, thus affecting the SP wavelength[91]. The more the relief deepens, the more the structure periods should decrease to ensure the optimum SP-laser coupling[91]. Via FDTD simulation it was shown that the deeper the grating, the more enhanced the electric field within the groove[91]. Figure 28 illustrates the result of the FDTD simulation for different depths of the groove schematically shown in Figure 28, a. Figure 28, d, shows the amplitude of the electric field as a function of the ratio between the ripple period (Λ) and the laser wavelength (λ). Figure 28 b, and c illustrate the intensity of the electric field for two different depths as indicated by the arrows. The positive feedback in this case is enhancing the deepening of the grooves by localizing the energy absorption.

A similar trend relating the increasing depth of the structures and the reduction of the ripple period is reported for silicon[27], silver[98], nickel[29] and steel[64]. In silicon[27], an increase of carrier density leads to an increase of surface plasmon wavelength. After the ripple formation, even though that an intensity increase is expected locally inside the wells, the average energy deposition decreases leading to the reduction of the SP wavelength. In steel, the trend is observed experimentally and predicted theoretically for three different wavelengths[64].

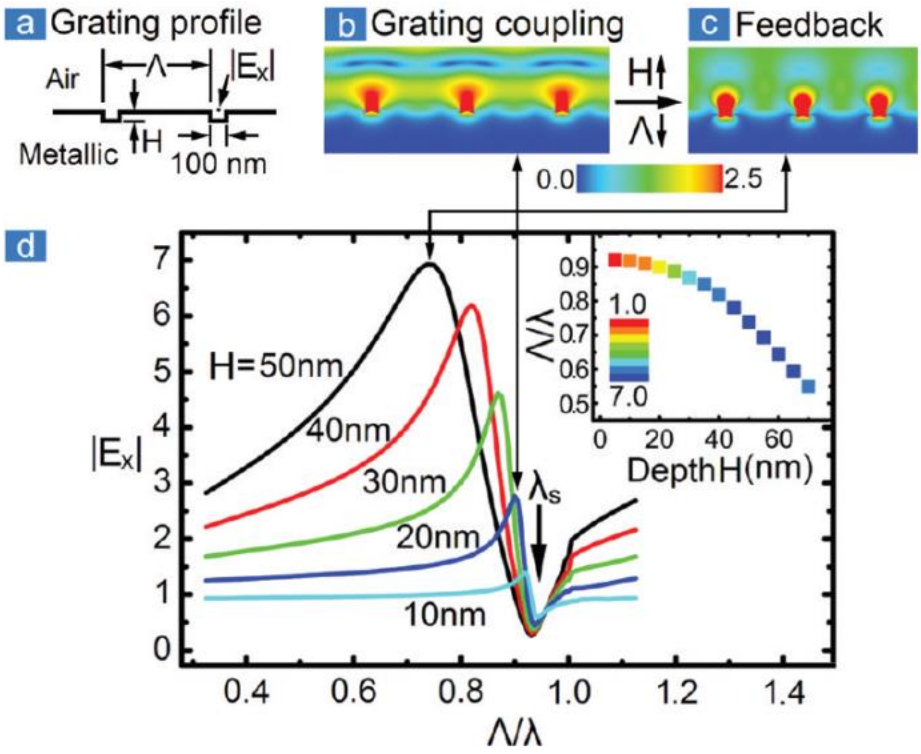

Figure 28 (Taken from ref. [91]). Simulation results for the grating assisted SP-laser coupling. a: grating profile. b & c: Electric field intensity for different groove depths as indicated b the arrows. d: Electric field intensity for the different depths of the grating profile.

2.2.1.5.2. Isolated structure feedback

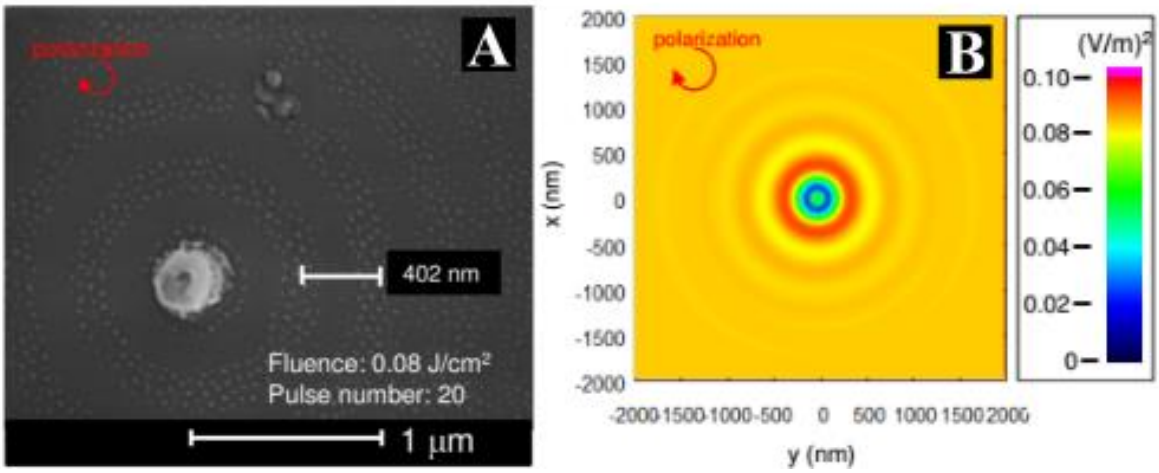

Figure 29 (reproduced from ref. [99]) A & B: SEM images of the silicon surface after the laser irradiation. (a) Ripples. (b) Close-up picture near the center (different area). λ = 400 nm, N = 20 and Φ = 80 mJ/cm^2 (below the bulk silicon ablation threshold). C: The simulated optical field intensity ripples induced by a single gold particle on silicon substrate. The incident electric field strength is 1 V/m and λ = 400 nm. The optical intensity distribution is shown on *xy* plane at *z* = -5 nm for silicon.

A study of alternative configurations of polarization state and surface morphologies were carried out only for isolated surfaces of 1D or 2D structures. One single feature was found to direct the interference patterns[69,87,99]. FDTD simulations of irradiation of predefined surface features with a fs laser pulse showed that the electric field intensity can be strongly modulated by the presence of surface features[99]. The interference pattern produced by the incident electric field and the field scattered from the gold particle generate an intensity pattern in agreement with experimental results[99]. In Figure 29 the experimental result

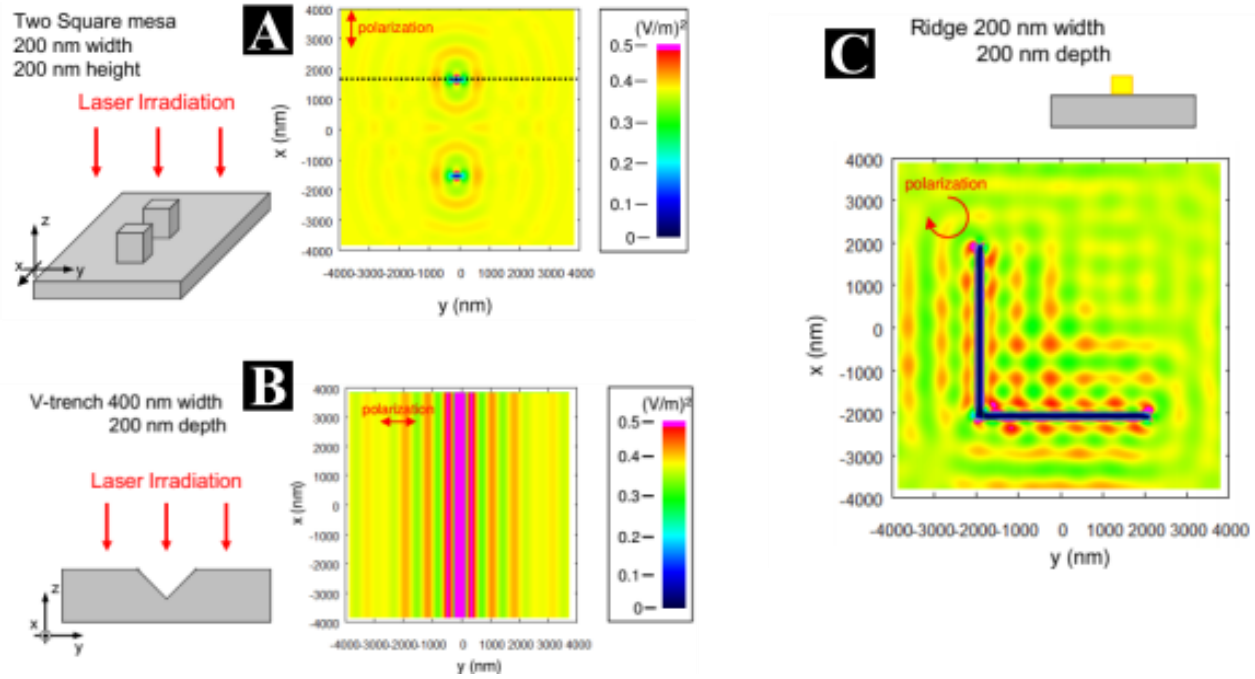

Figure 30 (reproduced from ref [99]) Simulated optical field intensity of irradiated features on metal like silicon observed at *z* = –5 nm. A: Around two square structures of silicon on silicon substrate. B: Around V-trench on silicon substrate. C: Around L-shaped gold ridge structure.

of gold particles on a silicon surface are compared to the result of a simulation of the incident electric field. In Figure 29 A, an SEM image of the irradiated particle is shown. The irradiation parameters were: $\lambda = 400$ nm, N = 20 and the fluence was below the ablation threshold. $\Phi = 80$ mJ/cm^2. The observed concentric rings formed during the irradiation (Figure 29, A) are attributed to the interference of the incident beam with the scattered electromagnetic field (Figure 29, B)[99].

In the same study[99], different configurations of the incident beam polarization and surface morphologies were simulated. The irradiated particle composition and morphology, the material used as substrate, the incident polarization and the excitation level in silicon (metallic silicon or normal) were found to determine the way that the electric field is distributed[99]. In Figure 30 a few more examples are illustrated. It is demonstrated that in the vicinity of a single square particle, the ripple pattern reflects the square shape elliptically along the polarization direction, and the outer ripples converge to the circular ripple pattern. In Figure 30, A the case of two square nanoparticles are shown, and a ripple pattern is formed perpendicular to the laser polarization. The difference in that case is that the reflected electric field scattered from both structures generates a more complex interference pattern near the structures. In Figure 30, B a trench also behaves as a scatterer, were the two top edges and bottom edges act as the surface plasmon-polariton sources for the near field. In this case, the ripple pattern is formed perpendicular to the laser polarization and parallel to the trench. In Figure 30, C the behaviour of an L-shaped gold ridge on silicon is studied under irradiation with a circularly polarized beam. The simulation results show a 2D periodic dot arrays formation of the electric field. The interpretation lies in the fact that the circularly polarized beam has two components: *E*x and *E*y vectors. Each vector makes a linear interference pattern orthogonally, resulting in the formation of the 2D dotted arrays[99].

2.2.2. Microfluidic motion of the material

After the surface ablation, or in sub-ablation conditions, in areas that the melting temperature is reached, laser irradiation entails the generation of a melted layer on top of the surface. This melted layer, until its resolidification, will undergo dynamical motion. Modelling of the melting and resolidification of the material under a spatially periodic excitation of the surface reveals the impact of microfluidic movement in ripples formation[27]. The model described here, takes into account the Marangoni effect to describe a liquid flow under the existence of temperature gradients and the contribution of the recoil pressure induced by ablation[27]. During the melted phase of the material the hydrodynamical effects can be influenced by the recoil pressure, the surface tension pressure and the surface tension gradient whilst the Navier-Stokes equations are employed to describe the resolidification process[27]. In the simulation, the ablation of the first shot induces a crater with a depth in the order of 10 nm. Due to the contribution of surface tension and the recoil pressure, the crater is deepened to about 20 nm and a protrusion is formed in the outer part of the

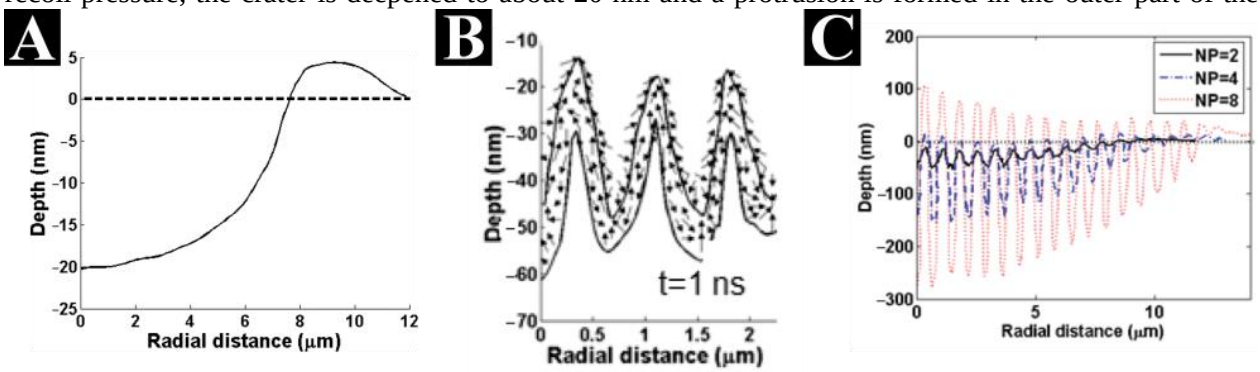

Figure 31 (Reproduced form ref. [27]) A: Theoretical results for *n* = 1: surface modification as a function of radial distance (axial symmetry) B: Cross section of the surface showing the flow pattern at t = 1 ns. C: Crater profile showing ripple formation after repetitive irradiation.

crater[27]. Both the rim formation and the crater depth are confirmed experimentally. The radial profile of the crater is shown in Figure 31, A. Irradiation with a second pulse gives rise to a surface plasmon wave and produces a spatially modulated energy deposition. The periodic deposition of laser intensity leads to localized surface tension gradients that ultimately drive to rise and depress the molten surface. The recoil pressure is now a periodic function and further assists the shaping of the surface. A clockwise melt flow is developed, and ripples are formed perpendicular to the electric field[27].

For repetitive irradiation the ripple amplitude is increased (Figure 31, C) due to an increased gradient in energy deposition as described in 2.2.1.5.1 (Collective structure feedback). Both, the ripple period as well as the groove depth are in good agreement[27]. Lastly, even though the determination of the ripple period derives from optical effects, the simulations signify that the hydrodynamics and the evolution of the melt flow can maintain the surface structures.

Although the described above model provides quite satisfactory data for the microfluidic movement of the material, the role of the Marangoni effect is critically viewed in the literature. An argument about the timescale necessary for the development of the Marangoni effect comes from R. Fang, et al.[62]. In a pump-probe experiment elaborating on the ripple formation process, the structures appear on the surface in the picosecond timescale (the structure appearance is discussed in § 2.2. A characteristic timescale for the Marangoni effect was estimated to be in the order of t_M = 20 ns, two orders of magnitude higher than the structure appearance timescale[62]. Excluding that way the case that Marangoni can be the primary cause of the structure appearance but without excluding its effect at longer timescales[62].

Another argument comes from the estimation of the minimum necessary temperature difference between the periodically hot and cold areas induced during the irradiation[38]. In his analysis, E. Gurevich estimates a temperature difference that can enable temperature driven Marangoni instabilities two orders of magnitude larger than what can be laser induced[38]. It is suggested that during the ablation or during the surface cooling, Rayleigh–Taylor instabilities can be developed and the temperature-dependent recoil pressure can affect the underlining mechanism for ripple formation[38].

2.3. 2D structure generation & double-pulse irradiation

In addition to normal ripples with 1D periods, which are induced by trains of linearly polarized pulses, 2D periodic morphologies can be laser induced in the near micron scale. Those structures can derive from various irradiation conditions: Irradiation with single pulses having circular[43] or radial[44] polarization, successive surface scanning with orthogonal polarization[100] or irradiating with subsequent pulses having different polarization[101,102] or by different colour and cross polarization[103].

Moreover, 2D structures (2D-LIPSS) can be induced by irradiation with double (or multi) pulses[104,105]. Figure 32 shows 2D morphologies obtained with different techniques. In Figure 32, A, rhombic structures were fabricated after irradiation of Nickel with an azimuthally polarized beam[44] (pps[vi] = 62 and Φ = 0.24 J/cm^2). The SEM image in Figure 32, B, shows nano-protrusions produced in Titanium after irradiation with double fs pulses τ_p = 40 fs and $\Delta\tau$[vii] = 160 fs. Figure 32, C, illustrates the morphology obtained by simultaneous irradiation with two pulses with different wavelength (λ_1 = 800 nm , λ_2 = 400 nm and $\Delta\tau$ = 0 fs)[103]. Finally, Figure 32, C illustrates 2D the morphology obtained with double crossed-polarized pulses with $\Delta\tau$ = 1.2 ps and Φ = 0.18 J/cm^2 in tungsten[106].

[vi] pps is defined as pulses per spot, see Equation 7 in §3.1
[vii] $\Delta\tau$ is the interpulse delay between two pulses.

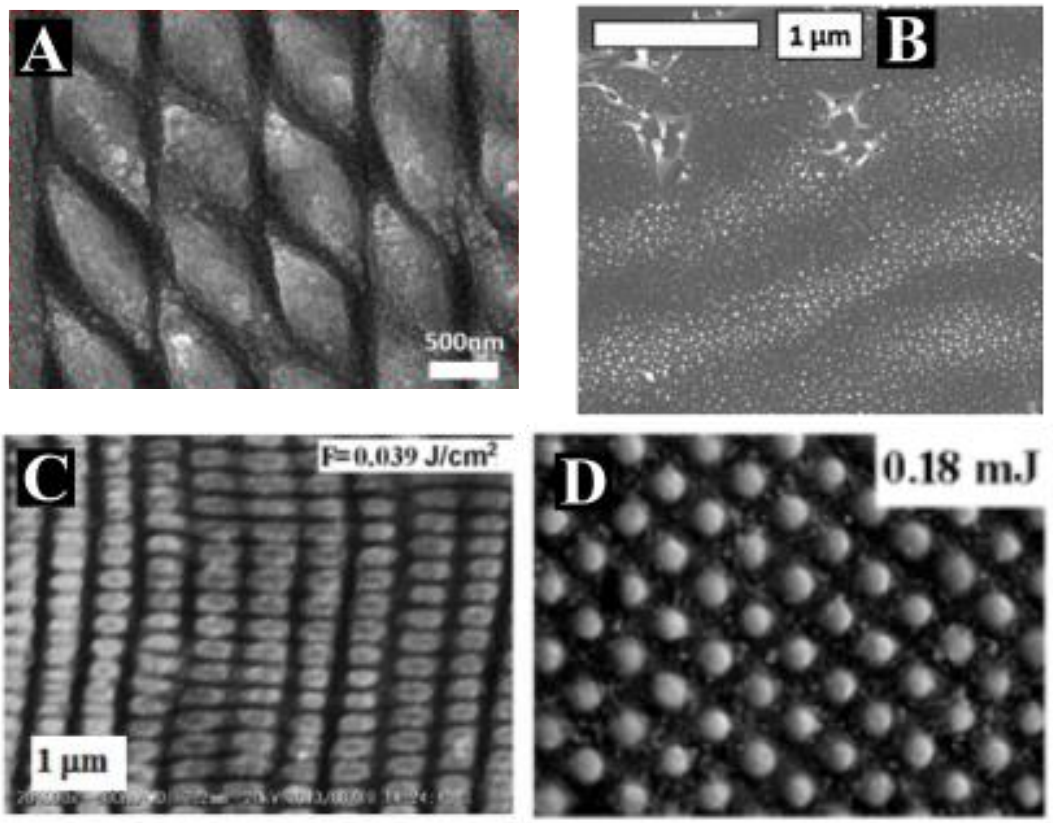

Figure 32 A: (from ref. [44]) Top-view SEM images depicting line scans produced by azimuthally polarized beams, respectively, at v = 0.5 mm/s (pps=62), and Φ = 0.24 J/cm^2 B: (from ref. [107]) SEM images of surface structures on Ti produced by 1 double pulse ($\Delta\tau$ = 160 fs τ_p = 40 fs Φ = 0.125 J/cm^2. C: (from ref. [103]) SEM images of the structures on Mo surfaces by simultaneous two-colour irradiation. Φ = 0.071 J/cm^2 and Φ = 0.039 J/cm^2 D: (from ref. [106]): SEM image of Tungsten irradiated with double fs pulses with $\Delta\tau$ = 1.2 ps and Φ = 0.18 J/cm^2.

The double-pulse irradiation method has a greater potential in controlling nanostructuring compared to single pulse approaches. On the one hand, double pulse irradiation offers a dynamic approach in controlling laser induced nanostructuring. In single pulse irradiation, the surface structuring is a deterministic result of the irradiation parameters (fluence, polarization, number of pulses etc.), while double-pulse irradiation enables the possibility to intervene in the ripple formation process, during the evolution of the ultrafast phenomena. On the other hand, in double-pulse irradiation the degrees of freedom in the irradiation parameters are qualitatively different. Apart from the delay, which is considered the key parameter of the process, double-pulse irradiation offers several levels of control on the irradiation conditions since it enables the combinations of different pulse fluence[107], pulse polarization state[108] and irradiation wavelength[109].

The method uses the first femtosecond pulse to initiate an avalanche of interdependent processes. Each of the processes occurs in a characteristic timescale (§2.1). During this transient state, the surface undergoes several transformations until it reaches the equilibrium. The electron and lattice temperature[110] (Figure 33), the electronic structure of the material[111], the surface reflectivity[50,59], the phase of the surface and the level of structure appearance[60,62] are constantly changing. Each phenomenon occurs in a different, characteristic timescale. Indeed, changes in reflectivity and in the electronic band structure occur in the first picoseconds while changes in the materials phase and shape occur later, in hundreds of ps extending to the ns regime[59,75].

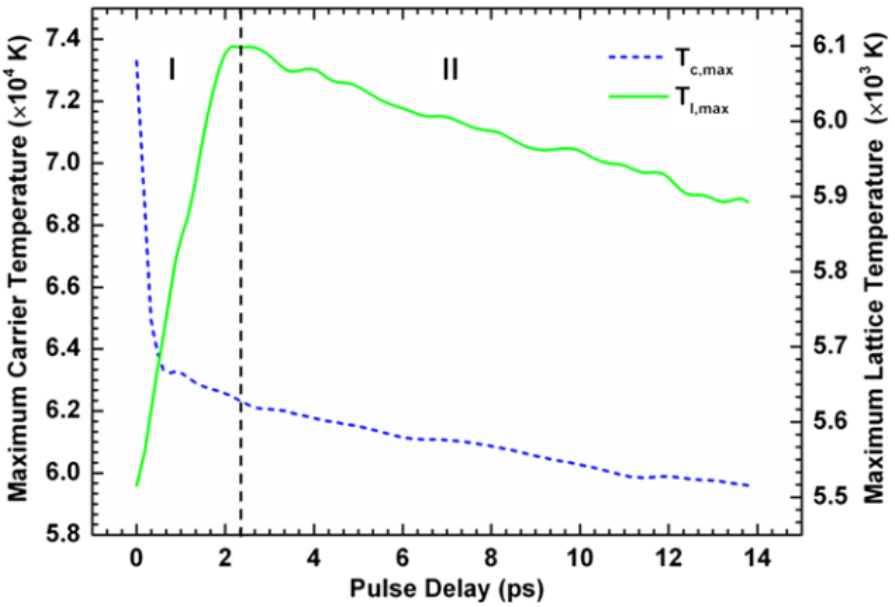

Figure 33 (reproduced from [110]). Maximum electron (T_c) and lattice (T_l) temperature dependence on the interpulse delay ($\Delta\tau$). (N = 12, Φ = 0.48 J/cm^2 τ_p = 430 fs and λ = 800 nm).

The effect of the delay, irradiation wavelength and polarization configuration on the induced ripple morphologies has been extensively investigated for $\Delta\tau$ ranging in the picosecond timescale. S. Hohm, J. Bonse, J. Kruger, T. Derrien et al. which study the nanostructure formation in metals, dielectrics and semiconductors[49,109,112–118]. Tsibidis et al. have studied the effects of the double-pulse interpulse delay on surface plasmon polariton excitation and the ripple formation. Comparing simulations and experimental data[48,110] they showed that when $\Delta\tau$ ranges in the picosecond timescale, electron-phonon interactions can be controlled. Hot electron diffusion and electron-phonon coupling, which are two competing mechanisms of electron relaxation, can be controlled by $\Delta\tau$ variation and will lead to changes of maximum electron (T_c) and lattice (T_l) temperatures as shown in Figure 33. A study on Nickel proposed that for delays $\Delta\tau < 0.4$ ps, the surface electrons are excited by both pulses before their energy is transferred to the lattice[50]. For 0.6 ps $< \Delta\tau <$ 2 ps, the optical and thermodynamical properties of the material are strongly modified before the arrival of the second pulse[50]. For 0.6 ps $< \Delta\tau <$ 6 ps an increase of the Nickel absorptivity is expected amplifying the impact of the second pulse[50].

Ultrafast changes on the material properties impact on the laser induced surface structure. In the case of double linearly polarized pulses, a $\Delta\tau$ variation will affect the surface plasmon excitation, entailing changes in the ripple period[48,110,119] and the spot area (Figure 23)[110,113,118]. In metals and semiconductors, when irradiated with double crossed-polarized pulses with equal fluence, the ripples orientation is defined by the second pulse[108,112,120,121]. When the irradiation pulses are of different wavelength and crossed polarized, both pulses produce ripples on the surface when $|\Delta\tau| \leq 1$ ps. For $|\Delta\tau| > 1$ ps the ripples induced by the second pulse are dominant[112]. Irradiation with double circularly polarized pulses can eliminate the linear factor in the induced structures[108]. When the fluence is not equally distributed between the two pulses, the pulse fluence is found to have a stronger effect on the ripple orientation than the delay[108,117]. Furthermore, a systematic reduction of the rippled area is reported for increasing delay in the picosecond timescale[110,113,118].

As a summary, the potential of the method on controlling the surface morphology has been demonstrated for single spots and in some cases for double-pulse irradiation over single scanning lines. Generation of homogenous morphologies over large areas is still an open challenge. Moreover, to the best of our

knowledge, the effect of the interpulse delay in sub-nanosecond and nanosecond ranges ($\Delta\tau > \sim 0.1$ ns) is unexplored so far.

2.4. Grooves and spikes formation

Upon an increasing number of pulses, morphologies with periods greater than the laser wavelength namely grooves and spikes are formed on the surface. An example is shown in Figure 34 for silicon[46] irradiated with λ = 800 nm, τ_p=430 fs, Φ = 0.7 J/cm^2 and an increasing number of pulses (N). Ripples are formed for N = 10 (Figure 34 a & b), grooves for N = 40 (Figure 34 c & d), and spikes for N = 100 (Figure 34 e & f). While ripple formation - as extensively discussed in 2.2 - results from the inhomogeneous energy absorption of the incident light, the supra-wavelength structure formation cannot be attributed to that mechanism and is still under debate. Grooves are formed with spatial periods between 2 μm and 4 μm in indium phosphide irradiated with λ = 800 nm, τ_p=130 fs [90] and a number of pulses N> 20-30 and is strongly affected by the laser fluence.

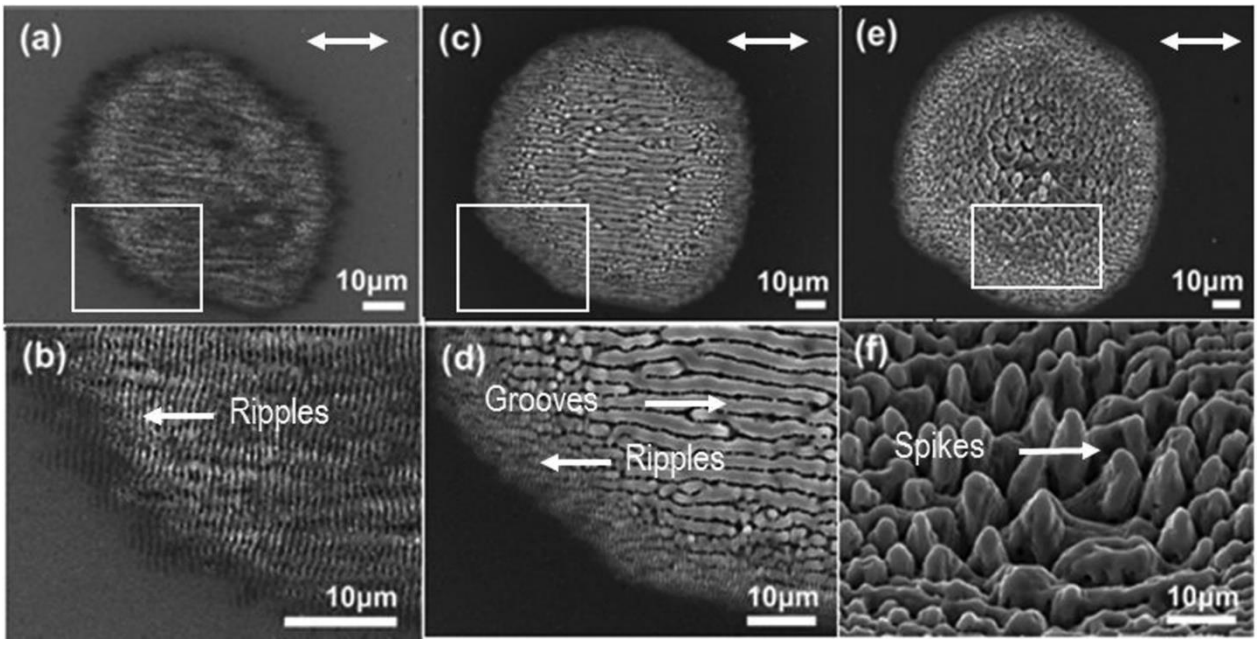

Figure 34 (Taken from ref. [46]) SEM of silicon surface after irradiation with λ = 800 nm, τ_p=430 fs, Φ = 0.7J/cm^2. Ripples are formed for N = 10 (a & b), grooves for N = 40 (c & d), and spikes for N = 100 (e & f). Double-ended arrows indicate the laser beam polarization.

2.4.1. Polarization impact on groove and spike formation

Both ripples and spikes are linked to the polarization direction for linearly polarized incident pulses. Grooves are formed parallel to the laser polarization and their period is in the range of a few microns [46,54,96]. Spike formation is the subject of many published works that report on the main parameters that determine their size[34,122], shape[123] and orientation[34].

In silicon irradiated with λ = 800 nm, τ_p=120 fs, Φ = 1 J/cm^2 the spike shape was found to depend on the laser polarization[123]. For linear polarization, the shape of the base of the spikes is elliptical and the long axis is oriented perpendicular to the orientation of the polarization[123]. When the pulse polarization is circular the shape of the spikes is conical[123]. Figure 36 illustrates the effect of the polarization.

The spike shape dependence on the polarization can be interpreted taking into account the transmissivity of the beam under the incident conditions[123]. The geometry of incidence is shown in Figure 36, A. Assuming a perfectly conical formation for the spike (Figure 36, A) the transmissivity of the incident light varies with the incident angle for the s & p-polarized cases (Figure 36, B)[123]. For a fixed angle of incidence $\theta_i = 70°$ derived from the average spike geometry the transmissivity for the s-polarized and p-polarized incidence was $T_p = 99.32\%$, and $T_s = 29.48\%$, respectively[123]. In between the two values a continuous variation of the transmissivity is derived based on the Fresnel and Snell's law and is shown in Figure 36, C where the incident polarization is marked with a red arrow[123]. As can be seen, in the direction parallel to the laser polarization (a = 0°, 180°) the transmissivity is much higher than in the direction perpendicular to the laser polarization (a = 90°, 270°)[123]. Therefore, for angles close to a = 0° or 180° the ablation volume per pulse must be higher than angles of roughly a = 90° & 270° ultimately forming an elliptical spike base[123]. The large axis of the ellipse is expected to be oriented perpendicular to the laser polarization. That hypothesis is experimentally confirmed[123,124].

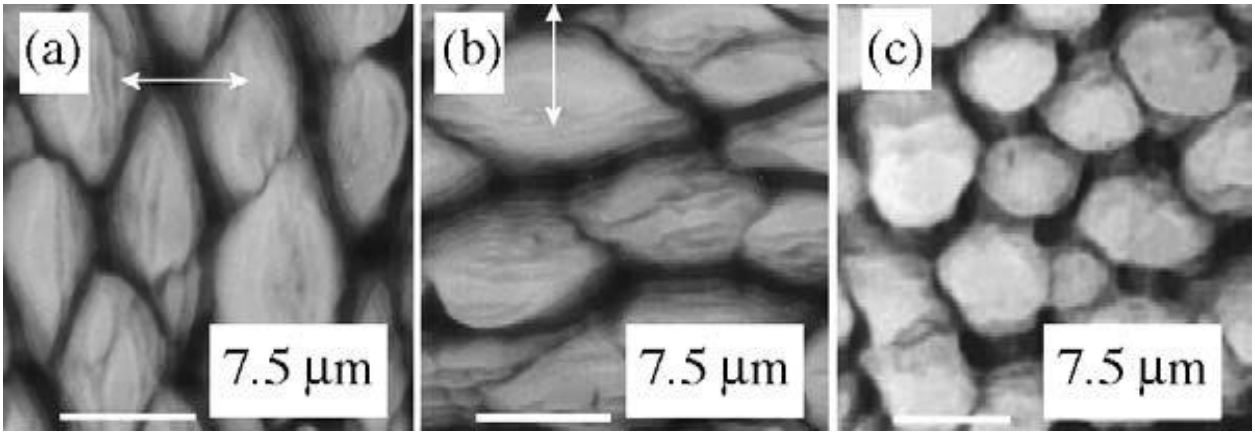

Figure 36 (Taken from ref. [123]) SEM images (top view) of silicon surface micro-structured by a linearly polarized laser beam (a and b), and a circularly polarized beam (c)

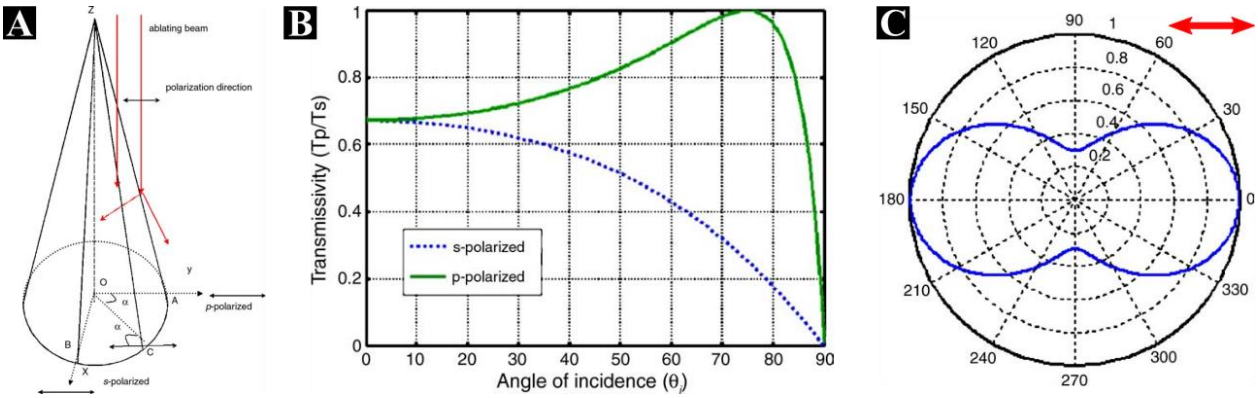

Figure 36 (reproduced from ref. [123]). A: Schematic diagram of a linearly polarized laser beam incident on the spike. B: Transmissivity as a function of the angle of incidence (θ_i). C: Transmissivity as a function of the angle of the polarization with the plane of incidence α, for $\theta_i = 70°$.

2.4.2. Fluence impact on groove and spike formation

The fluence has a huge bearing in the spike formation process. Initially, spike formation is observed upon a specific fluence threshold[34,54]. Above that point, the fluence was found to determine the structure size and shape[34,124]. In Ti irradiated with λ = 800 nm, τ_p=130 fs, 1kHz spikes appear above Φ = 0.5 J/cm^2 which is higher than the ablation threshold[34]. By varying the fluence value, the spike size can be varied[34]. Figure 37 A to D show the resulting morphology after irradiation with Φ = 0.5, 0.7, 0.9 and 1.1 J/cm^2, respectively. That way the spike size was varied from ~ 6 µm to ~ 24 µm as shown in the graph in Figure 37, E. Three different slopes are observed on the curve: In the low fluence range, from Φ = 0.5 to 0.7 J/cm^2, the spike size increases slowly with fluence. Then, from Φ = 0.7 to 1.0 J/cm^2, the curve exhibits a higher slope and the spike size rapidly increases with fluence. Finally, for Φ = 1.0 up to 1.2 J/cm^2, the slope is lower and the spike size slowly increases with fluence [34]. In the latter case, a saturation of the spike size can be observed. The spike size increases with the number of pulses reaching a saturation size at around N = 500[34].

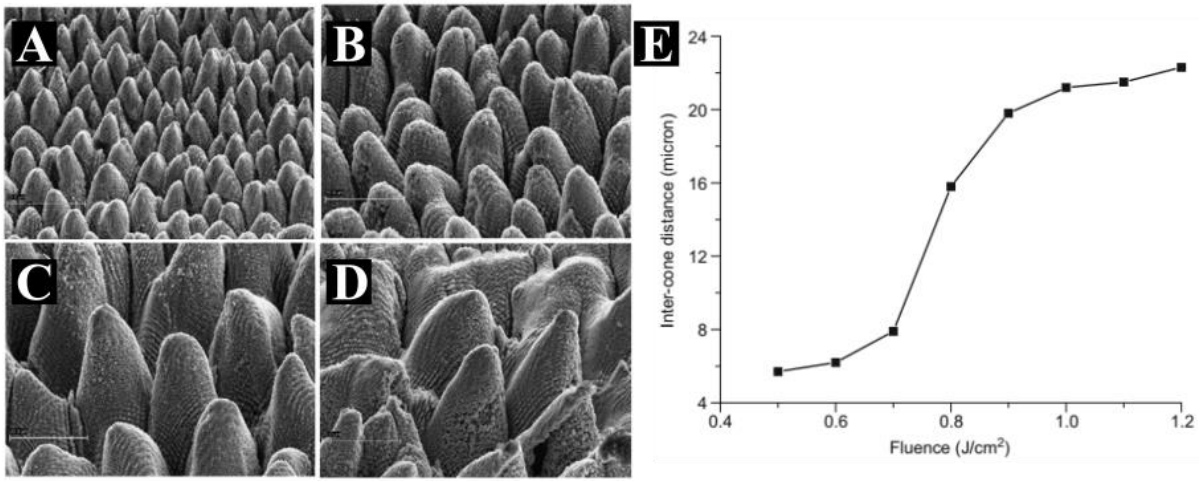

Figure 37 (reproduced from ref. [34]). A-D: SEM images of the spike size after irradiation with Φ = 0.5, 0.7, 0.9 and 1.1 J/cm^2, respectively, and N = 450. E: graph showing the inter cone distance.

2.4.3. Groove and spike formation mechanism

With the exception of shallow grooves, which are proposed to result from light scattering below the materials' rough surface,[96] the semi periodic structures (grooves and spikes) ranging in the 10 µm-scale cannot be interpreted solely by light interference. Two mechanisms are proposed to describe the spike formation. One describes grooves and spikes formation in the frame of microfluidic movement of material driven from temperature gradients[46] and the other proposes that light scattering from surface defects leads to conical surface formation[124]. Although the two mechanisms seem to contradict each other, they are complementary describing the spike formation in two district fluence regimes.

2.4.3.1. Ablation-based spike formation mechanism

In the low fluence regime, for the irradiation of stainless steel fluences ranging from Φ = 0.17 to 3.85 J/cm^2 were chosen to study the evolution of surface morphology[124]. The other laser parameters were λ = 800 nm, τ_p < 100 fs and f = 10 kHz[124]. For Φ = 0.11 J/cm², small and randomly distributed surface protuberances, called bumps,are observed in an underlining LIPSS terrain[124]. Similar structures were observed in high throughput ablation study[125]. These bumps grow with increasing number of scans, and merge between each other as shown in Figure 39 (right)[124].

The bumps appear after multiple laser scans; it is possible to visualize their appearance and morphology evolution using scanning electronic microscopy (SEM) as shown in Figure 38[124]. After the first scan the surface is exclusively covered by LIPSS. After the second scan ellipsoidal surface protrusions appear on the surface. When the number of scans (N) increases, their average diameter increases as well. For example, in Figure 38 the average diameter increases from 5.5 μm (N = 2) to 13.3 μm (N = 4), 25.8 μm (N = 7), and then finally to 39.1 μm (N = 10). This indicates that cones originate from certain surface precursors which then grow in size[124]. Moreover, cones can appear after different numbers of scans. In Figure 38, c two

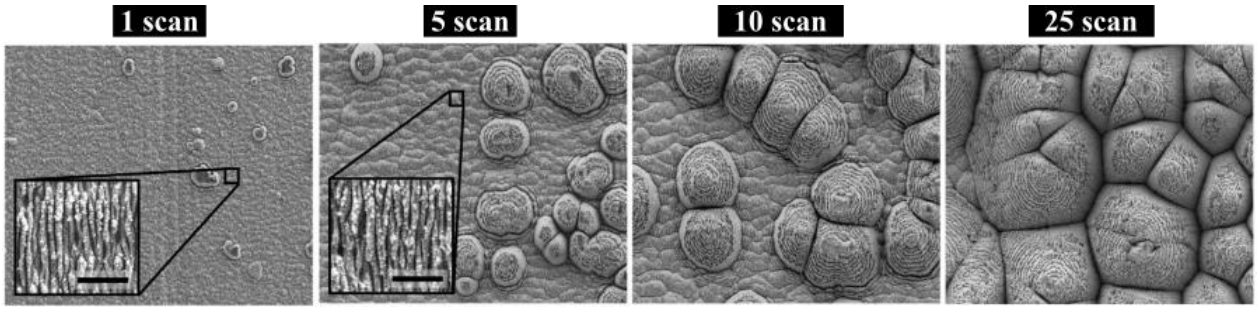

Figure 39 (reproduced from ref. [124]) SEM images of stainless steel surface processed with Φ = 0.11 J/cm^2, pps = 1826 and multiple scans as indicated.

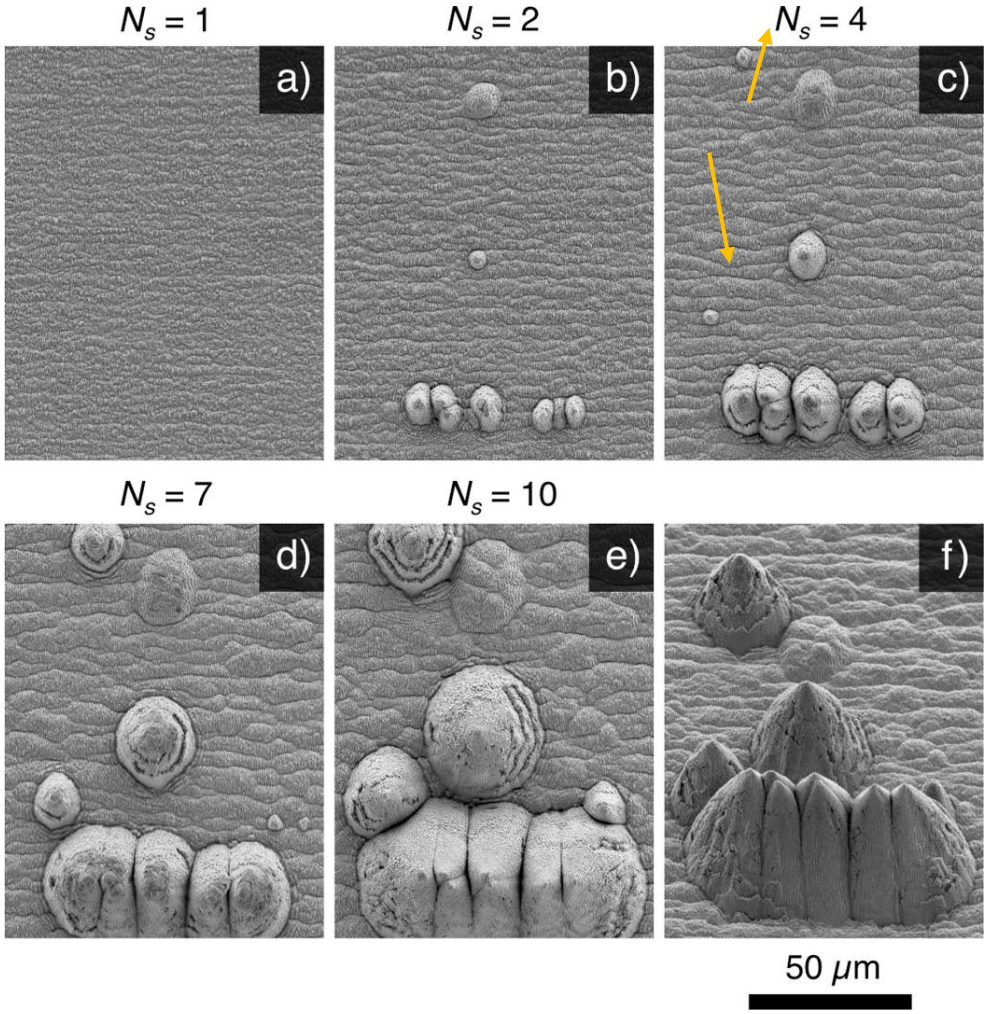

Figure 38 (taken from ref. [124]): Stop-motion SEM images tracking the formation and growth of ellipsoidal cones on the same area of stainless steel under multiple scans (N).

protrusions marked by yellow arrows appear, and which were not present in Figure 38, b. Thus, bumps have a broad distribution of sizes after a few scans.

A crystallographic analysis of the cones showed that cones are composed of crystal grains and there is a continuity in the lattice structure between the substrate and the cone or two joint adjacent cones. This is an evidence that the steel within the ellipsoidal cones was neither strain hardened nor underwent plastic deformation during fs-laser processing[124]. The proposed mechanism is illustrated in Figure 40. The formation and growth of spikes is an ablative process. Debris of the ablation, which is agglomerated together, acts as precursors for spike formation by shielding the surface underneath upon the subsequent scans. Upon an increasing number of scans, the size and the aspect ratio of the cone increases, that entails an increase of the light reflection by the cones and a reduction of ablation of the cone. The elliptical shape of the spike base is attributed - as discussed above - to the variation in the absorbance of the s and p component of the incident polarization. Lastly, this conical morphology is more favourable for low fluence values and almost vanishes for $\Phi = 0.45$ J/cm^2.

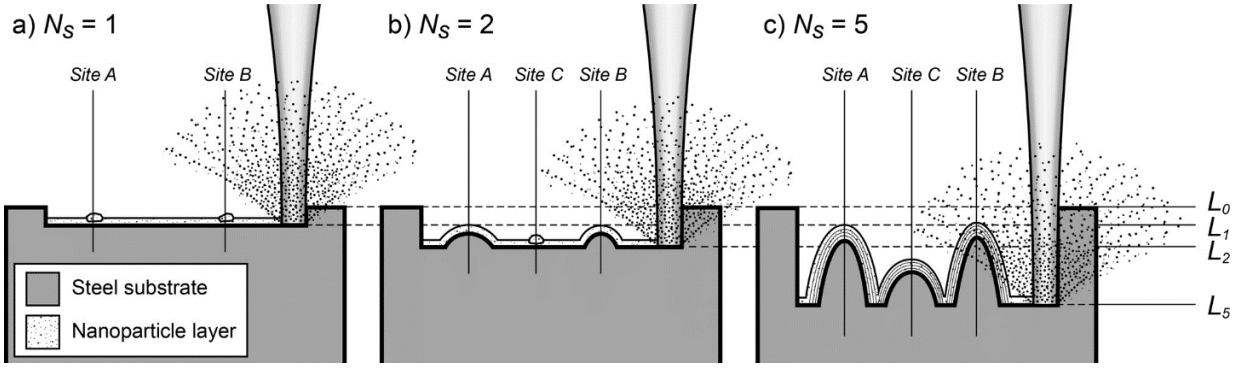

Figure 40 (taken from ref. [124]) Schematic of the proposed mechanism of ablation growth of spikes at low fluences.

2.4.3.2. Microfluidic spike formation mechanism

A model based on the microfluidic movement of molten material is proposed to explain the spike formation under femtosecond pulses at high fluence and low repetition rate[46]. The model includes the ablative mass removal process and the microfluidic movement of the surface. Taking into account the periodical energy absorption on the surface (§2.2.1) two mechanisms are responsible for the microfluidic movement. One is

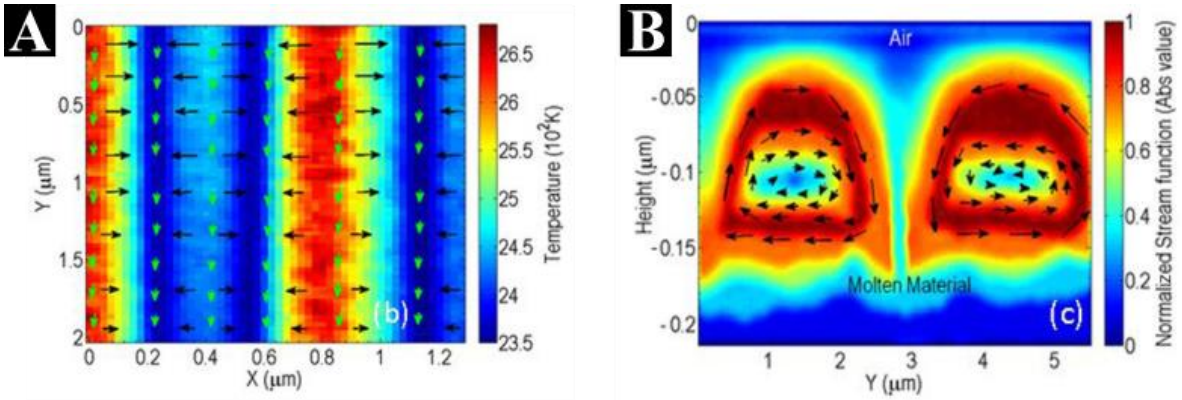

Figure 41 (Reproduced from ref. [46]) simulation results on silicon response after femtosecond irradiation. A: Surface temperature profile on top of the surface. Black and green arrows indicate the flow along X and Y direction 1 ns after irradiation. B: convection roll flow pattern inside the material for N = 20. The direction of the flow is indicated by black arrows.

the surface tension variance due to the temperature gradient of the molten layer. The second is the recoil pressure induced by the ablation process. Ultimately, these effects induce a microfluidic movement of the molten material that evolves in amplitude and orientation as the surface roughness increases upon multi-pulse irradiation[46].

For a low number of pulses ripples appear on the surface (Figure 34, a) giving a positive feedback on the efficacy of the inhomogeneous energy absorption as discussed in §2.2.1.5.1. Nonetheless, as the number of pulses increases, the ripple relief will grow deeper. Deeper structures lead to higher localized field intensity. The deeper the structure the higher the carrier density will be. In the opposite, the efficacy factor diminishes above a certain carrier density N_{cr}, which in our case is proportionally related to structure depth. Above N_{cr}, the inhomogeneous absorption is not efficient, the surface plasmon polariton (SPP) excitation will be

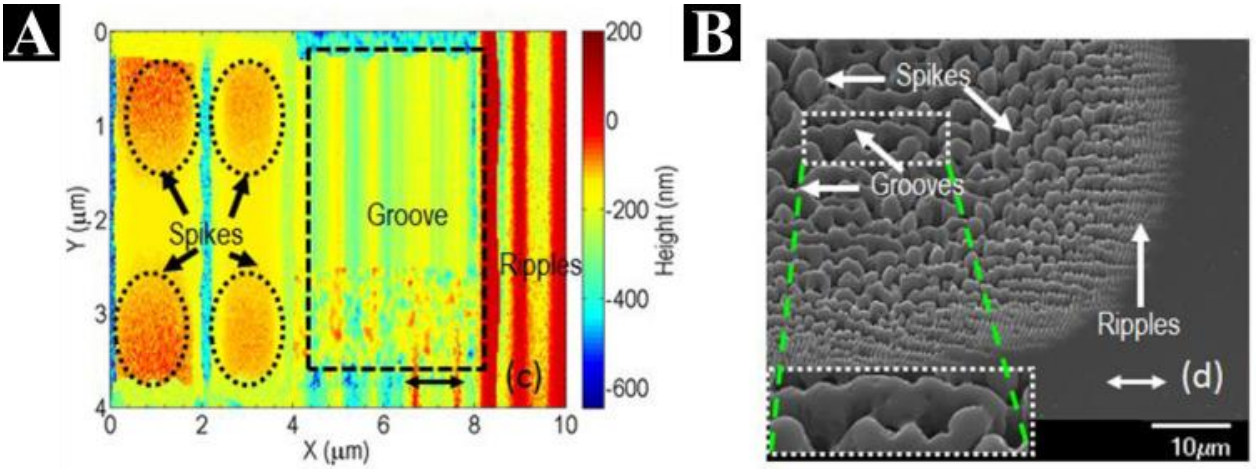

Figure 42 A: Surface morphology in silicon after irradiation with N=120 derived from simulation. B: SEM image of silicon surface after irradiation with N_p = 200 and Φ = 0.45 J/cm^2 (Double-ended arrow indicates the laser beam polarization).

supressed and the ripples formation will not be favourable[46]. Under these conditions, grooves are formed on the surface. Their formation is not attributed in this case to the structure feedback (2.2.1.5.1) rather than to microfluidic movement. The shear flow (green arrows in Figure 41, A) combined with the temperature profile are proposed to be capable of destabilizing the molten layer to Marangoni convection. Marangoni convection flow (indicative for fluids with low Prandtl number) occurs perpendicular to the surface temperature gradient in the form of counter rotating rolls as shown in Figure 41, B for N = 20. The period of the structures was estimated in the simulation based on the stability of the convection flow upon variation of the spatial period. A value of 2.92 μm was derived from the simulation for the groove period at N = 20 and it was shown that the groove period increases upon an increasing number of pulses[46].

As the pulse number increases above N_p = 40 the surface morphology changes again. The ripples on top of the grooves disappear gradually and bumpy protrusions are formed on the surface that ultimately lead to spike formation for N_p = 100. Those changes will affect the geometry of the flow by setting the X axis as preferential for the development of the convection flow. After several cycles of melting and resolidification the grooves will break into forming round protrusions with a period of 2.1 microns on the surface. The height of the structures increases with the number of pulses giving rise to spike-like assemblies. The simulated surface is shown in Figure 42, A where the different morphologies are indicated. Figure 42, B shows the experimental results compared to the theoretical prediction. The excellent agreement between the experiment and the simulation underlines the success of the model to interpret the spike formation[46].

2.4.3.3. The role of heat accumulation

After irradiation and solidification, even with sub-picosecond pulses, a part of the pulse energy remains within the target material (~30-40%)[50,64] and increases upon increasing dose on the surface[126,127]. The residual heat dissipates into the bulk in the microsecond time regime due to thermal conduction[63,77]. When the repetition rate increases above a few hundreds of kHz the time between the pulses becomes comparable with the heat relaxation time[84,128]. Thus, irradiating with high repetition rate and above a certain fluence threshold will result in heat accumulation in the surface of the material which is followed by a detrimental effect on the surface morphology. If the offset temperature reaches about 600°C on steel, the surface morphology changes from a smooth, reflective and melt-free surface to a bumpy, dark and oxidized surface[84].

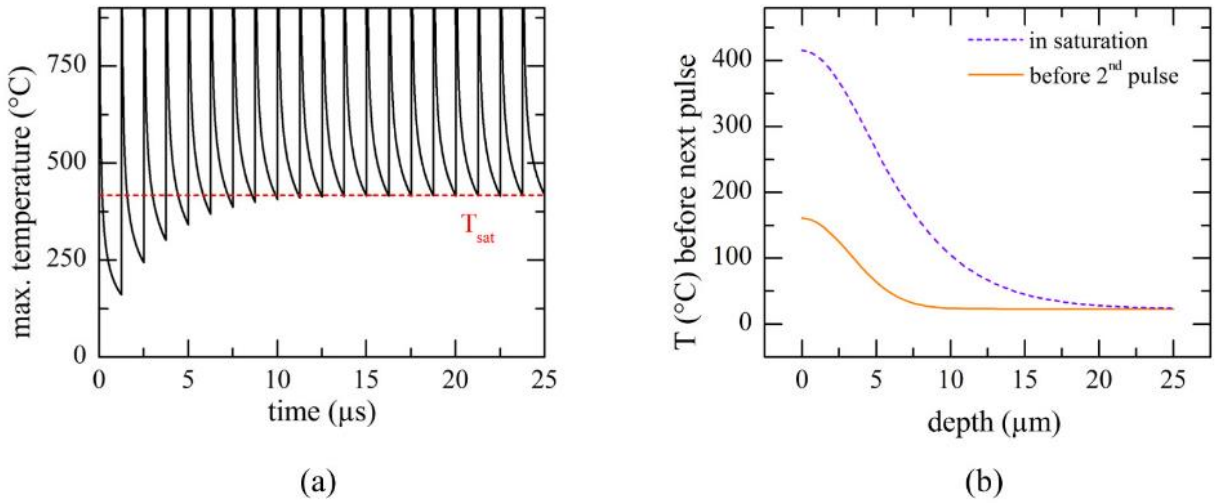

Figure 44 (Taken from ref. [84]): (a) Simulation of heat accumulation using f = 800 kHz, Φ = 0.37 J/cm^2, v = 4 m/s, for 1.4301 stainless steel. The maximum temperature at the surface is plotted against time. In (b) the temperature before the next pulse at the position of maximum temperature is plotted against depth z.

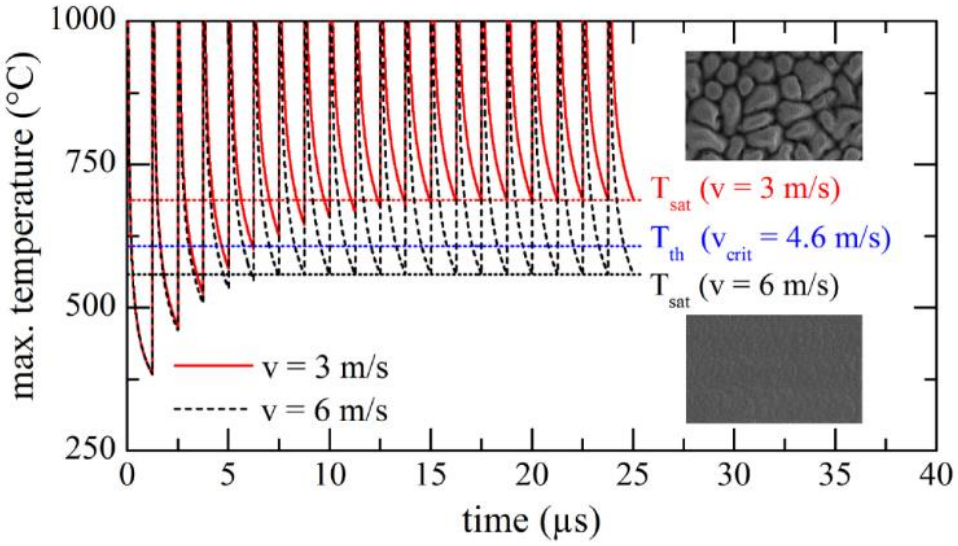

Figure 44 (Taken from ref. [84]). Maximum temperature value plotted as a function of time for a fluence of 0.37 J/cm^2, a spot diameter of 50 µm, a repetition rate of 800 kHz and different scanning speeds.

Figure 44 a, illustrates the phenomenon for irradiation of stainless steel at f = 800 kHz. The results obtained via simulation of the surface irradiation with sub-ps pulses show that after approximately 10 pulses (N_p ~10), a saturation temperature (T_{sat}) is reached. The steady state occurs due to the higher rate of heat dissipation at higher surface temperatures. In other words, the higher the surface temperature, the faster the heat is dissipated. In this way an equilibrium is established between the heat intake and the heat dissipation. In Figure 44, b, the temperature gradient is shown for N_p = 10 (in saturation) and is much higher compared to the one before N_p = 2 allowing a more efficient heat conduction[84]. As intuitively expected, the value of T_{sat} is affected by the linear overlap of the pulses on the surface: smaller scanning speed leads to higher T_{sat} value (Figure 44)[84].

In high repetition rate regimes (f > 500 kHz), both types of spike formation reported in the low repetition rate regime, namely melting related[46] and ablation related[124] are also reported[122]. For melting-related spike formation, the spike density does not change upon an increase of number of scans, while in the second case the spike density increases, as more and more spikes appear on the surface until a saturation point is reached[122]. In low fluence regimes, a reduction of the ablation plume after the spike formation on the surface points out that the increase in surface area and the change of incidence angle favours the absorption and prevents the ablation[122,124].

In the case of high repetition rates (f = 500 kHz & f = 1000 kHz) the spike formation threshold is not defined exclusively by the fluence, but rather by the combination of fluence and scanning speed[122]. Compared to the low repetition rate where the spike size is defined by the fluence[34], here the spike size also varies with the scanning speed both in the low and the high fluence regime[122]. Figure 45 illustrates that the spike size can be varied by varying the scanning speed whilst maintaining the overall dose the same[122]. This behaviour can be interpreted assuming heat accumulation conditions[122] (f = 1 MHz and Φ = 0.789 J/cm^2), where the saturation temperature varies upon the linear overlap[84] (Figure 44). In that case, the saturation temperature reaching several hundreds of degrees is expected to affect the microfluidic movement of the material[46] that leads to spike formation.

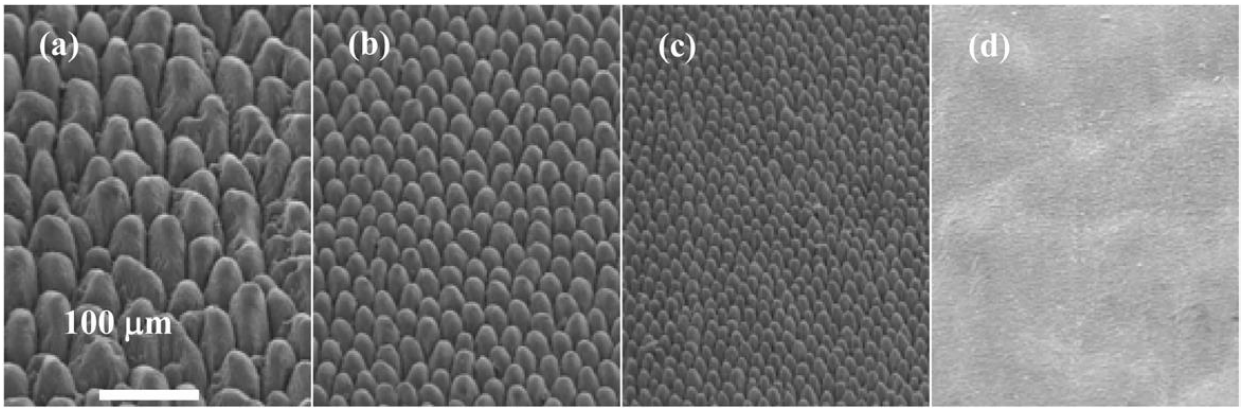

Figure 45 (Taken from ref. [122]) SEM images of 4340 steel surface after N/v = 1/2smm^{-1}. Φ = 0.789 Jcm^{-2} at f = 1MHz are scanned with (*a*) v = 240mm s^{-1}, (*b*) 480 mms^{-1}, (*c*) 1200 mms^{-1} and (*d*) 2400mms^{-1}. Each SEM image is taken at a 45° angle to the surface.

2.5. Progress beyond the state of the art

As explicitly discussed in the introduction, each surface functionality derives from a specified surface morphology. Laser induced surface structures enable a wide variety of surface morphology and functionalities. Nevertheless, the long processing time and the lack of control of the laser induced morphology prevent this technology from being employed for surface functionalization at an industrial level. Moreover, surface structure homogeneity on large areas is still an unsolved key issue for process upscaling.

Our work aims to broaden the understanding of laser induced structure formation mechanisms in order to control the structure morphologies and ultimately optimize the macroscopic surface properties. We approach this aim considering the scalability of the process both in terms of reducing the cycle time and applying the developed structures over large areas. The processing rate cannot be solely optimized by increasing the repetition rate since heat accumulation phenomena are limiting the process window. The increase of scanning speed is one approach; an iridescent surface texturing was produced at a rate of ~ 650 cm^2/min combining a high repetition rate and high average power laser with a fast scanning system[13]. Another approach considers the increase of spot size at low repetition rate to produce hydrophobic texture at a rate of ~ 1 s/cm^2 [14]. These works demonstrate the possibility of industrial exploitation of laser texturing. Nevertheless, the studies which are dedicated to explore the generation of novel functional textures[26] or to control surface morphology[122], often do not exceed processing rates in the order of ~1hour/cm^2.

In this work, a comprehensive study of the impact of process parameters is considered and an upscaling strategy is proposed to overcome the heat accumulation issues. Furthermore, an increasing level of control over the structure morphology simply by varying the process parameters such as fluence and overlap has shown its limitations in the submicron regime. On the contrary, utilizing double-pulses or multi-pulses permits an intervention in the structure formation process in a dynamic way and exhibits a virtually endless potential. To this end we aim to explore the combined effect of polarization and interpulse delay in controlling laser induced morphologies at the submicron scale over areas much larger than the spot size.

3. Methods and parameter definition

3.1. Parameter definition

The quantification of the experimental parameters used is based on the equation described in this section. We define the spot size diameter (w), schematically illustrated in Figure 46, A, in the focal position by the radius (ω_0) with $I = 1/e^2 \cdot I_0$, where I_0 is the maximum intensity of the spot.

Equation 5 Spot size diameter

$$w = 2 \cdot \omega_0$$

The fluence value (Φ), defined in Equation 6 describes the average energy per unit surface for a single pulse irradiation.

Equation 6 Fluence definition

$$\Phi[J/cm^2] = \frac{E}{\pi \cdot {\omega_0}^2}$$

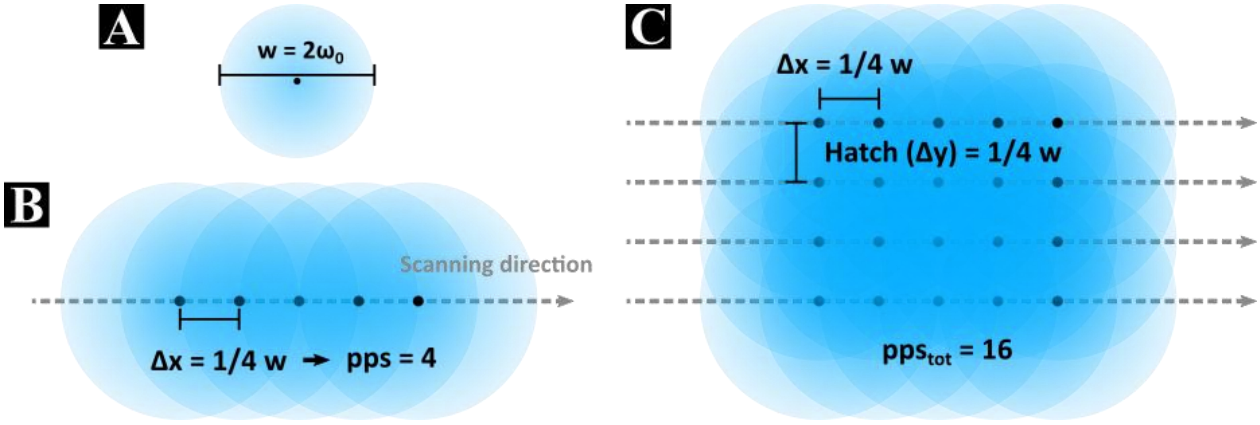

Figure 46 Schematic of the single spot (A) and spot arrangement (B & C) on the material surface.

A moving beam was utilized for the irradiation. The average number of pulses per spot (pps) for a single line scan is given by Equation 7 where u is the moving speed of the focus center and f is the repetition rate. In Figure 46, B, the case of pps = 4 is exemplified.

Equation 7 Scanning overlap (pulses per spot)

$$pps = \frac{2 \cdot \omega_0 \cdot f}{u} = \frac{w \cdot f}{u}$$

For scanning over large areas two approaches have been used to quantify the average cumulative number of pulses delivered on the surface, referred to as total number of pulses per spot (pps_{tot}). The first one, where the hatch H = Δy is kept constant, close to the spot size, pps_{tot} was varied by increasing the number of scans. In that case the lateral overlap (Figure 46, C, Δy) is neglected to facilitate the comparison of the results and pps_{tot} was calculated based on Equation 8.

Equation 8 Cumulative number of pulses (total number of pulses per spot) pps_{tot} when the pulses do not overlap in y

$$pps_{tot} = pps \cdot N_s$$

For the second approach, where the lateral overlap, Δy or the hatch H is varied, usually in the range of 1 μm < H < 20 μm, the contribution of Δy is accounted and the pps_{tot} value is given by Equation 9.

Equation 9 pps_{tot} when the pulses do overlap y

$$pps_{tot} = pps \cdot \frac{w}{H} = \frac{2 \cdot \omega_0 \cdot f}{u} \cdot \frac{2 \cdot \omega_0}{H} = \frac{w^2 \cdot f}{u \cdot H}$$

The dose, describing the cumulative fluence irradiated on the surface is given by Equation 10.

Equation 10 Dose (D)

$$D = pps_{tot} \cdot \Phi$$

3.2. Laser sources, scanning systems and focal lenses

An industrial femtosecond laser source emitting at λ = 1030 nm (Tangerine, Amplitude Systèmes) with a pulse duration of τ_p = 350 fs with average power up to 20 W and f ≤ 2 MHz was employed for the spike generation (§4.1.1). For the experiments with λ = 1030 nm, the surface was scanned using two Galvo scanners (IntelliSCAN 14 (u_{max} = 2.0 m/s) and HurrySCAN II 14 (u_{max} = 1.5 m/s)) provided by Scanlab. The beam was focused using a 100-mm f-theta lens into a w = 35-μm spot diameter, measured by a beam profiler (Win Cam).

A second harmonic generation module was combined with the laser (Tangerine, Amplitude Systèmes) to generate λ_{SHG} = 515 nm (§4.1.1.3). A galvo scanner (IntelliSCAN 14, Scanlab) was used for surface scanning combined with a 100-mm f-theta lens giving a w = 20 μm, measured by a beam profiler (Win Cam).

For the experiment with f = 10 MHz (§4.1.1.5), a Tangor laser source (Amplitude Systèmes) was coupled with a polygon scanner head (Next Scan Technology LSE170), which can reach scanning speeds of u_{max} = 100 m/s. In this case the beam is focused with a focusing lens embedded in the scanning system which gives w = 45 μm, measured by a beam profiler (Win Cam).

For UV irradiation (§4.1.2) a Satsuma HP3 laser source (Amplitude Systemes) was coupled with a Fourth Harmonic Generation module to produce fs pulses at λ = 257 nm. The scanning system (TurboScan from Raylase) was combined with a 160-mm f-theta lens. The spot diameter on the sample was estimated to w =18 μm as described by J. M. Liu[129].

For the double-pulse experiments (§4.2) generated by a delay line, an industrial femtosecond laser (Satsuma HP2, Amplitude) (LS2) with τ_p = 350 fs emitting at λ = 1030 nm with repetition rates up to 2 MHz was used to texture. The spot size was w = 25 μm, measured by a beam profiler (Win Cam).

For the experiment utilizing double-pulses produced by birefringent crystals (§4.2.1.24.2), a femtosecond laser, delivering τ_p = 200 fs pulses at λ = 1030 nm (Pharos from Light Conversion) (LS3) operating at f = 200 kHz was utilized for the texturing. The spot size was w = 24 μm, measured by a beam profiler.

3.3. SEM characterization

For characterizing surface morphologies with average sizes bigger than a micrometre a desktop Scanning Electron Microscope was utilized (Phenom G1, Phenom world). Structures ranging in the near-micron and the submicron scale are characterized by an SEM Inspect F50 (FEI) in LMA - Laboratorio de Microscopías Avanzadas Zaragoza, by Teobaldo Torres Molina and Carlos Cuestas Ayllón.

3.4. AFM characterization

AFM characterization of the structures was carried out by Gilles Pecastaings at the LCPO laboratory, a mixed research unit of the University of Bordeaux and the CNRS (UMR 5629) utilizing an Atomic Force Microscope (AFM, Bruker, Dimension fast scan).

3.5. Calorimetric measurement and simulation

The calorimetric measurement was carried out using a PT100 sensor probed by an open-source electronics platform (Arduino). The calibration was realized utilizing a commercial infrared thermometer (FLUKE 62 MAX +). The irradiated piece was free standing and in contact with the sensor in a setup similar to ref. [130]. As an outcome of the calorimetric measurement the average absorbance was estimated to 33% in agreement with reports in the literature (§2.1). A commercial software (COMSOL) was employed for the FDTD simulations; the time step was 1ns. A piece of stainless steel of dimensions (150 x 80 x 50) μm^3 was considered for the simulation model. For the laser excitation, an instantaneous heating source with a gaussian shape and w = 25 μm was considered. Ablation is not considered in the model and the expected change in the reflectivity upon spike formation[122,124] is neglected.

3.6. Materials

The materials processed are two types of stainless steel. The first utilized in parametric studies is commercially available stainless steel 316 (refer to as stainless-steel) of thickness 0.5 mm provided by RS Components Ltd. For the decorative application of blackening ferritic stainless-steel (X6Cr17) having a thickness of 0.5 mm was used (refer to as ferritic stainless-steel); the samples were provided by BSH Electrodomésticos España.

3.7. Double-pulse setup based on delay lines

The double-pulses were generated by a delay line (DL) setup. The setup consists of a modified Michelson interferometer (Figure 47) capable of producing double cross-polarized pulses with an interpulse delay ranging from $\Delta\tau$ = 0.1 ps to $\Delta\tau$ = 50 ps on one arm and from $\Delta\tau$ = 0.1 ns to $\Delta\tau$ = 4 ns on the second arm. The beam was divided into two parts using a non-polarizing beam splitter (BS) and then guided into the two arms. Half-waveplates (λ/2) allowed for tuning the fluence and different translation stages for adjusting the delay individually in each arm. Equation 11 is employed to calculate the interpulse delay in the case of a delay line. $\Delta\tau$ is in ps, and the displacement of the delay line in μm. The factor of 2 comes from the fact that the pulse travels two times the displacement of the arm due to the setup geometry. C is the speed of light.

Equation 11 Time delay definition

$$\Delta\tau[ps] = 2 \cdot \frac{\Delta x\ [\mu m]}{c} \cdot 10^6$$

The stage of Arm A was computer controlled and had a maximum displacement of 15 mm, which gives delays of up to 100 ps; the accuracy was δx_A < 0.1 μm corresponding to a $\delta\Delta\tau$ smaller than 1 fs. In Arm B, two mirrors were simply placed on a rail and could move up to 600 mm corresponding to a delay of 4 ns. In this arm, we were able to set the delay with an accuracy δx_B = 1 mm corresponding to 6.6 ps. The two beams were recombined using a linear polarizing cube (LPC). Compared to previous setups utilized for double-pulse generation[117,121], where 50 % of the laser energy was lost, our setup enables the generation of double-pulses exploiting 100 % of the laser energy (despite some reflection losses on the cube and the mirrors), which is an important feature for a highly efficient manufacturing process.

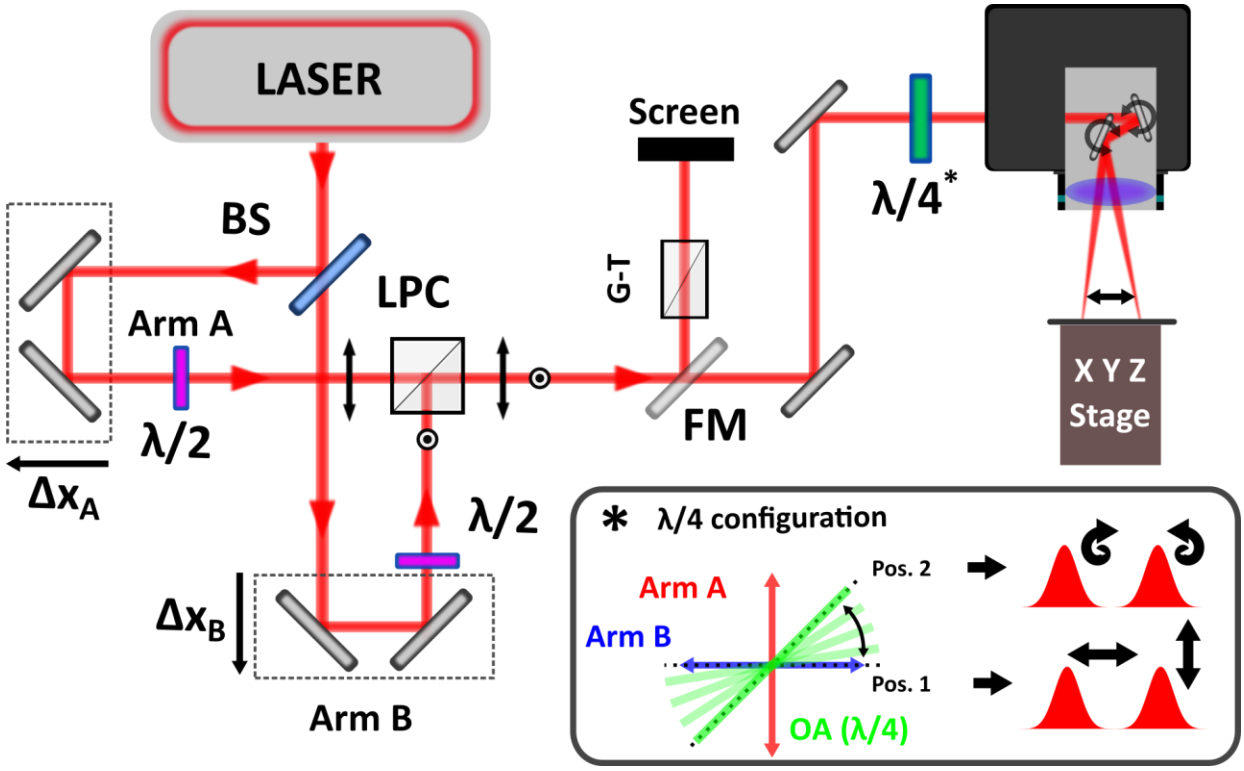

Figure 47 Setup: A beam splitter (BS) divides the beam to the two movable arms. A half wave plate (λ/2) in each arm regulates the power. A linear polarizing cube (LPC) recombines the beam. A flip mirror (FM) guides the beam to the characterization part (Frame 2). A Glan-Thomson polarizer and a screen are utilized to determine the temporal overlap of the two pulses. The beam is thereafter guided to the Galvo scanner which positions the beam on the surface. An f(θ) lens focalizes the beam. A rotating QWP modifies the polarization for both arms. *: Schematic representation of the relative position of the two-pulse polarizations (red and blue vectors) and the QWP fast axis: Linear (position 1) and circular (position 2) polarization is generated.

A quarter-waveplate (QWP, λ/4) fixed on a rotational mount was placed before the galvo scanner in order to change the polarization state of the pulses before focusing. The frame in Figure 47 illustrates the relation between the polarizations of Arm A and Arm B (red and blue arrow, respectively) and the fast axis of the QWP (green line). Double linearly crossed-polarized pulses (XP) are produced when the fast axis of the QWP is in position 1 (Figure 47, frame, Pos. 1) and double counter-rotating circularly polarized pulses (CP) are produced when the fast axis of the QWP is in position 2 (Figure 47, frame, Pos. 2.).

The zero delay, which corresponds to a spatial and temporal overlap of the double-pulse, was defined by guiding the double-pulse into a Glan-Thomson polarizer (G-T) oriented at 45 degrees with respect to the polarizations of the two XP pulses. As the two pulses undergo an overlap in time and space, a periodic variation of the intensity of the laser beam is observed after the G-T[108]. $\Delta\tau = 0$ ps was defined as the delay with the maximum variation in the intensity with an accuracy of $\delta\Delta\tau = 50$ fs.

A schematic of the interaction between two cross-polarized, overlapping 10 fs pulses upon $\Delta\tau$ variation is shown in Figure 48. The electric field is plotted in 3D graph and presented in frond view and side view for different delays. The dot green line corresponds to the G-T optical axis which is placed at 45° with respect to the polarization axis of the two pulses. When the two pulses do not overlap (∞ π) both pulses have a projection on the G-T. For 2π ($\Delta x = \lambda$) the combination of the two pulses maximises the projection of the electric field on the optical axis and therefore the intensity in the output of the crystal is maximized. In

contrary, for π (Δx = λ/2) the electric field projection is minimized, minimizing the output intensity. A measurement of the fluctuation of the intensity versus Δτ, was carried out for two crossed polarized 40 fs[108].

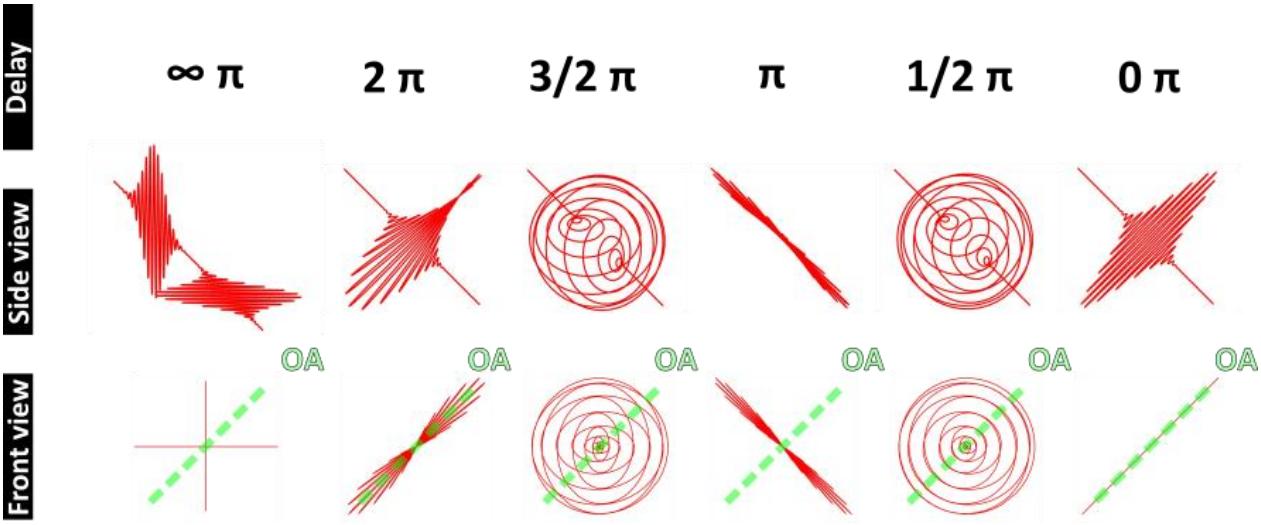

Figure 48 Simulation of the electric field of two cross-polarized pulses when they are separated in space and when they overlap. The delay of the two pulses is indicated in multiples of π. The optical axis of the polarizer in shown with the green dot line.

3.8. Double-pulse setup based on birefringent crystals

Double-pulses with different delays (Δτ) were generated by splitting the pristine linearly polarized laser pulse by birefringent crystals (BCs) of different lengths (§4.2.1.2). The principle of the setup is shown in

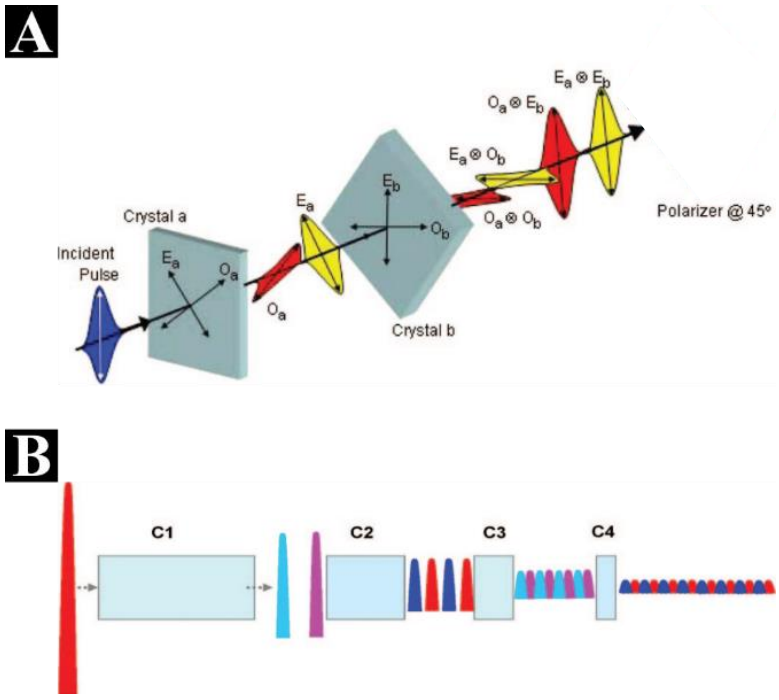

Figure 49 Schematic of the generation of burst using birefringent crystals. A: Reproduced from Ref. [131]. A single pulse (blue) is incident on Crystal a, splits into two pulses that have traversed the slow (Oa, red) and fast (Ea, yellow) axes. These two pulses are then incident on Crystal b which has twice the thickness of crystal a and the pulses are split again. B: Reproduced from Ref. [132]. Principle of pulse splitting by consecutive birefringent crystals (C1–C4). Each colour of the pulses presents one orientation of polarization. The output pulse sequence has alternating linear polarizations.

Figure 49. Within a single crystal, the difference of the refractive index along the two optical axes (OAs) and the length of the crystal determines the $\Delta\tau$ value between the two output pulses. Furthermore, the angle comprised between the polarization vector of the pristine pulse and each OAs defines the relative intensity of the two pulses[131,132]. In our experiment, this angle was fixed at 45°, meaning that the intensity and the fluence (the spot size is unchanged) of the two pulses are the same. The beam was guided through a sequence of four $CaCO_3$ crystals, which can be mounted individually producing crossed-polarized (XP) pulses. The used crystals enable inter-pulse delays of $\Delta\tau$ = 1.5 ps, 3 ps, 6 ps and 12 ps, respectively. When crystals having different lengths are placed consecutively the pulses are further split (Figure 49, B). The necessary condition is just the length of the $(n+1)^{th}$ crystal to be the double than the n^{th} crystal[131,132].

By passing through a quarter-waveplate, counter rotating circularly polarized (CP) pulses are obtained. Finally, the beam is delivered on the samples by means of a galvo scanner (IntelliSCAN 14 from SCANLAB) equipped with a 56-mm focal length F-theta lens giving a spot size of $2w_0$ = 24 µm. During this study, we only processed stainless steel samples (316). The fluence value was fixed to $\Phi = \Phi_{low}$ = 0.1 J/cm^2 and $\Phi = \Phi_{high}$= 0.2 J/cm^2. The pulse overlapping along a scanning line, which is determined by the number of pulses per spot delivered (pps), was fixed to pps = 20, whilst the offset between scanning lines or hatch (H) was fixed to H = 2 µm in the first series of experiments. The total pulses per spot on the surface can be estimated by $pps_{tot} = (pps \cdot 2w_0)/H$ and the total dose ($d_{tot} = pps_{tot} \cdot \Phi$).

3.9. Image processing and analysis

The period of the structures was derived from SEM micrographs by means of Fourier Transformation analysis carried out using Gwyddion, a free and open source software. Image correction (denoise, despecle, contrast and brightness adjustment) were realized with ImageJ software. All figures, schemes etc. were designed using Inkscape, a professional vector graphics editor, free and open source.

4. Results and discussion

Here, we employ three different approaches, to control the surface morphology. The first approach uses single pulses with λ in IR and visible to control the spike size §4.1.1. A comprehensive study of the impact of process parameters is carried out[7,8]. As an outcome, an upscaling strategy is proposed, demonstrating the possibility to generate spikes with f up to 10 MHz avoiding detrimental thermal effects. The second approach employs a wavelength of λ = 257 nm in the UV region to induce nanometric features[12] (§4.1.2). Lastly double-pulses are employed to control structure symmetries and sizes in the submicron scale §4.2.

4.1. Single pulse sequence

Several morphologies can be laser induced on metals by irradiating the surface with linearly polarized femtosecond pulses. The formation process of the structures, whether that refers to ripples, grooves, or spikes, involves the microfluidic movement of the molten part of the surface (§2.2.2). Therefore, the heat accumulation that occurs when the pulse-to-pulse delay is shorter than the mean heat relaxation time should impact the microfluidic movement and the induced surface morphology (§2.4.3.3). From a practical point of view, the heat accumulation takes place when the repetition rate (f) is higher than a few hundreds of kHz[133].

To demonstrate the heat accumulation effect on the micro-nanostructure morphology we carried out a comprehensive comparative study dealing with the effects of fluence, overlap and number of successive scans on the surface morphology for increasing repetition rate values[8]. We considered the cases of f = 100 kHz, 1 MHz and 2 MHz. The process parameters utilized are summarized in Table 1. The surface morphologies obtained for fixed overlap (pps = 70) with increasing fluence ranging from $\Phi = 0.04$ J/cm^2 to $\Phi = 0.40$ J/cm^2, and for scan numbers varying from N = 1 to N = 50 are shown in Figure 50[8].

Areas having similar morphologies can be identified after comparing the irradiated surfaces for the three repetition rate values. Ripples, periodical formations, with a period close to the laser wavelength, occur for low dose values with an orientation perpendicular to the laser polarization and are identified in Figure 50 by a red frame. Diverse types of grooves, which are formed parallel to the laser polarization with a period significantly larger than the laser wavelength are indicated by a yellow frame. Coral like structures are marked by a blue frame. Spikes, the conical formations with diameters in the range of tens of microns, formed for higher doses are indicated by a black frame and finally holes by a green frame.

The effect of heat accumulation is more pronounced for higher energy doses; the same N and Φ values lead to different surface morphologies for different repetition rate values. For instance, the couple $\Phi = 0.09$ J/cm^2 and N = 50 enables the formation of ripples at f = 100 kHz (Figure 50), micro-grooves superposed to ripples at f = 1 MHz (Figure 50) and, finally, spikes at f = 2 MHz (Figure 50). The combination $\Phi = 0.19$ J/cm^2 and N=10 enables the formation of a hole's net at 100 kHz, inhomogeneous spikes at 1 MHz and an inhomogeneous distribution of melted and re-casted material along the scanning axis at 2 MHz. When the dose increases further ($\Phi > 0.19$ J/cm^2 & N > 5) the material surface morphology shows two distinctive behaviours between 100 kHz and the MHz range.

Table 1 **Process parameters and values considered in the single pulse experiments.**

Parameter	Considered Values
Fluence, Φ [J/cm²]:	0.04, 0.11, 0.22, 0.27, 0.37, 0.42, 0.54
Number of scans, [N]:	1-500
Pulses per spot [pps]:	15-200
Repetition rate, f [MHz]:	0.1, 1, 2, 10

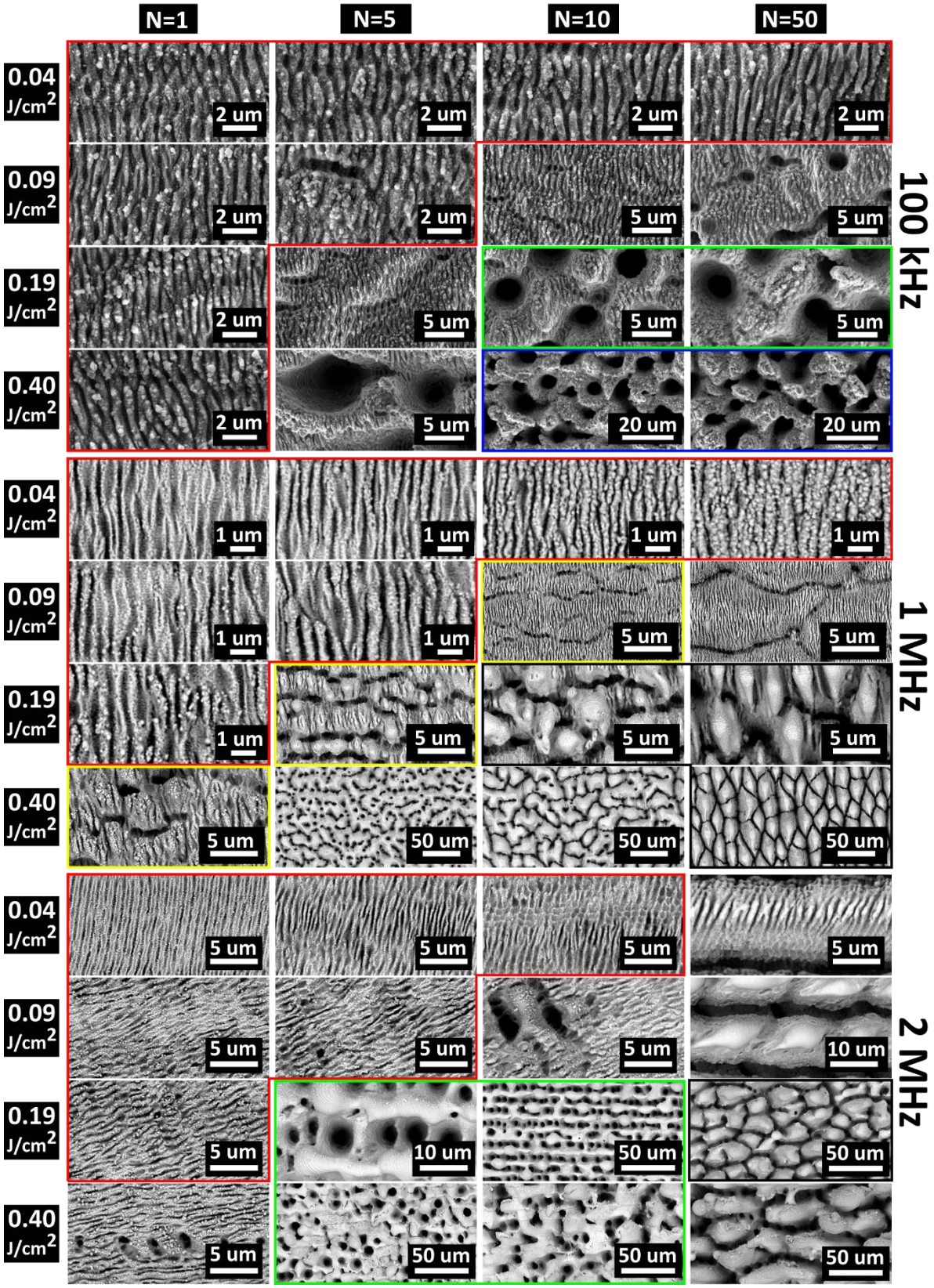

Figure 50 SEM images of stainless-steel surface obtained at different repetition rates as indicated. N indicates the number of scans in each column. The fluence Φ increases from top to bottom and is the same in each row. The overlap was fixed to 70 pps. Different types of nanostructures are indicated with different color frames[8].

A detailed examination of the surface evolution upon variation of number of scans from N = 1 to N = 50 (pps = 70, and Φ = 0.19 J/cm^2) for the two repetition rates provides valuable insight into the structure formation (Figure 51) . For f = 100 kHz shown in Figure 51, top, the surface evolution is illustrated for an increasing number of scans from N = 1 to N = 50 (Figure 51, top, a-d). Starting from N = 1 we see that ripples are formed perpendicularly to the polarization direction (see red arrow). At the same time, shallow undulations arise parallel to the laser polarization. Their orientation and period are similar to micro grooves observed in solids[46,134]. Between the undulations, craters are generated (see orange ellipse) and become denser and more pronounced with an increasing number of scans (N = 5). Their pristine formation should be attributed to the mechanism described for grooves[46,54]. At N = 10, craters are transformed into holes of nearly 5 μm in diameter. This transformation could be attributed to an enhancement of light absorption around the crater. As discussed extensively in §2.2.1.5.2 (Isolated structure feedback) irradiation of long surface depressions with microscale size can localize the electric field inside and in the vicinity of the structures[99]. Of course, this phenomenon is strongly affected by the configuration of the polarization direction with respect to the geometry of the groove and thus an enhanced contribution of the light localization is expected perpendicular to the polarization direction and the long axis of the groove. That's quite likely why the grooves are enlarged perpendicularly to their long axis and form holes (Figure 51, ii).

Another feature coming from the scanning conditions is observed on the surface. For N = 5 the scanning hatch (see white arrow) impacts the surface with the formation of relatively wide and shallow, parallel,

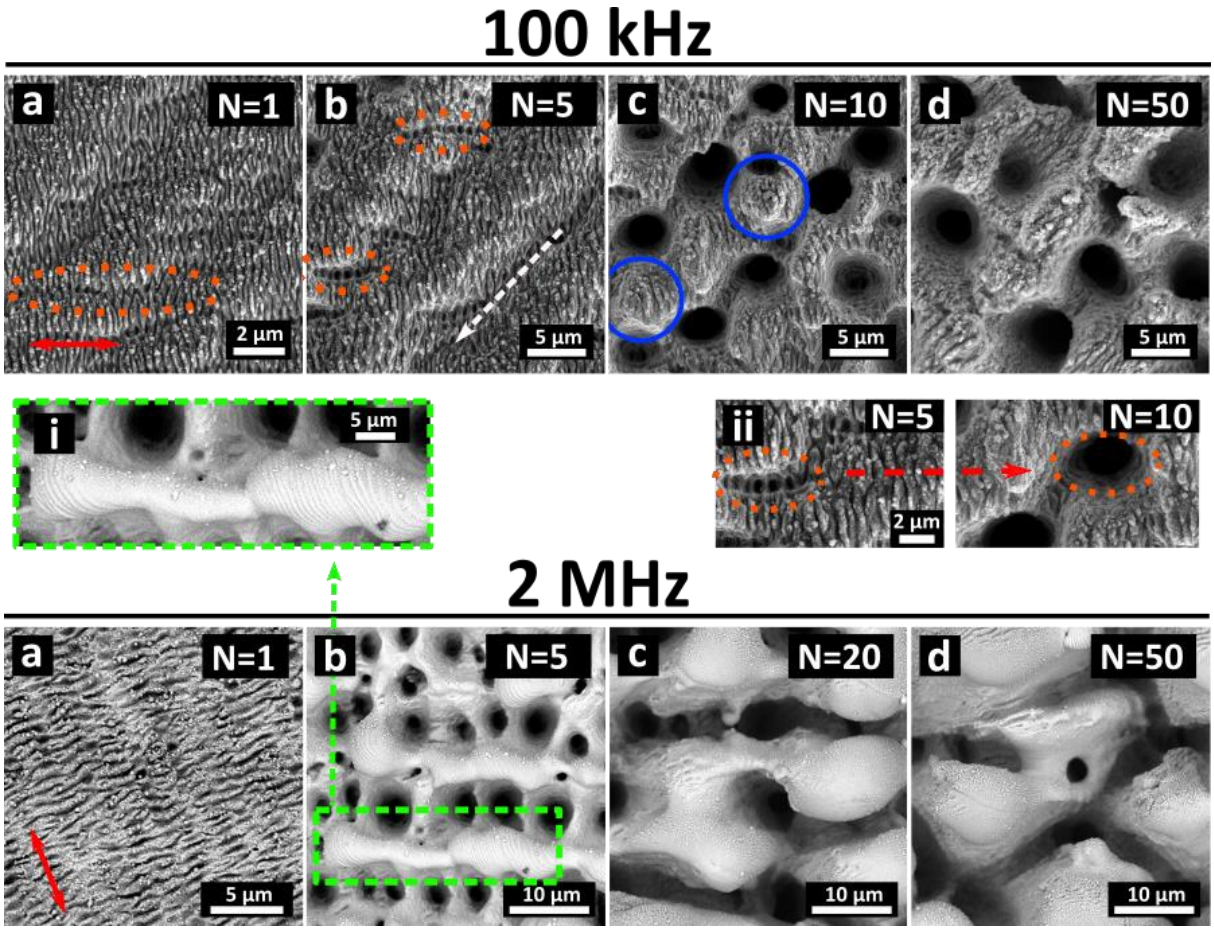

Figure 51 SEM images of stainless-steel showing the surface evolution at f = 100 kHz & f = 2 MHz obtained with Φ = 0.19 J/cm^2 and pps = 70[8]. N indicates the number of scans. The red arrow shows the polarization direction, and the white dotted arrow indicates the scanning axis.

trenches spaced of 10 μm. For N = 10 spare spikes (see blue circle) are also formed but, in the range of the applied process parameters, micro-holes constitute the predominant morphology on the surface. Finally, for N = 50 the predominant surface morphology becomes a net of 5-μm diameter micro-holes aligned along the laser scanning direction and regularly spaced of nearly 10 μm combined with a coral-like roughness. In Figure 50 we observe that the micro-hole diameter depends not only on the number of scans N, but, for a fixed N value, also on the fluence Φ and, the higher the fluence the larger the diameter. For instance, in the case of N = 50, the micro-hole diameter passes from nearly 1 μm (Φ = 0.09 J/cm^2) to more than 5 μm (Φ = 0.40 J/cm^2). Interestingly, once the micro-holes are formed, their number does not change remarkably with the variation of the process parameters. Moreover, the increase of the micro-hole diameter with Φ and N jointly with coral-like roughness ascertains, to a large extend, the prevailing of ultrafast ablation phenomena on thermofluidic effects in determining material removing and local material reallocation.

In comparison to f = 100 kHz, Figure 51, bottom, illustrates the structures obtained for f = 2 MHz for the same process parameters, (Φ = 0.19 J/cm^2 and pps = 70). Compared to f = 100 kHz, the surface evolution is much more intense. For N = 5 micro-holes of 5-10 μm diameter are already formed and distributed along the laser scanning lines. Moreover, melted and re-casted material characterized by a smooth and bumpy external surface is clearly visible between two scanning lines spaced of nearly 10 μm (Figure 51, i). Those rippled morphologies quite likely originate from the melted and resolidified material. Each laser shot should create a protrusion due to the inhomogeneous energy distribution[27]. In fact, the ripple spacing is 385 ± 6 nm measured in the area shown in Figure 51, i, is comparable with the pulse-to-pulse distance which is estimated to be 500 nm. Increasing the number of scans to N = 20 further movement of material tends to fill the holes and coalesce in larger aggregates consisting of bumpy protrusions. Finally, for N = 100 the surface morphology mostly consists of a uniform distribution of bumpy spikes (referred as spikes). The equivalent average spike diameter δ was measured to be δ = 22 ± 3 μm. Interestingly, once the spikes are formed, δ is barely affected by increasing the number of scans, even for N >> 50 (δ = 22 ± 4 μm for N=200). On the contrary, δ changes with the repetition rate f. Indeed, for Φ = 0.19 J/cm^2, N=100, pps = 70 and f = 1 MHz we obtained δ = 14 ± 3 μm. This observation is consistent with the idea that the spike formation is driven by hydrodynamical flow resulting from temperature gradients[46]. A higher repetition rate is expected to lead to higher T_b and thus to a deeper penetration of the heat during the irradiation. As a consequence, we expect the volume of the material subjected to Marangoni driven flow to be more extended as f increases, subsequently leading to the formation of larger features.

Even though several morphologies were obtained within the given range of parameters, fabrication of homogeneous spike formation was not successful for f = 100 kHz & f = 2 MHz while for f = 1 MHz, Φ = 0.19 J/cm^2 and N = 50 elliptical spikes appear with the long axis perpendicular to the polarization. The detrimental effect related to the heat accumulation resulting in surface melting is profound, especially in the case of f = 2 MHz. That points out that in order to optimize surface morphology spikes homogeneously in high repetition rates, a wider range of process parameters should be considered, including a variation of the pps value and the role of each parameter should be elucidated.

4.1.1. Controlling the morphology at high repetition rates

In this part, the impact of heat accumulation on the evolution of ultra-short pulse laser-induced surface structures morphology is investigated. The evolution of the surface morphology is presented in a systematic way for varying fluence values, number of scans and repetition rates from 100 kHz up to 2 MHz. We employ simulation methods to link the morphological changes observed on the surface to the saturation temperature (T_{sat}). In the case of high repetition rates (1 and 2 MHz) we show that by a systematic variation of process key parameters, it is possible to tune the size of the micro-spikes while at the same time avoiding detrimental effects related to heat accumulation. As an outcome, we propose an upscaling strategy for reproducing spike morphology at high repetition rates (§4.1.1.5).

4.1.1.1. The role of fluence

A dependence between fluence and spike size has been previously reported for low repetition rates in several metals[34]. Moreover, this behaviour seems to be independent from the irradiation wavelength[7]. In the following part, we show the impact of the fluence on the induced structures for f = 1 MHz. In our experiment, we deliver the same number of pulses (pps_{tot} = 3500), using the same strategy in all cases (pps = 70, N = 50) and we varied the fluence between Φ = 0.11 J/cm^2 and Φ = 0.54 J/cm^2. Results are illustrated in Figure 52[8].

The graph (top) in Figure 52 shows the δ values versus the fluence Φ. For relatively low fluence values ($0 < \Phi < 0.16$ J/cm^2) no spikes are formed. Similar threshold behaviour for spike formation is mentioned in

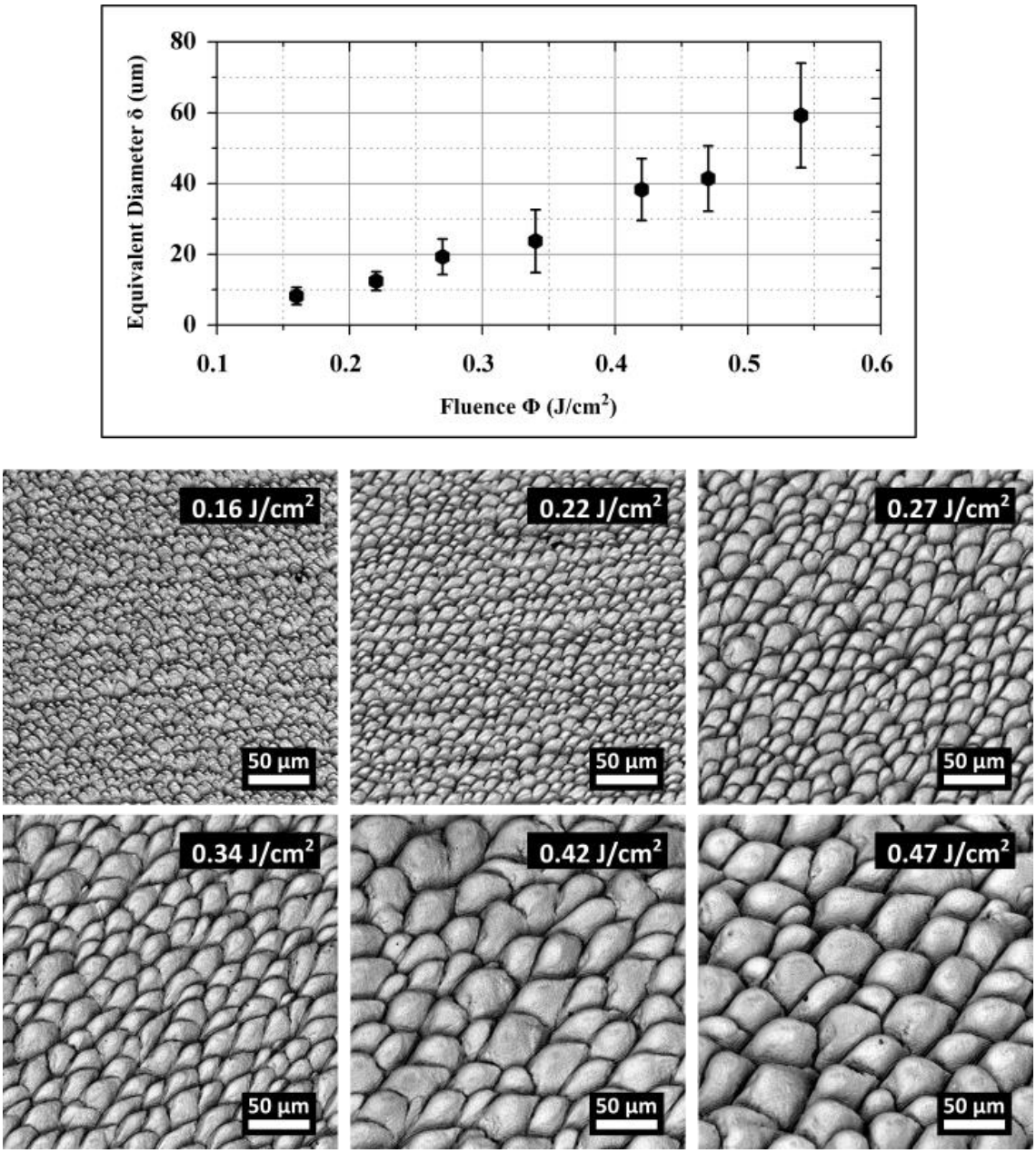

Figure 52 Graph (top) and SEM images (bottom) illustrating the continuing change of the equivalent diameter δ with increasing fluence on stainless-steel. The SEM images correspond to the data shown on the graph and were obtained at a 45° tilt. The fluence values are inserted in the corresponding SEM images.

low[34,54] and high[122] repetition rates. In these experimental conditions, a uniform distribution of spikes comes out only beyond a threshold value of ≈ 0.16 J/cm^2 having an equivalent diameter δ = 8 ± 2 μm. Within the experimental fluence range (0.16 J/cm^2 < Φ <0.54 J/cm^2), δ increases monotonically from δ =8 ± 2 μm to δ =59 ± 15 μm. Therefore, we observe that it is possible to control the resulting spike size over a relatively wide range by varying the fluence. Interestingly, within the used fluence values destruction of the surface due to thermal effect has been avoided enabling the formation of uniform and well defined, bumpy surface structures.

Our hypothesis that heat accumulation plays a role in the spike formation process was formulated in ref.[8]. Here we provide additional data validating this hypothesis. The simulation model used (for details see § 3.5) is based on a commercial multiphysics platform (COMSOL) and calculates the temperature profile for a moving beam on a stainless steel surface following the example of Bauer et al.[84,130]. In our case, we compare the saturation temperature (T_{sat}) variation considering a varying Φ value, while Bauer et al.[84] studied the impact of the linear overlap variation on T_{sat}. The same fluence values utilized for the spike size variation (Figure 52) were fed into the model. The speed of the moving beam was adjusted accordingly to fit the experimental conditions corresponding to pps = 70. For each timestep (δt) and for each Φ the maximum surface temperature was derived. The temporal profile of the maximum surface temperature is shown in Figure 53, A for Φ_1 = 0.11 J/cm^2 (blue line), Φ_2 = 0.27 J/cm^2 (green line) and Φ_3 = 0.47 J/cm^2 (orange line). The corresponding T_{sat} are T_{sat1} = 213° C, T_{sat2} = 497° C and T_{sat3} = 834° C marked by a dotted line.

In Figure 53, B, the graph illustrates the calculated saturation temperature (T_{sat}) value versus the experimentally obtained equivalent diameter for the same Φ. A clear increasing trend is observed between the T_{sat} and the δ.

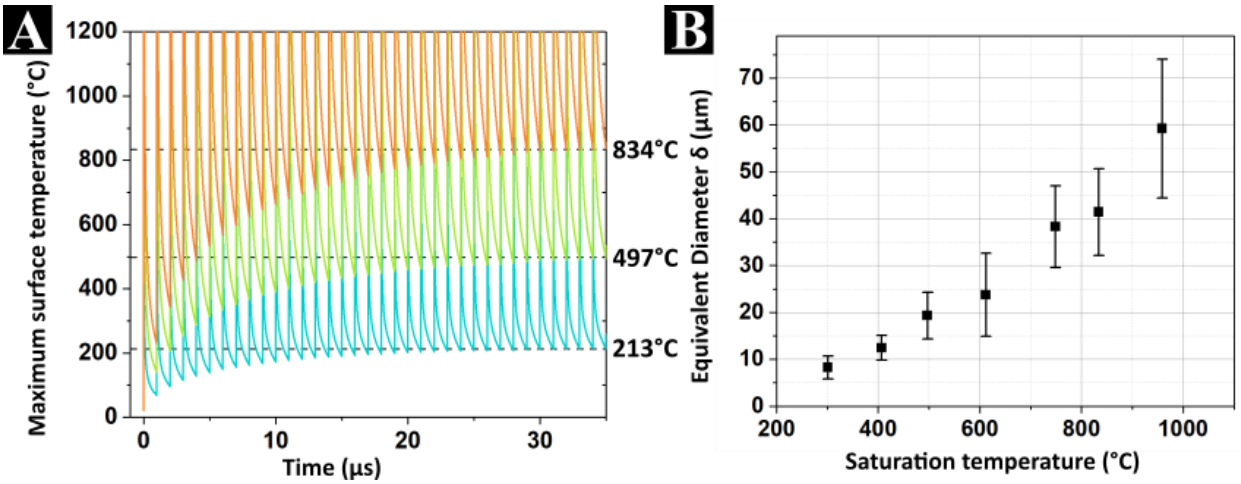

Figure 53 A: simulation results showing the evolution of the maximum temperature value on stainless-steel during the irradiation shown for Φ = 0.11, 0.27 and 0.47 J/cm^2. The noted values and the dotted lines illustrate the saturation temperature values for the rest of the fluences shown in Figure 52.

4.1.1.2. The role of overlap

Recently, it has been shown[7] for 1 MHz that when keeping the same dose values, e.g. delivering the same number of pulses (pps_{tot}) having the same fluence, is it possible to modify the spike morphology by varying the number of pulses per spot (pps). A threshold in terms of fluence and overlap is observed for passing from smooth to bumpy surface[125,135]. Similarly to the previous chapter, this behaviour can be linked to T_{sat} which was found to vary upon varying scanning speed[84]. Here we elaborate on the role of overlap in spike formation upon high repetition rate processing. By comparing results obtained with f = 1 MHz & f = 2 MHz we elucidate the role of heat accumulation on the spike size. The evolution of spike diameter versus the pps_{tot} is shown in Figure 54, which illustrates the results for f = 1 MHz (left) and f = 2 MHz (right), respectively. For both f values two different pps values were considered i.e. pps = 70 and pps = 300 for 1

MHz and pps = 30 and pps = 70 for 2 MHz. Finally, a fixed fluence value (Φ = 0.19 J/cm^2) means that the same pps_{tot} corresponds to the same overall energy dose.

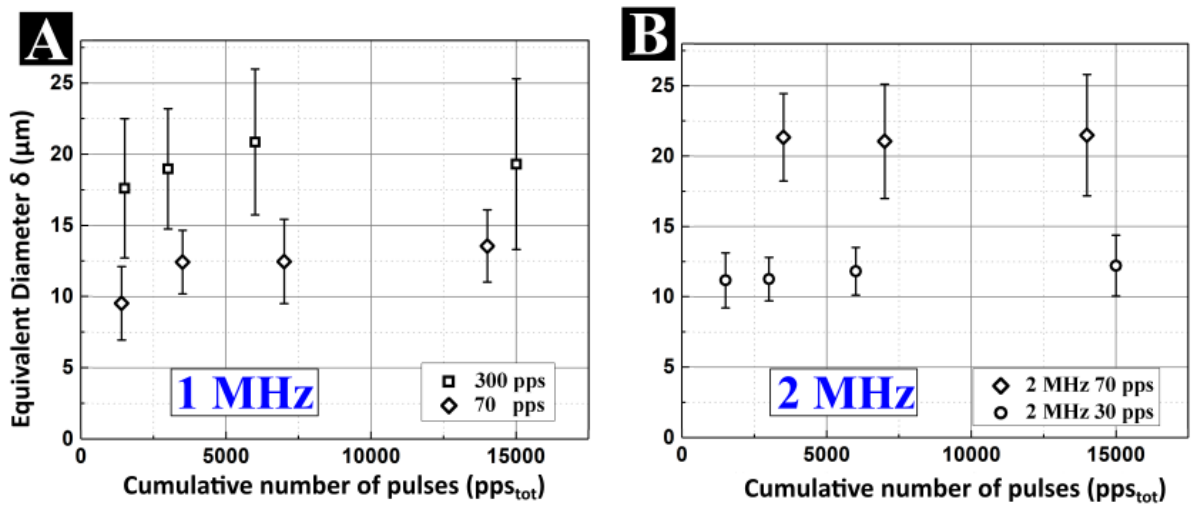

Figure 54 Evolution of average equivalent spike diameter (δ) under successive scan irradiation for different overlaps and repetition rates on stainless-steel. On the left side, the results obtained with f = 1 MHz, and on the right side those obtained for f = 2 MHz are shown. Different shapes indicate different overlaps. The fluence was constant in all cases (Φ = 0.19 J/cm^2)[8].

Within our experimental conditions, spikes are formed starting from a threshold value of nearly pps_{tot} = 1400 independently of the overlap and the repetition rate. It can be clearly observed that δ increases, when the overlap (pps) increases. At 1 MHz, the initial diameter corresponding to similar doses is δ = 9.5 ± 2.5 μm for pps = 70 (pps_{tot}=1400) and δ = 13.5 ± 2.5 μm for pps = 300 (pps_{tot} = 1500). In this case, we can extract an increment of roughly Δδ/Δpps = 0.0174 μm/pps. Variations in the value of overlap for 2 MHz seem to have more significant impact. For similar doses, the diameter is δ = 11 ± 2 μm for pps = 30 (pps_{tot} = 3000) and δ = 21 ± 3 μm for pps = 70 (pps_{tot}=3500), respectively, showing an increment of Δδ/Δpps = 0.25 μm/pps. Finally, a dose value of pps_{tot} = 3500 delivered with the same strategy (N = 50, pps = 70) will lead to structures with δ = 12.5 ± 2 μm for f = 1 MHz and δ = 21 ± 3 μm for f = 2 MHz, highlighting the brunt of repetition rate in the thermofluidic mechanism that leads to spike formation.

Moreover, a specific trend in spike evolution is observed as the pps_{tot} increases. Starting from 1 MHz we observe for 1400 ≤ pps_{tot} < 5000, δ clearly increases and tends to be stable for pps_{tot}> 5000 reaching a saturation value δ_s which is δ_s = 13.5 ± 2.5 μm for pps = 70 and δ_s = 19.5 μm ± 6 μm for pps = 300, respectively. On the contrary for 2 MHz the spike size does not change after they emerge and the saturation value varies between δ_s = 11 μm ± 2 μm for pps = 30 and δ_s = 21 μm ± 3 μm for pps = 70, respectively. Saturation in the growth of spikes could be interpreted by the fact that the delay between two successive scans is much longer than the time required for the diffusion of the heat accumulated during one laser scan.Therefore, it can be concluded that for fixed fluence and dose values the impact of the pulse overlap and repetition rate on the spike morphologies is confirmed at 1 MHz and 2 MHz[8].

4.1.1.3. The role of wavelength

Figure 55 illustrates the obtained structure for two different wavelengths, λ = 1030 nm (IR) and λ = 515 nm (VIS). The average equivalent spike diameter obtained was the same, δ = 12 ± 3 μm, obtained for similar fluence values: Φ = 0.19 J/cm^2 for IR and Φ = 0.23 J/cm^2 for VIS, yet, for different overlap pps = 70 and pps = 100, respectively. We conclude therefore that the spike size does not depend on the irradiation wavelength but on the values that determine the induced heat in the material (Φ and pps). For both wavelengths, the transition from ripples to conical formation is shown in Figure 55. Yet, the spikes obtained with VIS are much less homogeneous compared to those obtained with IR for higher doses.

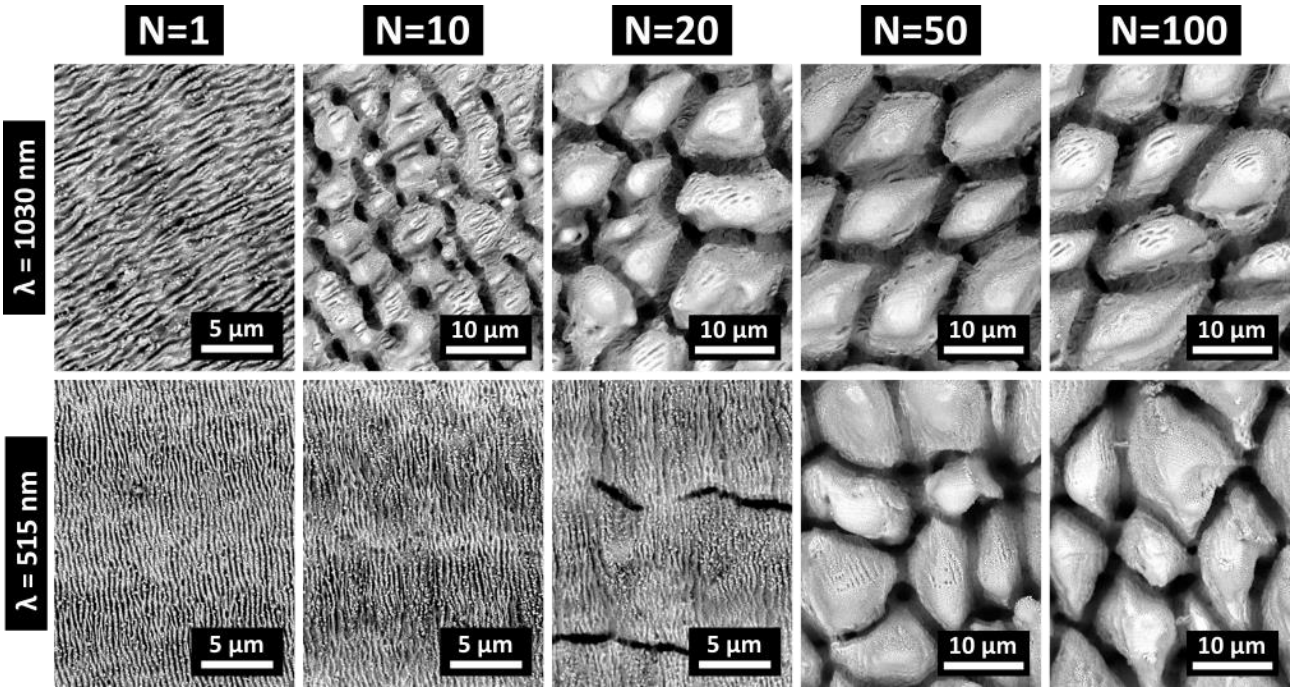

Figure 55 SEM images of stainless-steel surface evolution upon irradiation with two different wavelengths at f = 1 MHz. Top: λ = 1030 nm, Φ = 0.23 J/cm^2, pps = 70. Bottom: λ = 515 nm, Φ = 0.22 J/cm^2, pps = 100

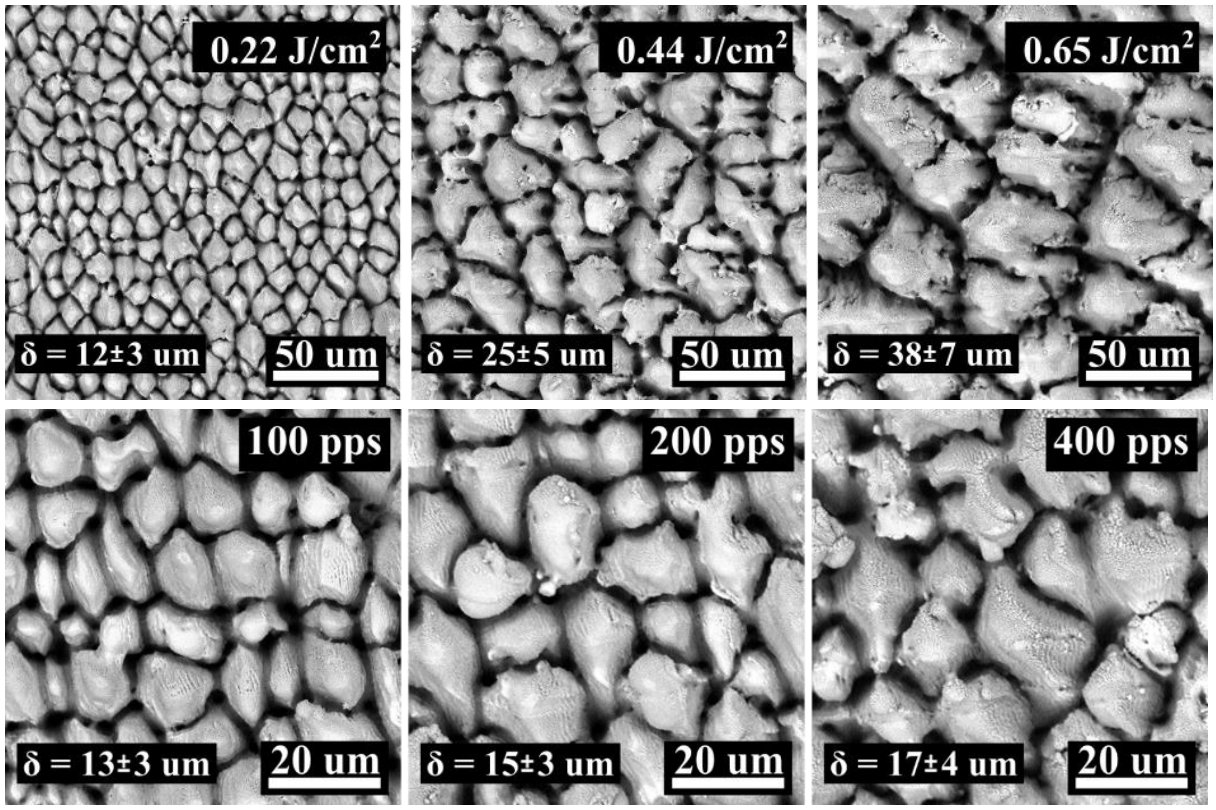

Figure 56 SEM images of stainless-steel 316 surface showing bumpy spikes obtained with λ = 515 nm at f = 1 MHz. Top row illustrates the surface obtained under variation of fluence as indicated. Bottom row illustrates the morphology obtained under variation of overlap for the same dose on the surface when Φ = 0.22 J/cm^2.

Similarly, to the IR case, the spike size was found to vary upon variation of fluence and overlap in VIS. In fact, by varying the fluence between $\Phi = 0.22$ J/cm^2 and $\Phi = 0.65$ J/cm^2 feature sizes comprised between 12 µm ± 3 µm and 38 µm ± 7 µm were obtained (Figure 56). Similarly, for overlap variations from pps = 100 to pps = 400 (when $\Phi = 0.22$ J/cm^2) feature sizes comprised between 13 µm ± 3 µm and 17 µm ± 4 µm were observed (Figure 56). Lastly, in contrast to the spike size, the ripple period changes as expected with the wavelength. Ripples with $\Lambda_{LSFL} = 387 \pm 5$ nm were obtained with VIS and $\Lambda_{LSFL} = 642 \pm 6$ nm were obtained with IR.

4.1.1.4. The role of repetition rate

Even though an indirect conclusion of the repetition rate impact can be deducted from Figure 54, the explicit demonstration of the role of repetition rate is necessary for a complete description of spike formation. In Figure 57 we illustrate the resulting structure for the case where we increase f from f = 1 MHz to f = 2 MHz maintaining the pps = 70 and the $\Phi = 0.23$ J/cm^2. As expected, we observe higher T_{sat} and larger structures

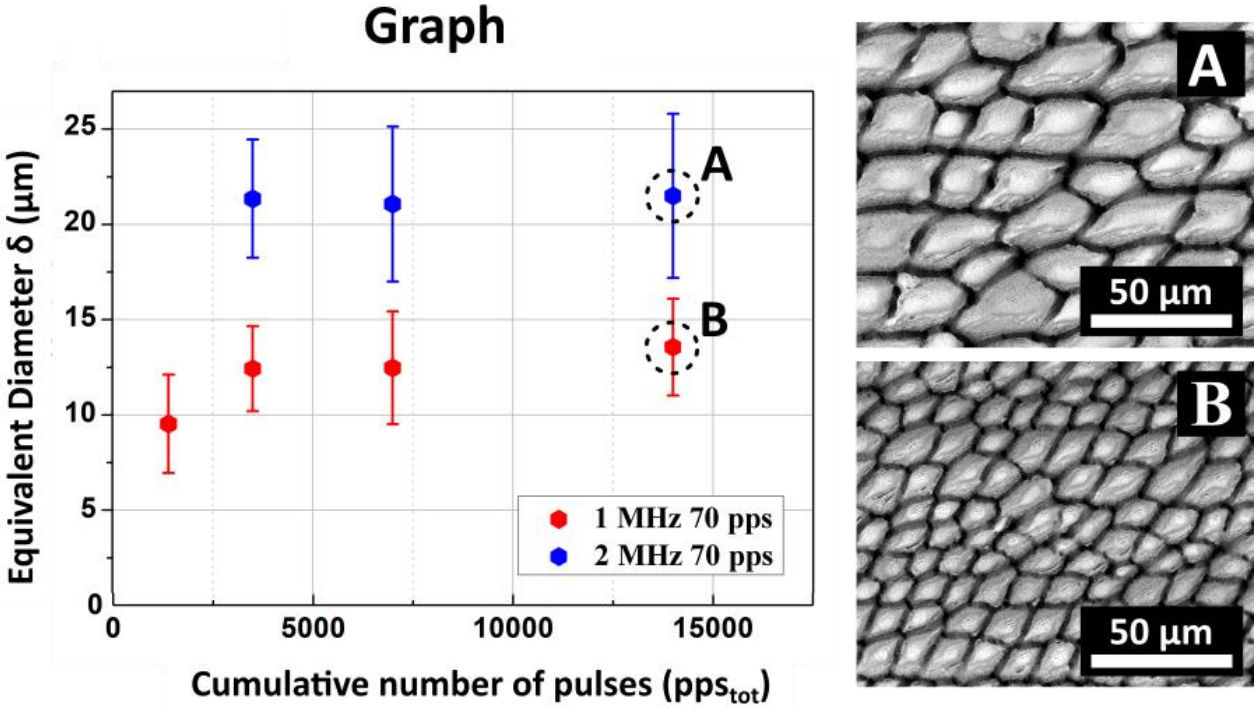

Figure 57 Equivalent diameter δ evolution versus cumulative number of pulses pps$_{tot}$ for 1 MHz and 2 MHz, 70 pps and 0.23 J/cm² (left). Corresponding SEM pictures of stainless-steel for 15 000 pps, 1 MHz (right A) and 2 MHz (right B)"

for higher repetition rates. The spike diameter obtained for 14000 pps$_{tot}$ was 14 ± 3 µm for f = 1 MHz and 22 ± 4 for f = 2 MHz showing that the spike size can be significantly increased upon increase of repetition rate.

4.1.1.5. Upscaling strategy

Upscaling of spike fabrication requires a fine tuning of all the factors discussed in the previous paragraphs. As shown in Figure 57, reproducing the same spike size when increasing the repetition rate cannot be realized by utilizing the same process parameters (pps, Φ). Assuming that the underlying mechanism responsible for the enlargement of spikes upon increasing repetition rate is heat accumulation, a compensation of Φ and pps is necessary to reproduce the same morphology. In Figure 58 we demonstrate the success of this hypothesis by reproducing the same spike size employing 4 different sets of parameter combinations of f, pps and Φ.

Table 2 Spike size obtained with different strategies (values correspond to Figure 58 A & B N=100, C & D N=200)

f	Fluence (J/cm^2)	pps	N	pps_{tot}	dose (J/cm^2)	τ_{pros} (min/cm^2)	δ (µm)	dδ (µm)
1 MHz	0.23	70	100	7000	1610	35	12.5	3
2 MHz	0.11	70	100	7000	770	17.5	11.6	2
2 MHz	0.23	30	200	6000	1380	14	11.8	1.7
1 MHz	0.34	15	200	3000	1020	14	12.5	0.9

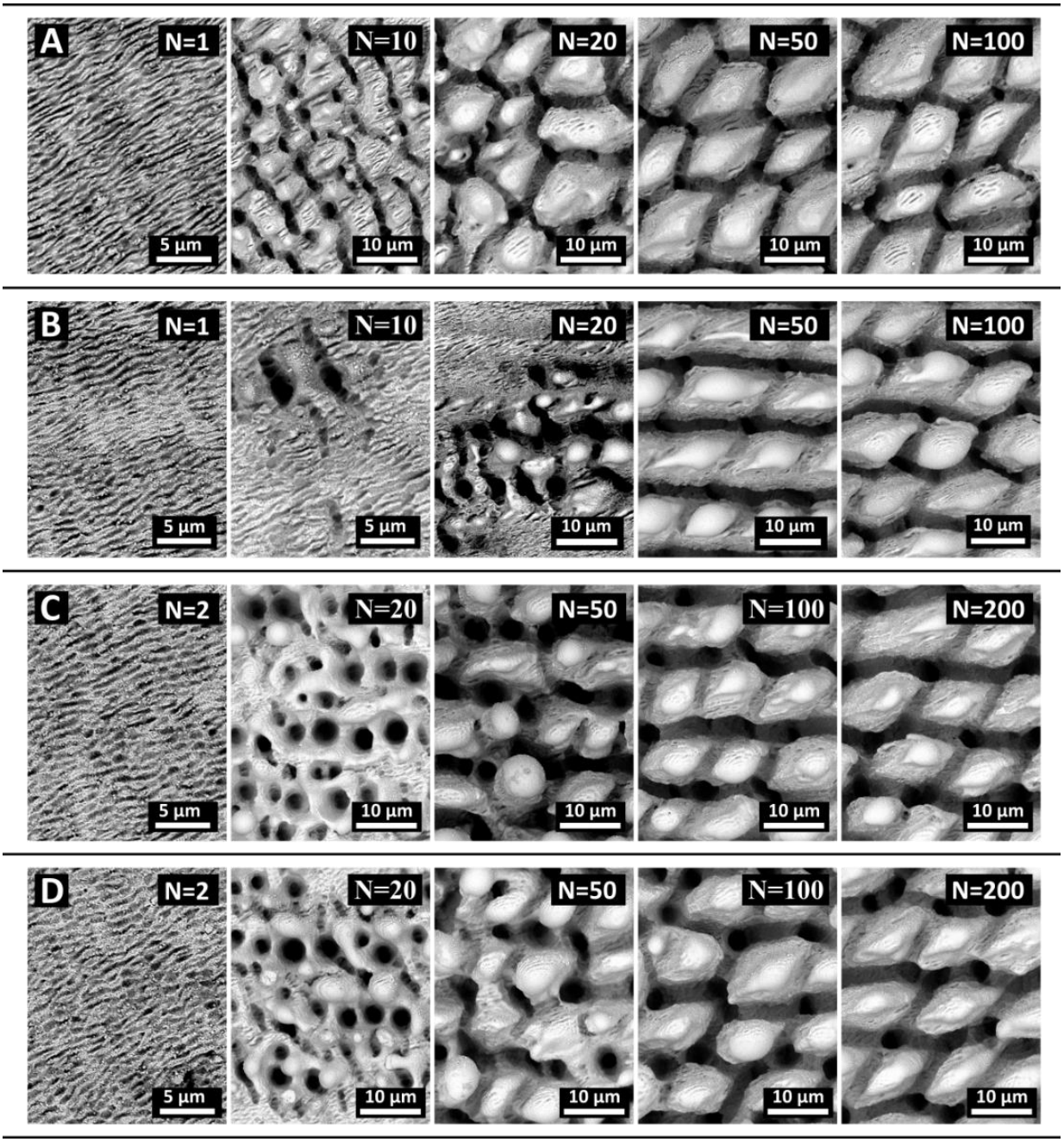

Figure 58 SEM images of stainless-steel surface illustrating the structure evolution under successive scan irradiation. Each row corresponds to a different strategy. A: 1 MHz, 70 pps 0.23 J/cm^2. B: 2 MHz 0.11 J/cm^2 70 pps. C: 2 MHz, 30 pps 0.23 J/cm^2. D: 1 MHz, 15 pps 0.34 J/cm^2. N indicates the number of scans.

Starting from Figure 58, A, we see a transition from ripples to spikes for f = 1 MHz, overlap of 70 pps and Φ=0.23 J/cm^2. For the given experimental conditions, the surface evolves from ripples when N=1 into grooves N=10 and then spikes N>50. For N = 100 the processing rate was 35 min/cm^2 and the obtained diameter $\delta = 12.5 \pm 3$ μm. Each consecutive set of parameters used to process the surface shown in Figure 58, B, C & D was chosen in that way that an increase of one or more of the parameters f, pps and Φ, that contribute in heat accumulation, is followed by a compensating decrease of the other parameters. According to that we present a sequence of experiments resulting in quite similar morphologies obtained in a significantly increased processing rate. Figure 58, B shows the results when we increase the repetition rate from f = 1 MHz to f = 2 MHz and decrease the fluence from Φ = 0.23 J/cm^2 to Φ = 0.11 J/cm^2 while we keep the overlap constant (pps = 70). For N=100 we obtained $\delta = 11.6 \pm 2$ in 17.5 min/cm^2. In Figure 58, C, we increase the repetition rate from f = 1 MHz to f = 2 MHz and decrease the overlap from pps = 70 to pps = 30 while we keep constant the fluence (Φ = 0.23 J/cm^2). For N=200 we obtained $\delta = 11.8 \pm 1.7$ in 14

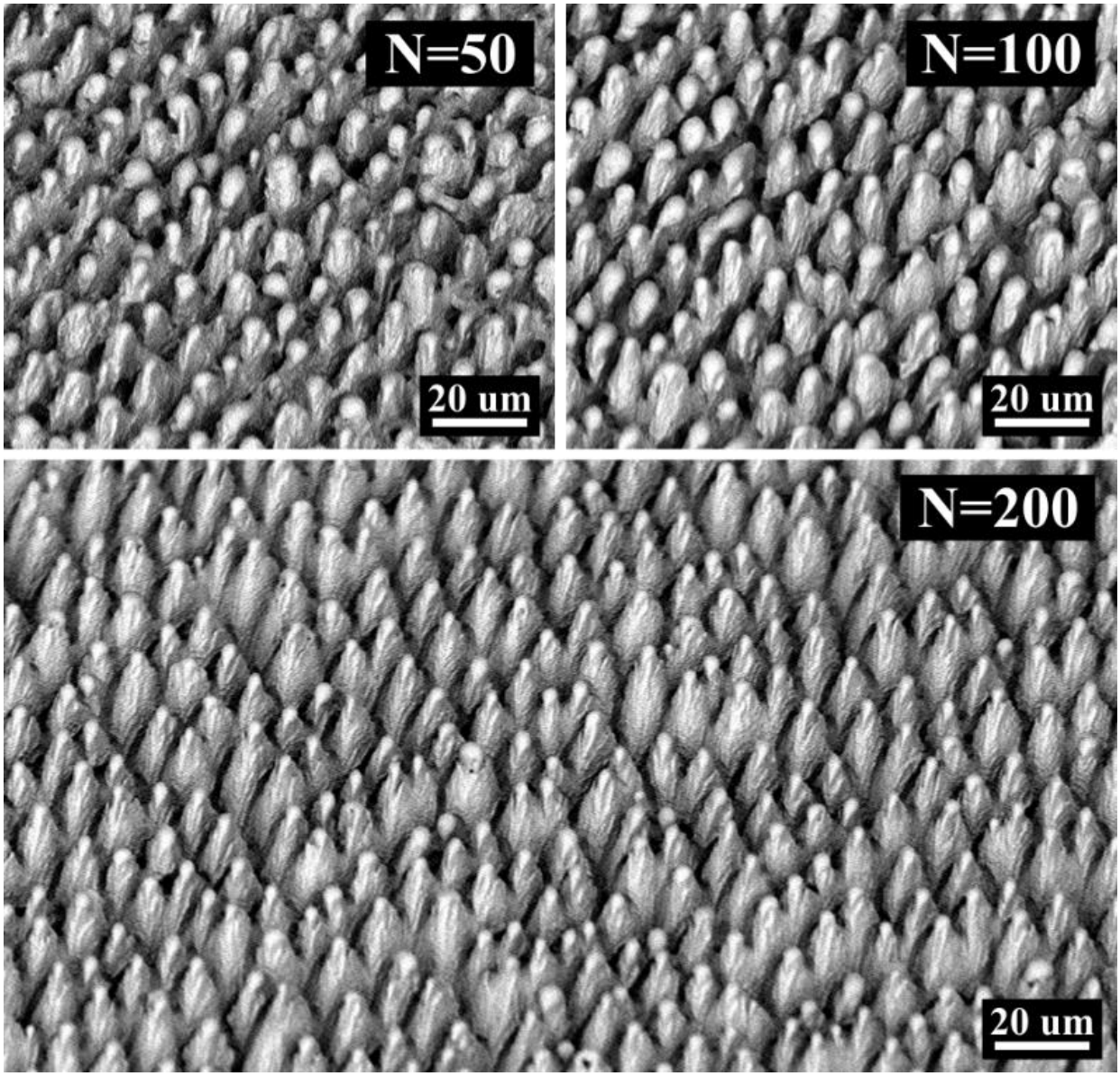

Figure 59 SEM image of stainless-steel surface irradiated with f = 2 MHz, Φ = 0.23 J/cm^2 and pps = 30 and varying number of scans as indicated by N. The image is taken under 40º tilt angle.

min/cm^2. In Figure 58, D we keep constant the repetition rate f, we increase the fluence from $\Phi = 0.23$ J/cm^2 to $\Phi = 0.34$ J/cm^2 and decrease the overlap from pps = 70 to pps = 15. For N=200 we obtained $\delta = 12.5 \pm 0.9$ in 14 min/cm^2. The details are summarized in Table 2.

Apart from the spike size, secondary features of the structure evolution differ in between the different sets of parameters. For 2 MHz (Figure 58, C and N=20) the clear groove formation is not observed as for 1 MHz (Figure 58, A, N=10 and pps_{tot}=700). Instead for almost the same dose (pps_{tot}=600) at 2 MHz the surface is dominated by aggregations resulting quite likely from the melting of the surface. The drops that are formed on the surface (Figure 58, C, N=20 and N=50) later form the peaks of the spikes. In both cases the spike major axis is oriented parallel to the ripples and so, vertically to the laser polarization. Additionally, for pps_{tot}> 3500 (Figure 58, A & N>50 and Figure 58, C & N>100) the spike size and shape do not seem to change significantly. Finally, in Figure 58, D, for f = 1 MHz an increase of 32% in fluence is enough to counterbalance a decrease of 80% in overlap. This signifies that the overall procedure is not linear, especially in the case of the fluence. Even though detailed computations are required in order to estimate the amount of accumulated heat, a simple qualitative estimation is quite effective.

The morphology obtained for f = 2 MHz, $\Phi = 0.23$ J/cm^2 and pps = 30 is illustrated in tilt view under 40º in Figure 59. There we illustrate the final stages of spike formation: small aspect ratio inhomogeneous spikes, with bumpy tops for N = 50, spikes with higher aspect ratio for N = 100, and finally for N = 200, spikes become homogeneous conical formations with pointy tops. The processing rate for the final morphology (Figure 59, N = 200) is approximately 14 min/cm^2.

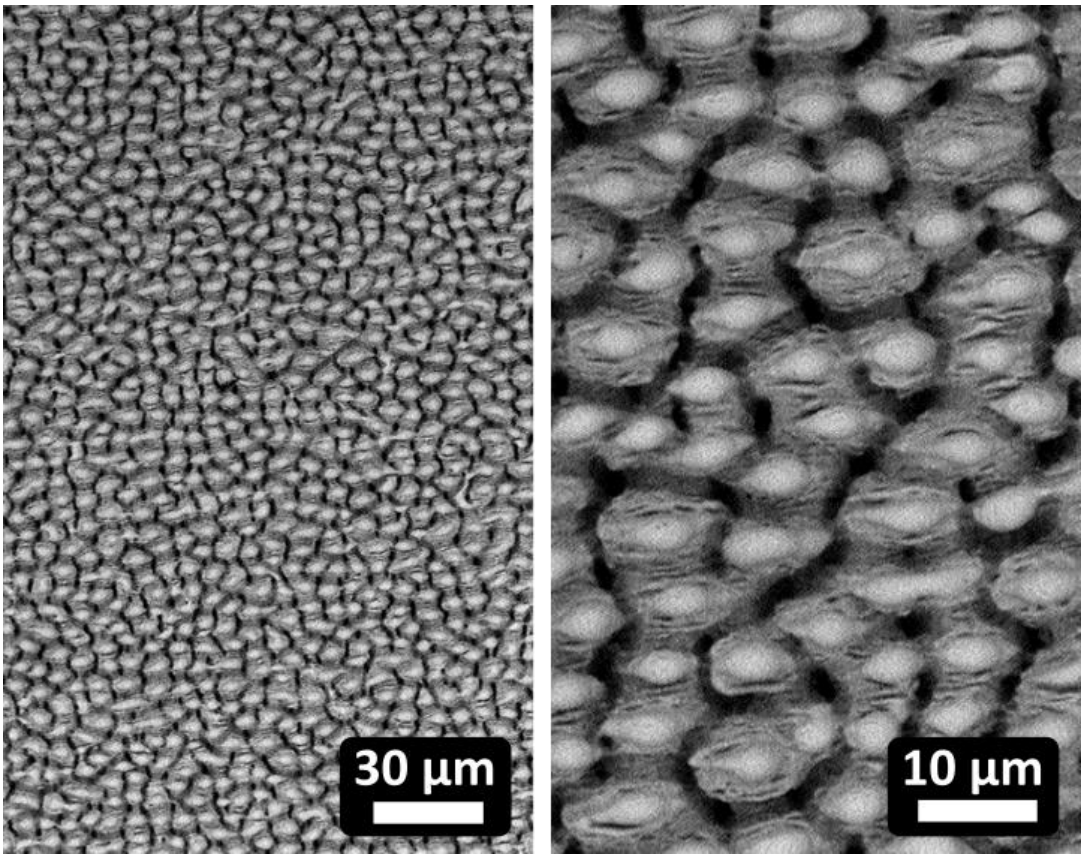

Figure 60 SEM images of stainless-steel surface obtained after irradiation with f = 10 MHz, H = 10 µm, N = 100, pps = 20, and $\Phi = 0.1$ J/cm^2.

Employing this approach, it is possible to exploit repetition rates even up to f = 10 MHz. The case shown in Figure 60 was obtained with f = 10 MHz, H = 10 μm, N = 100, pps = 20, and $\Phi = 0.1$ J/cm^2. The processing rate was astonishingly high compared to the usual fabrication process and it was in the range of 1 min/cm^2.

Nevertheless, the spikes obtained with high repetition rate (f > 1 MHz) are not as absorptive as the ones obtained at low repetition rates. The hierarchical morphology of the structures plays a key role, since the sides of the spikes are mainly melted like lacking the presence of the nano-roughness which plays key role in the light absorption as will be presented in chapter §5.2.3.

4.1.2. Controlling the laser induced morphology by UV fs laser

Achieving control of surface morphology in the nanoscale is of paramount importance for developing a variety of applications. Up-to-date industrial laser systems are able to generate femtosecond pulses in the UV range. UV is suitable for fabricating LIPSS in the nanoscale, due to the dependence between the wavelength and the LIPSS period. UV fs pulses at $\lambda = 257$ nm were generated by combining a 350-fs laser source (Satsuma HP^3, Amplitude Systèmes) emitting in the near infrared ($\lambda = 1030$ nm) with a fourth harmonic generation module. The repetition rate was fixed for the UV generation to f = 250 kHz. We utilized this laser to irradiate the surface of stainless-steel samples.

In Figure 61 we show the evolution of the surface morphology upon irradiation with $\Phi = 0.11$ J/cm^2 and variation of pps_{tot}. A progressive evolution of the surface structures is presented for increasing pps_{tot}, from

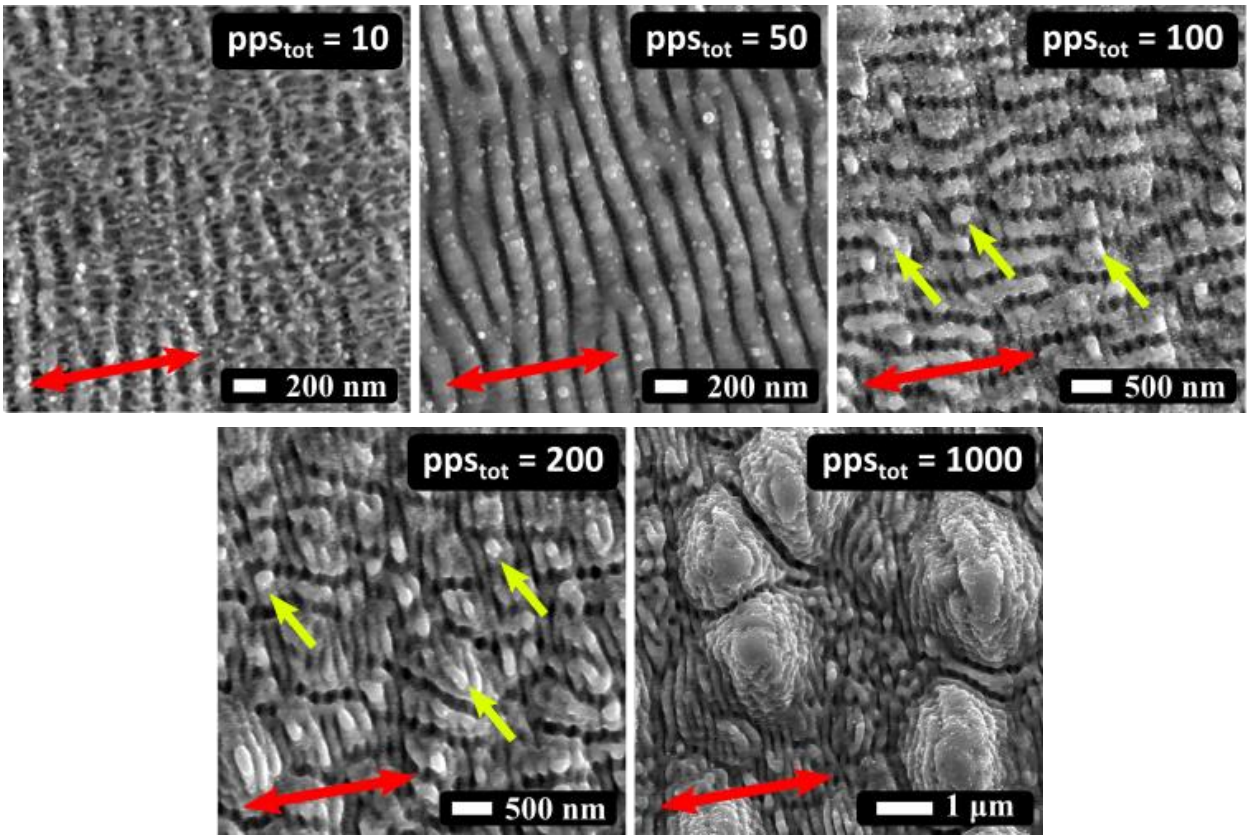

Figure 61 SEM images of stainless-steel surface morphologies obtained under irradiation with $\Phi = 0.11$ J/cm^2 and variation of pps_{tot}. The red arrows indicate the polarization orientation. The total number of pulses is indicated by the pps_{tot} value in each image. HFSL are formed for pps_{tot} = 10, ripples (LFSL) for 50 pps_{tot}, grooves for pps_{tot} = 100, pre-spikes for pps_{tot} = 200, and inhomogeneous spikes for 1000 pps_{tot}. The yellow arrows point to the small protrusions formed in the edge of the groove for 100 pps_{tot} and in the center of the rim for 200 pps_{tot}[12].

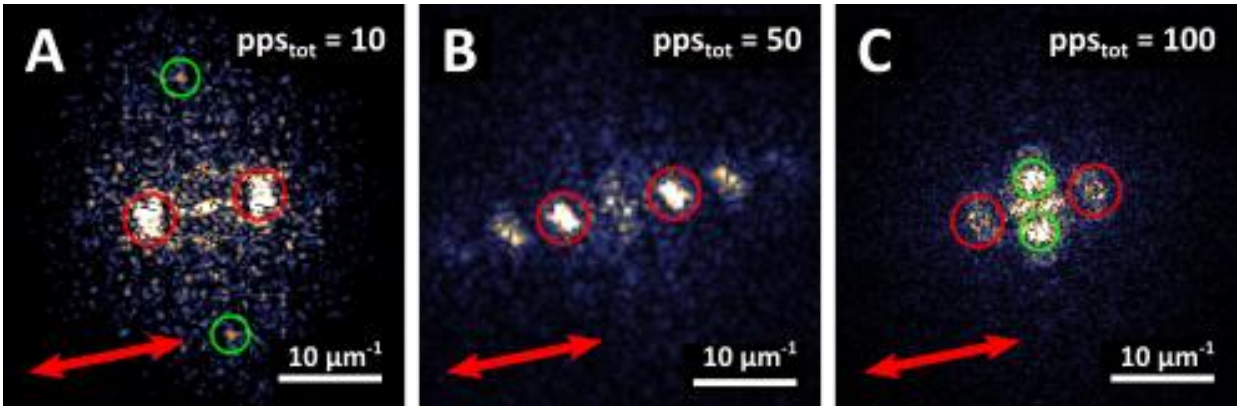

Figure 62 FT diagrams corresponding to the SEM images of Figure 61 as indicated by the pps_{tot} value. The red arrows indicate the polarization orientation. Ripple periodicities are marked with red dotted circles in A, B and C. Green circles indicate HSFL in image A and groove structure in image C[12].

HSFL (pps_{tot} = 10) to an inhomogeneous spike formation (pps_{tot} = 1000). For pps_{tot} = 10, HSFL were obtained oriented parallel to the polarization direction (indicated with a red arrow) with a period as short as $\Lambda_{HSFL} = 76 \pm 2$ nm while at this point, ripples start to form on the surface. For pps_{tot} = 50 the ripples, oriented perpendicular to the laser polarization (leading to LSFL), become well defined with $\Lambda_{LSFL} = 153 \pm 4$ nm. For pps_{tot} = 100 the predominant morphology on the surface consists of shallow structures oriented parallel to the laser polarization but with a period almost 6 times longer than for HSFL. Those structures mentioned as grooves are considered as an intermediate structure between ripples and spikes[46]. Similar formations on the same material were also reported using different wavelengths[8]. For the given conditions, a period of $\Lambda_{groove} = 426 \pm 7$ nm could be extracted[12].

The various periods of the structures were determined using Fourier transformation (FT). The FT images corresponding to the SEM images for pps_{tot} = 10, pps_{tot} = 50 and pps_{tot} = 100, are presented in Figure 62, A, B and C, respectively. Peaks corresponding to different structures are marked as followed. Red circles indicate periodicities that correspond to ripples. Green circles in Figure 61, A, indicate $HSFL_{\parallel}$ and in Figure 61, C grooves.

A detailed examination showed that in some cases, small protrusions are formed at the edges of the grooves, indicated with yellow arrows in Figure 61 for pps_{tot} = 100. Under further irradiation (Figure 61, pps_{tot} = 200) the number of protrusions, marked with yellow arrows, is higher and the grooves are shorter in length. Elliptical, submicron, spiky protrusions with low aspect ratio are formed around those protrusions. We assume that their formation mechanism is similar to the one described by Tsibidis et al.[46] for silicon. In their work, simulations show that the spike formation process can be explained as a result of Marangoni flow over lateral and in-depth temperature gradients. This model could possibly be applied to our results on stainless steel. However, the extend of the process should be expounded in the frame of the experimental conditions: The optical penetration depth which determines the depth of the absorbing zone is expected to be smaller for UV than for IR irradiation[136]. Thus the residual thermal gradient which is considered to be the dominant mechanism for groove and spike formation should differ substantially from the one described in ref. [46]. Consequently, the groove depth, the size ratio between ripples and grooves as well as the aspect ratio between spike height and width is expected to be smaller than in silicon. Furthermore, a wavelength dependent formation mechanism[54] should be considered in this case due to the very low fluence value.

For increasing pps_{tot} the surface changes radically. The inhomogeneity increases and conical formations start to develop on the surface (Figure 61, 1000 pps_{tot}). These conical formations densify and grow as the number of pulses increases. As shown in Figure 63, spikes become the predominant shape on the surface for pps_{tot} = 2000. In Figure 63 B a cross section of conical spike formation gives additional information

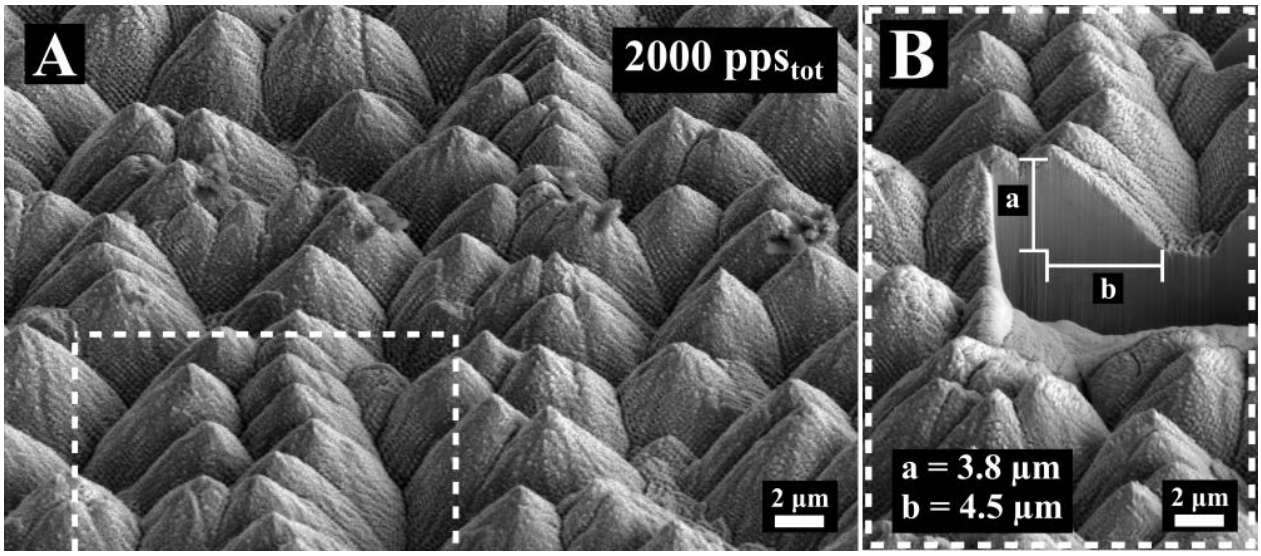

Figure 63 SEM image of stainless-steel illustrating the surface morphology obtained for 2000 pps$_{tot}$. B: detail of A showing the cross section of a spike[12].

about the size and the aspect ratio of the features. In this particular case, the height was estimated to be 3.8 µm and the half of the base 4.5 µm, relatively smaller compared to IR spike formation on steel[8,137].

In contrary to shallower structures investigated in the previous part with lower overlap (pps ≤ 100), the main growth mechanism of the cones (pps ≥ 200) should be linked to the ablation rather than hydrodynamical movement of molten material. On one hand, the fluence utilized here is relatively low ($\Phi = 0.11$ J/cm^2) and for low fluences spikes are described to result from the ablation process[124]. On the other hand, spikes appear randomly on the surface (Figure 61, 1000 pps$_{tot}$) and as the pps$_{tot}$ increases they are densified on the surface (Figure 63). A similar evolution of stainless steel surface has been observed for IR femtosecond pulse irradiation and is attributed to the anisotropy of beam absorption due to surface defects[124].

Additionally, the ablation-related formation mechanism is proposed here due to the systematic appearance of concentric grooves (CG) around the spikes also reported in literature as interference fringes[122]. Figure 64 illustrates stainless steel surface before the homogeneous spike formation covers homogeneously the surface. The surface in the proximity of the spikes is covered by concentric grooves. We punctuate that the CG most likely are the result of light interference between the incident pulse and a part of the pulse which is reflected by the spike. Light interference results in a periodical modulation of the laser intensity on the surface and periodic structures can result from it[138]. The pulse length in space is sufficiently large (~100 µm for 350 fs) to permit the interference. Moreover, the structure orientation is independent of the laser polarization and their amplitude fades as the distance from the spikes increases. Lastly, the CG appear to have a different period than LIPSS.

A rough geometrical correlation between the CG period and the incident condition was realized to further justify our hypothesis. Structure period can be derived by Fourier transform (FT) analysis of the the SEM image shown in Figure 64 A. Two areas of Figure 64 marked as B and C were analysed**.** These areas are shown in magnification in Figure 64 B1 and C1. The FT diagrams are presented in B2 and C2, respectively. The circled peaks in Figure 64 B2 and C2 indicate the most prominent periods present on the surface. The red circled peaks correspond to ripples with a period of $\Lambda_{LSFL} = 197 \pm 6$ nm in B2 and $\Lambda_{LSFL} = 188 \pm 8$ nm in C2**.** The ripple period differs giving $\Lambda_{LSFR} = 176 \pm 3$ nm far from spikes. The peaks which are enclosed

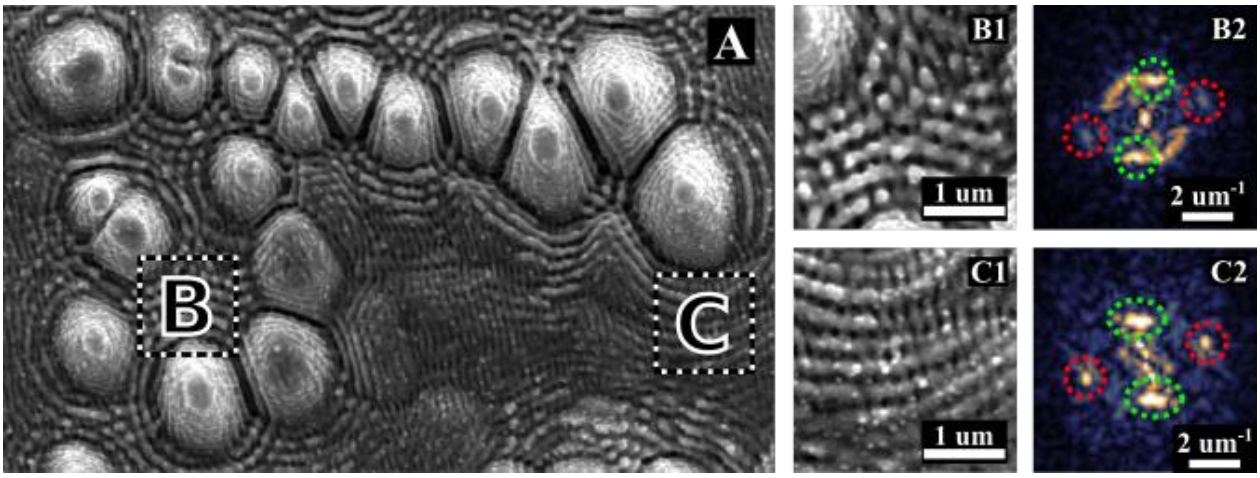

Figure 64 SEM images of stainless-steel surface (A). B1 and C1 are the zoomed areas marked as B and C. B2 and C2 are the FT images of B1 and C1, respectively.

in green dotted circles correspond to the concentric groove (CG) structure formed around the spikes. CG have a period of Λ_{CG}= 315 ± 6 nm in B2 and Λ_{CG} = 301± 7 nm in C2. General analysis in the area gave a minimum value of Λ_{CG} = 270 ± 3 nm and a maximum of Λ_{CG} = 315 ± 6 nm. Those periods are significantly different than those of ripples observed in Figure 64 (Λ_{LSFL} = 153 ± 4 nm) and are smaller compared to grooves shown in Figure 64, C with Λ_{groove} = 426 ± 7 nm.

Equation 12 Light interference period (Λ) with respect to irradiation wavelength (λ) and the angle between the two interfering beams (θ)

$$\Lambda = \lambda/(2\ sin\,\theta\ )$$

For light interference patterning, the equation associating the wavelength, the angle and the resulting structure period is given by Equation 12 [139]. Where Λ is the period of the structures, θ the angle between the incident and the reflected beam, and λ the wavelength. Setting Λ_{min} = 270 nm as the min period value Λ_{IP} from the FT analysis and λ = 257 nm, we deduce an angle between two interference beams of θ_{max} = 28.5° and for the maximum CG period, Λ_{max} = 315 ± 6 nm, θ_{min}= 240°. In this simplified scenario, the structures reflecting the light should have a height to base ratio ~ 1. Of course, the actual case differs since it includes scattering of a Gaussian wavefront around the sides of the spike.

As discussed in §2.4.3 there are two different types of spikes. The first, for low Φ values, results from the ablation process around the surface defects (§2.4.3.1) and the second for higher Φ values from microfluidic movement (§2.4.3.2). Surprisingly, an increase of fluence from Φ_{Low} = 0.11 J/cm^2 to Φ_{High} = 0.42 J/cm^2 does not enable melted like spike generation. For each fluence value we vary the overlap between pps = 10 and pps = 100 and the number of scans between N = 1 and N = 50. The results are illustrated in Figure 65. Same pps_{tot} values are indicated with different symbols ▲: pps_{tot} = 100, ●: pps_{tot} = 500, ■ pps_{tot} = 1000.

For Φ_{Low} as the pps_{tot} increases, independently of the irradiation strategy, the structures evolve from ripples into grooves and conical spikes. Surface structuration obtained with the same pps_{tot} exhibits only minor differences for different irradiation strategies. Interestingly, when the fluence is set to Φ_{High} the obtained surface morphologies differ substantially from the ones obtained for Φ_{Low}. In this case the surface does not change as the pps_{tot} increases and is dominated in all cases by inhomogeneous ripples. This behaviour leads us to the conclusion that for this fluence value a significant part of the surface which participates in the interaction is ablated. Enhanced ablation for increasing fluence has been observed in metals irradiated with IR femtosecond pulses[140] but for much higher fluences, in the range of 2-10 J/cm^2. Furthermore, multi-pulse

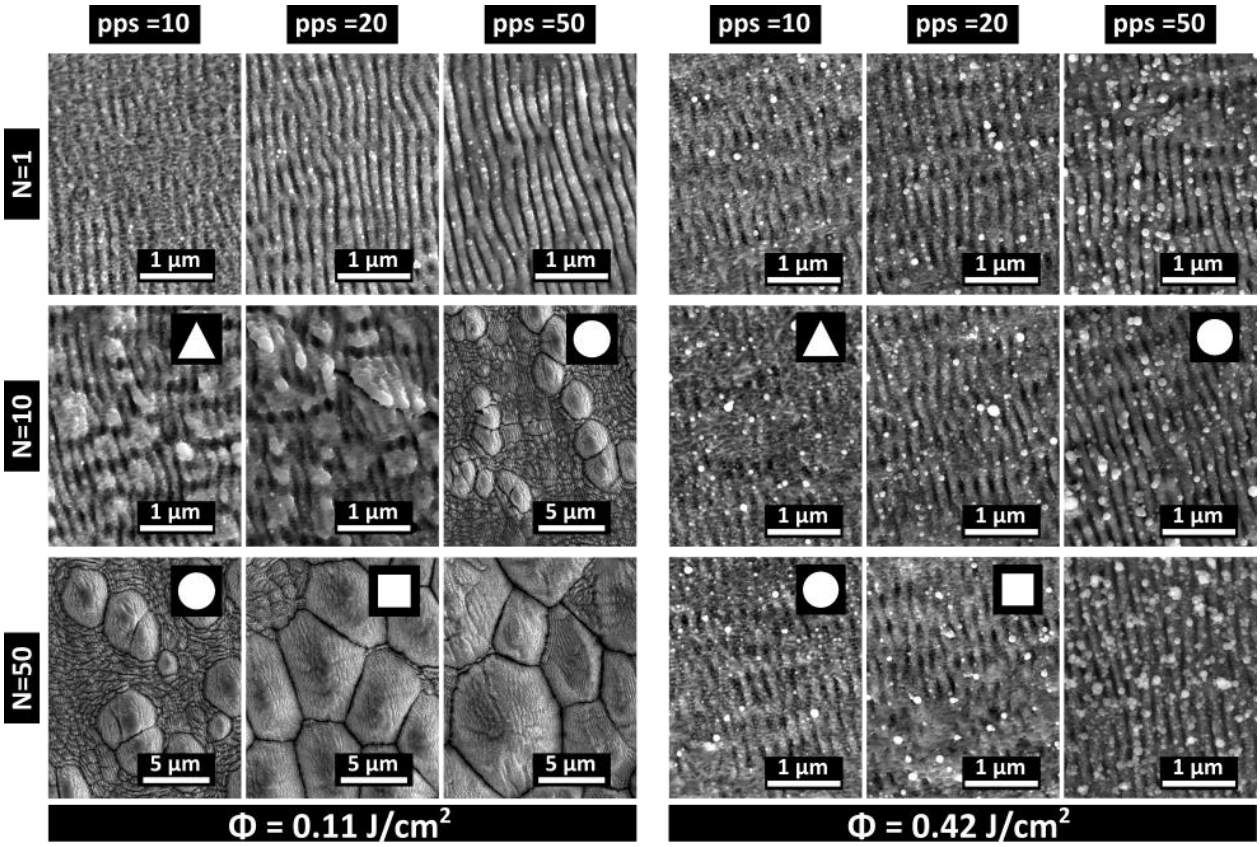

Figure 65 SEM images of stainless-steel surface obtained with two fluence values, Φ_{Low} = 0.11 J/cm^2 and Φ_{High} = 0.42 J/cm^2. Different overlaps (pps) and number of scans (N) were studied. Morphologies obtained after irradiation with the same number of pulses pps_{tot} are indicated with the same symbol ▲: pps_{tot} = 100, ●: pps_{tot} = 500, ■ pps_{tot} = 1000[12].

LIPSS formation is the cumulative result of the coupling of the incident pulse with the pre-existing surface roughness[46]. The pps value defines the spatial relation between the crater which is formed by the previous pulse and the incident pulse intensity distribution. Therefore, variations of the pps value can affect the resulting morphology even when the pps_{tot} value is the same. As we can see in Figure 65, this phenomenon is negligible for Φ_{Low} but intensified for Φ_{High}. In that case we expect that the crater formed by each pulse is bigger and thus has greater impact on the irradiation.

In this paragraph the possibility to control the structure size from a few tens of μm to a few tens of nm is demonstrated using trains of single pulses[6–8,10,12]. That was possible by varying key process parameters such as fluence, overlap and irradiation wavelength. The significance of the heat accumulation in defining the spike size was extensively discussed and a scaling up strategy was introduced achieving homogeneous spike fabrication over a large area at f = 10 MHz. Nevertheless, in the submicron scale single pulse irradiation has little to offer in controlling laser induced morphologies. In the next section results on controlling submicron morphology utilizing double-pulse irradiation are presented.

4.2. Double-pulses

Apart from the size of the structures, controlling the symmetry of the laser induced morphology in the submicron scale is essential for surface functionalization. Fabricating and tailoring 2D-LIPSS could enable us to mimic functional textures found in nature, introducing functionalities such as antireflectivity[3] and bactericidity[16].

As discussed in §2.3 (2D structure generation & double-pulse irradiation), several works demonstrate the impact of polarization control and double-pulse irradiation on determining texture symmetry and size. In this section, a comprehensive study on controlling laser induced structures by double femtosecond pulse irradiation is presented. The effect of pulse polarization and interpulse delay is elucidated and the generation of novel 2D surface morphologies is reported. Finally, a plausible interpretation of the structure formation mechanism is proposed in the frame of non-linear convection flow.

Moreover, our approach is transferable to industrial processing, as we show results using an industrial femtosecond laser source with a pulse duration of 350 fs emitting at 1030 nm with repetition rates up to 2 MHz to texture large areas (δ = 10 mm) much wider than the spot size.

4.2.1. Nanostructures obtained with double pulses

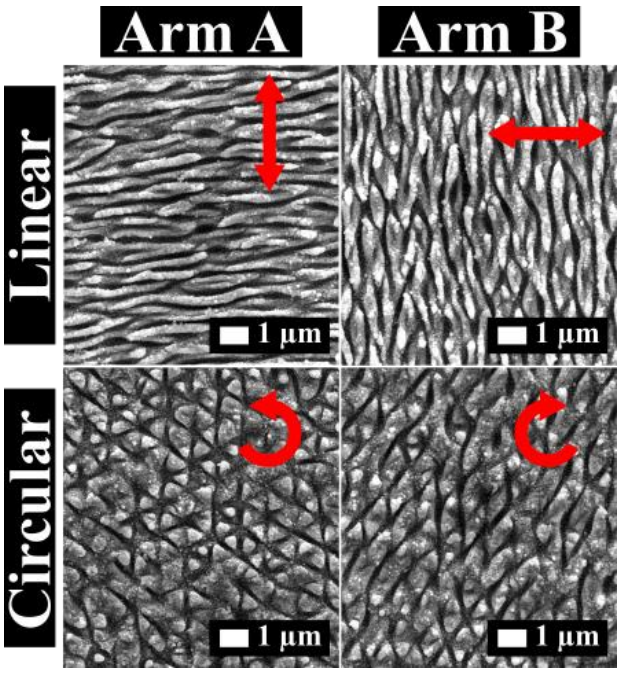

Figure 66 SEM images of stainless-steel surface after single arm irradiation for linear and circular pulse configuration as indicated. The polarization direction is indicated by a red arrow. The irradiation parameters were the same for both arms: H=1 µm, pps = 10 and Φ = 0.1 J/cm^2.

Exploiting the surface transient state, induced by a fs pulse irradiation, a second incident will intervene in the evolution of the ultrafast dynamics and the usual structure formation process will be interrupted. Depending on the interpulse delay Δτ, the second pulse will have an impact at different stages of the structure formation process and the induced surface morphology is expected to vary with respect to Δτ. When Δτ ranges in the picosecond timescale, electron-phonon dynamics can be regulated (2.1.1). For longer interpulse delays (Δτ > ~ 0.1 ns), double-pulse irradiation will mainly affect the microfluidic movement of the molten surface.

According to that, the role of Δτ is investigated in two distinct parts according to the delay, picosecond regime and nanosecond regime and in detail from 1 ps to 4 ns[9]. The pulse polarization role is elucidated by studying the different morphologies induced by double cross-polarized (XP) and double circular counter rotating polarized (CP) pulses for irradiation. The fluence was varied from Φ = 0.1 J/cm^2 to Φ = 0.8 J/cm^2. The values used are summarized in Table 3.

Table 3 Parameters used for double pulse irradiation with delay line

Parameter[viii]	Considered Values
Fluence[ix], Φ [J/cm^2]	0.1, 0.15, 0.2,
Overlap, [pps]	5, 10, 20
Hach, H [µm]	1, 2, 5,
Small delays [ps]	± 0.1, 0.2, 0.5, 1, 2, 5, 10, 20, 50

[viii] The surface was scanned once (N = 1) except §4.2.1.6.
[ix] The fluence value corresponds to the pair of double-pulses.

Large delays [ns]	0.1, 0.5, 1, 2, 3, 4

The results of single arm irradiation are presented for comparison with the double-pulse irradiation case. Figure 66 illustrates the obtained morphology on stainless steel after single arm irradiation for linear and circular polarization. We utilized Φ = 0.1 J/cm^2, pps = 10 and H = 1 µm to obtain homogeneous ripple formation. Two polarization configurations are shown, linear (Figure 66, top) and circular (Figure 66, bottom). The polarizations of the two arms are indicated by red arrows[9].

Linear polarization leads to ripples, formed perpendicular to the laser polarization, meanwhile circular polarization leads to inhomogeneous triangular structures (Figure 66, bottom). Our results are consistent with those reported in scientific literature for linear[8] and circular polarization[43] and similar irradiation conditions.

4.2.1.1. Double-pulses produced by delay line (DL) with $\Delta\tau$ in ps

Figure 67 depicts the variation of surface morphologies of stainless steel after double-pulse irradiation versus interpulse delay ranging from 0 to 10 ps, for both polarization configurations (XP and CP). The

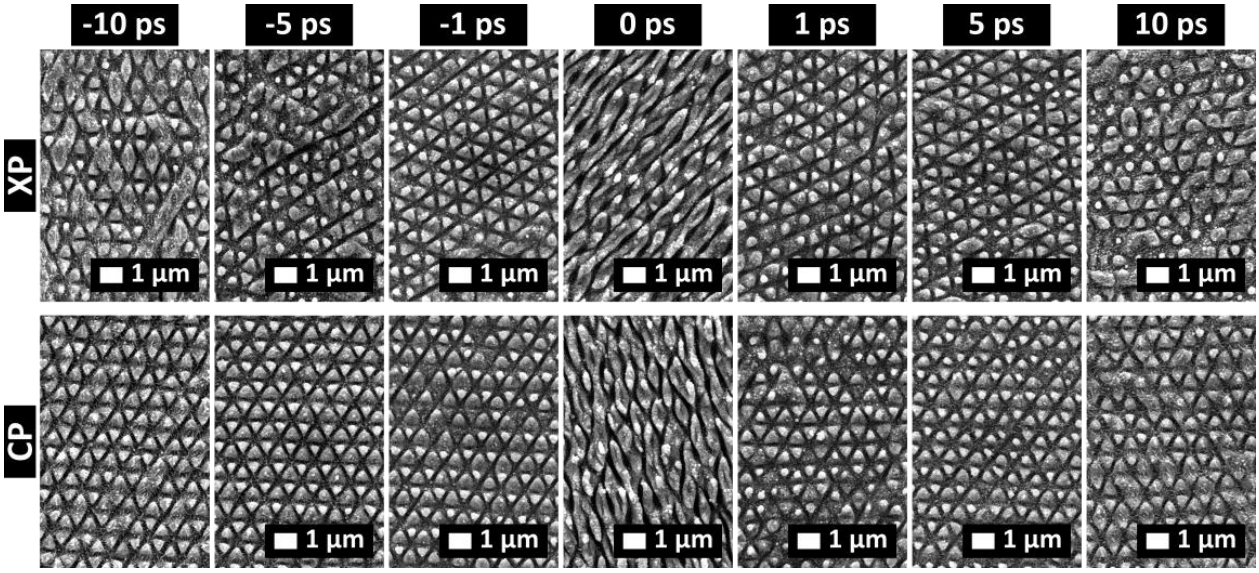

Figure 67 SEM images of stainless-steel surface irradiated with two different polarization configurations (XP and CP) as indicated[9]. The rest of process parameters were fixed; pps = 10 and H = 1 µm while the fluence was Φ = 0.1 J/cm^2.

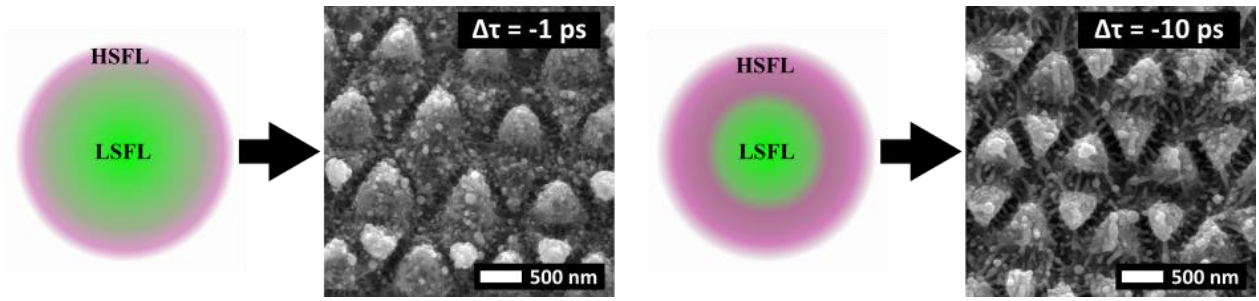

Figure 68 SEM images of stainless-steel showing the appearance of HSFL for CP configuration, $\Delta\tau$ = -1 ps and $\Delta\tau$ = -10 ps. pps = 10, H = 1 µm and Φ = 0.1 J/cm^2. Schematic representation of the ratio between the areas of HSFL and LSFL corresponding to the two delay values is shown as expected according to literature[94,118].

fluence was fixed to $\Phi = 0.1$ J/cm^2, the hatch to H = 1 μm and the linear overlap to pps = 10. The pulse from Arm A (vertically polarized) arrived first on the surface for positive delays, while the pulse from Arm B (horizontally polarized) arrived first on the surface for negative delays.

For both polarization configurations (XP and CP) the morphology varies in a symmetric way with respect to $\Delta\tau = 0$ ps as the $|\Delta\tau|$ increases. When $\Delta\tau = 0$ ps ripples were obtained for both XP and CP configuration. This is attributed to the fact that when the two linearly polarized pulses overlap, their electric fields interfere. Then, the polarization of the single generated pulse, varies from linear, elliptical, or circular polarization depending on the interpulse delay, if the latter is in the order of a femtosecond[108].

For XP configuration, homogeneous triangular structures were obtained for interpulse delays $\Delta\tau = \pm 1$ ps. As the interpulse delay increases (1ps $<|\Delta\tau|<$ 10 ps), the structures become progressively less homogeneous. Finally, for $\Delta\tau = \pm 10$ ps the triangular structures are barely present on the surface. For CP configuration, a similar trend is observed. Indeed, homogeneous triangular structures were obtained for $\Delta\tau = \pm 1$ ps and $\Delta\tau = \pm 5$ ps. For increasing delay, the structures become less homogeneous ($\Delta\tau = \pm 10$ ps) similarly to XP configuration. Thus, the smaller the delay, the more homogenous the triangular structures are for both XP and CP configuration.

A high correlation is observed here between the maximum $\Delta\tau$, during which the structures appear homogeneously on the surface, and the time we expect that structural effects take place on the surface[60,85] (see also §2.1.2). In both XP and CP configuration, the structures obtained with $|\Delta\tau| = 10$ ps are less homogeneous than those obtained with $|\Delta\tau| < 10$ ps. It is worth mentioning that the structures obtained with 0.1 ps $< |\Delta\tau| <$ 1 ps are quite similar to those obtained with $\Delta\tau = \pm 1$ ps and are not shown here. As described in literature the lattice thermalization occurs in metals after a few picoseconds[64] initiating the lattice decomposition after a few tens of picoseconds[71]. As $\Delta\tau$ increases the lattice expansion starts and melting occurs[71]. The coupling of the second pulse with the surface is expected to be severely influenced by the surface transformation and the periodically inhomogeneous energy distribution[96,141,142] will be disturbed entailing the less homogeneous structure formation.

Depending on the delay high spatial frequency LIPSS (HSFL) on top and in between the 2D-LIPSS are observed[9]. Figure 68 shows two SEM images of the nanostructures obtained with two different delays, $\Delta\tau = -1$ ps and $\Delta\tau = -10$ ps. In the case of $\Delta\tau = -10$ ps HSFL are prominent on the surface while for $\Delta\tau = -1$ ps are barely visible. The HSFL appearance is linked to a fluence threshold; when Ti is processed with linear polarized femtosecond pulses with fluence values below the ripple formation threshold, high spatial frequency HSFL can be obtained oriented parallel to the laser polarization[53]. Experiments with double femtosecond pulses in metals showed that an increase of the interpulse delay up to $\Delta\tau = 5$ ps entails a reduction of the LIPSS area coinciding with an increase of the HSFL area of the irradiated spot[118]. Similarly, a reduction of the LSFL area is observed in silicon ascribing this phenomenon in the surface to a plasmon polariton active area determined by electron relaxation processes[94]. Therefore, a delay increase will entail the decrease of the area where the threshold for LSFL is exceeded. A scheme of the expected type of formation, HSFL and LSFL induced upon irradiation are shown in Figure 68 for two $\Delta\tau$ values. In our case, for a moving beam, during the surface scanning, the different areas will overlap, and a mixture of LSFL and HSFL is expected for interpulse delays bigger than a few ps. In this way, the hierarchical morphology of the 2D-LIPSS can be tailored by the choice of the interpulse delay.

As the delay increases to $\Delta\tau = 20$ ps, the exclusive generation of HSFL was observed (Figure 69)[10]. In this case, the irradiation fluence was $\Phi = 0.1$ J/cm^2 and H = 1 μm. The HSFL morphology evolves upon increasing pulse overlap. Figure 69 (top) illustrates the obtained morphology versus the pps value. For low pps values, when pps = 5, random HSFL were obtained. When pps = 10, nano dots start to appear on the

surface in sizes similar to the HSFL ripple width. For further increase, HSFL are diminishing compared to nanodots (pps = 20) and vanish completely for pps = 50. When pps = 50, the surface is almost solely covered with nanodots. Compared to the structures obtained for single pulse irradiation[53], the HSFL obtained with double-pulse irradiation do not have a clear preferential axis. Moreover, the observation that high frequency ripples can evolve upon an increase of pps is reported here for the first time to our knowledge[10].

A Fourier analysis of the SEM image of Figure 69 with $\Phi = 0.1$ J/cm^2, $\Delta\tau = 20$ ps, H = 1 μm and pps = 5 gives an average spatial period between the HSFL $T_{average} = 284 \pm 8$ nm. No preferred axis of symmetry can be identified in that case. Strikingly, for pps = 50 the obtained morphology is similar to the morphology of the structuring found on the dragonfly (Rhyothemis phyllis chloe) wing membrane as shown in[143]. Grain analysis distribution over 321 grains for the case of $\Phi = 0.1$ J/cm^2, $\Delta\tau = 20$ ps, H = 1 μm and pps = 50, gives an average grain diameter $\delta_{average} = 146 \pm 50$ nm.

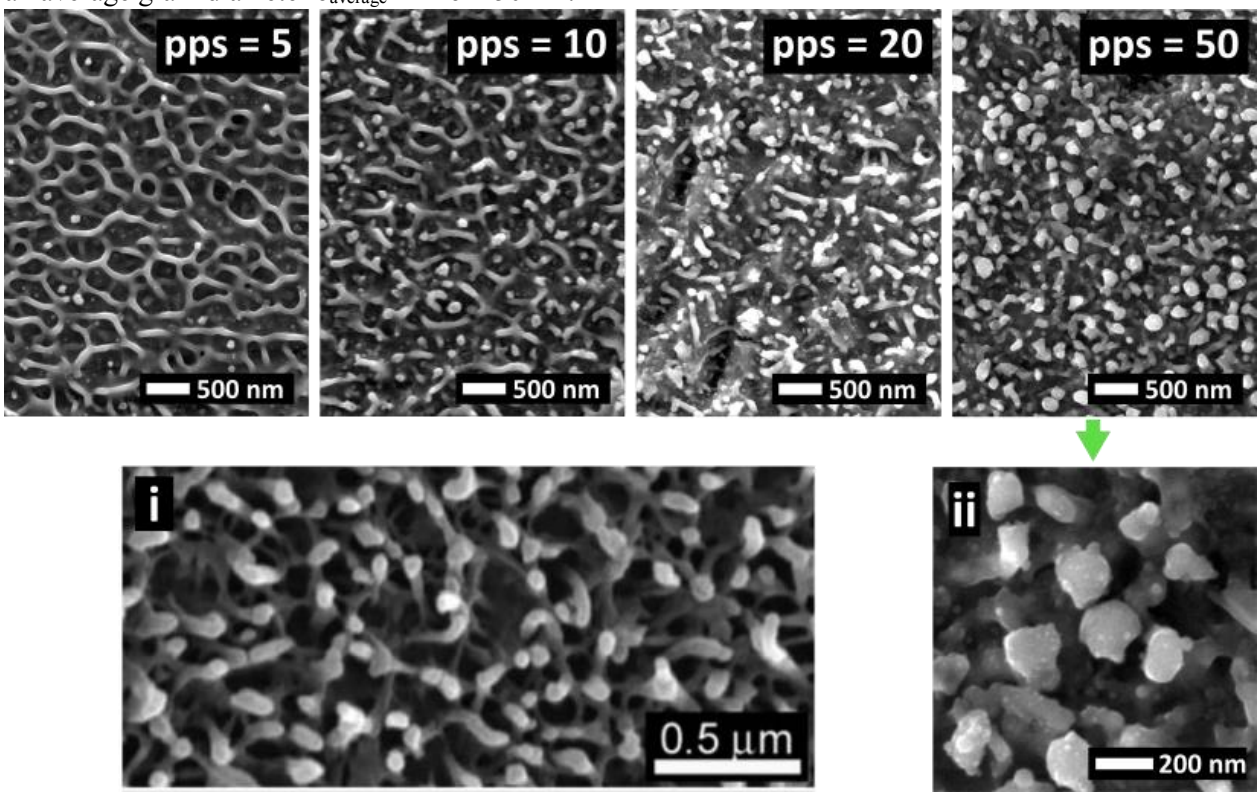

Figure 69 SEM images of stainless-steel showing the nanostructure obtained with CP pulses and variable pps as indicated. $\Phi = 0.1$ J/cm^2, $\Delta\tau = 20$ ps and H = 1 μm. Bottom: i: SEM image of Rhyothemis phyllis chloe wing taken from ref. [143] ii: SEM image of the structures obtained for pps = 50 under high magnification[10].

4.2.1.2. Double-pulses produced by birefringent crystals (BC)

Here, we demonstrate the generation of 2D laser induced periodic surface structures on stainless steel upon irradiation with double- and multi-pulses of fs duration utilizing a simple array of birefringent crystals (BC). That way the scalability of the process is assured by using a robust and easy to handle experimental set-up based on a high-power, high repetition rate, femtosecond laser source (details in §3.8). We considered interpulse delay values in the range between 0 ps and 12 ps, and we define the process window in terms of delay and dose for achieving an optimum 2D surface structuring concerning spatial period homogeneity. The process parameters utilized are summarized in Table 4. The obtained structures (size ≈ 900 nm) were characterized via SEM and their height was measured via atomic force microscopy (approximately 310 nm). A topographical study of the surface with an evaluation of the structure symmetry and homogeneity was

accomplished via Fourier Transform Analysis. Lastly, we utilized the setup for demonstrating the importance of single pulse fluence in generating LIPSS.

Table 4 Parameters used for double pulse irradiation with birefringent crystals

Parameter[x]	Considered Values
Fluence[xi], Φ [J/cm^2]	0.1, 0.2, 0.4,
Overlap, [pps]	5, 10, 20
Hatch, H [μm]	1, 2, 5, 10
Crystal delays [ps]	1.5, 3, 6, 12, 24

4.2.1.3. Double CP pulses produced by BC

As discussed in §2.1.1 and 4.2.1.1, within the first picosecond after irradiation with the first pulse the surface undergoes rapid transformation [59,75]. Electron relaxation, realized approximately in $\tau \sim 1$ ps and lattice thermalization[64] are the underlying mechanisms that lead to a modification of the surface temperature and state. Irradiation with a second pulse, having $\Delta\tau$ in that timescale will impact the structure formation[110,115]. $\Delta\tau$ is considered the key parameter since it defines the state of the surface upon the arrival of the second pulse. Lastly, pulse fluence[117] and polarization state[108] have been found to have a strong impact on the induced morphology under double-pulse irradiation.

Here we demonstrate the effect of the delay and the polarization for discrete values of $\Delta\tau$ and for CP and XP pulses. In Figure 70 the surface structure morphologies obtained in the case of CP are shown, for Φ_{low} and Φ_{high} versus $\Delta\tau$. Starting from Φ_{low} (upper row) and SP (i.e. single pulse) we observe the formation of triangular structures with a relatively low uniformity. For 1.5 ps $\leq \Delta\tau \leq$ 3 ps, the uniformity level increases and periodic structures are observed. By further increasing $\Delta\tau$ ($6 \leq \Delta\tau \leq 12$), high spatial frequency LIPSS (HSFL) appear showing a period of a few hundreds of nanometres and following the crystal lattice

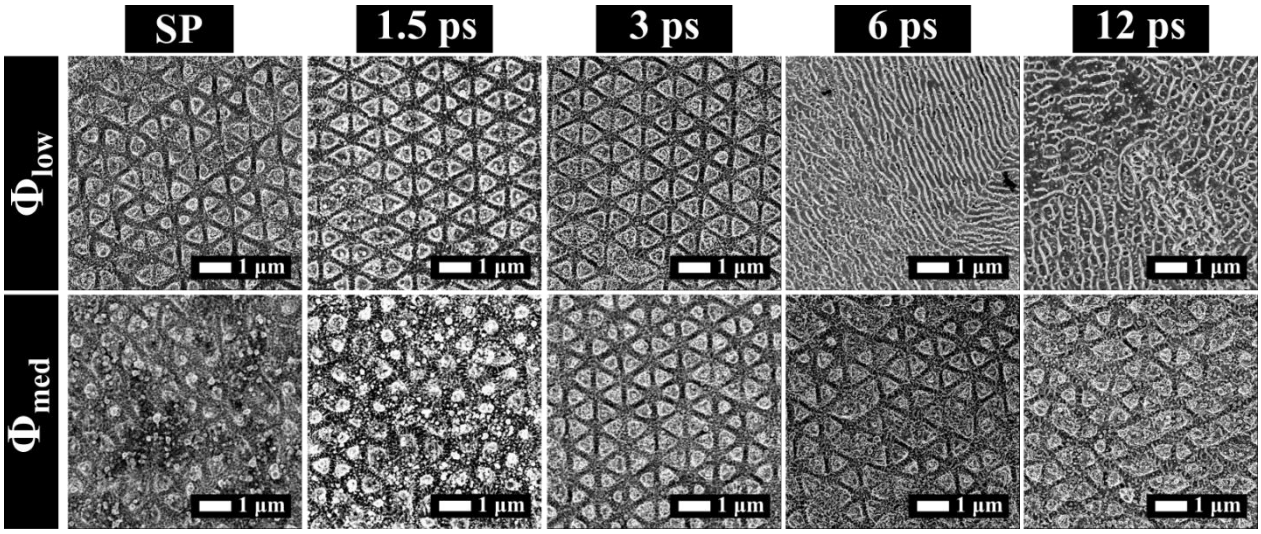

Figure 70 SEM images of stainless-steel surface processed with double, counter rotating, circularly polarized (CP) pulses for different inter-pulse delay values. Two different fluences were utilized Φ_{low} = 0.1 J/cm^2 (up) and Φ_{high} = 0.2 J/cm^2 (bottom). We fixed pps = 20 and H = 2 μm. SP signifies the single pulse irradiation.

[x] The surface was scanned once (N = 1) except §4.2.1.6.
[xi] The fluence value corresponds to the pair of double pulses.

orientation[144]. A decrease of the low spatial frequency LIPSS (LSFL) area, followed by an increase of the HSFL area was observed upon increasing $\Delta\tau$ in metals for $\Delta\tau < 5$ ps and linear polarization[118]. Here we extend the interpulse delay window up to $\Delta\tau$ =12 ps and we observe that for $\Delta\tau$ = 6 ps and $\Delta\tau$ =12 ps, Φ_{low}, only HSFL were observed for double CP pulse irradiation.

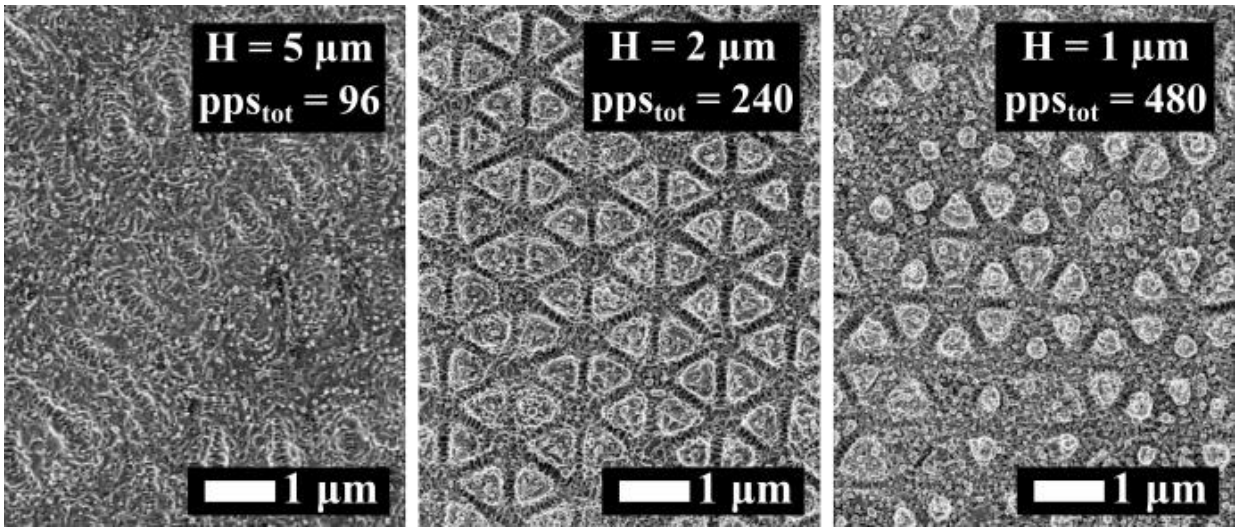

Figure 71 SEM images of stainless-steel surface irradiated with different dose as indicated. $\Phi = \Phi_{low}$ = 0.1 J/cm^2, pps = 20 and $\Delta\tau$ = 3 ps.

Passing to Φ_{high}, for SP and $\Delta\tau$ = 1.5 ps, barely regular 2D structures are formed. The structures obtain a triangular shape when 3 ps $\leq \Delta\tau \leq$ 12 ps. These results not only confirm the important role that the time delay plays in determining the final structure morphology, but also point out the interplay between the fluence value and $\Delta\tau$ in the 2D-LIPSS formation. In fact, for Φ_{low} triangular structures appear in correspondence of $\Delta\tau$ values (1.5 ps $\leq \Delta\tau \leq$ 3 ps) which are lower than for Φ_{high} (3 ps $\leq \Delta\tau \leq$ 12 ps).

An optimum number of pulses is necessary to achieve homogeneous structure formation. In Figure 71 we show the surface evolution upon a variation of pps$_{tot}$ when $\Phi = \Phi_{low}$, pps = 20 and $\Delta\tau$ = 3 ps. For pps$_{tot}$ = 96 the surface morphology consists of HSFL randomly oriented along the surface and locally organized in a periodic way. For pps$_{tot}$ = 240 prominent well defined periodic 2D-LIPSS were produced, whereas for pps$_{tot}$ = 480 the surface structures lose their homogeneity. Our results, which are in line with the case of single pulses[43], point out that triangular structure formation occurs for an optimum pps$_{tot}$ value.

The interplay between the Φ and $\Delta\tau$ can be elucidated in this context. The effective value of pps$_{tot}$, which determines the evolution of the structures, is expected to vary with respect to Φ and $\Delta\tau$ since both affect the LIPSS textured area. An increase of $\Delta\tau$ will significantly reduce the effective value of number of pps$_{tot}$ as the delay increases[9,94,118], preventing the 2D-LIPSS formation for Φ_{low} and 6 $\leq \Delta\tau \leq$ 12. That way a higher Φ value means a larger LIPSS textured area whilst longer $\Delta\tau$ means a smaller textured area[53].

4.2.1.4. Double XP pulses produced by BC

Figure 72 shows the structure morphologies obtained under the same experimental conditions than in Figure 70 except the pulse polarization state, which are here XP. In all cases, sub-wavelength structures are observed. For SP and both Φ_{low} and Φ_{high} ripples are obtained. In the specific case of Φ_{low}, 2D, barely uniform, triangular structures are generated when 1.5 ps $\leq \Delta\tau \leq$ 6 ps. Structures become 1D for $\Delta\tau$ = 12 ps. Also, for Φ_{high} and 1.5 ps $\leq \Delta\tau \leq$ 6 ps 2D, barely uniform structures are generated with a shape evolving from squared ($\Delta\tau$ = 1.5 ps) to quite circular ($\Delta\tau$ = 3 ps) and finally triangular ($\Delta\tau$ = 6 ps). As well as in the case of Φ_{low}, also for Φ_{high} structures tend to 1-D for $\Delta\tau$ = 12 ps. By comparing Figure 70 and Figure 72 a remarkable difference between CP and XP pulses is observed, not only for the resulting morphology

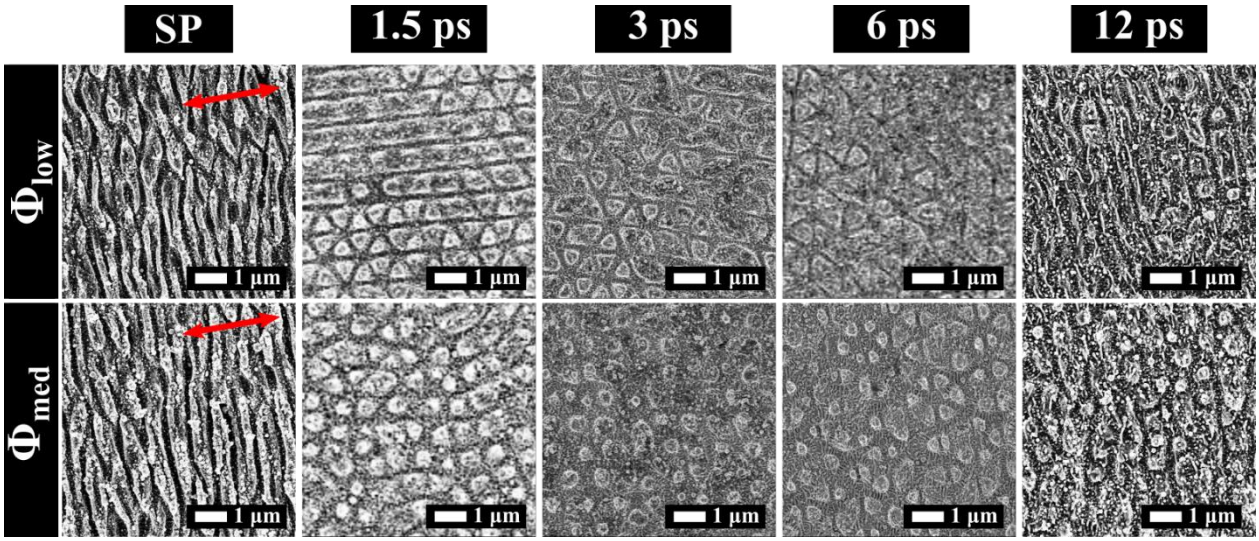

Figure 72 SEM images of stainless-steel surface processed with double cross-polarized (XP) pulses for different inter-pulse delay values. Two different fluences were utilized Φ_{low} = 0.1 J/cm^2 (up) and Φ_{high} = 0.2 J/cm^2 (bottom). We fixed pps = 20 and H = 2 µm. SP signifies the single pulse irradiation.

structures but also for their uniformity. For example, when $\Delta\tau$ = 1.5 ps and Φ_{low} triangular structures were obtained for CP pulses while for XP pulses the surface is covered by a combination of ripples and triangular structures. When $\Delta\tau$ = 12 ps and Φ_{low} we obtained ripples for double XP pulses and HSFL for CP pulses.

4.2.1.5. Structure optimization for double-pulses produced by BC

Interestingly, for both polarization configurations, homogenous structures were obtained for $\Delta\tau$ < 3 ps. Strong indications[59,60] point out that for $\Delta\tau$ < ~ 3 ps structural effects expected as a result of the first pulse

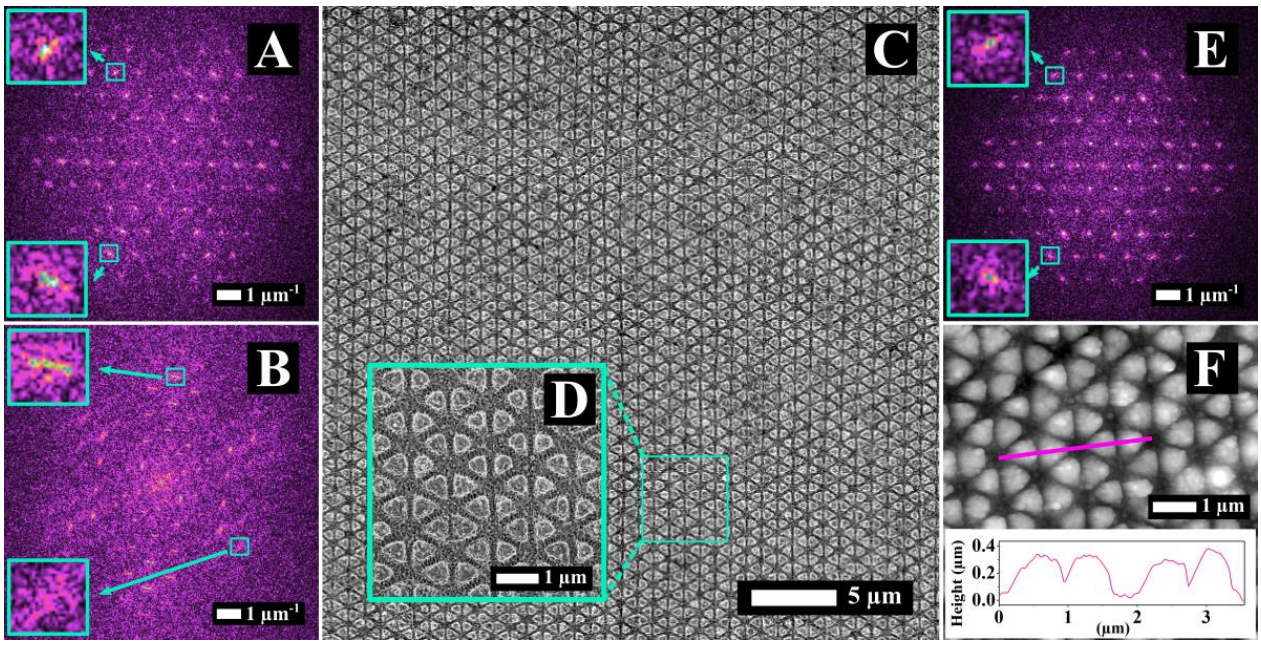

Figure 73. A: 2D-F-T of SEM image relative to double CP pulses (see, Figure 70, $\Delta\tau$ = 3 ps, pps = 20 H = 2 µm). B: 2D-FT of SEM image relative to XP pulses (see Figure 72, 0.1 J/cm^2 $\Delta\tau$ = 3 ps, pps = 20 H = 2 µm). C and D: SEM images of stainless-steel surface textured with 2D structures after irradiation with double XP pulses (Figure 70, $\Delta\tau$ = 3 ps, pps = 10 H = 1 µm) are shown with two different magnifications. E: 2D-FT of C. F: Profile of C structures obtained by AFM analysis carried out along the magenta segment.

are not yet taking place on the surface, when the thermal relaxation time of the lattice is completed[64]. That entails that during the impact of the second pulse the surface has a lattice structure. Consequently, both of the pulses are absorbed before surface structuring occurs when homogenous structures were obtained. Furthermore, the results obtained with birefringent crystals are in line with the obtained results discussed in §4.2.1.1. However, in the specific case of $\Delta\tau$ = 3 ps and Φ_{low}, similar structures arise for both CP and XP polarization states. Differently from CP pulses, results from XP pulses are barely uniform and inhomogeneous. A straightforward confirmation obtained by comparing the F-T analysis of the two cases reported in Figure 73. A and B, respectively, for CP and XP pulses. In the first case (CP), peaks are symmetric and sharp meaning that the structures are homogeneous, with a well-defined period along some specific directions. In the second case (XP), peaks are blurry (see magnification bottom-left), poorly contrasted with respect to the background, signifying the inhomogeneity of the structures.

In order to optimize the latter morphology, we varied pps (we chose pps = 2, 5, 10, 20, 50) and H (from H = 1, 2, 5, 10, 20 μm) in this series of experiments. Figure 73, D shows the SEM image relative to the process parameters of pps = 10 and H = 1 μm processed with XP pulses which enable an optimum condition. In this case well defined and homogeneous triangular structures appear. Furthermore, we extended the process over a surface which is much larger than the spot size as shown in Figure 73, C. F-T analysis reported in Figure 73, E reveals a distribution of spatially well-defined peaks with high contrast with respect to the background. This confirms the regularity of the surface morphology with high order level over a large area. From the F-T graph we extract an average structure size of 917 ± 9 nm. We also carried out the analysis of the structure profiles via AFM. In particular, we extracted the profile along the magenta segment shown in Figure 73, F. The structures have an approximately squared profile and the average height (measured for 10 random structures) was found to be 313 ± 46 nm.

4.2.1.6. Nanostructures produced with bursts of pulses

Among the benefits of the birefringent crystal setup is that the crystals can be combined for generating bursts of pulses[131,132]. One of the recently reported applications for such bursts is the increase of ablation efficiency[145]. Here this setup is employed for demonstrating the possibility to induce novel structures on stainless-steel surface. Figure 74 shows SEM images of stainless-steel surface after irradiation with bursts of n = 32 sub-pulses with fluence, hatch and polarization state as indicated. The surface was scanned five times (N = 5). We vary the hatch to vary the effective number of pulses on the surface.

Figure 74, A illustrates the morphology for low dose (H = 10 μm). Rippled structures, with period in the range of 1 μm and oriented randomly, were obtained in this case. In the inserted image of higher magnification (Figure 74, i), HSFL are visible perpendicular to the ripples with longer period. Upon an increase of dose, when H = 1 μm, the surface morphology consists of protrusions of a few micrometres fully covered with HSFL oriented randomly and together consisting a hierarchical morphology.

For a low fluence value (Φ_{burst} = 0.1 J/cm^2), employing the same parameters for irradiation (n = 32 and N = 5) solely nanometric scale features were obtained (Figure 74, C). The structures in Figure 74, C, resemble the HSFL dots obtained for $\Delta\tau$ = 20 ps[10]. Furthermore, the polarization does not seem to affect the overall process; the same hierarchical morphology as in Figure 74, C, was obtained for the same process parameters for XP pulse configuration and is shown in Figure 74, D. Furthermore, the absence of the micrometric scale

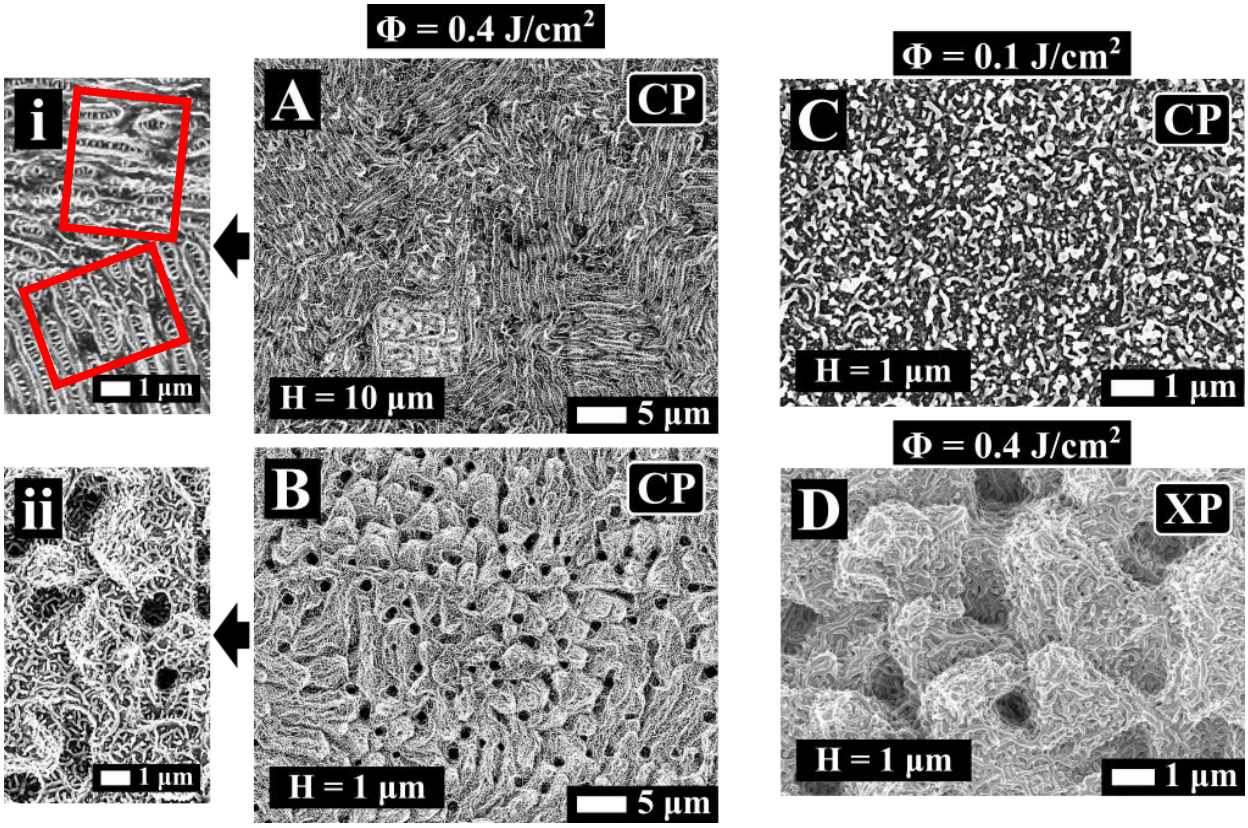

Figure 74 SEM images of stainless-steel processed with bursts of n = 32 sub pulses with $\Delta\tau$ = 1.5 ps. Scanning parameters were: overlap, pps = 20 number of scans, N_s = 5. Fluence and hatch are indicated.

features when Φ_{burst} = 0.1 J/cm^2 (Figure 74, C) points out that their formation only occurs above a certain fluence threshold.

It is proposed that ripple formation derives from inhomogeneous absorption of light during surface irradiation[58,69,95], this process depends strongly on the irradiation amplitude. The inhomogeneously absorbed light drives a microfluidic movement[27]. For single pulse irradiation within the range discussed here (Φ = 0.1 - 0.4 J/cm^2) both the amplitude of the inhomogeneous absorption and the dissipated heat are suitable for generating LIPSS[64].

Yet, those conditions are not matched in the case of burst irradiation. Considering that each pulse of the burst has $\Phi_{1/32}$ = 0.003 J/cm^2 in case of Φ_{burst} = 0.1 J/cm^2 and $\Phi_{1/32}$ = 0.013 J/cm^2 in case of Φ_{burst} = 0.4 J/cm^2, each pulse fluence is below the damage threshold of the surface and way below the ripple formation threshold[53]. Thus, the inhomogeneous absorption irradiation cannot enable the ripple formation. In contrary, the total fluence of the burst is way above the melting threshold of the material. It has been shown that for n = 32 bursts and $\Delta\tau$ = 1.5 ps the melting threshold fluence value is lowered compared to the case of single pulse irradiation[145]. Moreover, higher fluence melts a deeper surface layer[71] and for that a thicker melted layer is expected for Figure 74, B where Φ = 0.4 J/cm^2 than in C where Φ = 0.1 J/cm^2. Therefore, it is assumed that the underlying formation mechanism for the peculiar micro-structures obtained with CP (Figure 74, B) and XP (Figure 74, D) bursts lies in the microfluidic motion of the melted surface.

Interestingly, rippled structures shown in Figure 74, A and under high magnification in Figure 74, i, are oriented randomly in between adjacent regions (see red frames in Figure 74, i). The same behaviour was

observed for the generation of HSFL in our experiments (Figure 70, $\Delta\tau$ = 12 ps and Φ_{burst} = 0.1 J/cm^2) and reported for nickel that HSFL follow the lattice orientation[144]. It seems that for low fluence values the crystal orientation plays a key role in the interaction between the incident pulse and the surface.

4.2.1.7. Double-pulses in nanosecond regime produced by DL

A few tens of picoseconds after the irradiation of the first pulse, the electron relaxation and the lattice thermalization are completed (§2.1.1). Afterwards, the surface top layer (~ 40 nm) is considered melted and structural effects take place. Depending on the fluence, surface ablation occurs, and the remaining melted part grows in depth[71,73]. Due to temperature gradients induced by the inhomogeneous laser absorption along the surface, the molten layer is subjected to microfluidic motions (t > 0.1 ns)[38,46]. Finally, solidification occurs within a few nanoseconds depending on the pulse fluence[59–61,71,73] (see also §2.1.2). In that case, structure formation will be ongoing (§2.2).

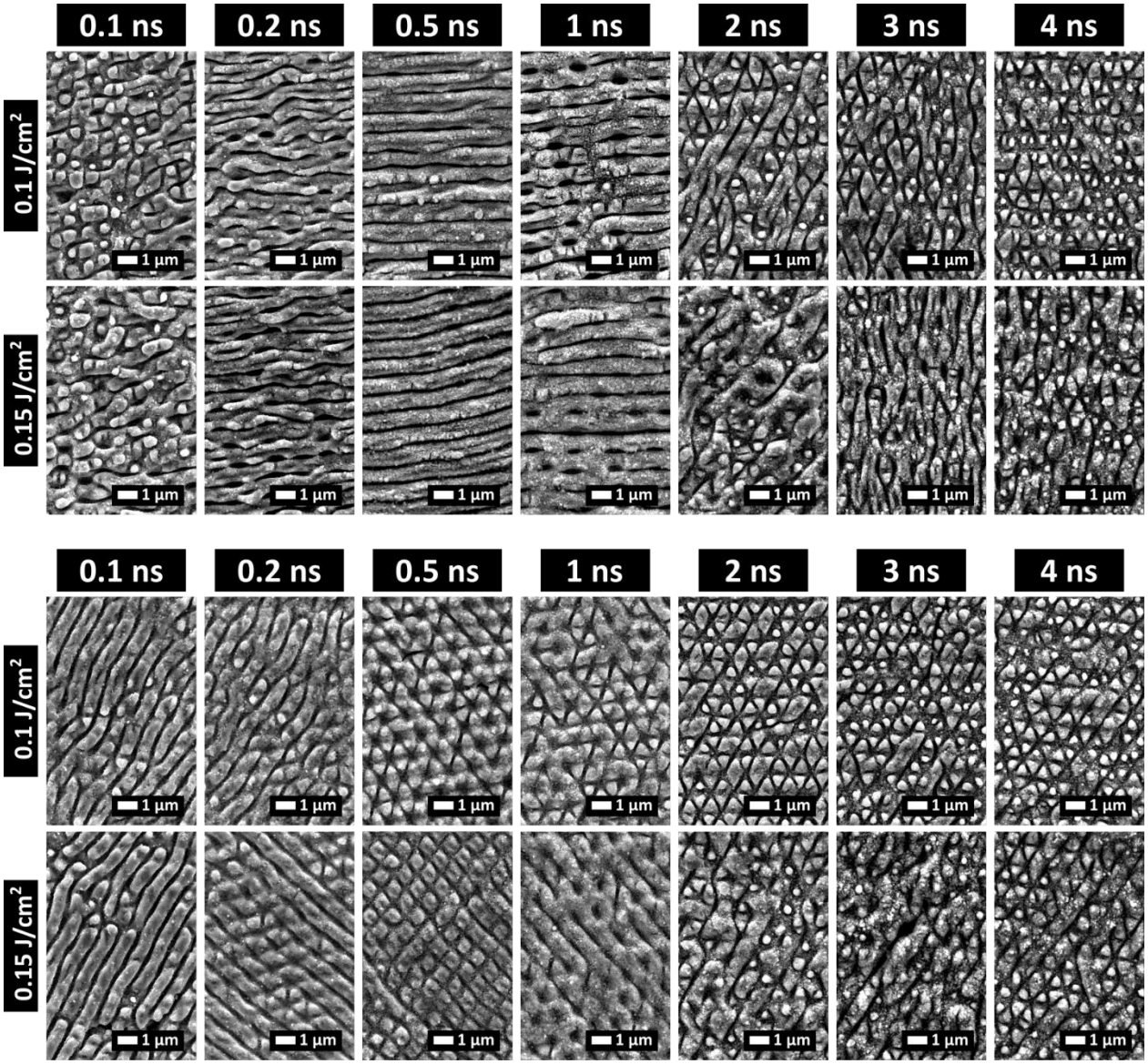

Figure 75 SEM images of stainless-steel surface irradiated with double-pulses for two different polarization configurations, XP (top) and CP (bottom). Interpulse delay and fluence were varied as indicated. The beam positioning parameters were fixed to pps = 10 and H = 1 µm.

Irradiating with a second pulse during that timescale will severely impact the conditions that determine the microfluidic movement; the surface temperature gradient will be modified[27], the depth of the melted layer will increase[71], and an extension of the time that the surface remains melted is expected. During the interaction expected changes in reflectivity[66] will affect the coupling of the pulse to the surface. Moreover, the absence of the lattice structure will impact the electron relaxation and material thermalization. Figure 75 illustrates SEM images of stainless steel surface after irradiation with double XP (Figure 75 top) and CP pulses (Figure 75 bottom) and with interpulse delays of 100 ps < $\Delta\tau$ < 4 ns as indicated[9]. The structures obtained for H = 1μm, pps = 10, and two different fluence value (Φ = 0.1 J/cm^2 and Φ = 0.15 J/cm^2) are shown. The laser induced surface morphologies vary with the interpulse delay for both fluence values and polarization configurations (XP and CP).

For XP configuration, no homogeneous structures were obtained at Φ = 0.1 J/cm^2 and $\Delta\tau$ = 0.1 ns. For increasing interpulse delays up to $\Delta\tau$ = 0.1 ns a progressive appearance of ripples, which are perpendicular to the first pulse polarization, is observed. When the interpulse delay is $\Delta\tau$ = 0.5 ns, the ripples become long, regular and homogeneous. Surprisingly, there is no evidence of the irradiation of the second pulse in the symmetry of the structures. The same morphology was observed for different process parameters, for the same dose ($pps_{tot} \cdot \Phi$); Φ = 0.2 J/cm^2 pps = 5 and H = 1 μm[11]. For $\Delta\tau$ = 1 ns, the ripples become less homogeneous, and finally, when the delay increases furthermore (2 ns ≤ $\Delta\tau$ ≤ 4 ns), the ripple orientation changes and they are transformed into inhomogeneous triangular structures[9].

In the case of CP configuration, inhomogeneous diagonal grooves are formed at Φ = 0.1 J/cm^2 and $\Delta\tau$ = 0.1 ns or $\Delta\tau$ = 0.2 ns. When the interpulse delay $\Delta\tau$ = 0.5 ns, a superposition of round and triangular structures appears on the surface. The triangular structure becomes less prominent in favour of round structures for $\Delta\tau$ = 1 ns and reappear for $\Delta\tau$ = 2 ns. Further delay increases do not have a notable effect, and the morphologies obtained with 2 ns ≤ $\Delta\tau$ ≤ 4 ns are quite similar.

When Φ = 0.15 J/cm^2 and $\Delta\tau$ = 0.1 ns horizontal ripples are formed on the surface similarly to Φ = 0.1 J/cm^2. For $\Delta\tau$ = 0.2 ns, the ripples are rotated unexpectedly by 90 degrees with respect to the ripples obtained at $\Delta\tau$ = 0.1 ns. Strikingly, when $\Delta\tau$ = 0.5 ns and Φ = 0.15 J/cm^2, a novel 2D morphology is observed for the first time on stainless steel. It consists mainly of square structures. Lastly, for $\Delta\tau$ = 2 ns and $\Delta\tau$ = 3 ns, the morphology is completely chaotic, whilst for $\Delta\tau$ = 4 ns triangular structures reappear comparably with Φ = 0.1 J/cm^2.

Even though the structures obtained for CP pulses differ compared to XP pulses, similar trends in the transitions between the morphologies can be identified with respect to the delay[9]. Unclear or mixed structures are observed for $\Delta\tau$ = 0.1 ns and $\Delta\tau$ = 0.2 ns. Homogeneous structures were obtained for all fluence values and for both polarization configurations when $\Delta\tau$ = 0.5 ns. At that particular time, the maximum thickness of the molten layer is reached in Ni for similar fluence values[71]. We expect therefore that for $\Delta\tau$ = 0.5 ns, steel is melted and the irradiation with a second pulse will encounter a melted surface, extending significantly the duration of the melted phase of the material and the microfluidic motion. Finally, when $\Delta\tau$ ≥ 2 ns, inhomogeneous triangle formation reappears for Φ = 0.1 J/cm^2, independently of the polarization configuration, in a similar way as for small delays. At this timescale, the surface solidification occurs for low fluences (Φ = ~ 0.1 J/cm^2)[59–61,71,73,85]. Thus, irradiation with a second pulse occurs while the surface is in an equilibrated state and entails the reinitialization of the nanostructure formation process. For CP configuration, the polarization of the consecutive incident pulses does not differ in terms of symmetry, and therefore results similar to single pulse irradiation are expected in this case. On the contrary, for the XP configuration, the two perpendicular symmetry axes of the crossed polarized pulses alternate. This is equivalent to an irradiation with pulse trains, where the polarization rotates by 90 degrees during the pulse

train, and a non-uniform 2D morphology is expected in an analogy to what was obtain for crossed polarized pulses in a single spot[102]..

4.2.1.8. Surface evolution for increasing dose

The appearance of LIPSS on a material surface is usually a multi-pulse process. The surface morphology in the early stages of structure formation as well as the subsequent surface evolution can provide valuable information about the formation mechanism. When large areas are processed, the surface evolution can be analysed by comparing the morphologies obtained when varying the cumulative dose (pps_{tot}). Figure 76 , B & C, illustrates SEM images of stainless-steel surface under irradiation with double CP pulses upon variation of pps_{tot} as indicated. In Figure 76 , B the surface was processed with $\Delta\tau$ = -1 ps and Φ = 0.1 J/cm^2 giving rise to triangular formation and in C the surface processed with $\Delta\tau$ = 0.5 ns and Φ = 0.15 J/cm^2 was

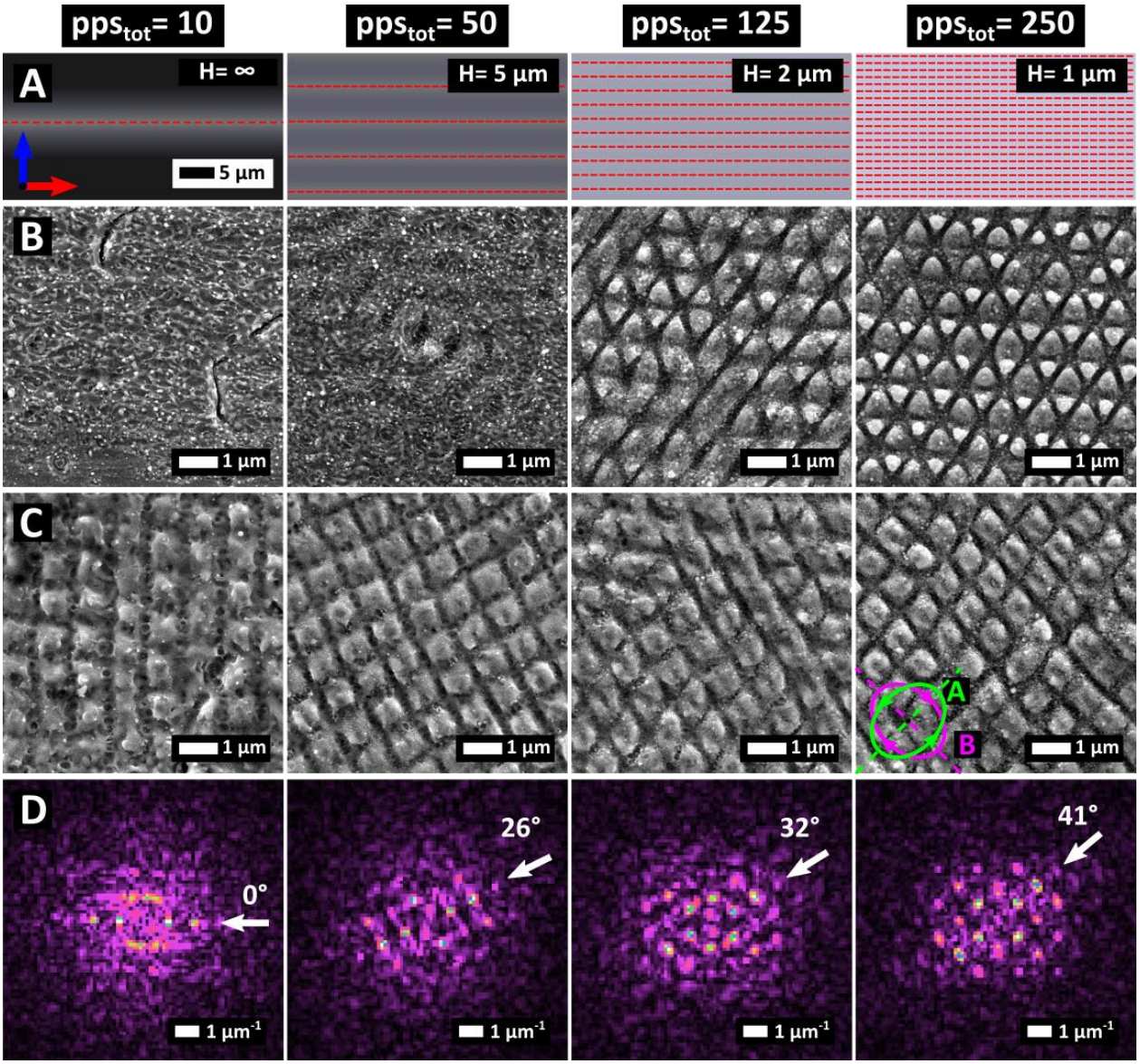

Figure 76 A: schematic representation of the irradiation. Red dotted lines represent the scanning line of the irradiation according to the H value. B & C: SEM of stainless-steel surface showing the structure evolution leading to triangular and square structures, respectively. D: Fourier transforms of images of square formation. The white arrow indicates the direction of the structure main symmetry axis[9].

covered with squared structures. The pps_{tot} value was modified by changing the hatch H, while the linear overlap was kept constant (pps = 10). We considered according to Equation 9 single line scans giving pps_{tot} = 10, a hatch with H = 5 µm giving pps_{tot} = 50, a hatch with H = 2 µm giving pps_{tot} = 125, and a hatch with H = 1 µm giving pps_{tot} = 250. The scanning direction is indicated by the red arrow, and the hatch direction by a blue arrow. Figure 76, A, shows a scheme of the irradiation process. The red dotted lines indicate the centre of the scanning line and the grayscale gives a qualitative indication of the depth of the groove formed after the irradiation. In Figure 76, D, the corresponding Fourier transformations of the SEM images of line C are shown.

In Figure 76, B we see the progressive evolution of the surface leading to homogeneous triangular formation at pps_{tot} = 250. For pps_{tot} = 10 the surface is covered exclusively with HSFL. For pps_{tot} = 50 a few undulations distributed in a random way are observed. For pps_{tot} = 125 the surface is covered by a mix of grooves and triangles. In contrary to pps_{tot} = 50, the structures are spatially coherent even though not homogeneous. Lastly for pps_{tot} = 250 the surface becomes homogeneously covered with triangles. The existence of HSFL in the first steps points towards the assumption that the fluence is lower than the LSFL threshold. Therefore, the triangular formation requires a feedback of the roughened surface as discussed in §2.2.1.1(Light interference and the efficacy factor).

In contrary to triangular structures, squared structures appear directly on the surface without the intermediate step of HSFL. Quite likely, for Φ = 0.15 J/cm^2 the LIPSS formation threshold is exceeded for a smaller number of pulses (pps_{tot} = 10). For pps_{tot} = 10 unclear square formation is observed on the surface. For increasing pps_{tot} values from pps_{tot} = 10 to pps_{tot} = 250 the squares become more prominent and well defined. Strikingly, the symmetry axis of the squares rotates progressively when the scanning lines come closer and the pps_{tot} value increases. A rough estimation of the angle becomes possible by analysing the F-T diagrams of the SEM images and a rotation of 41 degrees is derived. The symmetry axes of the structures in the last case (pps_{tot} = 250) coincide with the axes of the two polarization components of the roughly circular polarizations marked as “A” and “B” in the SEM image. The notable rotation between the initial and the final symmetry axis of the 2D-LIPSS contradicts the corresponding observations for 1D-LIPSS were the symmetry axis of the structures is firmly determined by the polarization orientation[146]. Even in the case where simulation results predicted the generation of 2D-LIPSS (crossed-LIPSS) the features are expected to be aligned with the polarization and affected by the surface morphology[97]. In our experiment, the polarization effect appears later on for the square morphology[9].

4.2.1.9. The plausible role of convection flow

A plausible explanation for the formation of 2D-LIPSS as well as for the long and homogeneous grooves[11] can be derived considering the microfluidic movement of the molten material after the irradiation. Different types of flow are possible to form in a liquid heated in an inhomogeneous way. Convection flow can occur when a layer of liquid or gas is subjected to strong temperature gradients. Convection flow is observed in the stars, in the currents of the ocean, in the earth’s atmosphere, and it is believed that it is the main cause of most of the tectonic processes in earth’s crust. Several types of convection flow have been predicted theoretically and observed experimentally. To name a few, roll flow, cross roll flow, hexagonal flow, the zigzag flow and others[147–151]. In Figure 77, column A, we show the scheme of the ideal flow states of rolls, hexagons and squares derived from theoretical analysis[150]. In column B of Figure 77, photographs of liquid layer subjected to the different types of convection flow are depicted as indicated[150,151]. The excitation conditions and the defects on the liquid surfaces determine the type of convection flow for each material[148–151]. Small symmetry perturbations may strongly favour the one or the other pattern formation[150].

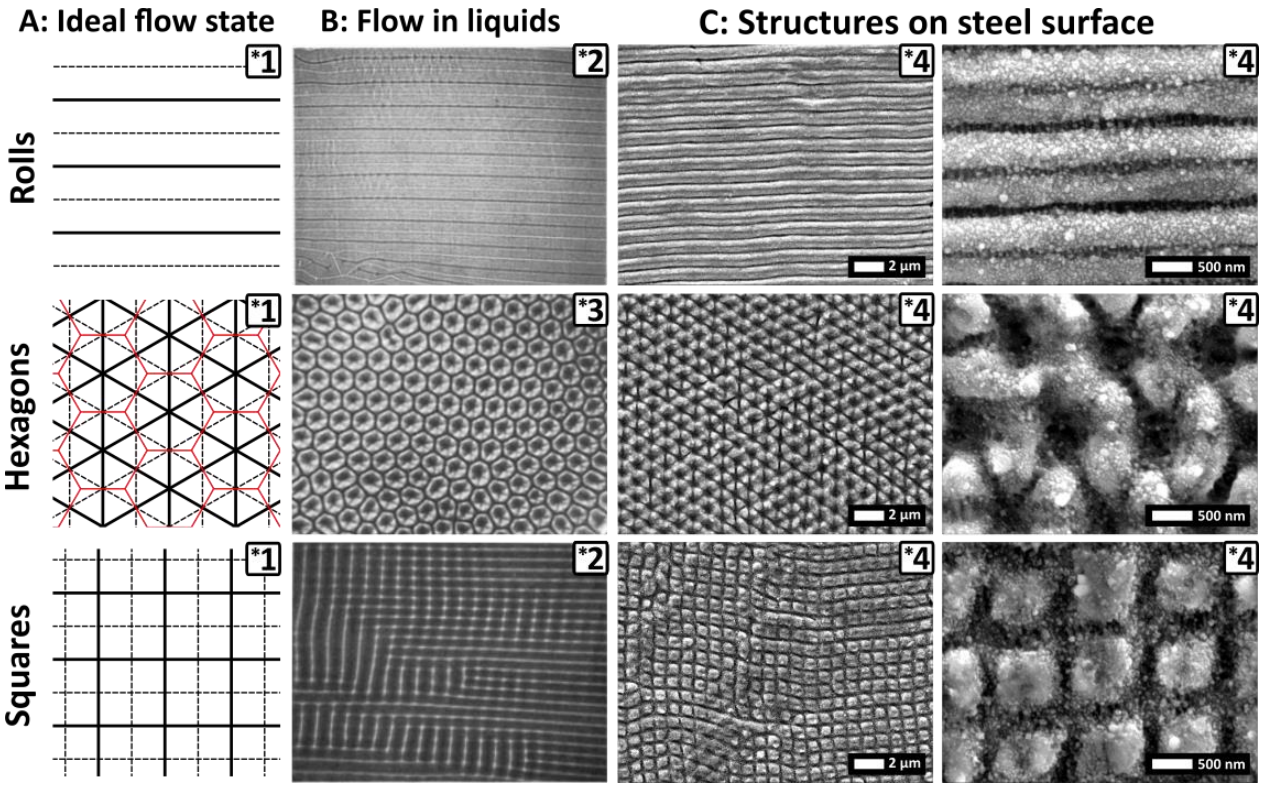

Figure 77 A: Convection flow schemes: solid lines indicate the fluid upflow and dotted lines the fluid downflow. B: Photographs of convection flow in liquids. C: SEM images of stainless-steel surface textured with double femtosecond pulses for $\Delta\tau$ = 0.5 ns, pps = 10 and H = 1 µm. Indication: *1: Based on; Cross, M. C., et al (1993)[150]. *2: Pictures reproduced from Busse, F. H. (1978)[151]; © 2018, IOP Publishing. *3: Picture reproduced from Koschmieder E.L. et al. (1974)[154]; © 2018, Elsevier. *4 Experimental data of stainless steel texturing (this work).

In some cases, after a temperature gradient is applied, different convection flow patterns alternate with time[149]. Recent publications linked the formation of grooves and spikes in silicon[46] and grooves in fused silica[152], and HSFL on metallic surfaces[153] to Marangoni convective roll flow. This particular type of convection flow is driven by temperature gradients along the surface of the material[152].

Some of the morphologies obtained under double-pulse irradiation for XP and CP pulses on stainless steel can be identified with convection flow patterns observed in liquids as shown in Figure 77. SEM images of structures obtained with $\Delta\tau$ = 0.5 ns when pps = 10 and H = 1 µm, are illustrated in Figure 77, C. Striking morphological similarities are observed by comparing the types of convection flow in liquids with the nanostructures formed on stainless steel surface. Long grooves were obtained for double XP pulses for Φ = 0.1 J/cm^2 (Figure 77, C top) similarly to previous results[11]. A hexagonal pattern was obtained for double CP pulses and Φ = 0.1 J/cm^2 (Figure 77 , C middle). Lastly, a pattern consisting of squares was obtained for double CP pulses and Φ = 0.1 J/cm^2 (Figure 77, C bottom). The fourth column shows a magnification for better comparison with the ideal theoretical schemes (column A).

As discussed in §2.1.2 (Thermal effects and resolidification), when $\Delta\tau$ = 0.5 ns a melted surface is assumed upon arrival of the second pulse affecting the microfluidic movement. In the case of long grooves (Figure 77, C top) we assume that the first pulse generates an inhomogeneous pattern[97] and double-pulse irradiation permits the development of convection roll flow. Furthermore, the alternation of deep and shallow grooves observable in the SEM image can be identified with the alternation of upflow and downflow in roll flow as shown in Figure 77 (column A, top). The observed shift from 1D to 2D LIPSS, when the polarization changes from linear to circular, can be ascribed to the different symmetries in the inhomogeneous absorption[97]. For circularly polarized pulses, we expect that the energy will be distributed without any linear

symmetry permitting the development of 2D flow on the surface since the flow is driven by surface temperature inhomogeneities.

Considering a convection flow, the triangular 2D-LIPSS formation for extremely different irradiation conditions can be understood[9]. The triangular structures were obtained with circularly polarized single pulses[43] and double XP and double CP pulses at delays of different order of magnitude ($\Delta\tau < 5$ ps as shown in Figure 67 or $\Delta\tau > 2$ ns as shown in Figure 75). Furthermore, the change of symmetry between squares and triangles, observed when the fluence increases from $\Phi = 0.1$ J/cm^2 to $\Phi = 0.15$ J/cm^2 (Figure 77, C) cannot be interpreted solely in the frame of the inhomogeneous light absorption since the polarization remains unchanged. On the other hand, in the case of convection flow, the development of stable patterns depends on the excitation conditions in liquids and specific threshold areas can be identified between patterns of different symetry[150,151]. In our results, a fluence variation will affect the melted layer thickness, the materials viscosity, the thermal conductivity, and the inhomogeneity in fluence allocation[142]. Therefore, assuming that a convection flow is developed under double-pulse irradiation, the pattern of the flow can be in principle determined by the fluence variation.

Furthermore, the rotation of the symmetry axis of the structures discussed in §4.2.1.8 can be ascribed to the boundary conditions during the scanning. When the scanning lines are far apart, the convection flow is aligned according to the boundaries of the melt pool, and therefore, are paralleled to the scanning direction. In convection flow, the boundaries of the liquid have a huge bearing on determining the pattern formation[151,154]. When H = 1 μm, the interval between the lines is much smaller than the width of the textured surface (~10 μm for the given conditions) and thus scanning does not produce a groove. It is assumed in this case that the structures are not affected anymore by the boundary conditions rather than by the excitation conditions and are aligned with the axes of the elliptical polarization.

Lastly, the type of convection flow should depend strongly on the material and same patterns are expected in materials other than steel for different excitation conditions. A characteristic example is the square morphology obtained in Tungsten after irradiation with double fs pulse with $\Delta\tau = 1.2$ ps and $\Phi = 0.2$ J/cm^2 [106]. Conclusively, synergistic contribution of the laser polarization and the induced convection flow is considered as the plausible explanation leading to 2D-LIPSS[9].

5. Conclusions

In this last chapter, our results presented in §4 are summarized in §5.1. In §5.2 the macroscopic properties of selected textures are presented. In §5.3 our conclusion is discussed

5.1. Summary of the results

For single pulse experiments elaborating on spike formation, a systematic variation of the structure diameter was observed as a result of a comprehensive study on the influence of key process parameters. The structure size was varied from $\delta = 8 \pm 2$ µm to $\delta = 59 \pm 15$ µm by varying the fluence value[7,8,10]. A similar trend is demonstrated for the overlap and the repetition rate. We assume that a combination of overlap, fluence and laser repetition rate regulates the amount of accumulated heat and we provide simulation data for the case of the fluence. Our hypothesis is that heat accumulation can regulate the microfluidic movement and therefore, impacts the spike size. Moreover, above a certain point heat accumulation has a detrimental effect on the laser structuring leading to destruction of the surface. To overcome this limitation, an upscaling strategy is proposed based on compensating the expected T_{sat} when f in increased. Employing this strategy, it is possible to reproduce the same morphology utilizing different combinations of pulse per spot, fluence and repetition rate. Moreover, it's possible to avoid thermal effects and scale up spike formation utilizing up to 10 MHz and average power in the order of 10 W. By these means, we ultimately achieved a processing rate for homogeneous spike fabrication of ~ 1 min/cm^2 almost 60 times faster compared to our starting point[122]. This was possible by putting together a high average power femtosecond laser and a polygon scanner head which can reach scanning speeds of 100 m/s. Quite recently, a processing rate in the order of 1 s/cm^2 was demonstrated for ripple and groove formation employing larger spot size and lower repetition rates[14]. Lastly for decorative generation of LIPSS a processing rate of 0.1 s/cm^2 was presented[13].

Reducing the laser induced feature size is necessary for developing specific applications. Since LIPSS can be controlled by the irradiation, a wavelength employing a fs laser in UV (λ = 257 nm) can generate structures in the nanoscale[12]. The generation of ripples, grooves and spikes with ultraviolet femtosecond pulses at 257 nm was demonstrated. We mention the fabrication of HSFL with $\Lambda_{HSFL} = 76 \pm 2$ nm, LSFL $\Lambda_{LSFL} = 153 \pm 4$ nm and $\Lambda_{groove} = 426 \pm 7$ nm[12]. Interestingly, in this case, referring to the low fluence regime ($\Phi = 0.1$ J/cm^2), the groove size was found to be much smaller than the grooves reported for other materials indicating that the wavelength can play a role in groove formation. In that case, a wavelength-dependent mechanism[54] is assumed rather than the microfluidic motion expected for higher fluences[46]. The sequence of structure appearance upon increasing dose was presented and a detailed description and interpretation of the transition between the different structures was provided. For higher doses on the surface we obtained ablated-like spikes while for higher fluence values spikes were not obtained. According to the formation mechanism this behaviour can be explained considering the intense ablation expected within the experimental conditions utilized.

Further control of the structures in the submicron scale can be achieved by means of double-pulse irradiation[9–11]. Double-pulse irradiation provides the possibility to dynamically control the structure formation. As an outcome of our experiments a variety of 2D-LIPSS was generated on stainless steel surface[9–11]. Utilizing a delay line, the interpulse delay could be varied in a continuous way. Homogeneous triangular 2D-LIPSS were obtained for interpulse delays ($\Delta\tau$) smaller than 5 ps, both for double linearly crossed polarized pulses (XP) and double counter-rotating circularly polarized pulses (CP) pulses[9]. Upon delay variation it was possible to produce simultaneous triangles with HSFL, only LSFL triangles or only 2D-HSFL[9]. The evolution of 2D-HSFL to nanodots is demonstrated[10].

Employing birefringent crystals for the generation of double-pulses produce similar results to the delay line for similar process windows. To this end, the possibility to utilize birefringent crystals to reproduce results

obtained with the delay line was demonstrated improving the technological readiness of the process. Furthermore, a uniform distribution of well-defined, sub-wavelength, triangular structures we obtained over a large area on stainless steel. By a fine-tuning of the main process parameters (inter-pulse delay, pps, fluence, hatch) we optimized the structure morphologies for two different polarization states, CP and XP proving that circular polarization is not necessary for the generation of triangular structures. Furthermore, an optimum process window in terms of pps_{tot} fluence and delay that leads to homogeneous surface texturing was defined.

For longer interpulse delay values homogeneous square 2D-LIPSS were obtained for $\Delta\tau$ = 0.5 ns for CP pulses[9]. Both morphologies were successfully applied simultaneously over large areas of radius ~ 10 mm with the use of an industrial femtosecond laser. The induced morphology varies with $\Delta\tau$ for values up to $\Delta\tau$ = 2 ns. The impact of the interpulse delay is elucidated and specific time delay zones were identified with respect to the laser induced structure morphology. Before structural effects start ($\Delta\tau$ < 1ps), during the molten phase of the surface ($\Delta\tau$ ~500 ps) and during the surface resolidification ($\Delta\tau$ > 2 ns). Furthermore, we investigated the impact of the polarization on the surface morphology, and a plausible explanation of 2D-LIPSS formation is proposed. Finally, the presented process is compatible with large area surface texturing and copes with the industrial standards, increasing the technological readiness level of the process.

5.2. Surface functionalities

Some of the obtained structures were applied over large areas and the macroscopic surface properties were evaluated. Among others we demonstrate that superhydrophilicity and blackening can be enabled by smaller structures than spikes. We showed that triangular structures can be fabricated upon irradiation in the MHz regime. Those results are mentioned in the following paragraphs

5.2.1. Blackening and decorative applications

Laser surface blackening[25] lies among the applications with the biggest industrial interest. The main goal is substituting ink-jet processes which are not stable against mechanical forces. In laser blackened surfaces the marking is a result of topographical change of the surface, therefore additive chemical compounds are not involved and the surface – in case of stainless steel- maintains its biocompatibility. Nevertheless, decreasing the laser blackening cycle time is of paramount importance. An optimum processing rate for permitting the introduction of this process in the production is in the order of a few seconds per cm^2 (information provided by BSH Electrodomésticos España). In order to tackle this issue, we carried out an extended experimental study for f = 1 MHz employing an industrial 350 fs laser (Amplitude, Satsuma). We consider the variation of hatch, fluence and overlap for a single scan process. Interestingly, surfaces with extremely low reflectivity were obtained, an example is shown in Figure 78. To increase the processing speed, we expand the laser beam having a spot diameter of 70 μm ($1/e^2$). The fluence was Φ = 0.5 J/cm^2 and the scanning speed 0.5

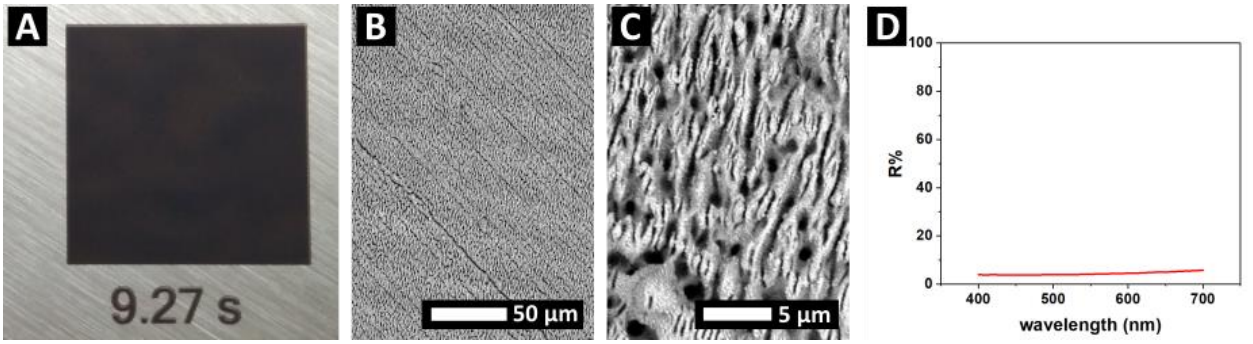

Figure 78 Surface blackening. A: Photograph of processed ferritic stainless-steel surface. B&C SEM images of processed part of A. D: reflectivity spectrum (R) of the processed surface shown in A.

m/s delivering an average of 140 pulses per surface spot. The surface was scanned once and the processing rate was ~ 9 s/cm^2.

Interestingly, the structures are not resulting from spiky or bumpy structures on the surface. The surface shown under different magnifications in Figure 78, B and C, consists mainly of ripples, grooves, holes and bumpy structures. Finally, the reflectivity (R) spectrum of the surface is shown in Figure 78, D. The reflectivity values in the visible (λ = 400 nm to λ = 700 nm) vary from R_{min} = 3.8 % for λ_{Rmin} = 450 nm to R_{max} = 5.8 % for λ_{Rmax} = 700 nm.

When ripples are applied over a large surface, they form a grating and they can generate an iridescence effect. Surface blackening was combined with ripple formation to create a decorative marking shown under different angles in Figure 79. Ripples produced by an industrial 350 fs laser (Amplitude, Satsuma) emitting at λ = 1030 nm in combination with a SHG module giving λ = 515 nm. The process parameters were varied to achieve homogeneous structuring of ripples with Λ = 452 nm.

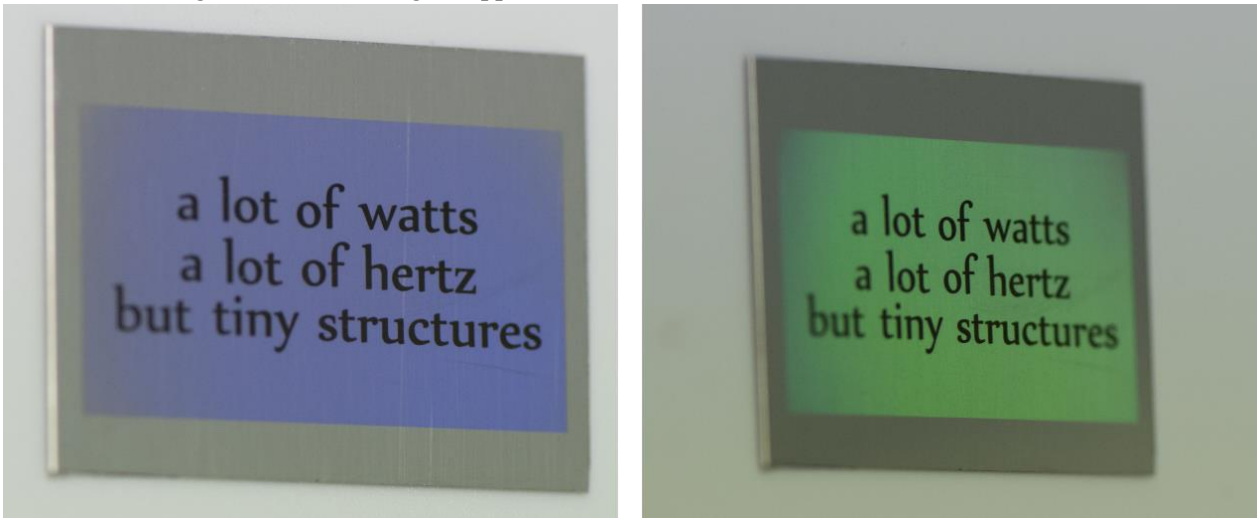

Figure 79 Decorative effect produced by combining LSFL generation and surface blackening on stainless-steel surface. The size of the textured area is 1 cm x 2 cm.

5.2.2. Subwavelength grating consisting of ripples

Periodic structures with one or two symmetry axes and periods smaller than the incident wavelength behave as subwavelength gratings[155]. Such subwavelength gratings have a variety of applications and can be utilized

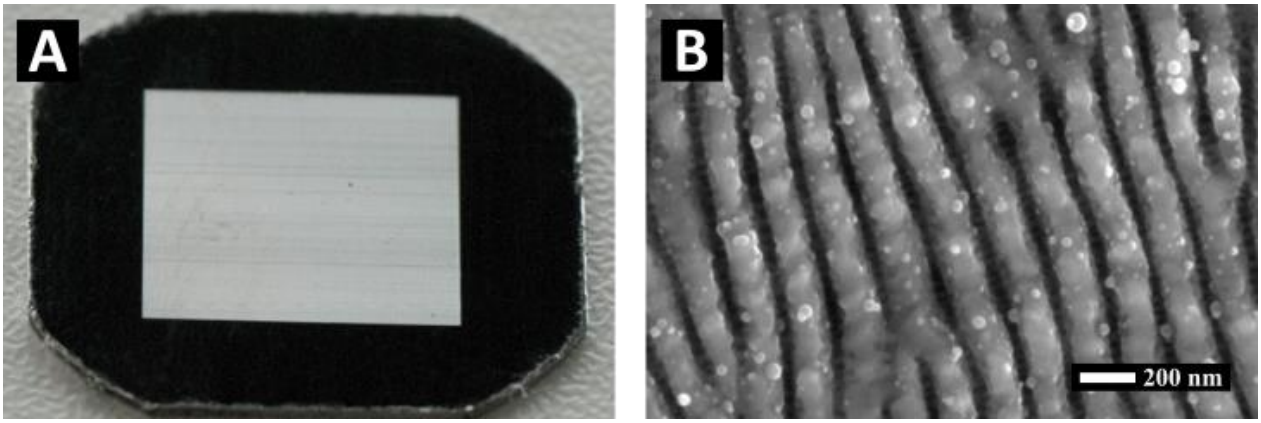

Figure 80 A: Visual appearance of a stainless-steel surface 1 cm^2 textured with ripples as shown in B. B: SEM image of stainless-steel surface rippled surface produced with trains of λ = 257 nm fs pulses..

as polarization converters [156], broadband mirrors [157], and in the case of two dimensional surface structures the surface obtains antireflection properties [158,159]. Nevertheless, the structures should have a period close to or smaller than a couple of hundreds of nanometres. So far it was not possible to produce LSFL at this scale. Utilizing a UV femtosecond laser with λ = 257 nm it was possible to fabricate a surface that behaves as a subwavelength grating for visible light[12]. That was possible by texturing homogeneously stainless steel over an area of a cm^2 with a ripple period in the order of Λ_{LSFL} = 150 nm (Figure 80, A). The particular, macroscopic visual appearance of the surface is shown in Figure 80, A, where all visible wavelengths are reflected at the same angle making the surface appearing white while the non-processed area appears black.

5.2.3. Superhydrophobic surface enabled by nano roughness

Employing the same UV laser (λ = 257 nm) we produced a superhydrophobic surface which results only of laser induced nano-roughness. Surface hydrophobicity or super hydrophobicity is another desired surface property that can be laser induced either by direct laser writing [25] or as a result of micro spike texturing[5]. It can be argued that wetting properties are an outcome of the combined effect of microstructure and nano-roughness as well as from changes in chemical composition of the surface[160]. Interestingly, it is shown that solely the nano-roughness structuration (Figure 81, B) exhibits by itself superhydrophobic behaviour and a contact angle of 154° was measured after processing (Figure 81, A)[12]. The structure was produced by irradiating the surface with Φ_{High}, N = 1 and pps = 1000 and was cleaned in an acetone ultrasonic bath for several minutes to remove dust.

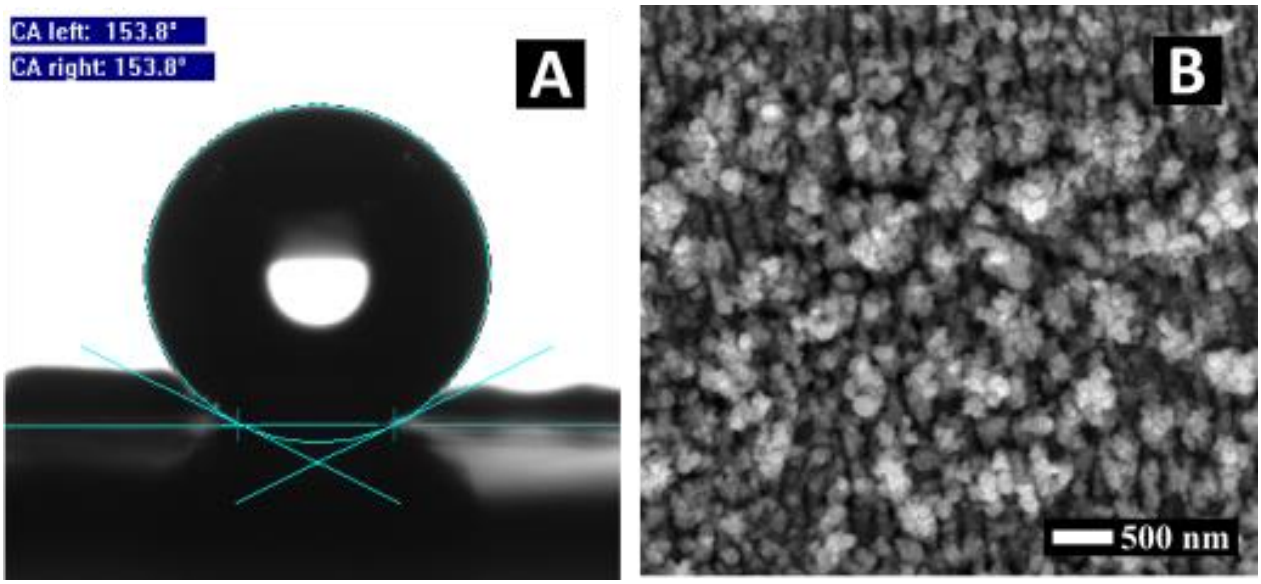

Figure 81 A: Contact angle measurement of a superhydrophobic 5 mm x 5 mm stainless-steel surface with nano-roughness texture. B: SEM image of surface processed with Φ_{High} = 0.42 J/cm^2, N = 1 and pps = 1000 corresponding to the morphology of the superhydrophobic surface.

5.2.4. Holographic colours produced by 2D-LIPSS

The novel surface morphologies illustrated in Figure 67 and Figure 75 are highly interesting for applications since 2D-LIPSS can lead to an isotropic surface functionalization, featuring some advantages compared to 1D-LIPSS[9]. For example, the enhanced iridescence and the variety of the generated optical effects make it a good candidate for holographic[161] and anticounterfeiting[162] applications. Processing of large areas is necessary to evaluate the macroscopic properties of the novel textures. Three different textures were selected for this proof of concept: squares (Figure 82, A & A'), triangles (Figure 82, B) and random shallow ripples (Figure 82, C & C'). An optimization process was followed to improve the homogeneity of the structures

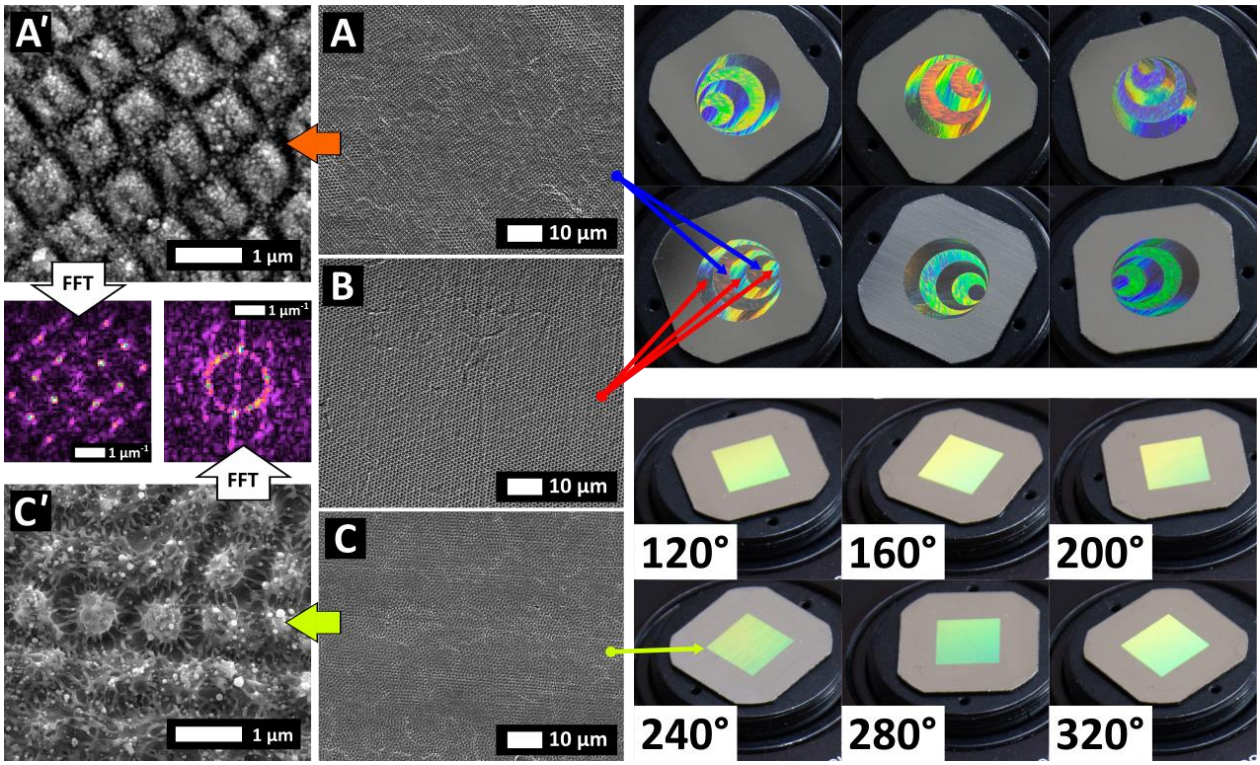

Figure 82 (published in ref [9]) Left: SEM of different 2D morphologies obtained on stainless-steel. Squares (A & A') and random ripples/dots (C & C'). F-T corresponds to the textures as indicated. Right: Photographs of the surface after homogeneous large area irradiation corresponding to different textures as indicated by arrows: Top: a two-colour holographic figure produced by surface texturing with squares and triangles as indicated. Bottom: Large area 8 x 8 mm textured with random ripples. The indicated angle is the azimuthal angle of the rotational stage.

over large areas as well as the optical appearance of the surface. A systematic variation of the fluence, overlap and hatch was considered. For the squares (Figure 82, A), the parameters used were: pps = 13, H = 2 µm, Φ = 0.2 J/cm^2 and $\Delta\tau$ = 500 ps. For the triangles (Figure 82, B) pps = 12, H = 2 µm, Φ = 0.14 J/cm^2 and $\Delta\tau$ = 3 ps, and for the random ripples (Figure 82, C): pps = 11, H = 4 µm, Φ = 0.12 J/cm^2 and $\Delta\tau$ = 3 ps. From the F-T analysis of 11 x 11 µm areas an average period of 933 ± 9 nm for the squares and for the random ripples an average period of 921 ± 17 nm was derived.

Squares and triangles were applied on the same surface shown in Figure 82 (center, up) under different azimuthal angles. Interestingly, due to the different number of symmetry axes (two for squares and three for triangles) a two-colour holographic pattern is formed. Finally, surface texturing with random shallow ripples (Figure 82, C) creates a particular optical behaviour of the surface; they exhibit iridescence independent of the azimuthal angle, generating a smooth optical effect shown in Figure 82 (center, bottom) [9].

5.3. Conclusion

Valuable data were provided within this work, both in surface functionalization, in understanding and controlling of laser induced structuring and in upscaling of a lab developed process. A variety of novel morphologies were obtained over large areas, and their macroscopic properties were demonstrated. In particular cases, the produced structures resemble functional surfaces found in nature. As an outcome of an extensive parametric study, a systematic link between the process parameters and the induced surface morphology was presented and elucidated. Spike sizes were controlled from from $\delta \sim 8$ µm to $\delta \sim 60$ µm by a variation of fluence, laser repetition rate and pulse-to-pulse overlap. Combining experimental data with simulations elaborating on surfaces temporal profile during processing we underline the role of T_{sat} in the

spike formation. Double-pulses were employed to tailor the surface morphology in the submicron scale and a variety of novel 2D submicron morphologies is presented. The forceful impact of the interpulse delay on controlling LIPSS formation process was illustrated. Specific time delay zones are identified in the ps and ns regime with respect to the laser induced structure morphology. Apart from interpulse delay, fluence and polarization play a key role in controlling 2D morphologies. We proposed the convection flow mechanism in order to interpret the various patterns formed upon double pulse irradiation.

Our approach is aimed on upscaling surface texturing both in terms of processing rate and surface area. Spikes were fabricated with a high repetition rate femtosecond laser employing single pulses at high processing rate (~1 min/cm^2). Areas much larger than the spot size were textured homogeneously with submicron ripples and novel 2D-LIPSS. We believe that our results pave the way for exploiting fs laser texturing in everyday applications combining state of the art know how with up to date technological advances.

References

1. Guay J-M, Calà Lesina A, Côté G, et al. Laser-induced plasmonic colours on metals. *Nat Commun*. 2017;8:16095. doi:10.1038/ncomms16095

2. Vorobyev AY, Guo C. Femtosecond laser blackening of platinum. *J Appl Phys*. 2008;104(5). doi:10.1063/1.2975989

3. Siddique RH, Gomard G, Hölscher H. The role of random nanostructures for the omnidirectional anti-reflection properties of the glasswing butterfly. *Nat Commun*. 2015;6(1):6909. doi:10.1038/ncomms7909

4. Hasan J, Webb HK, Truong VK, et al. Selective bactericidal activity of nanopatterned superhydrophobic cicada Psaltoda claripennis wing surfaces. *Appl Microbiol Biotechnol*. 2013;97(20):9257-9262. doi:10.1007/s00253-012-4628-5

5. Zorba V, Stratakis E, Barberoglou M, et al. Biomimetic artificial surfaces quantitatively reproduce the water repellency of a lotus leaf. *Adv Mater*. 2008;20(21):4049-4054. doi:10.1002/adma.200800651

6. Fraggelakis F, Mincuzzi G, Lopez J, Manek-Hönninger I, Kling R. Controlling laser-induced features morphology on stainless steel surfaces using high average power femtosecond laser. *2017 Eur Conf Lasers Electro-Optics Eur Quantum Electron Conf*. 2017. http://www.osapublishing.org/abstract.cfm?URI=CLEO_Europe-2017-CM_7_3.

7. Fraggelakis F, Mincuzzi G, Lopez J, Manek-hönninger I, Kling R. Ultrashort pulse laser-induced texturing of stainless steel at 1 MHz and high average power : impact of process parameters. *Proc SPIE*. 2017;10092(1):1-7. doi:10.1117/12.2251867

8. Fraggelakis F, Mincuzzi G, Lopez J, Manek-Hönninger I, Kling R. Texturing metal surface with MHz ultra-short laser pulses. *Opt Express*. 2017;25(15):18131-18139.

9. Fraggelakis F, Mincuzzi G, Lopez J, Manek-Hönninger I, Kling R. Controlling 2D laser nano structuring over large area with double femtosecond pulses. *Appl Surf Sci*. 2019;470:677-686. doi:https://doi.org/10.1016/j.apsusc.2018.11.106

10. Fraggelakis F, Mincuzzi G, Lopez J, Kling R, Manek-Hönninger I. Controlling Micron and Submicron Scale Laser Induced Surface Structures on Stainless Steel with Industrial Femtosecond Lasers. *J Laser Micro/Nanoengineering*. 2018;13(3):206-210. doi:10.2961/jlmn.2018.03.0010

11. Fraggelakis F, Mincuzzi G, Lopez J, Manek-Hönninger I, Kling R. 2D laser induced periodic surface structures with double cross-polarized pulses. *Laser-based Micro- Nanoprocessing XII*. 2018;(February):22. doi:10.1117/12.2287841

12. Fraggelakis F, Mincuzzi G, Manek-Hönninger I, Jopez J, Kling R. Generation of micro- and nano-morphologies on a stainless steel surface irradiated with 257 nm femtosecond laser pulses. *RSC Adv*. 2018;8(29):16082-16087. doi:10.1039/C8RA01774C

13. Schille J, Schneider L, Streek A, Mauersberger S, Loeschner U. Study on high-average power ultrashort pulse laser processing of AISI 304 stainless steel. In: *39th MATADOR Conference*. ; 2017.

14. Faas S, Bielke U, Weber R, Graf T. Scaling the productivity of laser structuring processes using picosecond laser pulses at average powers of up to 420 W to produce superhydrophobic surfaces on stainless steel AISI 316L. *Sci Rep*. 2019;9(1):1933. doi:10.1038/s41598-018-37867-y

15. Xia F, Jiang L. Bio-Inspired, Smart, Multiscale Interfacial Materials. *Adv Mater*. 2008;20(15):2842-2858. doi:10.1002/adma.200800836

16. Elbourne A, Crawford RJ, Ivanova EP. Nano-structured antimicrobial surfaces: From nature to synthetic analogues. *J Colloid Interface Sci*. 2017;508:603-616. doi:10.1016/j.jcis.2017.07.021

17. Dan Tan YX and YL. Biopatterning of Keratinocytes in Aqueous Two-Phase Systems as a Potential Tool for Skin Tissue Engineering. *MRS Adv*. 2017;357(May):1-8. doi:10.1557/adv.201

18. Lasagni A, Benke D, Kunze T, et al. Bringing the Direct Laser Interference Patterning Method to Industry : a One Tool-Complete Solution for Surface Functionalization. *Proc LPM*. 2014.

19. Pronko PP, Dutta SK, Squier J, Rudd J V., Du D, Mourou G. Machining of sub-micron holes using a femtosecond laser at 800 nm. *Opt Commun*. 1995;114(1-2):106-110. doi:10.1016/0030-4018(94)00585-I

20. Zoubir A, Richardson M, Canioni L, Brocas A, Sarger L. Optical properties of infrared femtosecond laser-modified fused silica and application to waveguide fabrication. *J Opt Soc Am B*. 2005;22(10):2138. doi:10.1364/JOSAB.22.002138

21. Lasagni A, Alamri S, Aguilar-Morales A, Rößler F, Voisiat B, Kunze T. Biomimetic Surface Structuring Using Laser Based Interferometric Methods. *Appl Sci 2018*. 2018;8:1260. doi:10.3390/APP8081260

22. Aguilar-Morales AI, Alamri S, Lasagni AF. Micro-fabrication of high aspect ratio periodic structures on stainless steel by picosecond direct laser interference patterning. *J Mater Process Technol*. 2018;252(September 2017):313-321. doi:10.1016/j.jmatprotec.2017.09.039

23. Lasagni AF, Menéndez-Ormaza BS. Two- and Three-Dimensional Micro- and Sub-Micrometer Periodic Structures Using Two-Beam Laser Interference Lithography. *Adv Eng Mater*. 2010;(1):54-60. doi:10.1002/adem.200900221

24. Kietzig A, Mirvakili MN, Kamal S, Englezos P, Hatzikiriakos SG. Nanopatterned Metallic Surfaces : Their Wettability and Impact on Ice Friction. *J Adhes Sci Technol*. 2011;25:1293-1303.

25. Vorobyev AY, Guo C. Multifunctional surfaces produced by femtosecond laser pulses. *J Appl Phys*. 2015;117(3):3-8. doi:10.1063/1.4905616

26. Kirner S V., Hermens U, Mimidis A, et al. Mimicking bug-like surface structures and their fluid transport produced by ultrashort laser pulse irradiation of steel. *Appl Phys A*. 2017;123(12):754. doi:10.1007/s00339-017-1317-3

27. Tsibidis GD, Barberoglou M, Loukakos PA, Stratakis E, Fotakis C. Dynamics of ripple formation on silicon surfaces by ultrashort laser pulses in subablation conditions. *Phys Rev B*. 2012;86(11):115316. doi:10.1103/PhysRevB.86.115316

28. Bonse J, Baudach S, Krüger J, Kautek W, Lenzner M. Femtosecond laser ablation of silicon-modification thresholds and morphology. *Appl Phys A Mater Sci Process*. 2002;74(1):19-25. doi:10.1007/s003390100893

29. Tsibidis G, Skoulas E, Stratakis E. Ripple formation on nickel irradiated with radially polarized femtosecond beams. *Opt Lett*. 2015;40(22):5172-5175.

30. Liu B, Wang W, Jiang G, et al. Evolution of nano-ripples on stainless steel irradiated by picosecond laser pulses. *J Laser Appl*. 2014;26(1):012001. doi:10.2351/1.4824310

31. Höhm S, Rosenfeld A, Krüger J, Bonse J. Femtosecond laser-induced periodic surface structures on

silica. *J Appl Phys*. 2012;112(1):014901. doi:10.1063/1.4730902

32. Papadopoulos A, Skoulas E, Tsibidis GD, Stratakis E. Formation of periodic surface structures on dielectrics after irradiation with laser beams of spatially variant polarisation: a comparative study. *Appl Phys A*. 2018;124(2):146. doi:10.1007/s00339-018-1573-x

33. Epperlein N, Menzel F, Schwibbert K, et al. Influence of femtosecond laser produced nanostructures on biofilm growth on steel. *Appl Surf Sci*. 2017;418:420-424. doi:10.1016/j.apsusc.2017.02.174

34. Nayak BK, Gupta MC. Self-organized micro/nano structures in metal surfaces by ultrafast laser irradiation. *Opt Lasers Eng*. 2010;48(10):940-949. doi:10.1016/j.optlaseng.2010.04.010

35. Bonse J, Koter R, Hartelt M, et al. Tribological performance of femtosecond laser-induced periodic surface structures on titanium and a high toughness bearing steel. *Appl Surf Sci*. 2015;336:21-27. doi:10.1016/j.apsusc.2014.08.111

36. Simitzi C, Efstathopoulos P, Kourgiantaki A, et al. Laser fabricated discontinuous anisotropic microconical substrates as a new model scaffold to control the directionality of neuronal network outgrowth. *Biomaterials*. 2015;67:115-128. doi:10.1016/j.biomaterials.2015.07.008

37. Lutey AHA, Gemini L, Romoli L, et al. Towards Laser-Textured Antibacterial Surfaces. *Sci Rep*. 2018;8(1):10112. doi:10.1038/s41598-018-28454-2

38. Gurevich EL. Mechanisms of femtosecond LIPSS formation induced by periodic surface temperature modulation. *Appl Surf Sci*. 2016;374:56-60. doi:10.1016/j.apsusc.2015.09.091

39. Sipe JE, Young JF, Preston JS, Van Driel HM. Laser-induced periodic surface structure. I. Theory. *Phys Rev B*. 1983;27(2):1141-1154. doi:10.1103/PhysRevB.27.1141

40. Gnilitskyi I, Derrien TJ, Levy Y, Bulgakova NM, Orazi L. High-speed manufacturing of highly regular femtosecond laser- induced periodic surface structures : physical origin of regularity. *Sci Rep*. 2017;7(8485). doi:10.1038/s41598-017-08788-z

41. Gräf S, Müller FA. Polarisation-dependent generation of fs-laser induced periodic surface structures. *Appl Surf Sci*. 2015;331:150-155. doi:10.1016/j.apsusc.2015.01.056

42. Bonse J, Hohm S, Kirner S V., Rosenfeld A, Kruger J. Laser-Induced Periodic Surface Structures—A Scientific Evergreen. *IEEE J Sel Top Quantum Electron*. 2017;23(3):9000615. doi:10.1109/JSTQE.2016.2614183

43. Romano J-M, Garcia-Giron A, Penchev P, Dimov S. Triangular laser-induced submicron textures for functionalising stainless steel surfaces. *Appl Surf Sci*. 2018;440:162-169. doi:10.1016/j.apsusc.2018.01.086

44. Skoulas E, Manousaki A, Fotakis C, Stratakis E. Biomimetic surface structuring using cylindrical vector femtosecond laser beams. *Sci Rep*. 2017;7(1):45114. doi:10.1038/srep45114

45. Nayak BK, Gupta MC, Kolasinski KW. Formation of nano-textured conical microstructures in titanium metal surface by femtosecond laser irradiation. *Appl Phys A Mater Sci Process*. 2008;90(3):399-402. doi:10.1007/s00339-007-4349-2

46. Tsibidis GD, Fotakis C, Stratakis E. From ripples to spikes: A hydrodynamical mechanism to interpret femtosecond laser-induced self-assembled structures. *Phys Rev B*. 2015;92(4):041405. doi:10.1103/PhysRevB.92.041405

47. Varlamova O, Bounhalli M, Reif J. Influence of irradiation dose on laser-induced surface nanostructures on silicon. *Appl Surf Sci*. 2013;278:62-66. doi:10.1016/j.apsusc.2012.10.140

48. Tsibidis GD, Stratakis E, Loukakos PA, Fotakis C. Controlled ultrashort-pulse laser-induced ripple formation on semiconductors. *Appl Phys A Mater Sci Process*. 2014;114(1):57-68. doi:10.1007/s00339-013-8113-5

49. Rosenfeld A, Rohloff M, Höhm S, Krüger J, Bonse J. Formation of laser-induced periodic surface structures on fused silica upon multiple parallel polarized double-femtosecond-laser-pulse irradiation sequences. *Appl Surf Sci*. 2012;258(23):9233-9236. doi:10.1016/j.apsusc.2011.09.076

50. Sedao X, Abou Saleh A, Rudenko A, et al. Self-Arranged Periodic Nanovoids by Ultrafast Laser-Induced Near-Field Enhancement. *ACS Photonics*. 2018;5(4):1418-1426. doi:10.1021/acsphotonics.7b01438

51. Dufft D, Rosenfeld A, Das SK, Grunwald R, Bonse J. Femtosecond laser-induced periodic surface structures revisited: A comparative study on ZnO. *J Appl Phys*. 2009;105(3). doi:10.1063/1.3074106

52. Abere MJ, Torralva B, Yalisove SM. Periodic surface structure bifurcation induced by ultrafast laser generated point defect diffusion in GaAs. *Appl Phys Lett*. 2016;108:153110. doi:10.1063/1.4946861

53. Bonse J, Höhm S, Rosenfeld A, Kruger J. Sub-100-nm laser-induced periodic surface structures upon irradiation of titanium by Ti:sapphire femtosecond laser pulses in air. *Appl Phys A Mater Sci Process*. 2013;110(3):547-551. doi:10.1007/s00339-012-7140-y

54. Römer GRBE, Skolski JZP, Obona JV, Huis In 't Veld AJ. Finite-difference time-domain modeling of laser-induced periodic surface structures. *Phys Procedia*. 2014;56(C):1325-1333. doi:10.1016/j.phpro.2014.08.058

55. Borowiec A, Haugen HK. Subwavelength ripple formation on the surfaces of compound semiconductors irradiated with femtosecond laser pulses. *Appl Phys Lett*. 2003;82(25):4462-4464. doi:10.1063/1.1586457

56. Ji X, Jiang L, Li X, et al. Femtosecond laser-induced cross-periodic structures on a crystalline silicon surface under low pulse number irradiation. *Appl Surf Sci*. 2015;326:216-221. doi:10.1016/j.apsusc.2014.11.124

57. Reif J, Varlamova O, Uhlig S, Varlamov S, Bestehorn M. On the physics of self-organized nanostructure formation upon femtosecond laser ablation. *Appl Phys A Mater Sci Process*. 2014;117(1):179-184. doi:10.1007/s00339-014-8339-x

58. Skolski JZP, Römer GRBE, Vincenc Obona J, Huis in 'T Veld AJ. Modeling laser-induced periodic surface structures: Finite-difference time-domain feedback simulations. *J Appl Phys*. 2014;115(10):103102. doi:10.1063/1.4867759

59. Garcia-Lechuga M, Puerto D, Fuentes-Edfuf Y, Solis J, Siegel J. Ultrafast Moving-Spot Microscopy: Birth and Growth of Laser-Induced Periodic Surface Structures. *ACS Photonics*. 2016;3(10):1961-1967. doi:10.1021/acsphotonics.6b00514

60. Jia X, Jia TQ, Peng NN, Feng DH, Zhang SA, Sun ZR. Dynamics of femtosecond laser-induced periodic surface structures on silicon by high spatial and temporal resolution imaging. *J Appl Phys*. 2014;115(14). doi:10.1063/1.4870445

61. Sokolowski-Tinten K, Barty A, Boutet S, et al. Short-pulse laser induced transient structure formation and ablation studied with time-resolved coherent XUV-scattering. *AIP Conf Proc*. 2010;1278:373-379. doi:10.1063/1.3507123

62. Fang R, Vorobyev A, Guo C. Direct visualization of the complete evolution of femtosecond laser-induced surface structural dynamics of metals. *Light Sci Appl*. 2017;6(3):e16256-7.

doi:10.1038/lsa.2016.256

63. Sundaram SK, Mazur E. Inducing and probing non-thermal transitions in semiconductors using femtosecond laser pulses. *Nat Mater*. 2002;1(4):217-224. doi:10.1038/nmat767

64. Tsibidis GD, Mimidis A, Skoulas E, et al. Modelling periodic structure formation on 100Cr6 steel after irradiation with femtosecond-pulsed laser beams. *Appl Phys A*. 2018;124(1):27. doi:10.1007/s00339-017-1443-y

65. Hohlfeld J, Wellershoff SS, Güdde J, Conrad U, Jähnke V, Matthias E. Electron and lattice dynamics following optical excitation of metals. *Chem Phys*. 2000;251(1-3):237-258. doi:10.1016/S0301-0104(99)00330-4

66. Bonn M, Denzler DN, Funk S, Wolf M, Wellershoff S-S, Hohlfeld J. Ultrafast electron dynamics at metal surfaces : Competition between electron-phonon coupling and hot-electron transport. *Phys Rev B*. 2000;61(2):1101-1105.

67. Rethfeld B, Kaiser A, Vicanek M, Simon G. Ultrafast dynamics of nonequilibrium electrons in metals under femtosecond laser irradiation. *Phys Rev B*. 2002;65(21):214303. doi:10.1103/PhysRevB.65.214303

68. Sokolowski-Tinten K, Bialkowski J, Von Der Linde D. Ultrafast laser-induced order-disorder transitions in semiconductors. *Phys Rev B*. 1995;51(20):14186-14198. doi:10.1103/PhysRevB.51.14186

69. Bonse J, Rosenfeld A, Krüger J. On the role of surface plasmon polaritons in the formation of laser-induced periodic surface structures upon irradiation of silicon by femtosecond-laser pulses. *J Appl Phys*. 2009;106:104910. doi:10.1063/1.3261734

70. Corkum PB, Brunel F, Sherman NK. Thermal Response of Metals to Ultrashort-Pulse Laser Excitation. *Phys Rev Lett*. 1998;61(25):2886-2889.

71. Zhigilei L V., Lin Z, Ivanov DS. Atomistic modeling of short pulse laser ablation of metals: Connections between melting, spallation, and phase explosion. *J Phys Chem C*. 2009;113(27):11892-11906. doi:10.1021/jp902294m

72. Kelly R, Miotello A. Comments on explosive mechanisms of laser sputtering. *Appl Surf Sci*. 1996;96-98:205-215. doi:10.1016/0169-4332(95)00481-5

73. Sedao X, Shugaev M V., Wu C, et al. Growth Twinning and Generation of High-Frequency Surface Nanostructures in Ultrafast Laser-Induced Transient Melting and Resolidification. *ACS Nano*. 2016;10(7):6995-7007. doi:10.1021/acsnano.6b02970

74. Bolme CA, Funk DJ. Ultrafast dynamic ellipsometry measurements of early time laser ablation of titanium thin films. *Appl Phys A Mater Sci Process*. 2008;92(4):761-766. doi:10.1007/s00339-008-4612-1

75. Rapp S, Kaiser M, Schmidt M, Huber HP. Ultrafast pump-probe ellipsometry setup for the measurement of transient optical properties during laser ablation. *Opt Express*. 2016;24(16):17572-17592. doi:10.1364/OE.24.017572

76. Aspnes DE, Studna AA. High Precision Scanning Ellipsometer. *Appl Opt*. 1975;14(1):220. doi:10.1364/AO.14.000220

77. Sotrop J, Kersch A, Domke M, Heise G, Huber HP. Numerical simulation of ultrafast expansion as the driving mechanism for confined laser ablation with ultra-short laser pulses. *Appl Phys A Mater*

Sci Process. 2013;113(2):397-411. doi:10.1007/s00339-013-7849-2

78. Shugaev M V, Gnilitskyi I, Bulgakova NM, Zhigilei L V. Mechanism of single-pulse ablative generation of laser-induced periodic surface structures. *Phys Rev B*. 2017;96(20):1-9. doi:10.1103/PhysRevB.96.205429

79. Chan WL, Averback RS, Cahill DG, Ashkenazy Y. Solidification velocities in deeply undercooled silver. *Phys Rev Lett*. 2009;102(9):1-4. doi:10.1103/PhysRevLett.102.095701

80. Bonse J, Bachelier G, Siegel J, Solis J. Time- and space-resolved dynamics of melting, ablation, and solidification phenomena induced by femtosecond laser pulses in germanium. *Phys Rev B - Condens Matter Mater Phys*. 2006;74:134106. doi:10.1103/PhysRevB.74.134106

81. Winter J, Rapp S, Schmidt M, Huber HP. Ultrafast laser processing of copper: A comparative study of experimental and simulated transient optical properties. *Appl Surf Sci*. 2017;417:2-15. doi:10.1016/j.apsusc.2017.02.070

82. Wu C, Christensen MS, Savolainen JM, Balling P, Zhigilei L V. Generation of subsurface voids and a nanocrystalline surface layer in femtosecond laser irradiation of a single-crystal Ag target. *Phys Rev B - Condens Matter Mater Phys*. 2015;91(3):035413. doi:10.1103/PhysRevB.91.035413

83. Inogamov NA, Zhakhovsky V V., Khokhlov VA, et al. Ultrafast lasers and solids in highly excited states: Results of hydrodynamics and molecular dynamics simulations. In: *Journal of Physics: Conference Series*. Vol 510. ; 2014. doi:10.1088/1742-6596/510/1/012041

84. Bauer F, Michalowski A, Kiedrowski T, Nolte S. Heat accumulation in ultra-short pulsed scanning laser ablation of metals. *Opt Express*. 2015;23(2):1035-1043. doi:10.1364/OE.23.001035

85. Bévillon E, Colombier JP, Dutta B, Stoian R. Ab Initio Nonequilibrium Thermodynamic and Transport Properties of Ultrafast Laser Irradiated 316L Stainless Steel. *J Phys Chem C*. 2015;119(21):11438-11446. doi:10.1021/acs.jpcc.5b02085

86. Katsumata Y, Morita T, Morimoto Y, Shintani T, Saiki T. Self-organization of a periodic structure between amorphous and crystalline phases in a GeTe thin film induced by femtosecond laser pulse amorphization. *Appl Phys Lett*. 2014;105:031907. doi:10.1063/1.4890862

87. Emmony DC, Howson RP, Willis LJ. Laser mirror damage in germanium at 10.6 μm. *Appl Phys Lett*. 1973;23(11):598-600. doi:10.1063/1.1654761

88. Guosheng Z, Fauchet PM, Siegman AE. Growth of spontaneous periodic surface structures on solids during laser illumination. *Phys Rev B*. 1982;26(10):5366-5381. doi:10.1103/PhysRevB.26.5366

89. Fauchet PM, Siegman AE. Surface ripples on silicon and gallium arsenide under picosecond laser illumination. *Appl Phys Lett*. 1982;40(9):824-826. doi:10.1063/1.93274

90. Bonse J, Munz M, Sturm H. Structure formation on the surface of indium phosphide irradiated by femtosecond laser pulses. *J Appl Phys*. 2005;97(1). doi:10.1063/1.1827919

91. Huang M, Zhao F, Cheng Y, Xu N, Xu Z. Origin of laser-induced near-subwavelength ripples: Interference between surface plasmons and incident laser. *ACS Nano*. 2009;3(12):4062-4070. doi:10.1021/nn900654v

92. Raether H. Surface plasmons on smooth and rough surfaces and on gratings. *Springer Tracts Mod Phys*. 1988;111:136. doi:10.1007/BFb0048317

93. Derrien TJYY, Itina TE, Torres R, Sarnet T, Sentis M. Possible surface plasmon polariton excitation under femtosecond laser irradiation of silicon. *J Appl Phys*. 2013;114(8). doi:10.1063/1.4818433

94. Derrien TJ-Y, Krüger J, Itina TE, Höhm S, Rosenfeld A, Bonse J. Rippled area formed by surface plasmon polaritons upon femtosecond laser double-pulse irradiation of silicon. *Opt Express*. 2013;21(24):29643. doi:10.1364/OE.21.029643

95. Skolski JZP, Römer GRBE, Obona J V., Ocelik V, Huis In 't Veld AJ, De Hosson JTM. Laser-induced periodic surface structures: Fingerprints of light localization. *Phys Rev B*. 2012;85:075320. doi:10.1103/PhysRevB.85.075320

96. Skolski JZP, Römer GRBE, Obona J V, Ocelik V, Huis AJ, Hosson JTM De. Inhomogeneous Absorption of Laser Radiation:Trigger of LIPSS Formation. *J Laser Micro/Nanoengineering*. 2013;8(1):1-5. doi:10.2961/jlmn.2013.01.0001

97. Déziel J-L, Dumont J, Gagnon D, Dubé LJ, Messaddeq SH, Messaddeq Y. Toward the formation of crossed laser-induced periodic surface structures. *J Opt*. 2015;17(7):075405. doi:10.1088/2040-8978/17/7/075405

98. Tsibidis GD, Stratakis E. Ripple formation on silver after irradiation with radially polarised ultrashort-pulsed lasers. *J Appl Phys*. 2017;121(16). doi:10.1063/1.4982071

99. Obara G, Maeda N, Miyanishi T, Terakawa M, Nedyalkov NN, Obara M. Plasmonic and Mie scattering control of far-field interference for regular ripple formation on various material substrates. *Opt Express*. 2011;19(20):19093. doi:10.1364/OE.19.019093

100. Dar MH, Saad NA, Sahoo C, Naraharisetty SRG, Desai NR. Ultrafast laser-induced reproducible nano-gratings on a molybdenum surface. *Laser Phys Lett*. 2017;14(2). doi:10.1088/1612-202X/aa5129

101. Huang M, Zhao FL, Jia TQ, Cheng Y, Xu NS, Xu ZZ. A uniform 290 nm periodic square structure on ZnO fabricated by two-beam femtosecond laser ablation. *Nanotechnology*. 2007;18(50). doi:10.1088/0957-4484/18/50/505301

102. Gregorčič P, Sedlaček M, Podgornik B, Reif J. Formation of laser-induced periodic surface structures (LIPSS) on tool steel by multiple picosecond laser pulses of different polarizations. *Appl Surf Sci*. 2016;387:698-706. doi:10.1016/j.apsusc.2016.06.174

103. Cong J, Yang J, Zhao B, Xu X. Fabricating subwavelength dot-matrix surface structures of Molybdenum by transient correlated actions of two-color femtosecond laser beams. *Opt Express*. 2015;23(4):5357. doi:10.1364/OE.23.005357

104. Qin W, Yang J. Controlled assembly of high-order nanoarray metal structures on bulk copper surface by femtosecond laser pulses. *Surf Sci*. 2017;661(March):28-33. doi:10.1016/j.susc.2017.03.005

105. Liu Q, Zhang N, Yang J, Qiao H, Guo C. Direct fabricating large-area nanotriangle structure arrays on tungsten surface by nonlinear lithography of two femtosecond laser beams. *Opt Express*. 2018;26(9):11718-11727. doi:10.1364/OE.26.011718

106. Qiao H, Yang J, Wang F, Yang Y, Sun J. Femtosecond laser direct writing of large-area two-dimensional metallic photonic crystal structures on tungsten surfaces. *Opt Express*. 2015;23(20):26617. doi:10.1364/OE.23.026617

107. Gemini L, Hashida M, Miyasaka Y, et al. Periodic surface structures on titanium self-organized upon double femtosecond pulse exposures. *Appl Surf Sci*. 2015;336:349-353. doi:10.1016/j.apsusc.2014.12.135

108. Fraggelakis F, Stratakis E, Loukakos PA. Control of periodic surface structures on silicon by combined temporal and polarization shaping of femtosecond laser pulses. *Appl Surf Sci*.

2018;444:154-160. doi:10.1016/j.apsusc.2018.02.258

109. Höhm S, Rosenfeld A, Krüger J, Bonse J. Laser-induced periodic surface structures on zinc oxide crystals upon two-colour femtosecond double-pulse irradiation. *Phys Scr*. 2017;92:034003. doi:10.1088/1402-4896/aa5578

110. Barberoglou M, Tsibidis GD, Gray D, et al. The influence of ultra-fast temporal energy regulation on the morphology of Si surfaces through femtosecond double pulse laser irradiation. *Appl Phys A Mater Sci Process*. 2013;113(2):273-283. doi:10.1007/s00339-013-7893-y

111. Bévillon E, Colombier JP, Recoules V, Stoian R. Free-electron properties of metals under ultrafast laser-induced electron-phonon nonequilibrium: A first-principles study. *Phys Rev B - Condens Matter Mater Phys*. 2014;89(11):1-11. doi:10.1103/PhysRevB.89.115117

112. Höhm S, Rosenfeld A, Krüger J, Bonse J. Laser-induced periodic surface structures on titanium upon single- and two-color femtosecond double-pulse irradiation. *Opt Express*. 2015;23(20):25959. doi:10.1364/oe.23.025959

113. Derrien TJ-YJY, Krüger J, Itina TE, Höhm S, Rosenfeld A, Bonse J. Rippled area formed by surface plasmon polaritons upon femtosecond laser double-pulse irradiation of silicon : the role of carrier generation and relaxation processes. *Appl Phys A Mater Sci Process*. 2013;117(1):77-81. doi:10.1007/s00339-013-8205-2

114. Höhm S, Herzlieb M, Rosenfeld A, Krüger J, Bonse J. Formation of laser-induced periodic surface structures on fused silica upon two-color double-pulse irradiation. *Appl Phys Lett*. 2013;103(25):254101. doi:10.1063/1.4850528

115. Höhm S, Herzlieb M, Rosenfeld A, Krüger J, Bonse J. Dynamics of the formation of laser-induced periodic surface structures (LIPSS) upon femtosecond two-color double-pulse irradiation of metals, semiconductors, and dielectrics. *Appl Surf Sci*. 2015;374:331-338. doi:10.1007/s00339-012-7184-z

116. Höhm S, Herzlieb M, Rosenfeld A, Kruger J, Bonse J. Laser-induced periodic surface structures on fused silica upon cross-polarized two-color double-fs-pulse irradiation. *Appl Surf Sci*. 2015;336:39-42. doi:10.1016/j.apsusc.2014.09.101

117. Höhm S, Rohloff M, Rosenfeld A, Kruger J, Bonse J. Dynamics of the formation of laser-induced periodic surface structures on dielectrics and semiconductors upon femtosecond laser pulse irradiation sequences. *Appl Phys A Mater Sci Process*. 2013;110(3):553-557. doi:10.1007/s00339-012-7184-z

118. Höhm S, Rosenfeld A, Krüger J, Bonse J. Area dependence of femtosecond laser-induced periodic surface structures for varying band gap materials after double pulse excitation. *Appl Surf Sci*. 2013;278:7-12. doi:10.1016/j.apsusc.2012.10.188

119. Barberoglou M, Gray D, Magoulakis E, Fotakis C, Loukakos P a, Stratakis E. Controlling ripples' periodicity using temporally delayed femtosecond laser double pulses. *Opt Express*. 2013;21(15):18501-18508. doi:10.1364/OE.21.018501

120. Höhm S, Herzlieb M, Rosenfeld A, Krüger J, Bonse J. Femtosecond laser-induced periodic surface structures on silicon upon polarization controlled two-color double-pulse irradiation. *Opt Express*. 2015;23(1):61. doi:10.1364/OE.23.000061

121. Hashida M, Nishii T, Miyasaka Y, et al. Orientation of periodic grating structures controlled by double-pulse irradiation. *Appl Phys A*. 2016;122(4):484. doi:10.1007/s00339-016-0011-1

122. Kam D-H, Kim J, Song L, Mazumder J. Formation mechanism of micro-spikes on AISI 4340 steel

with femtosecond laser pulses at near-threshold fluence. *J Micromechanics Microengineering*. 2015;25(4):045007. doi:10.1088/0960-1317/25/4/045007

123. Zhu JT, Shen YF, Li W, et al. Effect of polarization on femtosecond laser pulses structuring silicon surface. *Appl Surf Sci*. 2006;252(8):2752-2756. doi:10.1016/j.apsusc.2005.04.048

124. Ling EJY, Saïd J, Brodusch N, et al. Investigating and understanding the effects of multiple femtosecond laser scans on the surface topography of stainless steel 304 and titanium. *Appl Surf Sci*. 2015;353:512-521. doi:10.1016/j.apsusc.2015.06.137

125. Lopez J, Mincuzzi G, Mishchik K, Audouard E, Mottay EP, Kling R. Correlation between ablation efficiency, surface morphology, and multipass capability using a 100-W 10-MHz ultrafast laser. In: *Laser Applications in Microelectronic and Optoelectronic Manufacturing (LAMOM) XXIII*. ; 2018:8. doi:10.1117/12.2286483

126. Vorobyev AY, Guo C. Enhanced energy coupling in femtosecond laser-metal interactions at high intensities. *Opt Express*. 2006;14(26):13113-13119. doi:10.1364/OE.14.013113

127. Vorobyev AY, Guo C. Direct observation of enhanced residual thermal energy coupling to solids in femtosecond laser ablation. *Appl Phys Lett*. 2005;86(1):2003-2006. doi:10.1063/1.1844598

128. Di Niso F, Gaudiuso C, Sibillano T, Mezzapesa FP, Ancona A, Lugarà PM. Role of heat accumulation on the incubation effect in multi-shot laser ablation of stainless steel at high repetition rates. *Opt Express*. 2014;22(10):12200. doi:10.1364/OE.22.012200

129. Liu JM. Simple technique for measurements of pulsed Gaussian-beam spot sizes. *Opt Lett*. 1982;7(5):196-198.

130. Bauer F, Michalowski A, Nolte S. Residual Heat in Ultra-Short Pulsed Laser Ablation of Metals. *JLMN-Journal of Laser Micro/Nanoengineering*. 2015;10(3):325-328. doi:10.2961/jlmn.2015.03.0016

131. Zepf M, Landreman M, O'Keeffe K, Dromey B, Robinson T, Hooker SM. Generation of a train of ultrashort pulses from a compact birefringent crystal array. *Appl Opt*. 2007;46(22):5142. doi:10.1364/ao.46.005142

132. Zhou S, Ouzounov D, Li H, et al. Efficient temporal shaping of ultrashort pulses with birefringent crystals. *Appl Opt*. 2007;46(35):8488-8492. doi:10.1109/CLEO.2007.4452976

133. Tünnermann A, Ancona A, Döring S, et al. Femtosecond and picosecond laser drilling of metals at high repetition rates and average powers. *Opt Lett*. 2009;34(21):3304. doi:10.1364/ol.34.003304

134. Faucon M, Laffitte A, Lopez J, Kling R. Surface blackening by laser texturing with high repetition rate femtosecond laser up to 1MHz. *Proc SPIE*. 2014;8972(February):89721M. doi:10.1117/12.2039469

135. Lopez J, Mishchik K, Mincuzzi G, Audouard E, Mottay E, Kling R. Efficient metal processing using high average power ultrafast laser. *J Laser Micro Nanoeng*. 2017;12(3):296-303. doi:10.2961/jlmn.2017.03.0020

136. Hügel H, Dausinger F. *Handbook of the EuroLaser Academy*. ch. Interaction Phenomena, Chapman & Hall; 1998.

137. Kam DH, Mazumder J, Kim J. Conical microspike morphology formation and control on various metal surfaces using femtosecond laser pulse. *J Laser Appl*. 2016;28(4):042001. doi:10.2351/1.4954839

138. Lasagni F, Shao P, Hendricks JL, Shaw CM, Martin DC, Das S. Direct fabrication of periodic patterns with hierarchical sub-wavelength structures on poly (3 , 4-ethylene dioxythiophene)– poly (styrene sulfonate) thin films using femtosecond laser interference patterning. *Appl Surf Sci*. 2010;256:1708-1713. doi:10.1016/j.apsusc.2009.09.099

139. Račiukaitis G, Gedvilas M, Stankevičius E, Voisiat B, Malinauskas M. Fabrication of periodic micro-structures by holographic lithography. *Lith J Phys*. 2014;53(4):227-237. doi:10.3952/physics.v53i4.2765

140. Harzic R Le, Breitling D, Weikert M, et al. Pulse width and energy influence on laser micromachining of metals in a range of 100 fs to 5 ps. *Appl Surf Sci*. 2005;249(1-4):322-331. doi:10.1016/j.apsusc.2004.12.027

141. Bonse J, Rosenfeld A, Krüger J. Implications of transient changes of optical and surface properties of solids during femtosecond laser pulse irradiation to the formation of laser-induced periodic surface structures. *Appl Surf Sci*. 2011;257(12):5420-5423. doi:10.1016/j.apsusc.2010.11.059

142. JJ Nivas J, He S, Rubano A, et al. Direct Femtosecond Laser Surface Structuring with Optical Vortex Beams Generated by a q-plate. *Sci Rep*. 2015;5:17929. doi:10.1038/srep17929

143. Hu H, Watson JA, Cribb BW, Watson GS. Fouling of nanostructured insect cuticle : adhesion of natural and artificial contaminants. *Biofouling*. 2012;27(10):37-41.

144. Sedao X, Maurice C, Garrelie F, et al. Influence of crystal orientation on the formation of femtosecond laser-induced periodic surface structures and lattice defects accumulation. *Appl Phys Lett*. 2014;104:171605. doi:10.1063/1.4874626

145. Gaudiuso C, Giannuzzi G, Volpe A, Lugarà PM, Choquet I, Ancona A. Incubation during laser ablation with bursts of femtosecond pulses with picosecond delays. *Opt Express*. 2018;26(4):3801. doi:10.1364/OE.26.003801

146. Tang Y, Yang J, Zhao B, Wang M, Zhu X. Control of periodic ripples growth on metals by femtosecond laser ellipticity. *Opt Express*. 2012;20(23):25826-25833. doi:10.1364/OE.20.025826

147. Smith MK, Davis SH. Instabilities of dynamic thermocapillary liquid layer. Part 1. Convective instabilities. *J Fluid Mech*. 1983;132:119-144. doi:10.1017/S0022112083001512

148. Pearson JRA. On convection cells induced by surface tension. *J Fluid Mech*. 1958;4(05):489. doi:10.1017/S0022112058000616

149. Busse FH, Whitehead JA. Instabilities of convection rolls in a high Prandtl number fluid. *J Fluid Mech*. 1971;47(2):305-320. doi:10.1017/S0022112071001071

150. Cross MC, Hohenberg PC. Pattern formation outside of equilibrium. *Rev Mod Phys*. 1993;65(3):851-1112. doi:10.1103/RevModPhys.65.851

151. Busse FH. Non-linear properties of thermal convection. *Reports Prog Phys*. 1978;41:1929.

152. Tsibidis GD, Skoulas E, Papadopoulos A, Stratakis E. Convection roll-driven generation of supra-wavelength periodic surface structures on dielectrics upon irradiation with femtosecond pulsed lasers. *Phys Rev B*. 2016;94(081305):1-18.

153. Kirichenko NA, Barmina E V., Shafeev GA. Theoretical and Experimental Investigation of the Formation of High Spatial Frequency Periodic Structures on Metal Surfaces Irradiated by Ultrashort Laser Pulses. *Phys Wave Phenom*. 2018;26(4):264-273. doi:10.3103/S1541308X18040027

154. Koschmieder EL, Pallas SG. Heat transfer through a shallow, horizontal convecting fluid layer. *Int*

J Heat Mass Transf. 1974;17(9):991-1002. doi:10.1016/0017-9310(74)90181-1

155. Lalanne P, Lemercier-Lalanne D. On the effective medium theory of subwavelength periodic structures. *J Mod Opt*. 1996;43(10):2063-2085.

156. Lerman GM, Levy U. Generation of a radially polarized light beam using space-variant subwavelength gratings at 1064 nm. *Opt Lett*. 2008;33(23):2782-2784. doi:10.1364/OL.33.002782

157. Mateus CFR, Huang MCY, Deng Y, Neureuther AR, Chang-hasnain CJ. Ultrabroadband Mirror Using Low-Index Cladded Subwavelength Grating. *IEEE PHOTONICS Technol Lett*. 2004;16(2):518-520.

158. Kanamori Y, Ishimori M, Hane K. High Efficient Light-Emitting Diodes With Antireflection Subwavelength Gratings. *IEEE PHOTONICS Technol Lett*. 2002;14(8):1064-1066.

159. Huang Y, Chattopadhyay S, Jen Y, et al. Improved broadband and quasi- omnidirectional anti-reflection properties with biomimetic silicon nanostructures. *Nat Nanotechnol*. 2007;2:770-774. doi:10.1038/nnano.2007.389

160. Gemini L, Faucon M, Romoli L, Kling R. High throughput laser texturing of super-hydrophobic surfaces on steel. *Laser-based Micro- Nanoprocessing XI*. 2017:100921G. doi:10.1117/12.2252649

161. Jwad T, Penchev P, Nasrollahi V, Dimov S. Applied Surface Science Laser induced ripples ' gratings with angular periodicity for fabrication of diffraction holograms. *Appl Surf Sci*. 2018;453:449-456. doi:10.1016/j.apsusc.2018.04.277

162. Ageev EI, Veiko VP, Vlasova EA, et al. Controlled nanostructures formation on stainless steel by short laser pulses for products protection against falsification. *Opt Express*. 2018;26(2):2117. doi:10.1364/OE.26.002117